

Facultad de Física
Departamento de Física Atómica, Molecular y Nuclear



VNIVERSITAT
DE VALÈNCIA

TRITIUM: Design, Construction and Commissioning of an In-Water Tritium Detector

Marcos Martínez Roig

PhD in Physics

January 18, 2022

Under the supervision of:

José Díaz Medina

Nadia Yahlali Haddou

*Dedicated to
my family*

Sometimes it is the people no one imagines anything
of who do the things that no one can imagine.

"Alan Turing"

I

Acknowledgements

Muchas personas han colaborado a lo largo de estos cuatro años para hacer posible este trabajo. En primer lugar me gustaría agradecer enormemente a mis tutores, Jose Díaz Medina y Nadia Yahlali Haddou, por intentar transmitirme en todo momento tantos conocimientos como les ha sido posible, sin los cuales nada de esto hubiera sido posible. También agradecer su tiempo ya que, a pesar de sus obligaciones, siempre han encontrado un hueco en sus agendas para ayudarme con cualquier problema. Estoy muy agradecido por su cercanía y sus consejos, tanto en el mundo laboral como en la vida personal, los cuales me han ayudado a llegar a donde estoy ahora.

En segundo lugar me gustaría agradecer a mis compañeros de laboratorio Andrea Esparcia Córcoles, Ana Bueno Fernández, Marcos Llanos Expósito y sobre todo a Mireia Simeo Vinaixa, con quienes los largos e interminables trabajos de laboratorio han sido mucho más fáciles, ayudandome en todo momento a comprender y mejorar los resultados experimentales obtenidos. También me gustaría agradecer a los técnicos e investigadores del LARAM, Clodoaldo Roldán García, Teresa Cámara García, Vanesa Delgado Belmar y Rosa María Rodríguez Galán, por su ayuda, su tiempo y sus esfuerzos en hacer todo esto haya sido posible.

En tercer lugar me gustaría agradecer a todos los investigadores del proyecto TRITIUM, gente que me ha acogido con los brazos abiertos, que me ha ayudado en todo lo que les ha sido posible y de la que he tenido

el placer de trabajar y aprender a su lado.

En cuarto lugar me gustaría agradecer a David Calvo Díaz-Aldagalán, ingeniero del IFIC, por su tiempo y su ayuda en los diseños de las distintas PCBs utilizadas en el proyecto TRITIUM.

Finalmente me gustaría dar las gracias a los investigadores de otros proyectos los cuales, pese a no ayudarme directamente en mi labor de investigación, si han aportado a mi trabajo debido a las sinergias existentes entre los objetivos experimentales de los proyectos:

- A los investigadores del proyecto DUNE, Anselmo Cervera, Miguel Angel García y Justo Martin-Albo, los cuales me han ayudado con su tiempo, sus conocimientos e su instrumentación experimental a completar la caracterización de los SiPMs.
- A los ingenieros del proyecto NEXT, Vicente Álvarez, Marc Querol, JAVIER, Sara Cárcel, con quienes he compartido laboratorio y, aun sin trabajar directamente con ellos, siempre estaban dispuestos a echar una mano.
- A los investigadores del IFIMED, Gabriela Llosá, Ana Ros, Marina Borja Lloret, John Barrio, Rita Viegas y Jorge Roser e investigadores del proyecto ATLAS (Urmila Soldevila y Carlos Mariña) por prestarnos sus instalaciones y, en concreto, sus sistemas de control de temperatura los cual fueron necesario para la caracterización de los SiPMs.
- A los investigadores del laboratorio HYMNS, Ion Ladarescu y César Domingo, quienes me ayudaron en mis primeros pasos con la electrónica PETsys además de asesorarme con las questiones que me han surgido a lo largo del camino.
- A los investigadores del ICMOL, Henk Bolink, Alejandra Soriano y

Lidón Gil Escrig, por ayudarnos con el protocolo de limpieza de las fibras centelleadoras además de permitirnos usar sus instalaciones.

- A toda la gente de los distintos departamentos del IFIC que hay ayudado con su tiempo y sus consejos. Me gustaría agradecer especialmente la ayuda de Jose Vicente Civera, Manolo Montserrat, Jose Luis Jordan y Daniel Tchogna del departamento de mecánica, Ximo Navajas, Ximo Nadal, Carlos Martinez y Francisco Javier Sanchez del departamento de informática y Manuel Lopez, Jorge Nacher y Jose Mazorra del departamento de electrónica.
- A mis compañeros del IFIC, Mireia, Pepe, Kevin, Jose, Pablo, Victor, Ana y David los cuales, aun sin haber aportado directamente a mi trabajo, compartir mis días con ellos ha sido uno de los mayores apoyos de esta aventura.

Finalmente me gustaría agradecer al programa INTERREG-SUDOE por financiar el proyecto TRITIUM.

Abstract

Tritium is one of the most abundantly emitted radioisotopes by nuclear facilities and, specifically, by nuclear power plants. Large amounts of tritium are normally produced in the water of their cooling system, which are finally emitted to the environment. Due to the fact that large releases of tritium could be dangerous for human health and for the environment, there exist several regulations around the world which try to control this radioactive emissions in each country, like the Directive Europeen 2013/51/Euratom, which establishes the tritium limit for drinking water in Europe to 100 Bq/L, or the U. S. Environmental Protection Agency, in United States, that limits tritium in drinking water to 20 nCi/L.

Due to the low energy of electrons emitted in the tritium decay, very sensitive detectors are needed for measuring them like LSC. The issue with LSC is that it is an off-line method and the measurement process can take 2 days or more, a time too long to detect a problem in the NPP.

Detectors based on solid scintillators are a promissing idea for building a tritium detector that works in quasi-real time. This type of detectors is developed so far succesfully but without achieving the required sensitivity of the legal limits.

The results of the TRITIUM project are presented in this thesis. In the framework of this project a quasi-real time monitor for low tritium

VIII

activities in water have been developed. This monitor is based on a tritium detector that contains several detection cells which are read in parallel, several active vetos and a passive shielding for reducing the natural radioactive background and a water purification system to prepare the sample before being measured. Each detection cell is made up of hundreds of scintillating fibers read out by PMTs or SiPM arrays.

The final objective of this monitor will be the radiological protection around the nuclear power plant. This monitor will provide an alarm in case of an unexpected tritium release that exceeds the legal limits established in Europe. The final idea will be to include this monitor in the early alarm system of Extremadura consisting of several detectors the objective of which is to control the impact of Nuclear Power Plants to the environment.

Keywords: Very low-energy charged particle detectors, radiation monitoring, tritium detection, scintillators, scintillating fibers and light guides, detector design and construction technologies and materials, instruments for environmental monitoring, detector modelling and simulations.

Nomenclature and Acronyms

Acronyms:

<i>ALARA</i>	— As Low As Reasonably Achievable
<i>APD</i>	— Avalanche Photodiode
<i>BIXS</i>	— Beta Induced X-ray Spectrometry
<i>BWR</i>	— Boiled Water Reactor
<i>CCD</i>	— Charge-Coupled Device
<i>CDF</i>	— Dose Conversion Factor
<i>CE</i>	— Collection Efficiency
<i>CL</i>	— Collection Efficiency
<i>CNRS</i>	— Le Centre National de la Recherche Scientifique, France
<i>CSN</i>	— Nuclear Safety Council
<i>C_t</i>	— Terminal Capacitance of the SiPM
<i>DAQ</i>	— Data Acquisition System
<i>DRIM</i>	— Detecção da Radiação e Laboratório Imagem Médica laboratoire (Laboratory for Radiation Detection and Medical Imaging)
<i>EEC</i>	— European Economic Community
<i>EPA</i>	— Environmental Protection Agency
<i>EU</i>	— European Union
<i>EURATOM</i>	— European Atomic Energy Community
<i>FF</i>	— Fill Factor of a SiPM
<i>G – APD</i>	— Geiger Avalanche Photodiode

X

GCR	— Gas-Cooled Reactor
GL	— Guideline Level
G_{PMT}	— Gain of the PMT
G_{SiPM}	— Gain of the SiPM
$HPGe$	— High Purity Germanium Detector
HV	— High Voltage
HWR	— Heavy Water Reactor
$IAEA$	— International Atomic Energy Agency
IC	— Ionization Chamber
$ICRP$	— International Commission on Radiological Protection
$ICRU$	— International Commission of Radioactivity Units and Measurements
I_{DC}	— Intensity of the PMT due to the dark current
I_{PMT}	— Intensity of the PMT when photons are detected
ISR	— International Society of Radiology
$LARUEX$	— Laboratorio de Radiactividad Ambiental of the University of Extremadura (Environmental Radioactivity Laboratory of the University of Extremadura)
LED	— Light-Emitting diode
LSC	— Liquid Scintillation Counting
LWR	— Liquid Water Reactor
$MAPD$	— Micro-Pixel Avalanche Photodiode
MDA	— Minimum Detectable Activity
$MPPC$	— Multi-Pixel Photon Counter
$MRS - ADP$	— Metal-Resistor-Semiconductor Avalanche Photodiode
NA	— Numerical Apertures
NPP	— Nuclear Power Plants
P_{av}	— Avalanche probability in a SiPM
PCB	— Printed Circuit Board
PDE	— Photodetection Efficiency of the SiPM
$PHWR$	— Pressurized Heavy Water Reactor
$PMMA$	— Polymethyl Methacrylates

<i>PMT</i>	— PhotoMultiplier Tube
<i>POF</i>	— Plastic Optical Fiber
<i>PVC</i>	— Polyvinylchloride
<i>PWR</i>	— Pressurized Water Reactor
<i>q</i>	— Annual Volume of drinking water consumed
<i>QE</i>	— Quantum Efficiency
<i>quasi-real</i>	— Less than 10 minuts
<i>RDL</i>	— Reference Dose Level
<i>REA</i>	— Red de Estaciones Automáticas
<i>REM</i>	— Red de Estaciones de Muestreo
<i>ROI</i>	— Region of interest
<i>R_q</i>	— Quenching resistance of the SiPM
<i>S</i>	— Energy loss by the particle per unit of path length
<i>SDD</i>	— Silicon Drift Detector
<i>SiPM</i>	— Silicon PhotoMultiplier
<i>SSPM</i>	— Solid State PhotoMultiplier
<i>STP</i>	— Standard Temperature and Pressure conditions
<i>UDL</i>	— Upper Detection Limit
<i>UN</i>	— United Nations
<i>UNSCEAR</i>	— United Nations Scientific Committee on the Effects of Atomic Radiation
<i>U.S.</i>	— United States
<i>USA</i>	— United States of America
<i>U.S.DOE</i>	— United States Department of Energy
<i>U.S.EIA</i>	— United States Energy Information Administration
<i>U.S.EPA</i>	— United States Environmental Protection Agency
<i>V_{BD}</i>	— Breakdown Voltage of the SiPM
<i>V_{bias}</i>	— Supply Voltage of the SiPM
<i>V_O</i>	— Potential difference between the n and p layers of the SiPM
<i>V_{OV}</i>	— Over voltage of the SiPM
<i>WHO</i>	— World Helth Organization

XII

ΔTV_{op}	— Temperature Coefficient (mV/ $^{\circ}C$)
δ	— Multiplication factor of a PMT dynode

Atomic and nuclear symbols

A_m	— Activity Measured
2_1D	— Deuterium (Non-Radiative Hydrogen Isotope)
D_2O	— Heavy Water
E_b	— Binding energy of the electron in a specific material
E_e	— Energy of the electron
$E_{\gamma} = h\nu$	— Energy of the photon
F_{sci}	— Active surface of the Plastic Scintillator
mip	— Minimum Ionizing Particle
m_0	— Rest mass of a electron
$NaI(Tl)$	— Thallium doped Sodium Iodide
OBT	— Organic tritium molecule
q_e	— Electron Charge
Q_{β}	— Energy released in a radioactive decay
S	— Specific Energy Lost
S_{ij}	— Single states of energy levels of electrons in scintillator
$T_{1/2}$	— Half-life Time of a Radioactive Element
T_{ij}	— Triple states of energy levels of electrons in scintillator
ε_{det}	— Specific Detector Efficiency
η_{det}	— Intrinsic Detector Efficiency
λ	— Wavelength
λ_p	— Maximum wavelength of the associated spectrum
σ	— Cross Section of a radioactive process
σ^{rel}	— Relative uncertainty
σ_{sys}	— Sistematically Component of the Uncertainty
σ_{st}	— Stadistical Component of the Uncertainty

- σ_t — Total Uncertainty of the Measurement
 σ_{TM} — Uncertainty present in the tritium measurement due to scintillating fibers

Units:

- kcps — Kilo Counts per Second
mrem — Millirem
STP — Standard Temperature ($0^\circ\text{C} = 273\text{K}$) and Pressure (1 atm)
S/cm — Siemen per Centimeter

Contents

Acknowledgements	III
Abstract	VII
Nomenclature and Acronyms	IX
List of Figures	XXXI
List of Tables	XXXVI
1 Introduction	1
1.1 Tritium and Nuclear Energy	1
1.2 Tritium Properties and Radiological Hazards	9
1.3 Current Legislation	18
1.4 This Thesis	20

2 Methods of Detection of Tritium In-Water	23
2.1 Tritium Detection State-of-the-Art	23
2.2 The TRITIUM Project	27
3 Design Principles and Components of TRITIUM	33
3.1 Detector System Overview	33
3.2 TRITIUM Detector	35
3.2.1 Interaction of Particles with Matter	35
3.2.2 Plastic Scintillators	39
3.2.3 Light Detection in Photosensors	46
3.2.4 Electronic Readout	63
3.3 Water Purification System	73
3.3.1 Objectives	73
3.3.2 Design of the Water Purification System	73
3.4 Background Rejection System	76
3.4.1 Passive Shield (Lead)	78
3.4.2 Active Shield (Cosmic Veto)	79
4 TRITIUM Monitor R&D	85
4.1 R&D for the Scintillating Fibers	85

4.1.1	Surface-Conditioning Method of Scintillating Fiber.	86
4.1.2	Light Collection Characterization of Scintillating Fibers	103
4.2	Characterization of the SiPM	115
4.3	Characterization of the Water Purification System	125
4.4	Characterization of the Cosmic Veto	128
5	TRITIUM Detector Prototypes	137
5.1	First Prototypes	138
5.1.1	TRITIUM-IFIC-0	138
5.1.2	TRITIUM-IFIC-1	144
5.2	Latest TRITIUM Prototypes	149
5.2.1	TRITIUM-Aveiro	150
5.2.2	TRITIUM-IFIC-2	156
5.3	Experimental Results in Arrocampo Dam	166
5.4	Modular TRITIUM Detector	168
6	Simulations	171
6.1	Geant4 Environment	171
6.2	Simulations to Optimize the TRITIUM Monitor Design	173
6.2.1	The Tritiated Water Source	174

6.2.2	Energy Deposition and Light Output of Scintillating Fibers	175
6.2.3	Fiber Length	179
6.2.4	Fiber Diameter	182
6.2.5	Effect of the PMMA windows	183
6.3	Simulations of the TRITIUM Monitor	185
6.3.1	Simulation of the TRITIUM-IFIC-2 Prototype	185
6.3.2	Lead Shield and Cosmic Veto	189
7	Conclusions and Prospects	197
 Appendices		
A	Electronic Readout for characterization the SiPM 13360-6075 Model	207
B	Water Purification System	211
C	Preparation of Liquid Radioactive Source of Tritium	215
D	Electronic System of TRITIUM-Aveiro prototype	217

List of Figures

1.1	Annual average distribution of the radioactive dose received by the population [IAE21].	2
1.2	Networks of automatic and sampling stations managed by the spanish CSN. (Above) Measurement locations of the REA [CSN21b]. The white box is the daily average of the gamma dose and the green box is the monthly average of the gamma dose. (Below) Measurement locations of the REM [CSN21c]. Blue dots are locations near nuclear facilities, and green dots are locations uniformly distributed throughout the country. .	6
1.3	Tritium sampling locations around Cofrentes NPP.	11
1.4	Tritium activity levels in surface water around Cofrentes NPP from January 2006 to November 2019. (Above) 6 km upstream. (Middle) 1 km downstream. (Below) 5 km downstream. The white points are the detection limit and the green points are the measured activity, when this is above the detection limit [CSN21c]. The maximum level of tritium measured since of January 2, 2006 is around 32 Bq/L	12

1.5	Tritium activity levels in groundwater around Cofrentes NPP from January 2006 to November 2019 [CSN21c]. (Above) 1 km before NPP. (Below) 1 km after NPP.	13
1.6	(Above) Tritium energy levels [IAEA]. (Below) Graphic representation of tritium decay [Pre19].	14
1.7	Energy spectrum of tritium electrons [Lin20].	15
2.1	(Above) Arrocampo dam and Almaraz Nuclear Power Plant. (Below) Tagus river along Spain and Portugal.	29
3.1	Scheme of the scintillator detector.	35
3.2	Domain regions of the three most probable types of interactions of gamma rays with matter. The lines show the values of Z and $h\nu$ where two interaction processes are equally likely [Kno99].	37
3.3	Jablonsky diagram [Kno99].	41
3.4	Stokes shift [Kno99].	42
3.5	Emission spectrum of BCF-12 scintillating fibers of Saint-Gobain [Cer05].	44
3.6	Photon collection in a single clad fiber [Cer05].	45
3.7	Scheme of a PMT [Kno99].	49
3.8	Quantum efficiency spectrum for the PMT used in TRITIUM R&D studies (R8520-406) [K.K19].	50
3.9	Hamamatsu commercial voltage divider electronic circuit with negative (up) and positive (below) supply high voltage [K.K19].	51

3.10 Electronic scheme of the voltage divider circuit used for working with PMTs without internal gain).	53
3.11 Scheme of a APD and electrical symbol used [Opt].	54
3.12 SiPM output pulses displayed on oscilloscope, model MSO44X from Tektronix [Tek21]. Several height pulses are observed, associated to a different number of SiPM pixels fired at the same time. The persistence function of the oscilloscope is used.	56
3.13 (a) Electronic scheme of a SiPM and (b) output current of a SiPM as a function of the reverse voltage. As shown, the quenching is an essential working mechanism of SiPMs [sl17].	57
3.14 Photon detection efficiency (PDE) spectrum for SiPM S13360-**75 models [Div16b].	61
3.15 Schemes of the different electronic for measuring with PMTs. a) Employed when only one PMT is used. b) Employed when two PMTs are used in time coincidence. c) Employed when four PMTs are used in time coincidence.	65
3.16 Different possibilities when time coincidences with PMTs are done. a) Event detected in only one PMT, one detector. b) Event detected in two PMTs, one detector. c) Event detected in two PMTs, other detector. d) Event detected in all PMTs, both detector.	68
3.17 Signal amplified and logical gate (input signals of MCA).	69
3.18 Different parts of PETsys system [PET].	70
3.19 a) Electronic board used to provide the SiPM bias voltage and to read the SiPM output signal. b) Electronical scheme in which this PCB is based.	72

3.20 Scheme of water purification system of TRITIUM.	74
3.21 a) Lead Bricks b) and c) Two layers for the lead bricks of the shield.	78
3.22 a) Scheme of the aluminium structure of the shield; b) The lead shield partially mounted.	79
3.23 Cosmic veto and Tritium-IFIC-2 prototype in an aluminum mechanical structure developed at IFIC.	80
3.24 Hard cosmic events detected with the cosmic veto of TRITIUM: a) Real coincidence event, b) randomly coincidence envent that may mimic a hard cosmic event.	81
3.25 Hard cosmic muon rate at different depths with respect to the sea level (10^0) [Szu15].	82
3.26 Emission energy spectrum of the plastic scintillator from Epic-Crystals used for the cosmic vetos [Cry20].	83
3.27 Different layers used to wrap the cosmic veto detectors. a) Scintillator without coating. b) PTFE coating. c) Aluminium coating. c) d) Black tape coating.	84
4.1 Unsuccessful results of using commercial techniques for cleaving the scintillating fibers a) Fiber end deformation b) Fiber end cracks. Pictures taken with the microscope PB 4161 from EUROMEX.	87
4.2 Plastic fiber cleaver developed in TRITIUM experiment. . . .	88
4.3 Fiber end after cleaving process using the home-made cleaver. Pictures taken with the microscope PB 4161 from EUROMEX.	89

4.4	Manual polishing method implemented by Thorlabs.	90
4.5	Result of the polishing process. a) Fiber end after cleaving b) Fiber end after cleaving and manual polishing with Thorlabs technique. Pictures taken with the microscope PB 4161 from EUROMEX.	91
4.6	Polishing machine developed for TRITIUM.	92
4.7	Components of the fiber polishing machine. a) Polishing ta- ble. b) Fiber with ballast metal piece. c) Horizontal screws and PMMA plate. d) A movement switch with its cables inserted inside its holding piece.	93
4.8	Electronic system of Polishing machine.	95
4.9	Setup used to test the effect of the fiber polishing on light transmission to the PMTs. This setup is placed in a dark test box for the measurements.	96
4.10	Energy spectra recorded with polished and unpolished fibers for the radioactive background.	97
4.11	Energy spectra recorded with polished and unpolished fibers. a) for the ^{60}Co source b) for the ^{90}Sr source	99
4.12	Schematic representation of the wetting properties of a flat surface (gray) in contact with a drop of liquid (blue). The wetting property is characterized by the angle formed be- tween the surface of both objects. The smaller angle, the better wetting property of the material. [comb]	100
4.13	Energy spectra of the radioactive background before and af- ter the cleaning process.	101

4.14 Energy spectra obtained before and after the cleaning process using a radioactive source of a) ^{137}Cs and b) ^{90}Sr	102
4.15 Setup used for fiber characterization.	104
4.16 Emission spectrum measured in the laboratory for the LED model 435-03 from Roithner LaserTechnik GmbH Company.	105
4.17 PMT photocurrent as a function of the first dynode voltage. Error bars are included but they are too small to be visible.	106
4.18 Number of photons measured by the PMT as a function of the polarization current of the LED. a) Response of the PMT in the intensity range of tritium events. b) Response of the PMT in the range 0 – 2500 photons/ns. Error bars are included but they are too small to be visible.	108
4.19 Number of photons/ns reaching the PMT for Uncladded fibers. Error bars are included but they are too small to be visible.	110
4.20 Number of photons/ns reaching the PMT for ten samples. a) Single clad fibers, b) Multi-clad fibers. Error bars are included but they are too small to be visible.	111
4.21 Average number of photons per ns versus LED current for 10 samples of each fiber type (uncladded, single clad and multi-clad fibers). Error bars are included but they are too small to be visible.	113
4.22 I-V curves measured for the SiPM model Hamamatsu S13360-1375 with the bias voltage applied in a) forward direction b) reverse direction. The measurements were taken at $T = 25^\circ\text{C}$ and humidity $H = 45\%$	117

4.23 Above) Trigger signal (green) and SiPM output pulses (yellow). Below) SPS spectrum obtained by integrating and histogramming the SiPM output pulses. This measurement was done at $T = 25^\circ\text{C}$, $V_{bias} = 53.98$ and humidity of $H = 60\%$	119
4.24 ROOT analysis performed to obtain the SiPM gain. a) Fit of the SPS spectrum to various Gaussian functions. b) Charge of successive number of pixels as a function of the number of pixels fired. Error bars are within point size. This experience was carried out at $T = 25^\circ\text{C}$, $V_{bias} = 53.98$ V and humidity of $H = 45\%$	120
4.25 Dependence of the SiPM gain with the a) Temperature b) Bias voltage.	122
4.26 SiPM gain measured as a function of the temperature after implementation of the gain stabilization method.	124
4.27 Reference points used for veto mapping.	129
4.28 Measurement of a radioactive source ^{137}Cs with the TRI-TIUM cosmic detector with and without wrapping.	130
4.29 Bidimensional graph of the count rate (Mapping) measured with two different TRITIUM cosmic detectors using a radioactive source of ^{60}Co	131
4.30 Counting rate a) as a function of high voltage for fixed thresholds and b) as function of thresholds for fixed high voltage. in semilogaritmic scale	133
4.31 Energy spectrum measured with the cosmic veto.	134

4.32 Measurement of the cosmic veto for several distances between the two scintillators. Above) Energy spectrum of the cosmic veto for several distance. Below) Fit of the cosmic veto rate versus distance to a second degree polynomial.	135
5.1 a) Metallic piece of the fiber bundle. b) and c) Bundle of 35 fibers, the length of which is 20 cm, used in TRITIUM-IFIC-0 prototype.	139
5.2 TRITIUM-IFIC-0 Prototype.	140
5.3 a) Fiber bundle in PMMA vessel b) illumination test of the bundle to visualize the light loss due to the fiber curvature. .	141
5.4 Energy spectra measured with TRITIUM-IFIC-0 prototype. a) Signal and background energy spectra. b) Tritium energy spectrum.	143
5.5 PTFE structure used to arrange the fibers of TRITIUM-IFIC-1 prototype in a matrix of 8×8	145
5.6 PTFE vessel of TRITIUM-IFIC-1 prototype.	146
5.7 A general view of TRITIUM-IFIC-1 prototype..	147
5.8 Energy spectra measured with TRITIUM-IFIC-1 prototype. a) Signal and background energy spectra. b) Tritium energy spectrum.	148
5.9 TRITIUM-Aveiro prototype.	151
5.10 PTFE structure and fiber bundle used in TRITIUM-Aveiro prototype.	151

5.11 Measurement of the background with TRITIUM-Aveiro prototype shielded with different layers of lead, A) without shielding, B) with a lead shield of 2.5 mm thickness and C) with two lead shields of 2.5 mm thickness each one [CA].	154
5.12 Measurements of the background and tritium liquid source (with an activity of 29.8 kBq/L) performed with the TRITIUM-Aveiro prototype and integrated during a minute [CA]. a) Counts per minute measured as a function of time. b) Distribution of the acquired data.	155
5.13 Measurements of the background and tritium liquid source (with an activity of 29.8 kBq/L) performed with the TRITIUM-Aveiro prototype and integrated during one hour [CA].	157
5.14 TRITIUM-IFIC-2 prototype (A) and active veto (E) within the metallic structure (D).	158
5.15 a) TRITIUM-IFIC-2 PTFE vessel. b) TRITIUM-IFIC-2 PTFE vessel with PVC caps in which a groove is made for the cable connection to the SiPM.	159
5.16 Light transmission spectrum of a 5 mm thick PMMA plate, measured at ICMOL laboratory.	160
5.17 Graphical User Interface (GUI) of PETsys.	161
5.18 Energy spectra measured with TRITIUM-IFIC-2 prototype. a) Signal and background energy spectra. b) Tritium energy spectrum.	162
5.19 a) Single photon distribution measured with TRITIUM-IFIC-2 prototype. b) Tritium energy spectrum measured with TRITIUM-IFIC-2 prototype in photons detected per event.	164

5.20 Signal and background rates for a long time measurement.	165
5.21 Background measured with the TRITIUM-Aveiro prototype during its installation in Arrocampo dam [CA].	167
5.22 A schematic design of the TRITIUM detector.	169
5.23 A TRITIUM monitor design based on the TRITIUM-IFIC-2 prototype.	170
6.1 Energy distribution of a) simulated tritium decays b) Initial energy of tritium decays that reach the scintillating fibers (red histogram) compared the all simulated tritium events (blue histogram) [Aze20].	175
6.2 a)Transversal cut of simulated scintillating fiber (yellow) and tritium source (green) with various tritium decays (red dots) b) Distribution of the radial distance between the position where the tritium decay takes place and the surface of the scintillating fiber [Aze20].	176
6.3 Distribution of the initial energy of tritium events that reach the scintillating fibers, blue histogram, and the energy deposited, red histogram [Aze20].	177
6.4 Energy distribution of photons produced in the scintillating fiber, without Birks coefficient (red histogram) and with Birks coefficient of $k_B = 0.126 \text{ mm/MeV}$ (blue histogram)[Aze20].	178
6.5 Number of photons produced versus the energy deposited in the scintillating fibers when a)the Birks coefficient is not considered ($k_B = 0$) b) the Birks coefficient is $k_B = 0.126 \text{ mm/MeV}$ [Aze20].	179

6.6 Number of photons produced in the fiber per tritium event for all tritium events that reach the fiber (blue histogram) and for only tritium events producing photons detected in coincidence by photosensors (red histogram) [Aze20].	180
6.7 Simulations of counts integrated over 60 min, normalized to the same active area and taken over a week for a fiber length of 1 m, dashed lines, and 20 cm, solid lines and two different activities, 0.5 kBq/L, blue lines, and 2.5 kBq/L, red lines [Aze20].	181
6.8 Comparison of the energy deposition by cosmic rays in scintillating fibers of 1 mm and 2 mm diameter.	183
6.9 Distribution of photons reaching PMMA windows. The red histogram corresponds to the photons guided by fibers and the blue histogram to photons traveling in the water [Aze20].	184
6.10 Distribution of the scintillating fibers in the simulation of Tritium-IFIC-2 prototype.	185
6.11 Simulation of Tritium-IFIC-2 prototype. PMTs (black), the optical grease (blue), PMMA windows (white), tritiated water (green) and scintillating fibers (yellow).	186
6.12 Tritium electron detected in the simulated TRITIUM-IFIC-2 prototype. The path of the optical photons is represented by green lines and the position in which they are absorbed is represented by red and blue dots (absorbed in water or PMT, respectively).	187
6.13 Photons detected by both PMTs per tritium event in the simulated TRITIUM-IFIC-2 prototype.	188

6.14 a) Tritium counts detected with a simulated TRITIUM-IFIC-2 prototype using a integration time of 10 min as a function of the time b) Distribution of detected counts for different activities and an integration time of 10 min.	190
6.15 Distribution of the tritium counts simulated for TRITIUM-IFIC-2 prototype for three different integration time: a)10 min, b) 30 min and c) 60 min.	191
6.16 Distribution of the tritium counts simulated for different number of TRITIUM-IFIC-2 prototypes: a) 1, b) 5 and c) 10, for an integration time of 10 min.	192
6.17 Resolution of the TRITIUM-IFIC-2 prototype as a function of the a) integration counting time b) number of prototypes.	193
A.1 Three PCBs used for the SiPM characterization a) The PCB 1 used to arrang 8 SiPMs and black box. b) The PCB 2 used to sum and amplify the output signals of SiPMs. c) The PCB 3 used to rearrange the different singals of the system. d) The LED emission spectrum.	209
B.1 Scheme of the water purification system.	211
B.2 Different stages of filtration of the water purification system. a) The gross filtering stage. b) The Fine filtering stage. c) The Super fine filtering stage.	212
B.3 a) Doble phase reverse osmosis stage b) Containers used to store the outlet water of the water purification system.	213
B.4 Siemens PLC, software for remote control of water purification system.	213

B.5	General photo of the complete water purification system.	214
B.6	Raw water, reject water and pure water obtained with this system.	214
D.1	a) The Electronic scheme of the PCB designed to power the PMTs of Aveiro prototype b) The graphical user interface developed to control it.	218
D.2	Simplified electronic scheme used to process and analyze the signal of TRITIUM-Aveiro prototype.	219
D.3	Graphical user interface used to manage the counter system.	221
D.4	Two different situations of the electronic chain response. a) Event accepted since veto has not detected it. b) Event rejected since veto has detected it.	222

List of Tables

1.1	Annual average distribution of the effective dose received by the population due to natural radioactivity [UNS21, CSN21a].	2
1.2	Emission of tritium per year from different types of nuclear reactors: Pressurized Water Reactor (PWR), Boiled Water Reactor (BWR), Heavy Water Reactor (HWR) and Gas-Cooled Reactor (GCR) [Hou18].	8
1.3	Most common nuclear reactions of artificial tritium production [Hou18].	10
1.4	Penetration depth for decay electron of mean (5.7 keV) and maximum (18.6 keV) energies in different media (tritium gas and air at STP, standard conditions of temperature (273 K) and pressure (1 atm), and water) [Bla].	16
1.5	Legal limit of tritium in drinking water established in several countries.	20

2.1	State-of-the-art tritium detection techniques. This table shows the measured quantity, the minimum detectable activity (MDA) and the sample form for four different techniques, liquid scintillator counting (LSC), ionization chamber (IC), calorimetry and beta induced X-ray spectrometry (BIXS).	24
2.2	Efficiencies of different scintillator detectors for tritiated water detection. This table shows the efficiency of the detector (ε_{det}), its active surface (F_{sci}), its specific efficiency ($\eta_{det} = \varepsilon_{det}/F_{sci}$), defined as its efficiency normalized to its active surface, and its MDA for each study listed above.	26
3.1	Critical angles associated to different interfaces created with polystyrene, $n_0 = 1.6$, and other materials.	46
3.2	Properties of BCF-12 fibers from Saint-Gobain Inc. [Cer05].	47
3.3	Characteristics of SiPM S13360-1375 and S13360-6075 from Hamamatsu Photonics [Div16b].	60
3.4	Classification of natural radioactive series [The96, Eva96]. The information displayed for each radioactive series is the multiplicity of the mass number, the name of the series, the primary and final element, and the half-life of the primary element.	77
3.5	Properties of plastic scintillators from Epic-Crystals used for the cosmic vetos [Cry20].	82
4.1	Mean and standard deviation (due to the fiber position in the setup) of the number of photons per nanosecond that reach the PMT for 0.1 mA LED intensity.	109

4.2	Number of collected photons per nanosecond versus LED intensity for the different type of fibers. The errors shown here are the standard deviation of the ten measured samples. . .	112
4.3	Relative standard deviation, $\sigma_{sys}^{rel}\text{(\%)}$, versus LED intensity for the different fiber types.	112
4.4	Relative standard deviations (σ_{sys}^{rel} , $\sigma_{sys-pos}^{rel}$ and σ_{sys-SF}^{rel}) measured in this test.	113
4.5	Number of the collected photons versus LED intensity for 10 different fibers of 10 cm length.	114
4.6	Collection efficiencies CE_{10}	115
4.7	Chemical components and turbidity measured in the raw water sample.	126
4.8	Measurements of the conductivity for several samples of water.	127
4.9	Measurements of the tritium activity for several samples of both, raw and purified water.	128
5.1	Counting rate obtained with the TRITIUM-IFIC-0 prototype.	142
5.2	Counting rate obtained with the TRITIUM-IFIC-1 prototype.	146
5.3	Counting rates measured by TRITIUM-IFIC-2 prototype. . .	161
5.4	Mean value and standard deviation of the counts of fourteen background measurements. Minimum net counts obtained by applying the Currie's Law, L_C and N_D	165

6.1	Difference in activity that can be resolved for the TRITIUM- IFIC-2 prototype, for different integration times and different number of prototypes.	189
7.1	Results of scintillator detector developed for several experiments (including the TRITIUM project) for tritiated wa- ter detection. This table shows the efficiency of the de- tector (ε_{det}), its active surface (F_{sci}), its specific efficiency ($\eta_{det} = \varepsilon_{det}/F_{sci}$), defined as its efficiency normalized to its active surface, and its minimum detectable activity (MDA) for each study listed above. The "*" symbol indicates that this is the specified activity that the detector can distinguish from the background, but it is not its MDA.	200

Chapter 1

Introduction

1.1 Tritium and Nuclear Energy

Radioactivity is the process in which an unstable atomic nucleus loses energy through the emission of particles such as photons, electrons, etc. This process has been present in the Universe since its inception as it was an important process of the Big Bang¹. This was also present during the formation of the earth which explains why the different layers that make up the earth contain radioactive elements.

Humanity has always been exposed to radioactivity, whether present in the Earth's crust or in extraterrestrial sources (external natural irradiation). The human being himself is radioactive as radioactive elements are contained in the human body such as ^{3}H , ^{14}C or ^{40}K , introduced into the body through food or water ingestion or air inhalation (internal natural irradiation). The annual average radioactive dose received by the world population is presented in Figure 1.1 and Table 1.1.

¹The Big Bang is the most acceptable hypothesis that explains the formation of the universe and its development over time so far.

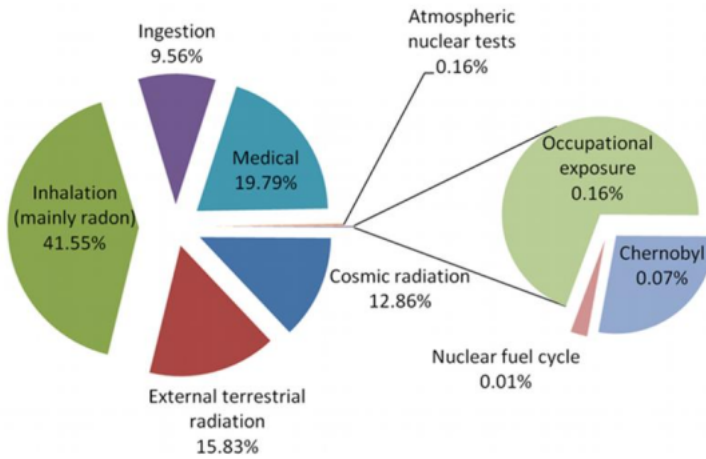


Figure 1.1 – Annual average distribution of the radioactive dose received by the population [IAE21].

As it can be seen in Figure 1.1, most of the radioactive dose received by the population is due to both internal and external natural radioactivity, the effective dose² of which is estimated to be 2.42 mSv/yr as shown in Table 1.1.

Since the discovery of radioactivity by Heri Becquerel in 1896, lots

²The effective dose is the radioactive dose absorbed by the population, taking into account the different radiosensitivity of each organ or tissue.

Radiation source	Eff. dose (mSv/yr)	Typical range (mSv/yr)
Cosmic (external)	0.39	0.3 – 1.0
terrestrial (external)	0.48	0.3 – 0.6
Inhalation (internal)	1.26	0.2 – 10
Ingestion(internal)	0.29	0.2 – 0.8
Total	2.42	1 – 12.4

Table 1.1: Annual average distribution of the effective dose received by the population due to natural radioactivity [UNS21, CSN21a].

of nuclear-based technology has been developed and applied to several fields such as energy production, research, medicine, industry, etc. Due to this nuclear technological development, various anthropogenic radioactive sources have appeared in society, resulting in a greater amount of radioactive elements released to the environment. It can be noticed in Figure 1.1 that the most important part of the dose received by the population from artificial sources comes from medical practices. The growing knowledge and development of measurement techniques of radioactivity, enable better assessment and characterization of the harmful effects of radioactivity in living organisms. Because of that, it is important to control the level of radioactive background to which the population is exposed and to ensure that these levels are kept below a safe limit. To accomplish this task, several organizations were created to propose recommendations in radiological protection to the different state organisms and governments at the international level:

1. A definition of concepts and units was necessary to quantify the negative effects of radioactivity and, for that, the International Commission of Radiological Units and Measurements, ICRU [ICR21b], was created during the first international conference of radiology held in London, in 1925.
2. The International Commission on Radiological Protection, ICRP [ICR21a], was created in 1928 by the International Society of Radiology, ISR [ISR21]. The ICRP aims to make recommendations and to provide guidance on different aspects of protection against radioactivity. The ICRP does not have the legal capacity to enforce its recommendations, but these are widely included in the legislation of most countries.
3. The United Nations Scientific Committee on the Effects of Atomic Radiation, UNSCEAR [UNS21], was created in 1955, with the goal of estimating and reporting the levels and effects of ionizing radiation on the population and the environment. These estimates are taken into account by governments worldwide to establish their safety standards.

4. The International Atomic Energy Agency, IAEA [IAE21], was created in 1957 to promote the peaceful use of nuclear energy and to avoid its use for military purpose such as nuclear weapons. Although IAEA is an independent agency, it must to periodically report to the United Nations, (UN) [UN21].
5. At the level of the European Union (EU), the European Atomic Energy Community (EURATOM) was created in 1957, which is an international organization created through and ruled by the EURATOM treaty. Its objective is to coordinate research programs for the peaceful use of nuclear energy and the sharing of knowledge, infrastructure and funding of nuclear energy.
6. In Spain, the Nuclear Safety Council (CSN) was created in 1980 [CSN21a]. The CSN is the only authority in Spain on nuclear safety and radiation protection and its objective is to protect employees, the general population and the environment from the harmful effects of ionising radiation from anthropogenic origins. For this task, the CSN ensure that nuclear and radioactive facilities are operated safely and establish the preventive and corrective measures to apply in all radiological emergencies. The CSN has created various networks consisting of several detectors of radioactivity that are in charge of controlling the levels of radioactivity in the environment and assessing the impact of radioactivity facilities. Two of the most important networks are the network of automatic stations (REA, "Red de Estaciones Automáticas") and the network of sampling stations (REM, "Red de Estaciones de Monitoreo"):
 - (a) The network of automatic stations, REA [CSN21b], shown in Figure 1.2a, consists of several gamma detectors³ distributed in Spain that measure the radioactive dose in real time. The REA

³Detectors that only measure gamma radioactivity

is employed for real-time detection of radiological issues, which enable taking prompt safety measures.

- (b) The network of sampling stations, REM [CSN21c], shown in Figure 1.2b, consists of several strategic points in Spain where samples are taken and transported to a laboratory to be measured. About twenty Spanish laboratories integrate this network, the objective of which is to characterize the concentration and evolution of various radioisotopes present in the radioactive background of Spain and to quantify the impact of radioactive facilities on the environment.

There are other networks that measure different parameters such as the concentration of ^{222}Ra in the air. The measurements of all the networks complies with to the EUROTAM treaty [Dir21].

The goal of this thesis and the *TRITIUM* project is to develop a monitor capable of automatically measuring low levels of tritium in water in quasi-real time⁴. This monitor is intended to be finally included in the REA.

Tritium is one of the radioactive isotopes routinely measured in REM tests and it is detected through the low-energy electrons produced in tritium beta decay, mainly using the liquid scintillation counter technique (LSC). Due to the limitations of the current tritium detection techniques, which will be described in section 2.1, the *TRITIUM* project has been recently created, the objective of which is to build a tritium detector based on scintillating fibers in contact with the water sample. The photons produced in these scintillating fibers are read out using photosensors, either photomultiplier tubes (PMTs) or silicon photomultipliers (SiPMs).

The *TRITIUM* collaboration is a international group consisting

⁴Quasi-real time is an approximation of real-time measurements. It means a relatively small time, like ten minutes.

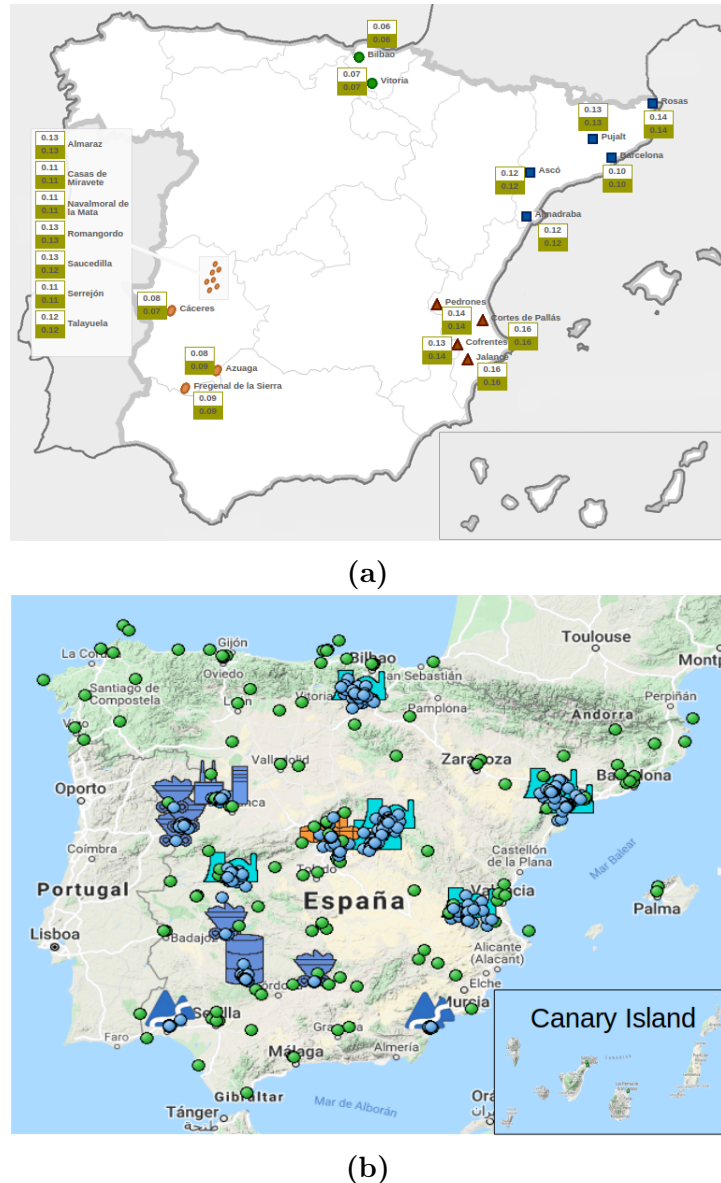


Figure 1.2 – Networks of automatic and sampling stations managed by the Spanish CSN. (Above) Measurement locations of the REA [CSN21b]. The white box is the daily average of the gamma dose and the green box is the monthly average of the gamma dose. (Below) Measurement locations of the REM [CSN21c]. Blue dots are locations near nuclear facilities, and green dots are locations uniformly distributed throughout the country.

of a consortium of 6 different european institutions of 3 different countries: Portugal, France and Spain. The final emplacement of the *TRITIUM* monitor is the Arrocampo dam (Extremadura, Spain), the water of which is used for the cooling system of the Almaraz nuclear power plant (NPP). This detector will be installed 4 km downstream from the Almaraz Nuclear Power Plant.

The monitor will be used to ensure that the tritium levels of the Arrocampo dam water are below the legal limit of 100 Bq/L specified in the EURATOM Directive 2013/59/Euratom [Dir21]. In addition, this will confirm the correct operation of the Almaraz NPP, since its malfunctioning may produce an increase of tritium activity released.

Tritium is one of the most abundantly produced radioisotope in a NPP, as it was verified in the United States Department of Energy complex, (U.S. DOE) [Berb, Bera] and in several research facilities in China [Hou18], and also places close to them (ground water, surface water and process waste water).

Tritium is produced in the water used for nuclear reactor cooling system of some NPPs by neutron capture of deuterium, existing in the heavy water (D_2O), semi-heavy water (HDO) or deuterium created by neutron capture in usual water (H_2O). All these processes have a large probability to happen due to the huge neutron flux of the order of $10^{14} \text{ n cm}^{-2}\text{s}^{-1}$ in the nuclear reactor [?]. This tritium is finally released partially or totally to the environment in a quantity that depends on the reactor type as it is shown in Table 1.2. The most common form in which tritium is released to the environment is HTO [Hou18].

NPPs are operational since more than 60 years and, nowadays, they are essential for providing a large part of the electric power used all over the world (more than 20% in Spain [dE19] and more than a 10% in the world [AIdlE14]). Although the Spanish government is planning to progres-

Reactor type	Gaseous discharge (GBq/y)	Liquid discharge (GBq/y)
PWR	$3.70 \cdot 10^3$	$2.59 \cdot 10^4$
BWR	$1.85 \cdot 10^3$	$3.70 \cdot 10^3$
HWR	$7.40 \cdot 10^5$	$1.85 \cdot 10^5$
GCR	$7.40 \cdot 10^3$	$1.11 \cdot 10^4$

Table 1.2: Emission of tritium per year from different types of nuclear reactors: Pressurized Water Reactor (PWR), Boiled Water Reactor (BWR), Heavy Water Reactor (HWR) and Gas-Cooled Reactor (GCR) [Hou18].

sively shut down all NPP, there are other countries like China [Pre16] or United States (USA) [New19] that promote their use. NPPs are a profitable investment since they are one of the cheapest source of energy production. Their energy production rate is stable as this doesn't depend on meteorological parameters. Moreover, NPPs do not emit greenhouse gases. Although there are alternative energy sources which are being developed quickly (photovoltaic, wind, tidal energy, etc.), as well as other concepts of energy production and saving (local production, solar roofs, energy efficiency, smart cities, etc.), they are currently not developed enough to fully cover the population needs. On the other hand, NPPs still have some important issues such as the contamination of fresh water from uranium mining, the nuclear waste produced, the nuclear proliferation or the risk of radioactive contamination from accidents as happened in the past: Chernobyl, Fukushima and Three Mile Island [Ass20].

In any case, world nuclear energy production is most likely not going to be stopped in the next decade. In fact, the United States Energy Information Administration (U.S. EIA) expects a future increase of nuclear energy production [Cap20]. Therefore the development of different types of alarm systems is an important investment. Safety is not a negotiable aspect and there must be safeguards that warn us of any malfunction of a nuclear power plant. Our objective is to ensure that the levels of tritium in the analyzed water are below the Spanish legal limit. It means that this

monitor could be used in many different places with radioactive facilities like the future fusion power plants⁵, nuclear research facilities⁶ or tracking the pathway of tritium discharges to ground water [AS00].

1.2 Tritium Properties and Radiological Hazards

Tritium is the only radioactive isotope of hydrogen present in the environment. It was produced for the first time in 1934 in neutron capture of deuterium by Ernest Rutherford, Mark Oliphant and Paul Harteck [MLO34] and it was isolated in 1939 by Luis Walter Alvarez and Robert Cornog [Alv39], who checked that tritium is a radioactive element.

Tritium is naturally produced in the environment through the interaction of cosmic rays and gaseous elements of the upper atmosphere like nitrogen ($^{14}\text{N}(\text{n}, ^3\text{H}) ^{12}\text{C}$) [USDoEW16] and oxygen ($^{16}\text{O}(\text{n}, ^3\text{H}) ^{14}\text{N}$) [Hai14]. Around 99% of cosmogenic tritium forms water (HTO) and reaches the Earth's surface as rain with an estimated production rate of $4 \cdot 10^6 \text{ Ci/yr}$ ($1.48 \cdot 10^8 \text{ GBq/yr}$), producing a tritium concentration of $0.6 - 1.2 \text{ Bq/L}$ in precipitation [Hou18, USDoEW16].

Tritium can be produced artificially in the environment from different anthropogenic sources [Hou18, USDoEW16]. There is a large amount of tritium which was produced in military nuclear test explosions between 1945 and 1975, with an estimated total production of $8 \cdot 10^9 \text{ Ci}$ ($2.96 \cdot 10^{11} \text{ GBq}$), a part of which remains to the date. In these nuclear explosions, tritium was produced mainly from the nuclear reactions $^{14}\text{N}(\text{n}, ^3\text{H}) ^{12}\text{C}$ and $^2\text{H}(\text{n}, \gamma) ^3\text{H}$. Tritium is produced by commercial producers of radioluminescent and neu-

⁵The International Thermonuclear Experimental Reactor, ITER, will need up to several tens of kilograms of tritium to function, which corresponds to various TBq of tritium.

⁶Tritium is one of the main emissions from these sites [Fer19], [(BN)].

tron generator devices ($1 \cdot 10^6$ Ci/yr), nuclear power and defense industries (around $2 \cdot 10^6$ Ci/yr) and several research facilities and nuclear reactors for energy production ($2 \cdot 10^6$ Ci/GWyr). The production cross sections of the relevant processes are shown in Table 1.3.

Source	Origin	Nuclear reaction	Cross section (b)
${}_1^2\text{H}$	Water coolant	${}_1^2\text{H}(\text{n}, \gamma) {}_1^3\text{H}$	$5.2 \cdot 10^{-4}$
${}_2^3\text{He}$	Helium coolant	${}_2^3\text{He}(\text{n}, \text{p}) {}_1^3\text{H}$	5330
${}_3^6\text{Li}$	Moderator	${}_3^6\text{Li}(\text{n}, \alpha) {}_1^3\text{H}$	940
${}_{10}^5\text{B}$	Moderator, control rods	${}_{10}^5\text{B}(\text{n}, 2\alpha) {}_1^3\text{H}$	3835

Table 1.3: Most common nuclear reactions of artificial tritium production [Hou18].

Tritium levels in the water of the environment, excluding the current anthropogenic radioactive sources, are between 1 and 4 Bq/L, larger than the expected due to the cosmogenic background levels (0.6 – 1.2 Bq/L) [Cal10]. This is attributed to nuclear weapons tests. Tritium levels in rivers around a NPP are between 1 and 10 Bq/L and even between 20 and 50 Bq/L at the water discharge site of NPPs [Cal10], where the produced tritium is partially or totally released into the environment, mainly in the HTO water form.

The effect of NPP on tritium levels can be observed in the REM data, for example for the case of Cofrentes. Cofrentes is the closest nuclear power plant to Valencia. The tritium level is measured in three different places along the Jucar river, marked on the map shown in Figure 1.3. The first place, P1, is located in the river, 6 km upstream from the NPP, the second place, P2, is located 1 km downstream and the third place, P3, is located 5 km downstream. The level of tritium measured in these three locations is shown as a function of the time in Figures 1.4a, 1.4b and 1.4c respectively.



Figure 1.3 – Tritium sampling locations around Cofrentes NPP.

In these figures, the detection limit and the measured activity are plotted with white and green dots, respectively. The measured activity is only displayed when this is larger than the corresponding detection limit. The tritium level in the river increases due to the discharge of the NPP and it is diluted again after 4 km downstream, as can be seen from these data. Two additional measurements of the tritium level in groundwater are included, points S1 and S2 on the map in Figure 1.3, located 1 km before and 1 km after the NPP. Both tritium levels are shown in Figures 1.5a and 1.5b, respectively, where it can be observed that they are below the detection limit.

It is important to note that, although environmental tritium level is affected by the NPP in the case of Cofrentes, these levels are below the maximum allowed limit. The maximum level of tritium measured since January 2, 2006 is around 32 Bq/L, below the limit of 100 Bq/L recommended by the Euratom 2013 Directive.

Tritium is a radioactive element with a half-life time of $T_{1/2} = 12.32$ years. It has one proton and two neutrons and decays exclusively

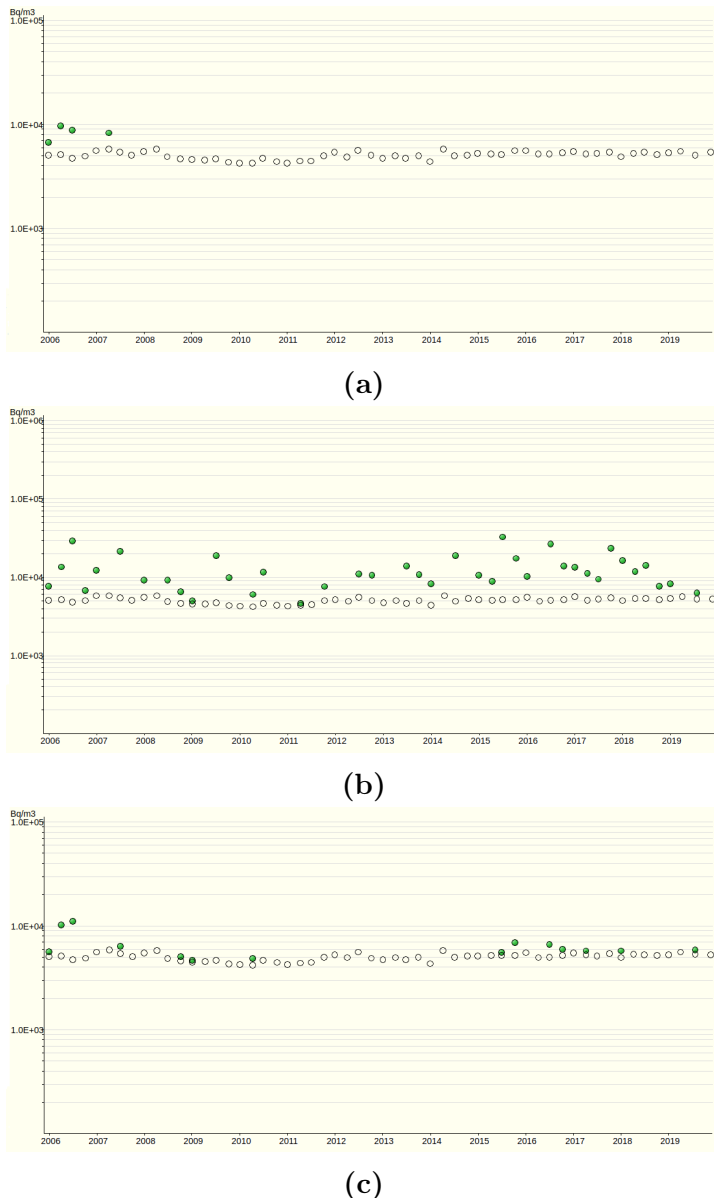


Figure 1.4 – Tritium activity levels in surface water around Cofrentes NPP from January 2006 to November 2019. (Above) 6 km upstream. (Middle) 1 km downstream. (Below) 5 km downstream. The white points are the detection limit and the green points are the measured activity, when this is above the detection limit [CSN21c]. The maximum level of tritium measured since of January 2, 2006 is around 32 Bq/L



Figure 1.5 – Tritium activity levels in groundwater around Cofrentes NPP from January 2006 to November 2019 [CSN21c]. (Above) 1 km before NPP. (Below) 1 km after NPP.



Figure 1.6 – (Above) Tritium energy levels [IAEA]. (Below) Graphic representation of tritium decay [Pre19].

through β radiation. Tritium decays 100% directly to the ground state of the ${}^3\text{He}$ isotope of helium, which is a stable nuclei, through the process,



In Figure 1.6, the scheme of tritium energy levels is shown. In this decay it is not possible to detect the neutrino because of its extremely weak interaction with matter ($\sigma \propto 10^{-44} \text{ cm}^2$ [Her07]) and, since ${}^3\text{He}$ has a much larger mass than electrons and neutrinos, by conservation of energy and momentum, the energy taken by the daughter nucleus is very small. Therefore, the detection of tritium is through its decay electron.

The energy released in the tritium decay is $Q_\beta = 18.6 \text{ keV}$, shared between the decay products. Therefore, the energy spectrum of the decay electrons is a continuum with a maximum value of 18.6 keV, as shown in Figure 1.7. This energy spectrum has an average energy of 5.7 keV and the most likely energy is slightly below, around 4.5 keV.

The released energy in tritium decay, is very low. In fact, it is the

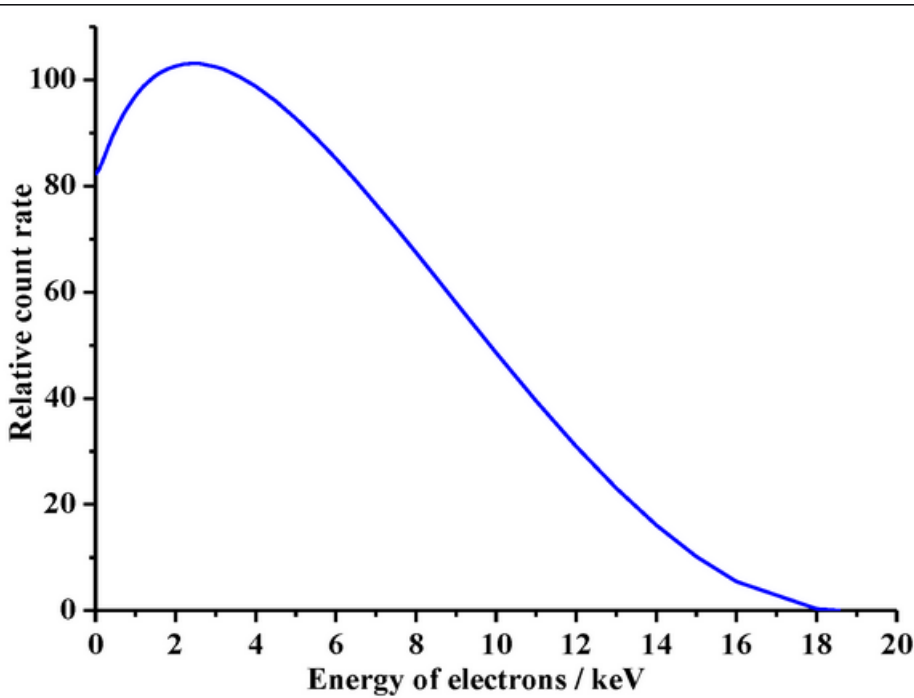


Figure 1.7 – Energy spectrum of tritium electrons [Lin20].

radioactive isotope with the lowest energy released in β decay [USDoEW16]. Consequently, the β particle emitted has a very short mean free path, given in Table 1.4.

This short mean free path is a major issue in tritium detection, as it makes more difficult the electron detection, which requires a highly sensitive detector. It also means that tritium electrons have a low penetration in human body and they are easily stopped by clothes or laboratory gloves, resulting in a low radiological hazard of external tritium. Nevertheless, the danger of tritium increases when this is ingested or inhaled since it binds and perform the same chemical reactions as hydrogen, sometimes with higher rate if the tritium concentration is high enough to catalyze the reaction.

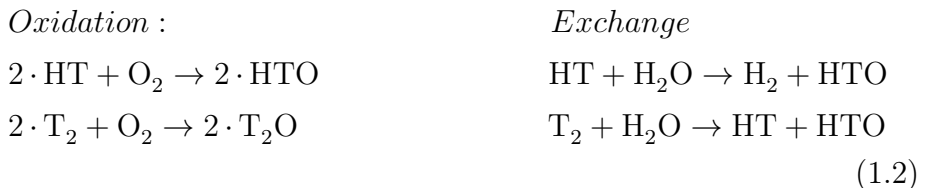
Tritium can be absorbed in our body in three different forms,

Material	P. Depth (5.7 keV)	P. Depth (18.6 keV)
${}^3\text{H}_2$	0.26 cm	3.2 cm
Air	0.036 cm	0.45 cm
Water, soft tissue (solid matter with a density of $1 \text{ g} \cdot \text{cm}^{-3}$)	$0.42 \mu\text{m}$	$5.2 \mu\text{m}$

Table 1.4: Penetration depth for decay electron of mean (5.7 keV) and maximum (18.6 keV) energies in different media (tritium gas and air at STP, standard conditions of temperature (273 K) and pressure (1 atm), and water) [Bla].

gaseous tritium (mainly HT), tritiated water (mainly HTO) and organically bound tritium (OBT).

1. Gaseous tritium, which is normally found mixed in the air, is the least harmful since less than a $3 - 5 \cdot 10^{-3}\%$ is absorbed by the human body, which is negligible [USDoEW16]. However, it can be transformed into tritiated water, more harmful from the radiological point of view [USDoEW16], through the oxidation and exchange reactions by equations 1.2:



2. Tritiated water, which is normally found in drinking water and food, has a larger impact since the 99% of it is absorbed [USDoEW16]. Its biological life-time corresponds to the water cycle in the body, around 9.5 days ($\pm 50\%$), during which tritium remains in our body

[USDoEW16, Cal10, Mas]. As in the case of water, the biological life-time of tritiated water can vary due to various external parameters such as temperature, humidity, drinking habits, etc. or reduced with the use of diuretics [USDoEW16].

3. Organically bound tritium, normally found in food, generally forms a covalent bond with a carbon. It corresponds to 5 – 10 % of tritium absorbed in the body. Although it is less absorbed in the body than tritiated water, it can be more dangerous since it has a longer biological life time. The biological life-time of this tritium compound depends on the affinity of the organic molecule to the different biological tissues and it can vary from tens to hundreds of days (larger than the ICRP estimate) [Cal10, Mas, PF81, Mar72].

There are many studies showing that tritium in living matter can cause the same effects than X-rays or γ rays, which are DNA mutations, tumors, cancer, genetic effects, reproductive effects, etc [Str93, Ryt]. In fact, the consequences of tritium radiation may be worse than a similar doses of γ radiations since its biological efficiency⁷ is two or three times larger [Str93].

In summary, tritium is a naturally occurring radioactive element. It affects health of living organisms if these are excessively or chronically exposed to tritium. Because of that, several countries have developed a legislation, described in section 1.3, to manage the release of tritium to the environment and ensure that its levels are safe for living organisms.

⁷The biological efficiency is used to quantify the damage produced in the living cells due to an external radiation.

1.3 Current Legislation

Due to the radiological risk of tritium, described above, it is important that the current legislation limits the release of tritium to the environment ensuring that the levels are below a safe value for public health.

The guidelines to limit the radioactive elements in drinking water for many countries. They are based on the radiation protection methodology developed by the ICRP [ICoRP91] and the recommendations of the world health organization (WHO) [WHO04]. The objective of the international radiation methodology is to protect people and the environment from the negative effects of ionizing radiations but allowing beneficial activities that involve a reasonable radiation exposure. It is based on three main points, which are:

1. The justification: The benefit from radiological exposure must outweigh the detriment to health that it causes.
2. The ALARA principle ("As Low As Reasonably Achievable"): The radiological exposure must be kept as low as possible considering social and economic factors.
3. The dose limitation: Limit that must never be exceeded.

While the ICRP recommends a maximum dose of 1 mSv/yr, excluding the natural background and medical interventions, the WHO is more conservative, recommending a maximum dose of 0.1 mSv/yr, which corresponds to less than 5% of the annual dose due to background radiation, 2.42 mSv/year.

The guideline reference level of each radionuclide in drinking water,

GL, is usually calculated from these recommendations using the equation,

$$GL(\text{Bq/L}) = \frac{RDL}{DCF \cdot q} \quad (1.3)$$

where RDL is the reference dose level in Sv/yr , DCF is the dose conversion factor (the normal used value for tritium is $1.8 \cdot 10^{-11} \text{ Sv/Bq}$, provided by ICRP [ICoRP96]) and q is an estimation of the annual volume of drinking water consumed (normally assumed two liters per day, 730 L/yr).

The GL calculated for tritium in drinking water according to the ICRP and WHO recommendations is $76\ 103 \text{ Bq/L}$ and $7\ 610 \text{ Bq/L}$ respectively. It means that tritiated water with activities below these values is considered not harmful for health.

Based on these recommendations, each country has created organizations in charge of developing its own legislation limits of exposure to radionuclides. In Spain, the responsible organization of this task is the CSN. Most of the countries in the world implement the RDL of 0.1 mSv/yr recommended by the WHO. The legal limit for tritium in drinking water in this case is $7\ 610 \text{ Bq/L}$ but it is often approximated in different ways. Some countries like Switzerland [Dfdl06] or some organizations like the WHO [WHO04] take this value as $10\ 000 \text{ Bq/L}$. Others like some territories of Canada, such as Ontario and Québec, truncate this value to the first number $7\ 000 \text{ Bq/L}$ [otE94, Que16]. There are other countries like Russia which use the much more accurate approximation value of $7\ 700 \text{ Bq/L}$ [ICfS07]. There are other countries like Australia that prefer to implement the RDL of 1 mSv/yr , recommended by the ICRP, the legal limit of which is $76\ 103 \text{ Bq/L}$ [AG21]. Other countries like Finland are based in the ICRP recommendations and use only half of this value, 0.5 mSv/yr , rounded to a legal limit of $30\ 000 \text{ Bq/L}$ for tritium in drinking water [NEA93].

There are two different exceptions to these recommendations:

1. Most of the USA states like California use a RDL of 4 mrem (0.04 mSv), which corresponds to a legal limit of 20 nCi/L (740 Bq/L) [OoEHHA07]. This value was proposed by the United States Environmental Protection Agency (US EPA) as a result of an analysis carried out on the available data. [USEPA76].
2. Most of the EU countries, such as France, Germany or Spain, consider a GL of 100 Bq/L, which is one of the most restrictive limit in the world [Idredsn17, BfS05, CdSN13]. This value arise from the consideration that it is an indicator of the presence of other radionuclides more dangerous than tritium. These limits are fixed by the EURATOM Council Directive [EAEC13].

All limits mentioned in this section are summarized in table 1.5.

Country/Agency	Legal limit of tritium in water (Bq/L)
ICRP	76 103
WHO	10 000
Switzerland	10 000
Canada	7 000
Russia	7 700
Australia	76 103
Finland	30 000
United States	740
European Union	100

Table 1.5: Legal limit of tritium in drinking water established in several countries.

1.4 This Thesis

This thesis is divided into nine different chapters that structure the information as follows:

1. **Chapter 1** provides a brief introduction to tritium detection, reports some important properties of tritium, and discusses the current legislation that limits tritium levels for human consumption in many countries around the world.
2. **Chapter 2** describes the State-of-the-Art of tritium detection and shortly introduces the TRITIUM project.
3. **Chapter 3** outlines the different parts of the TRITIUM monitor, which are the water purification system, the background rejection system (consisting of the lead shield and the active veto) and the tritium detector.
4. **Chapter 4** reports the calibrations of the different parts of the TRITIUM monitor and describes the developments aimed at improving the efficiency of tritium detection.
5. **Chapter 5** details the geometrical configuration of the different prototypes built in the TRITIUM project and the measurements taken with them.
6. **Chapter 6** details the Monte Carlo simulations performed in the TRITIUM project and show the results obtained with them.
7. **Chapter 7** summarizes the most important results achieved in this work.

Chapter 2

Methods of Detection of Tritium In-Water

2.1 Tritium Detection State-of-the-Art

Measurement of tritium activity is one of the routine environmental controls that are carried out in the vicinity of nuclear research facilities and nuclear power plants during their energy production lifetime. Consequently, this measurement is carried out with different available technologies to improve the state of the art of tritium detection. The most employed techniques are summarized in Table 2.1.

Nowadays, the most used technique for measuring tritium in water is liquid scintillator counting (LSC). This technique consists of mixing a liquid sample (some milliliters for environmental measurements or less for higher activities) with liquid scintillator. This mixture is usually made in a ratio of 50:50 but it depends on the detection system and on the activity of the samples [AH99, Hof92a]. In this technique, the β particles emitted from the sample excite the molecular energy levels of the liquid scintillator which

	LSC	IC	Calorimetry	BIXS
Measured quantity	Scintillation photons	Ionization current	Heat	X-rays
MDA	\sim Bq	10 – 100 kBq	\sim GBq	\sim MBq
Sample form	Liquid	Gas, vapor	All	All

Table 2.1: State-of-the-art tritium detection techniques. This table shows the measured quantity, the minimum detectable activity (MDA) and the sample form for four different techniques, liquid scintillator counting (LSC), ionization chamber (IC), calorimetry and beta induced X-ray spectrometry (BIXS).

promptly decays emitting several photons with a well-known energy (fluorescence), usually in the visible spectrum. Finally, these photons are detected with photosensors, which convert the optical signal into a measurable electrical charge. The liquid scintillator technique has a very good detection sensitivity for low activity levels of tritiated water (< 1 Bq/L) [Pal07] but it has the disadvantage of long measurement time (up to 2 days) and producing chemical waste, since liquid scintillator contains toluene which is toxic. In addition, this technique requires special staff for sampling, chain of custody and laboratory analysis which require economical and time resources. In order to overcome these difficulties some efforts have been made in order to build a tritium monitor with LSC but without achieving a low enough MDA[Sig94].

The ionization chamber technique (IC) consists of a gas chamber, filled with gas (sample), which contains electrodes that collect the ionization current produced by the energy deposition of the β radiation in the gas. It is a simple and fast system, but it has a high MDA (> 10 kBq) and requires the samples to be in a state of gas or steam [Khe02, ZC13]. The ionization chamber technique also requires sample conditioning, chain of custody and laboratory analysis.

The calorimetry method is based on the measurement of the heat

generated in the detection medium (normally platinum) [CGA17, BD13]. The disadvantage of this technique is its high MDA, of the order of a GBq, and requires long measurement time, 2 days or more.

The Beta Induced X-ray Spectrometry (BIXS) is based on the measurement of the bremsstrahlung radiation produced by the tritium decay electrons, using a NaI(Tl) crystal coupled to a PMT [Mat07, Mat08] or Silicon Drift Detector (SDD) [Nie15]. The problem with this technique is its high MDA, of the order of MBq.

There are additional methods for tritium detection, although they are less employed or less developed, each one with its own advantages and limitations. For example, the Avalanche PhotoDiode (APD) cannot be used in contact with water [Sha97], the mass spectrometry which needs to store the sample several months before taking the measurement for sample conditioning [JB10] and the Cavity ring spectroscopy requires a special optical configuration that is not possible outside a laboratory [Bra15].

All the above techniques are offline methods that need long time for sample collection, shipment to the laboratory and activity measurement. Therefore, they cannot be used for in-situ monitoring of tritium in water. The liquid scintillation technique is the only one with sufficiently small MDA to fulfill the requirement of 100 Bq/L of tritium in the water samples, established by the EURATOM directive.

The purpose of the TRITIUM project is to develop an alternative method, based on solid scintillators, that allows to accomplish the requirements of in-situ monitoring of levels as low as 100 Bq/L in quasi-real time. There are several studies with solid scintillators so far:

1. The study done by M. Muramatsu, A. Koyano and N. Tokunaga in 1967 who used a scintillator plate read out by two PMTs in coincidence [Mur67].

2. The study carried out by the A. A. Moghissi, H. L. Kelley, C. R. Phillips and J. E. Regnier in 1969 that used one hundred plastic fibers coated with anthracene powder and read out by two PMTs in coincidence [Mog69].
3. The study performed by R. V. Osborne in 1969 that used sixty stacked scintillator plates read out by two PMTs in coincidence [Osb70].
4. The study done by A. N. Singh, M. Ratnakaran and K. G. Vohra in 1985, that used a scintillator with several holes read out by PMTs in electronic coincidence [Sin85, MR00].
5. The study carried out by K. J. Hofstetter and H. T. Wilson in 1991, that tested different shapes of scintillator plastics like several sizes of beads, fibers, etc. The better result obtained for solid plastic scintillator was a tritium detection efficiency, ε_{det} , of the order of $10^{-3}(\frac{cps}{kBq/L})$ [Hof92b, Hof].

Study	$\varepsilon_{det}(\frac{cps \cdot 10^{-3}}{kBq/L})$	F_{sci} (cm ²)	$\eta_{det}(\frac{cps \cdot 10^{-6}}{kBq/L \cdot cm^2})$	MDA (kBq/L)
Muramatsu	0.39	123	3.13	370
Moghissi	4.50	> 424.1	< 10.6	37
Osborne	12	3000	4	37
Singh	41	3000	13.7	< 37
Hofstetter	2.22	~ 100	< 22.2	25

Table 2.2: Efficiencies of different scintillator detectors for tritiated water detection. This table shows the efficiency of the detector (ε_{det}), its active surface (F_{sci}), its specific efficiency ($\eta_{det} = \varepsilon_{det}/F_{sci}$), defined as its efficiency normalized to its active surface, and its MDA for each study listed above.

The results of these experiments are summarized in Table 2.2. As can be seen in the first column, the intrinsic detector efficiency, ε_{det} , is very different in these experiments. As one of the most important factors that affect the efficiency is the active surface of the plastic scintillator, F_{sci} , which

varies largely with the detector type, the specific detector efficiency (third column) is used in order to compare these detectors, which is the intrinsic detector efficiency normalized to its active surface. It can be checked that these specific efficiencies are quite similar. Finally, as can be seen in the last column, the MDA in all these experiments are of the order of a few tens of kBq/L. The development of a detector with a much lower MDA is thus essential to comply with the EURATOM directive of 100 Bq/L of tritium in water for human consumption.

2.2 The TRITIUM Project

As a conclusion of section 2.1, the current techniques cannot be used for tritium monitoring in quasi-real time since they have either a high MDA or they work in off-line method.

To overcome these limitations the *Tritium* project [Pro21], with the title of "Design, construction and commissioning of automatic stations for quasi-real time monitoring of low radioactive levels of tritium in water", was proposed.

The *Tritium* collaboration is an international consortium of six different European institutions from three European countries: The University of Aveiro, in Portugal, The University of Bordeaux and The *National Center for Scientific Research* (CNRS, Section Aquitaine-Limousin), in France and the University of Extremadura, The *Junta de Extremadura* and The University of Valencia, in Spain.

This project was funded by the Interreg Sudoe program of the European Economical Community, EEC, in year 2016 call, with the reference number SOE1/P4/EO214. The purpose of this project is the development of an automatic station for in-water tritium monitoring, in situ and in quasi-

real time. The tritium detector consists of a bunch of scintillating fibers in contact with the tritium water sample which are in charge of detecting the tritium decay electrons. These fibers are read out with several photosensors (photomultiplier tubs, PMTs, or silicon photomultiplier arrays, SiPM) in time coincidence. The specific efficiency obtained by Moghissi for scintillating fibers is sufficiently high to justify our choice of scintillating fibers as a detection medium. Additional elements are used to improve the tritium detection sensitivity such as a water purification system, which prepares the water sample before introducing it in the detector for tritium measurement and a cosmic veto and a passive shielding, which reduces the natural radioactive background of the tritium detector. Several electronic modules which control the different parts of the monitor, analyze the tritium measurement and send an alarm if the configured limit (100 Bq/L) is exceeded.

A crucial problem is to distinguish tritium signals from the background because tritium events have low energy (\sim keV) and fall in an energy range of the spectrum where background events are significant. To reduce the background counts of TRITIUM monitor, coincidence techniques are employed.

The TRITIUM monitor will be installed in the Arrocampo dam, Almaraz (Spain), displayed in Figure 2.1, where the Almaraz NPP releases the water from its secondary cooling circuit. This NPP has two nuclear reactors of PWR type. Arrocampo dam is located near the Tagus river, shown in Figure 2.1b, which is the longest river in Spain, with a length of 1007 km. This river, shown in Figure 2.1a, rises in Aragon (Spain) and flows into the Atlantic Ocean, through Lisbon (Portugal). The water of this river is used for agriculture and drinking water by both Spanish and Portuguese people. For this reason, an international cooperation is necessary in order to control and maintain the quality of the tagus river water.

Each institution of TRITIUM collaboration has focused its efforts in the development of a different part of this project:



Figure 2.1 – (Above) Arrocampo dam and Almaraz Nuclear Power Plant. (Below) Tagus river along Spain and Portugal.

1. The Extremadura group has developed and installed the water purification system to produce water with very low conductivity, $\sigma \approx 10 \mu\text{S}/\text{cm}$ (two orders of magnitude less than before the cleaning process, $1000 \mu\text{S}/\text{cm}$). This cleaning process is very important for two reasons. On the one hand, for maintaining the TRITIUM detector very clean, which is critical for its long-term functionality. On the other hand, to reduce the natural background since several natural radioactive isotopes present in this water (except tritium) are removed such as ^{222}Rn , ^{40}K or ^{137}Cs . This system is explained in section 3.3.
2. The French group has developed the passive shielding for the detector. The shielding is made of radiopure lead with very low intrinsic activity in order to reduce the external natural background of the system. This shielding is presented in section 3.4.1.
3. The Portuguese and Spanish groups have collaborated for designing, developing and building four different prototypes of the TRITIUM detector and active vetos for reducing cosmic events. These prototypes and vetos are explained in chapter 5 and section 3.4.2 respectively. They have also carried out simulations of this system. These simulations are explained in chapter 6.

The important characteristics of the TRITIUM detector must have

should be:

1. *Compactness.* Compactness is an important requirement because in the place where the detector is planned to be installed, Arrocampo, there is little space. Compactness also allows portability and cost reduction.
2. *Modularity.* The modularity of the TRITIUM detector is important for its flexibility in the geometrical configuration and to improve its tritium detection sensitivity, which increase in a scalability way. Modularity also makes it easy its construction and maintenance..
3. *Thin active volume and large active area.* The mean free path of the β particle of tritium decay is very short so thin detector active volumes are needed. In practice, active thickness beyond the mean free path of the tritium electrons only contributes to background. In addition, as reported in section 2.1, the efficiency of this type of detector scales with the active area, so it is crucial to design the detector with the largest possible active area.
4. *High efficiency detection for tritium.* As the tritium activities to be measured are very low, we cannot afford the loss of tritium events as it strongly affects the reliability of the tritium measurement..
5. *High specificity to tritium.* The monitor has to be able to distinguish the tritium signal from the signal due to other radioactive elements present in the sample.
6. *Quasi-real time response.* It is important that the system operates in quasi-real time (1 h or less) in order to detect any anomalous tritium release as fast as possible.
7. *Ruggedness.* The final goal of the project is to install an automatic system working during a number of years requiring only scarce in-

tervention of specialized operators. Therefore, a rugged monitor is required.

In order to get the measurement in quasi-real time, it is needed to work *in situ*, that is, in the same place where the water sample is taken. Working *in situ* has some advantages such as: 1) Faster and cheaper maintenance, since the sampling process, chain of custody, etc. are eliminated, 2) Continuous measurements are carried out and 3) Safer monitoring since personal exposure dose is reduced, 4) Changes in activity levels can be detected quickly.

Chapter 3

Design Principles and Components of TRITIUM

3.1 Detector System Overview

The objective of the TRITIUM project is the design, development, construction and commissioning of an automatic station for real-time monitoring of low levels of tritium in water. To achieve this aim, the TRITIUM collaboration has developed a monitor consisting of several parts, listed below:

1. The TRITIUM detector, described in detail in chapter 5, is based on several modules read out in parallel. Each module consists of hundreds of plastic scintillating fibers (section 3.2.2), which are in contact with the water sample measured, read out by two coincident photosensors (section 3.2.3). The photosensors considered are photomultiplier tubes (PMT) (section 3.2.3) and silicon photomultipliers (SiPM) (section 3.2.3).
2. The water purification system (section 3.3) that prepares the water

sample, taken from the Arrocampo dam, before measurement. This system removes all the organic particles dissolved and all the particles with a diameter greater than $1\text{ }\mu\text{m}$ without affecting the tritium content of the sample. This system is important for two reasons: first, because the mean free path of tritium in water is very short, 5 to $6\text{ }\mu\text{m}$, hence it is essential to avoid organic and mineral depositions onto the fiber surface since this would prevent the tritium decay electrons from reaching the fibers. The second reason is that minerals dissolved in water may contain radioactive isotopes like ^{40}K , which would increase the background. As the activity limit to be measured is low (down to 100 Bq/L), background reduction is crucial.

3. The background rejection system (section 3.4), that has two different parts. The first one is a passive shield (section 3.4.1), consisting of a lead castle inside which the TRITIUM detector is located. This castle is employed to suppress natural radioactive background and cosmic rays with energies up to 200 MeV/nucleon . The second part is an active veto (section 3.4.2), consisting of two plastic scintillating plates located inside the passive shield, above and below the tritium detector which are read out by photosensors. The goal of this active veto is to suppress the remaining high energy events ($> 200\text{ MeV}$), high energy events from cosmic rays that can travel through the passive shield and contribute to the background. The technique employed to suppress their contribution consists of reading the tritium detector in anti-coincidence with the active veto.
4. A readout electronic system which allows the acquisition and processing of the data, in order to provide an alarm signal in case the tritium level measure, within a short interval of time, exceeds the required limit of 100 Bq/L .

The TRITIUM system is planned to be part of the network of automatic stations, REA (section 1.1).

3.2 TRITIUM Detector

As discussed in section 2.1, the TRITIUM consists in a chain of three main elements, plastic scintillating fibers, that produce scintillating photons in response to a tritium electron decay detection, the photosensor, that detects the photons produced in the scintillator and produce an electronic pulse than gives information of the detected photons and the electronic system, which is in charge of processesing and analyzing (first analogically and later digitally) the electrical pulse given by the photosensor. A scheme of a scintillation detector is shown in Figure 3.1.

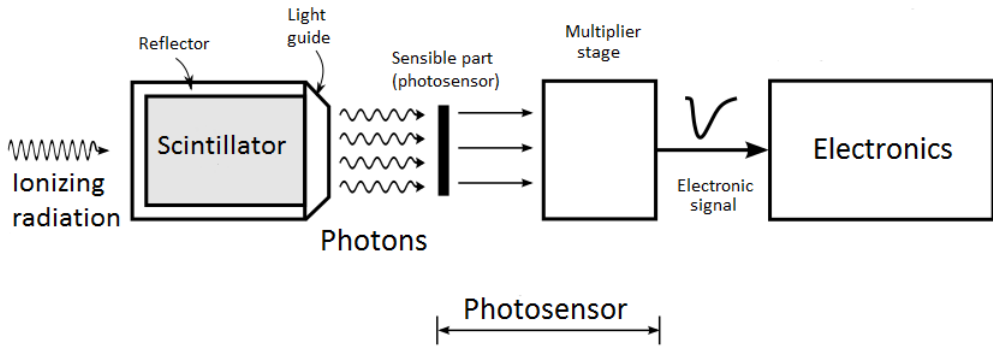


Figure 3.1 – Scheme of the scintillator detector.

3.2.1 Interaction of Fast Electrons and Photons with Matter

This section describes the interaction of particles with matter, focusing on the particles and energy range relevant for this thesis, electrons (0–18 keV), photons in the visible range (approx. 380 – 750 nm) and γ particles that come from the background and high energy events of cosmic rays.

Electrons have charge, so their interaction with matter is mainly

with the orbital atomic electrons through the Coulomb force. The electron trajectory is much more tortuous than heavier particles because the mass of both interacting particles is equal. Furthermore, for the same reason, these electrons lose a significant amount of energy in each collision. The specific energy loss is defined as $S = -\frac{dE}{dx}$ which gives the energy loss suffered by the particle per unit of path length. In the case of electrons, this total energy loss has two main contributions, the collisions (elastic and inelastic) and radiative processes (bremsstrahlung), which are roughly proportional [Kno99, Leo94]:

$$\frac{dE}{dx} \approx \left(\frac{dE}{dx} \right)_c + \left(\frac{dE}{dx} \right)_{br}; \quad \frac{\left(\frac{dE}{dx} \right)_{br}}{\left(\frac{dE}{dx} \right)_c} \approx \frac{EZ}{700} \quad (3.1)$$

where E is the energy of the electron in MeV and Z is the atomic number of the absorbing material. Due to this energy loss, the electrons penetrate a material to a depth where they have lost their total kinetic energy. This distance is known as range and, in the case of tritium electrons, its value is quoted in Table 1.4.

The material chosen for the detection of the tritium decay electrons are organic plastic since, due to its low density, the backscattering process is reduced, optimizing its detection. It has been chosen in a form of fibers in order to increase the active area and, therefore, the efficiency of the detector.

As photons do not have charge, their possible interactions with matter are photoelectric effect, Compton effect, coherent scattering and pair production. The probability of each process, displayed in Figure 3.2, depends on the energy of the photon, $E_\gamma = h\nu$, and on the atomic number of the material, Z . The optical photons have a wavelength between 400 and 700 nm, the visible range, that corresponds to energies of the order of the

eV. Therefore, pair production process does not play any role in optical photons since this requires a photon energy equal or more than 1.022 MeV.



Figure 3.2 – Domain regions of the three most probable types of interactions of gamma rays with matter. The lines show the values of Z and $h\nu$ where two interaction processes are equally likely [Kno99].

The photoelectric effect occurs when a photon interacts with an orbital electron in the material, losing all its energy. This energy is absorbed by the electron that is released from the atom (ionization). The energy of the resulting electron, E_e , is [Kno99, Leo94]:

$$E_e = E_\gamma - E_b \quad (3.2)$$

where E_b is the binding energy of the electron in this material. The probability of this effect depends on the number of available electrons in matter through the atomic number Z , and the energy of the electron according to the expression [Kno99]:

$$(Pr)_{Ph-eff} \approx \frac{Z^n}{E_\gamma^{3.5}} \quad (3.3)$$

Thus, the photoelectric effect is most probable for elements with high atomic number. This is the reason why this type of elements are the best insulators against gamma radiation and why the passive shield of TRITIUM monitor consists of lead bricks ($Z = 82$) (section 3.4.1).

The Compton effect occurs when a photon interacts with an orbital electron of the material, transferring part of its energy to the electron, which is released, scattered at an angle θ with respect to the direction of the incident photon. If the electron binding energy is neglected, the energy transferred to it, E_e , is given by [Kno99, Leo94]:

$$E_e = \frac{\frac{E_\gamma^2}{m_0 c^2} (1 - \cos\theta)}{1 + \frac{E_\gamma^2}{m_0 c^2} (1 - \cos\theta)} \quad (3.4)$$

where m_0 is the rest mass of the electron and c is the speed of the light in the vacuum. The probability of the Compton effect is proportional to the atomic number (available electrons in the matter), Z , and decreases with the energy of the photon. As it can be seen in Figure 3.2, for photon energies in the visible spectrum (of the order of eV), the Compton effect is only likely for very light materials, ($Z < 4$). For heavier materials the photoelectric effect is the dominant effect.

In the coherent scattering, the atom is neither excited nor ionized and the photon conserves its energy in the collision. Coherent scattering is more probable for photons with low energies and materials with high atomic numbers.

Finally, in the pair production process, the photon is converted

within a electron and a positron (anti-electron).



As can be seen in Figure 3.2, this is the dominant interaction process for high energy photons, which are the photons found in the background or in cosmic ray that can affect the TRITIUM detector.

3.2.2 Plastic Scintillators

Scintillators are materials widely employed for radiation detection in nuclear physics. Scintillators convert kinetic energy of the incoming particles into light¹ which can be detected and quantified. Light emission is produced due to the photon de-excitation of atoms of fluorescent molecules in the material.

Light production is linear in a wide energy range of incoming particles. Scintillators should have good optical properties, such as being transparent to the wavelength of their own emission and having a refractive index close to that of photosensors windows in order to optimize optical coupling and light transmission. Photon emission in scintillators is a statistical process, which means that identical events emit a different number of photons that follows a Poisson statistics.

Scintillators can be organic or inorganic material. Inorganic scintillators normally have a higher atomic number and density, so their light output is higher. For these reasons they are better for gamma-ray spectroscopy. Organic scintillators are generally faster and they are commonly used for charged particles and neutron detection. This section is focussed on organic scintillators since they are the ones used to build the TRITIUM detector.

¹The light is made up of photons in the visible energy range.

Organic scintillators are based on a fluorescent molecules dissolved in a base solvent, usually aromatic hydrocarbons as $C_{18}H_{14}$, $C_{24}H_{22}N_2O$ or $C_{15}H_{11}NO$ with an average atomic number between 3.5 and 5. The fluorescent molecules of organic scintillators have a π -electron structure. The energy levels of their electrons are commonly illustrated with a Jablonsky diagram, shown in Figure 3.3. This diagram shows the fundamental singlet states, S_{0i} , where the valence electrons are, the excited singlet states, S_{jk} , and the excited triplet states, T_{lm} . The energy difference between S_1 and S_0 states is around 3 to 4 eV, which corresponds to the visible photon emission. As it is shown in the figure, each energy state is split in close sublevels separated around 0.15 eV. This fine energy structure is due to excitations of molecular vibrational modes tagged by the second index of the energy states. As the energy levels and sublevels have an energy larger than the thermal energy, 0.025 eV, non-excited electrons are in the ground state S_{00} at STP².

When a particle deposits its kinetic energy in a scintillator, the valence electrons are excited to higher singlet energetic states very fast (times of the order of picoseconds) and are quickly de-excited to the first singlet excited state, S_{10} , through non-radiative processes known as internal conversion. These electrons can de-excite to the fundamental single state, S_{00} , through three different physical mechanisms:

1. Prompt fluorescence (process A in Figure 3.3), where the electron in the S_{10} energy level is de-excited to a sublevel of the ground state S_{0i} , emitting a photon. This process happens immediately after the excitation of the scintillator molecules (of the order of nanoseconds after excitation). Each scintillator has a characteristic emission spectrum that defines its response due to the fluorescence mechanism.

Organic scintillators are practically transparent to their own fluorescence emission because there exist a quenching effect in each de-

²Standard temperature and pressure conditions

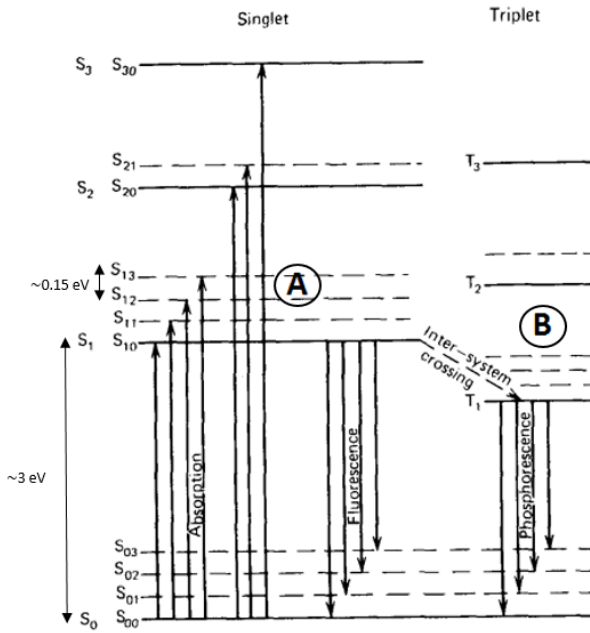


Figure 3.3 – Jablonsky diagram [Kno99].

excitation process by which the scintillating photons have less energy than the excitation energy. This effect is called Stokes shift and it is represented in Figure 3.4.

The intensity of the fluorescence emission in an organic scintillator versus time is the combination of two exponential functions, one associated with the lifetime of the level, τ (on the order of nanoseconds), and the other associated with the energetic level population, τ_1 (on the order of picoseconds) [Kno99].

$$I = I_0 (e^{-t/\tau} - e^{-t/\tau_1}) \quad (3.6)$$

2. Phosphorescence, where the electron that is in the first single excited state crosses to a triple excited state (process B in Figure 3.3). Such a transition process is called "intersystem crossing". This is a metastable state with a longer lifetime than fluorescence, of the order



Figure 3.4 – Stokes shift [Kno99].

of milliseconds after scintillator excitation.

3. Delayed fluorescence, which occurs when an electron is in a triple excited state but its transition to the ground state is forbidden. In this case, the electron interacts with another electron in a similar state, falling to the first singlet state and quickly de-exciting to the ground state.



This emission has the same emission spectrum as the prompt fluorescence, but with a longer lifetime.

As the prompt fluorescence light produces the scintillator signal, the detector design should optimize its collection and detection and reduce other possible physical mechanisms like phosphorescence or delay fluorescence. One of the most important parameters that characterizes the scintillator is

the scintillation yield³, defined as the the number of photons emitted per unit of absorbed energy. This yield depends on the type of particle and on other mechanisms that do not produce prompt fluorescence, like phosphorescence, delayed fluorescence, and non radiative processes like internal conversion. The scintillator yield is normally quoted by the manufacturer for mips⁴.

Plastic scintillators are easy to machine to any desired shape. The chosen shape for TRITIUM detector is the fiber, specifically, commercial fibers BCF-12 from Saint-Gobain Crystals Inc [Cer05]. This type of fiber was chosen as the result of a comparative study [Cam17] among some of the best-known commercial manufacturers. The BCF-12 fibers consist of scintillating polystyrene core covered by one or two polymethylmethacrylate (PMMA) claddings.

When a particle deposits all or part of its kinetic energy in the scintillating fiber, photons are produced in the fiber core as a result of the fluorescence process. The number of photons produced depends on the production light efficiency of the scintillator (scintillating yield) and its value is around 2.4% for the fibers used (BCF-12), which means that a scintillation yield of about 8000 photons will be produced per MeV for a mip. For instance, for tritium electrons of 18.6 keV maximum energy, these fibers release at most 148 photons, probably less as electrons of these energies are not mips. The emission spectrum of the fibers employed in this work, is shown in Figure 3.5.

The scintillation light is guided to the sensitive part of the photosensor. A single photon produces a signal with some probability, called the quantum efficiency. Fibers (and scintillators in general) use the optical property of Snell's law [Bor19] to guide their photons to the desired part

³The scintillation yield is a way of expressing the efficiency of the scintillator in converting the energy deposited by the particle into photons.

⁴The MIP, Minimum Ionized Particles, is a particle that has the speed that generates minimum ionization, that's, for example, electrons with 500 keV or more.

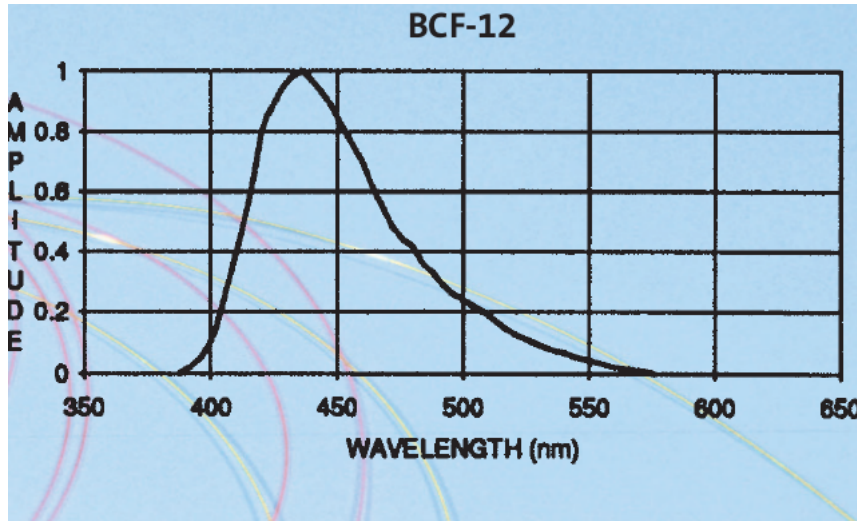


Figure 3.5 – Emission spectrum of BCF-12 scintillating fibers of Saint-Gobain [Cer05].

(ends of the fibers). The guiding mechanism is determined by the interface between the core and the surrounding material. When a photon hits this interface, it is refracted (and therefore lost) following the Snell equation, 3.8 [Bor19].

$$n_0 \sin(\theta_0) = n_1 \sin(\theta_1) \quad (3.8)$$

where θ_0 is the incident angle formed by the photon and the surface of in the first environment, with refractive index n_0 and θ_1 is the refracted angle formed by the photon and the second environment with refractive index n_1 . If the surrounding material has a lower refractive index than the core of the fiber, as it is the case with scintillating fibers, there exist a critical angle, θ_c , beyond which photons will be totally reflected ($\theta_1 = 90^\circ$) and therefore kept within the fiber as illustrated in Figure 3.6.

$$\theta_c = \arcsin \left(\frac{n_1}{n_0} \right) \quad (3.9)$$

The trapping efficiency or photon collection efficiency is defined

as the efficiency of the scintillator to guide photons. For BCF-12 fibers with optical clad this efficiency is between 3.44% and 7% per meter of fiber (depending on where the event is detected and is minimum near the fiber axis and maximum near the core-clad interface). Therefore, from the 148 photons initially created by a tritium decay electron detected with the maximum energy, 18.6 keV, and assuming a light yield of 8000 photons/MeV according to the manufacturer, only 52 photons are guided along the 20 cm fiber length of the TRITIUM detector (considering the maximum trapping efficiency (7%) and guessing a linear dependence with the length of the fiber). Thus, the output signal is weak and is in the energy range of the spectrum where electronic noise is already significant. As described in the following chapters, a great effort was made to minimize electronic noise by different techniques. In Figure 3.6 the light collection in a fiber is illustrated.

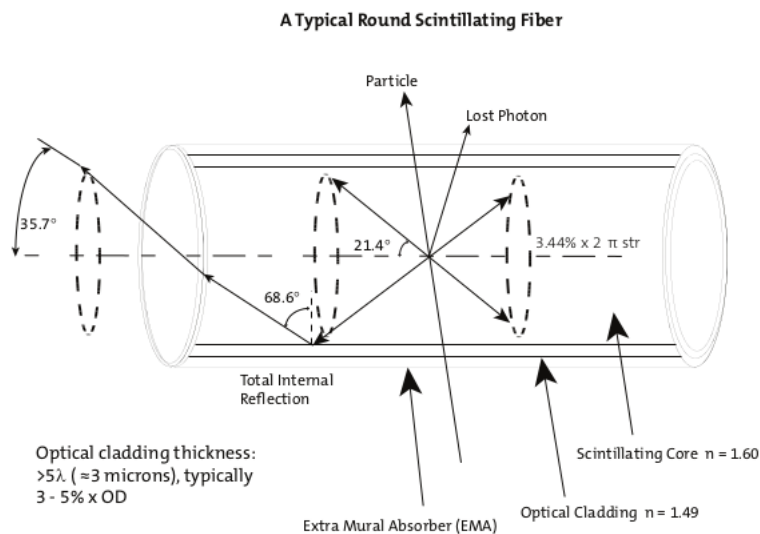


Figure 3.6 – Photon collection in a single clad fiber [Cer05].

The cladding material has a higher refractive index than air or water. Due to that, this is useful for protecting the core surface from dirt or aggressive external agents that may reduce the light collection but at the cost of increasing the critical angle with its corresponding loss of light.

Three different cases are shown in Table 3.1, where the cladding effect is illustrated.

Material	Refractive index	critical angle (°)
Air	1	42.98
Water	1.33	62.47
Cladding of PMMA	1.49	76.26

Table 3.1: Critical angles associated to different interfaces created with polystyrene, $n_0 = 1.6$, and other materials.

As can be seen, the trapping efficiency of uncladded fibers BCF-12 surrounded by water or air is larger than for cladded fibers. However, in the practice, it is difficult to achieve a perfect air-core or water-core interface, and this affects light collection. As commercial claddings are thicker (30 µm) than the mean free path of tritium decay electrons in water (around 5 µm), cladded fibers are not an option for the TRITIUM detector. Hence, special attention is needed for achieving a good enough water-core interface. To achieve this goal a special method was developed in the ICMOL laboratory for preparing fibers for tritium detection, detailed and tested in section 4.1.1. The relevant parameters of scintillating fibers used for TRITIUM detector are given in Table 3.2.

3.2.3 Light Detection in Photosensors

The scintillating photons created in the core of the fiber and guided to its ends are detected by photosensors. Photosensors have a sensitive part that is optimized to detect photons in a range of energy (usually in the visible range) with a certain probability, called quantum efficiency. The photosensors produce an electronic signal that carries information about the detected photons such as their number, detection time, etc. There are many available photosensors that rely on various physical processes, such as

Property	Value
Core material	Polystyrene
Core refractive index	1.60
Density (g/cm ³)	1.05
Cladding material	Acrylic (PMMA)
Cladding refractive index	1.49
Cladding thickness	3%
Numerical aperture	0.58
Trapping efficiency	3.44% minimum
No. of H atoms per cc (core)	$4.82 \cdot 10^{22}$
No. of C atoms per cc (core)	$4.85 \cdot 10^{22}$
No. of electrons per cc (core)	$3.4 \cdot 10^{23}$
Radiation lenght (cm)	42
Emission peak (nm)	435 (Blue)
Decay Time, (ns)	3.2
1/e Length (m)	2.7
Scintillator yield (# γ /MeV)	~ 8000
Operating Temperature	$-20^{\circ}C$ to $50^{\circ}C$

Table 3.2: Properties of BCF-12 fibers from Saint-Gobain Inc. [Cer05].

photomultiplier tubes (PMTs), silicon photomultipliers (SiPM) or Charge-Coupled Devices (CCD).

The optimization of the efficiency of a scintillation detector is essential. To do so, the emission spectrum of the scintillator (Figure 3.5 for the fibers used) must overlap as much as possible with the detection efficiency spectrum of the photosensor chosen. The detection efficiency spectrum of a photosensor gives the probability of detecting photons as a function of wavelength. The efficiency of a detector is proportional to the product of both, the emission and the detection efficiency spectra, and this is largest when both spectra match.

The requirements imposed on the photosensor of the TRITIUM detector are that they be very fast, have high gain and are able to detect a single photon with high photodetection efficiency. Two different proposals for the TRITIUM detector are investigated, SiPMs and PMTs. Both meet these requirements since they are very fast (of the order of ns), have high gain (of the order of 10^6) and have a high photodetection efficiency (around 50% for SiPMs and 30% for PMTs). Each proposal has their own advantage. SiPMs are more robust and need a lower supply voltage (of the order of 50 V) than PMTs (of the order of 1000 V). Furthermore, due to this difference in the supply voltage, SiPMs have a smaller cost per unit of channel than PMTs since a SiPM array, which can be feed with a single channel. However PMTs, which are the conventional choice, have lower dark count rate than SiPM and a much lower dependence with the temperature.

Photomultiplier Tubes (PMTs)

Photomultiplier tubes are employed as photosensors in nuclear physics since decades. They detect the scintillating photons that reach its sensitive part, the photocathode, and produce an electronic signal, large enough to be easily measured. In Figure 3.7 a schematic drawing of a PMT is given.

This consists of a vacuum tube that has a glass window through which photons can penetrate. The electrons created in the photocathode travel in vacuum.

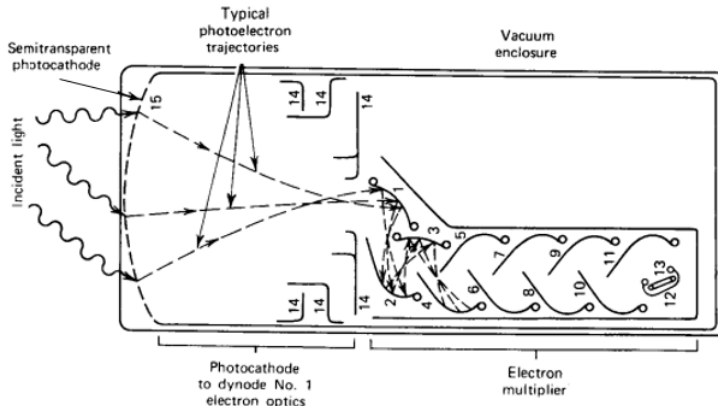


Figure 3.7 – Scheme of a PMT [Kno99].

The signal production has two phases:

1. In the photocathode, photons are converted into photoelectrons through photoelectric effect. The photocathode consists of a thin layer of material, of the order of nanometers, deposited on the inner surface of the PMT window. The material of the photocathode is chosen to optimize the probability of producing photoelectric effect with the scintillating photons. The PMTs used in different R&D setups of the TRITIUM experiment in the University of Valencia are the model R8520-406 from Hamamatsu [K.K19] and the material of their photocathode is Bialkali⁵.

The response of the PMT for long wavelengths is very weak, mainly because photon energy is not enough to produce a photoelectric effect or the emitted photoelectron does not have enough energy to overcome the material-work function. The response of the PMT at short wavelengths is very weak due to absorption in the window material, quartz

⁵The bialkali material is based on the elements $^{121}_{51}\text{Sb}$, $^{85}_{37}\text{Rb}$ and $^{132}_{55}\text{Cs}$

in our case. Thus, the response of the PMT has a strong dependence on the energy of the photon. The quantum efficiency (QE) spectrum, shown in Figure 3.8 for the PMTs mentioned above, is defined as the ratio of the number of photoelectrons produced at the cathode of the PMT and the number of photons reaching it.

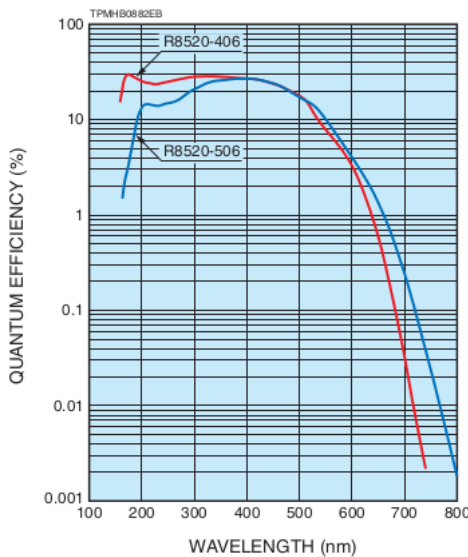


Figure 3.8 – Quantum efficiency spectrum for the PMT used in TRITIUM R&D studies (R8520-406) [K.K19].

The maximum values of the PMT quantum efficiency is usually between 20% and 30% [Kno99] (a little bit less than 30% for the PMTs employed by us). The emission spectrum of the scintillating fibers used, Figure 3.5, matches the quantum efficiency spectrum of the PMTs used, Figure 3.8, and the positions of both peaks are very close, 435 nm and 420 nm for fibers and PMT respectively. Because of that, the intrinsic efficiency of the TRITIUM detector is maximized.

2. As the number of photoelectrons produced in the photocathode is very small, an electron multiplication stage is employed to obtain an electronic signal of sufficient size to be processed by the electronic sys-

tem. The amplification stage is based on three elements, focusing electrodes, dynodes and anode, which are metallic plates with a shape and position designed to optimize the collection and multiplication of electrons. A high voltage (HV) is applied to the PMT which is distributed between all this elements, including the photocathode, with the help of an electronic circuit. A positive HV, grounded in the photocathode, is convenient for measuring PMT currents, and a negative HV, grounded in the anode, gives a faster response. The electronic scheme of the used electron multiplication stage (with negative supply HV) of Hamamatsu are shown in Figure 3.9.

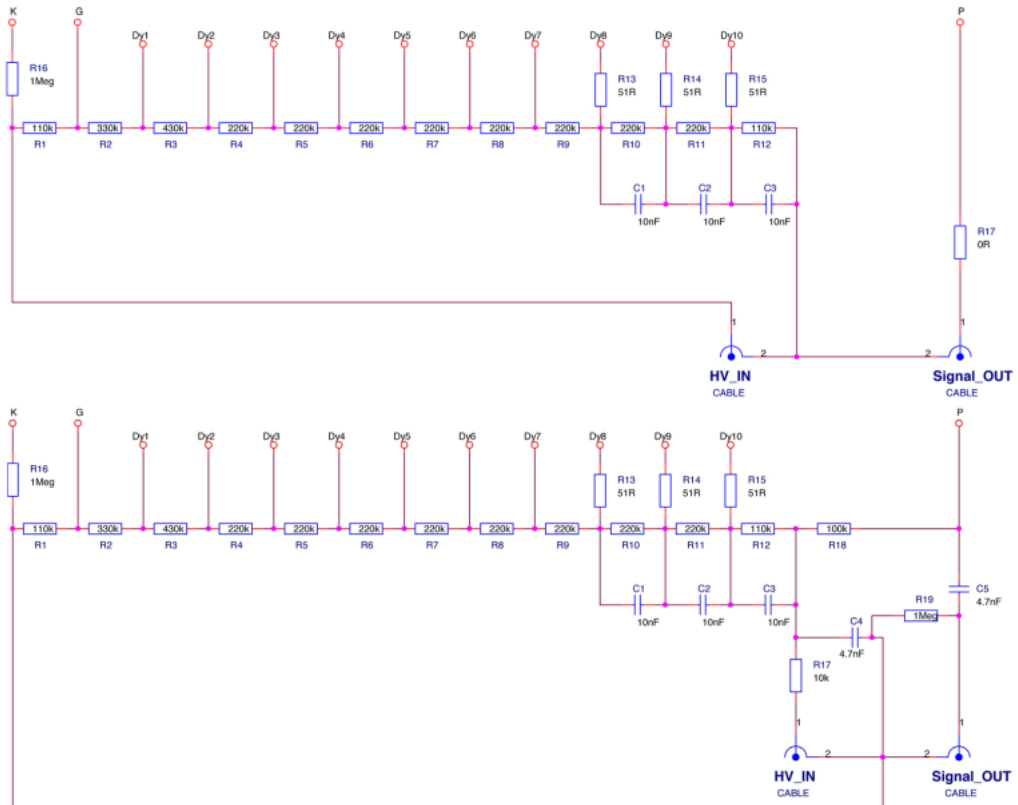


Figure 3.9 – Hamamatsu commercial voltage divider electronic circuit with negative (up) and positive (below) supply high voltage [K.K19].

Focusing electrodes guide the photoelectrons to the first dinode. They have a collection efficiency (CE) defined as the ratio of the number of photoelectrons reaching the first dinode and the number of photoelectrons leaving the photocathode. The value of CE depends on the bias voltage and, normally, it has a maximum of 80%. The dynodes achieve the electron multiplication. A voltage difference between adjacent dynodes accelerates the electrons and produce their multiplication. The multiplication factor of each dynode, δ , is usually around 5 and is strongly dependent on the HV. If all dynodes have the same gain, the overall gain of a PMT with N dynodes is [Kno99]:

$$G_{PMT} = CE \cdot \delta^N \quad (3.10)$$

that gives an overall gain of a PMT of the order of 10^6 , strongly dependent on the applied HV.

The multiplication stage adds an uncertainty to the measurement. Working without gain allows us to count the number of photons that reach the PMT. This can be done by short-circuiting all the dynodes and the anode and collecting the signal directly from the first dynode. This special multiplication stage, shown in Figure 3.10, was used for fiber characterization.

This PCB was designed to be supplied with a positive voltage smaller than the usual running voltage because this voltage is only needed to create a voltage difference between the photocathode and the first dinode.

The output pulse of a PMT has a width of the order of tens of nanoseconds. When the multiplication stage with gain are used, the multiplication process can be described as a Poisson statistical process. For each electron in the first dynode, G_{PMT} new electrons are created with a variance of $\sqrt{G_{PMT}}$.

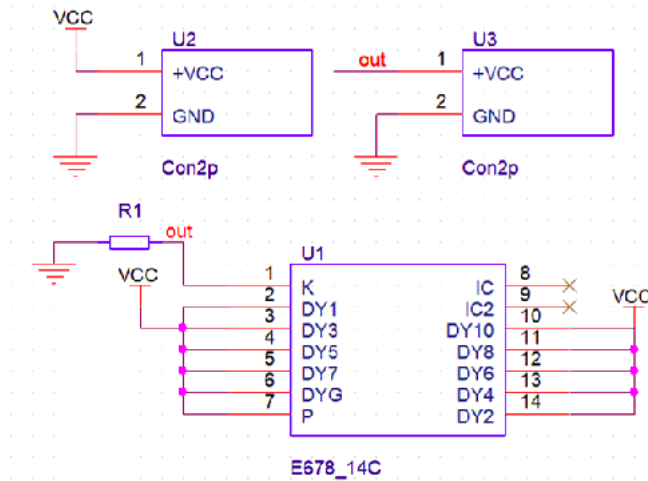


Figure 3.10 – Electronic scheme of the voltage divider circuit used for working with PMTs without internal gain).

The output signal of a PMT is linear with the number of photons that reach its sensitive part up to a saturation limit, at which the linearity is lost. This limit depends on the PMT characteristics.

The photocathode may emit electrons in absence of any scintillation light. This signal, called dark current, I_{DC} , can arise due to thermoionic emission. For the PMTs employed in this work, this value is around 2 nA according to their data sheet.

Silicon Photomultiplier Array (SiPMs array)

The Silicon Photomultiplier (SiPM), also called Multi-Pixel Photon Counter (MPPC), is a kind of photosensor based on semiconductor materials, developed in the last two decades. SiPMs are replacing progressively conventional PMTs in many experiments and applications. They have outstanding photon counting capabilities at the single photon level with higher photode-

tection efficiency than PMT and they have similar gain. SiPMs have, in addition, several advantages as insensitiveness to magnetic fields, low operating voltage, compactness (they may have down to 1 mm^2) and ruggedness. The only drawback with respect to the PMTs is their high dark count rate (between 100 kHz and 1 MHz).

SiPMs are formed by a matrix of Avalanche Photodiodes (APDs) connected in parallel and operating in Geiger mode. APDs, the scheme of which is shown in Figure 3.11, are based on p-n junctions⁶ made with special techniques to achieve a good contact between both surfaces.

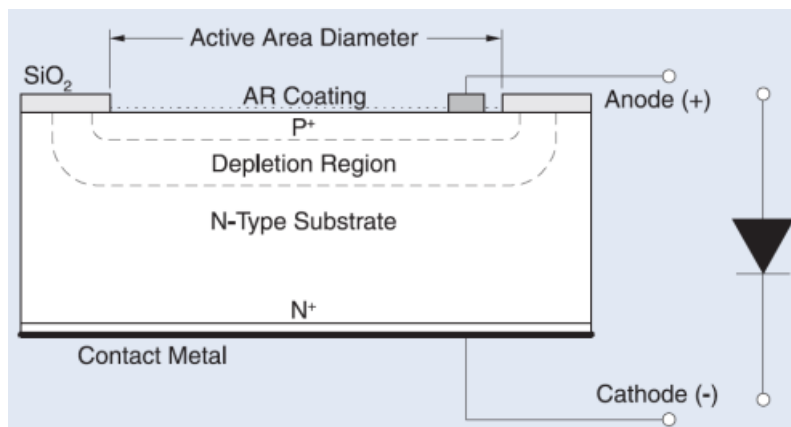


Figure 3.11 – Scheme of a APD and electrical symbol used [Opt].

The voltage at which the SiPM starts operating in Geiger mode is called the breakdown voltage, V_{BD} . At lower voltages, SiPMs work in proportional mode in which the signal of each APD is proportional to the energy deposited but their gain is lower than in Geiger mode. The experimental measurement of the breakdown voltage, described in section 4.2, is an important measurement to characterize a SiPM, since properties of SiPMs, as the gain, depend on the overvoltage, V_{OV} . The overvoltage is

⁶A p-n junction is a junction of a p+ and n+ layer, which are a tetravalent material doped with a trivalent or pentavalent material respectively, creating sublevels in the forbidden energy gap.

the voltage applied to the SiPM above its breakdown voltage and this is expressed as:

$$V_{bias} = V_{BD} + V_{OV} \quad (3.11)$$

These APDs, called pixels when they are part of a SiPM, are connected in parallel and the output signal of the SiPM is the sum of all of them. If the photon flux is low enough, each SiPM pixel detects only one photon and its output signal is similar compared to other pixels of the same SiPM, regardless of the energy deposited, with some difference because of the uncertainty due to the SiPM manufacturing process and the statistical nature of photoelectron production. Therefore, the charge of the output signal when n pixels are simultaneously fired is n times the charge of a single pixel, as can be checked in Figure 3.12. Due to this property, the number of detected photons is linearly proportional to the value of the output signal area. In addition, as the detected photons are proportional to the incident photons when the SiPM are working in the linearity range, after an accurate calibration of SiPM gain, described in section 4.2, the linearity of the SiPM output signal versus the number of incident photons and, therefore, the deposited energy of tritium events, is recovered.

If the photon flux is high (typically several thousands of photons per event) more than one photon will impinge on the same pixel, but the output signal would be that of one only detected photon. This effect, known as saturation, produces a loss of linearity of the output signal. However, this effect is not important for the TRITIUM detector since its scintillating signals are far from producing so many photons.

Different sizes of the SiPM pixel can be chosen⁷. For the same active area of the SiPM, the smaller pixels allow the SiPM to have more pixels, which implies a higher dynamic range, at the cost of reducing its

⁷Pixel sizes for commercial SiPMs are 25, 50 or 75 μm [Div16a], [Div16c], [Div16d]



Figure 3.12 – SiPM output pulses displayed on oscilloscope, model MSO44X from Tektronix [Tek21]. Several height pulses are observed, associated to a different number of SiPM pixels fired at the same time. The persistence function of the oscilloscope is used.

quantum efficiency. As the TRITIUM detector signals have few photons, the SiPMs used have the largest pixel size as we are far from the limit of dynamic range and quantum efficiency is a critical parameter for tritium detection.

The SiPM can be modeled as an electric circuit, shown in figure 3.13a, in which, due to the charge distribution in the depletion zone, a capacitance is induced by the SiPM. This is schematized as a reverse biased diode in parallel with a capacitor of capacitance C_d , as shown in Figure 3.13a. When the pixel detects a photon, the capacitor is discharged, creating an output current (electronic pulse).

In addition, each pixel of a SiPM has a quenching resistance⁸ in

⁸The tipical value of this quenching resistance for commercial SiPMs is around 500 kΩ



Figure 3.13 – (a) Electronic scheme of a SiPM and (b) output current of a SiPM as a function of the reverse voltage. As shown, the quenching is an essential working mechanism of SiPMs [sl17].

serie, R_q , that stops the avalanche current produced when this pixel is fired, creating a time limited electronic pulse. When the discharge is produced, a current flows through the resistance, reducing the reverse voltage seen by the diode below the breakdown voltage. Then, the current that flows through the diode is stopped and the voltage within the diode is reset to the bias voltage. This pixel is ready to detect a new photon again. This behaviour is schematically shown in Figure 3.13b.

The recovery of the bias voltage within the SiPM pixel after photon detection is characteristic of a RC circuit, described by the equation:

$$V_{bias}(t) = V(t_0) (1 - e^{-t/\tau}) \quad (3.12)$$

where τ is the recovery time constant of the system, given by $\tau = C_d \times R_q$. In section 4.2 the capacitance C_d and the quenching resistance R_q are experimentally measured and the recovery time constant extrapolated from both.

SiPM gain (typically of the order of 10^6) is defined as the number of charges produced when a single pixel is fired. This can be measured experimentally from the SiPM Single Photon Spectrum (SPS), which is the spectrum obtained when the SiPM output signal is integrated (charge) and histogrammed. The experimental measurement of the SPS and the calculation of the gain is presented in section 4.2. It has to be taken into account that the SiPM gain is highly dependent on temperature, which cannot be controlled with sufficient sensitivity (less than 1°C) in the final location of the TRITIUM monitor. Therefore, a gain stabilization method was implemented to compensate for the temperature effect. This method is detailed in section 4.2.

An important parameter for the SiPM used in the TRITIUM project is the photon detection efficiency, PDE. This is defined as the probability of recording the electrical pulse produced by a photon that hit the SiPM. The PDE of a SiPM consists of a product of three different parameters, the fill factor (FF), which is the ratio between the active area of the SiPM and its total area, the quantum efficiency (QE), which is the probability of producing a photoelectron when a photon hits the SiPM and the probability that the generated electron or hole produces an avalanche, P_{av} .

$$PDE = FF \times QE \times P_{av} \quad (3.13)$$

Likewise PMTs, SiPMs produce pulses that are unrelated with any incident photon, called the dark current. The pulse rate of these events is called dark current rate and it depends on temperature. At temperatures around 25°C , these pulses are mainly produced by the thermal generation, i.e., when the temperature produce a thermal energy allowing electrons from the valence band to overcome the forbidden band and go up to the conduction band. The dark current signal is identical to the signal produced by a single photon, so they cannot be discriminated. Therefore, it is very

important to determine the magnitude of the dark current in the tritium signal from the detector.

Electrons contained in an avalanche of a SiPM pixel emit secondary optical photons⁹. These optical photons can reach other pixels, producing new avalanches. This effect, called optical cross-talk, produces photoelectrons that add to those truly induced by incident photons, and hence leads to an overestimation of the number of photons detected. The probability of producing an optical crosstalk event depends on the number of electrons produced in the avalanche (gain) and, therefore, on the temperature and the overvoltage. This probability at the overvoltage recommended at 25°C by the manufacturer is typically less than 10%.

The PDE, dark count rate and crosstalk are not experimentally measured yet since a different setup, shown in reference [Yah13], is needed. These parameters will be measured for the SiPM model used in the final version of TRITIUM monitor.

Due to imperfections existing in the cristal lattice of a SiPM, called traps, an electron of an avalanche can be captured and released after a characteristic time, τ_a . If this characteristic time is longer than the pixel recovery time, typically 3τ , this electron can trigger a new avalanche which will be seen as a new event. These events, called afterpulses, are often emitted around 1 μ s after the photon-incident pulses. The afterpulse probability was not measured since it is not relevant for the TRITIUM project. The reason is that the TRITIUM detector makes time coincidences using 10 ns time windows. At this level, the afterpulse probability is negligible since it normally happens 1 μ s after the SiPM output pulse.

The initial SiPM candidate for TRITIUM project and the one which was characterized is the model S13360-1375 from Hamamatsu Ph-

⁹Around 20 secondary optical photons are emitted in each SiPM output pulse with gains of the order of 10^6 [Spi97]

tonics [Div16b] because this model has interesting characteristics and properties, shown in Table 3.3. This model was mainly chosen due to its large pixel size, $75 \mu\text{m}$, which implies a high PDE and a high gain, both important parameters for the TRITIUM project due to the low activity to be detected and to the small signals produced by tritium events. High PDE and high gain are achieved at the cost of reducing the dinamic range, which is not an issue due to the small photon signals expected from tritium events in the scintillating fibers.

Parameter	S13360-1375	S13360-6075
Series	S13360	S13360
Model	1375	16075
Pixel Pitch (μm)	75	75
Effective photosensitive area (mm^2)	1.3×1.3	6.0×6.0
Number of pixels	285	6400
Fill factor	82%	82%
Refractive index of windows material	1.55	1.55
Operating temperature range ($^\circ\text{C}$)	$[-20, 60]$	$[-20, 60]$
Spectral response range, λ (nm)	[320, 900]	[320, 900]
Peak sensitivity wavelength, λ_p (nm)	450	450
PhotoDetection Efficiency, PDE, $\lambda = \lambda_p$ (%)	50	50
Dark counts, Typical/Maximum (kcps)	90/270	2000/6000
Terminal capacitance, C_t (pF)	60	1280
Gain, M,	$4 \cdot 10^6$	$4 \cdot 10^6$
Breakdown Voltage, V_{BD} (V)	50.97	53
Cross talk probability(%)	7	7
Temperature coefficient ΔTV_{op} (mV/ $^\circ\text{C}$)	54	54

Table 3.3: Characteristics of SiPM S13360-1375 and S13360-6075 from Hamamatsu Photonics [Div16b].

These parameters quoted in Table 3.3, are typical values provided by the manufacturer, Hamamatsu photonics. They can vary significantly from one SiPM to another of the same model. Thus, it is convenient and sometimes necessary to measure them. Some of these measurements for

TRITIUM are reported in section 4.2.

This SiPM was also chosen because, as it can be observed in Figure 3.14, its maximum PDE is reached at $\lambda_{p,SiPM} = 450$ nm, which is very close to the peak of the emission spectrum of the scintillating fibers used, $\lambda_{p,fiber} = 435$ nm.

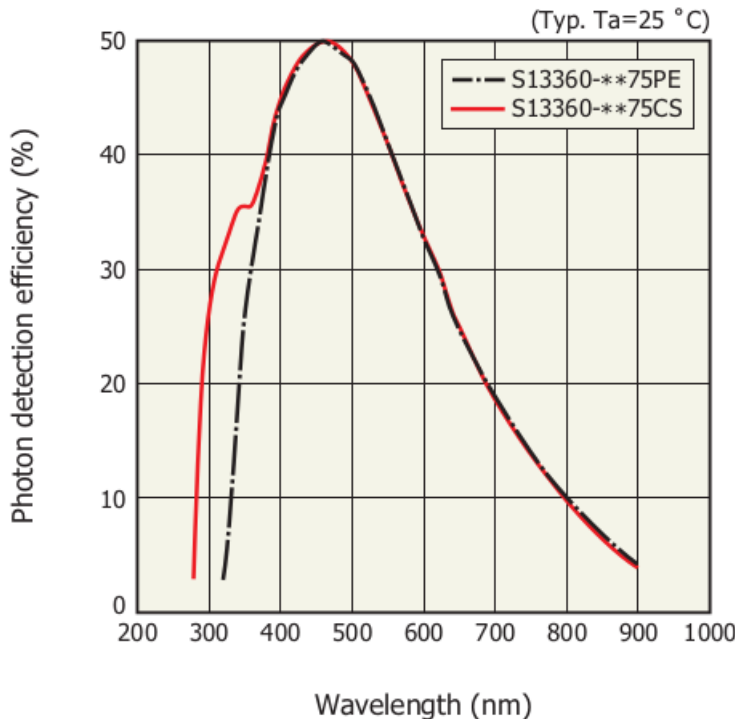


Figure 3.14 – Photon detection efficiency (PDE) spectrum for SiPM S13360-**75 models [Div16b].

This SiPM was later replaced by the model S13360-6075 from Hamamatsu Photonics [Div16d], whose properties are also listed in Table 3.3. The only difference between both models is their larger active area ($6 \times 6 \text{ mm}^2$), which is the largest active area of commercial SiPMs of Hamamatsu, that allows to read more scintillating fibers. This improvement is achieved at the price of a higher dark count rate (typically 2 Mcps). Finally,

arrays of this SiPM model are commercially available and were chosen for the TRITIUM detector prototypes built at IFIC.

Although TRITIUM detector uses SiPM matrices, the characterization has been carried out at the level of a single SiPM to learn about the values of the SiPM parameters and to test the gain control method.

Photosensors in TRITIUM

There exist two different proposals for the photosensors employed in the TRITIUM monitor, PMTs and SiPM arrays. Each type of photosensor has advantages and disadvantages and must be experimentally tested to ensure the most suitable option. PMTs are used in the TRITIUM prototypes developed by Aveiro experimental group while SiPM arrays are used in the TRITIUM prototypes developed at IFIC, in Valencia.

PMTs with and without gain have also been used in Valencia to perform various laboratory measurements such as R&D studies with fibers, characterization of the active veto and test measurements of the TRITIUM prototypes developed.

The IFIC experimental group of TRITIUM has chosen the SiPM matrix option for the TRITIUM photosensor option for its advantages over PMTs, which are compactness and robustness, necessary to work for several years without supervision, its larger efficiency for the detection of photons in the visible range, critical parameter for the TRITIUM monitor, and its economic price, which are cheaper than PMTs not only the photosensor itself, but also the electronic system necessary to feed them and process and analyze their output signal. However, the SiPM arrays have a higher dark count rate compared to the PMTs, which is a relevant disadvantage for the purpose of TRITIUM monitor since low activities of tritium are intended to be measured.

3.2.4 Electronic Readout

The electronic system is in charge of collect, processing and stores the output signals of photosensors (raw data) that have to be further analized. This electronic system depends on the type of output information and on the detector configuration used.

This section details the electronic readout used for the TRITIUM detector when SiPM arrays are used (PETsys). This section also shows the electron systems used for the laboratory characterization tests and I&D, in which a single SiPMs and one or several PMTs was used.

It is important to note that the electronic systems used for laboratory testing will not be used to read the TRITIUM detector in the final location, Arrocampo dam. For this task, as there are two different porposals, two electronic systems are used; the PETsys system are used when the TRITIUM detector use SiPM arrays and an especific electronic system has been developed, designed and tested by Aveiro experimental group is used to read the TRITIUM detector when PMTs are employed. This electronic system is explained in Appendix D.

Electronics for PMTs

PMTs were used in TRITIUM experiment for two main objectives. On the one hand, to determine the amount of incident photons that reach the PMT photocathode, which is important to characterize fibers, and, on the other hand, to measure the energy of events, which allows us to discriminate events according to their origin, obtaining an energy spectrum of tritium events in water from laboratory prototypes.

To know the amount of photons that reach the photocathode, as explained above, the PMT should work without internal gain since it intro-

duces a large uncertainty in the measurement. For that end, the homemade electron multiplication stage of Figure 3.10 is employed.

As the electrons are not multiplied, the output pulse of the photosensor is very small (currents of the order of tens of nanoamperes) and a special readout system is needed. The chosen system is Keithley 6487 Picoammeter/Voltage Source [KEI], a commercial system from Keithley. This system has some useful options such as automatic baseline correction, the ability to read currents of the order of picoamperes and the possibility of carrying out mathematical operation on the signal, such as the average of N measurements with the associated statistical error, where N is programmable by the user ($N = 100$ in all our studies).

To determine the energy of the events, the gain of the PMT has to be restored by removing the short-circuit of the electron multiplication stage. The number of PMTs used simultaneously was one, two or four, depending on the setup. A simplified scheme of the electronic chain employed in each case is shown in Figures 3.15a, 3.15b and 3.15c, based on various NIM modules¹⁰.

The PMTs were biased in all the cases by TC 952 High Voltage Supply from Tennelec [Cam], which has four channels. If two or more configurations are needed, a second voltage supply HV Power Supply N 1130-4 from Wenzel Elektronik company [Ele] with 4 additional channels, was employed. As it can be seen in the figures, there are two different lines followed by the PMT output signals, the amplification line, used to create an energy spectrum, and the time coincidence line, used to make time coincidences. Therefore, an analogic FAN IN-OUT module was used to duplicate the input signal. The module employed was the Quad linear FAN IN-OUT MODEL 740 from Philips Scintific [Sci], which has four channels.

¹⁰The Nuclear Instrumentation Module (NIM) is a standard specification convention for electrical and mechanical parameters defined in electronic modules used in experimental nuclear and particle physics.



Figure 3.15 – Schemes of the different electronic for measuring with PMTs.
 a) Employed when only one PMT is used. b) Employed when two PMTs are used in time coincidence. c) Employed when four PMTs are used in time coincidence.

One output signal was used as the input for the amplification part and the second output was used as input for the time coincidence electronics.

1. The amplification line, which is the same for the three configurations, provides the energy information and is based on two steps;
 - (a) The output signal is integrated by a preamplifier, which gives an output signal with a height proportional to the charge of the input pulse. This signal has a long tail¹¹ produced by the preamplifier capacitance. The preamplifier used was "MODEL 9326 FAST PREAMP" from ORTEC [ORTd].
 - (b) The output signal from the preamplifier is lead to the amplifier which gives a gaussian shaped output signal. The amplifier modules were 575A and 671 from ORTEC [ORTb, ORTc]. An example of the output signal for 575A module is shown in Figure 3.17, green color.
2. The time coincidence line contains the time information and gives the gate that triggers coincident signals of both PMTs. This line consists of the following branches,
 - (a) The output signal of the FAN IN-OUT module of each PMT is introduced into a discriminator module that gives a logic signal of -1.2 V height and of 240 ns width when a given threshold is exceeded. The discriminators employed are Octuple Constant-Fraction Discriminator CF8000 module from ORTEC [ORTe] and 4 channels discriminator model 84 from CAEN [CAEa].
 - (b) Time coincidences are required to ensure that detected events come from the scintillating fibers and to remove external light and dark current. The two logic signals given by the discriminator from the two PMTs that read a detector are introduced in a

¹¹The length of the tail is, $\tau = RC$, where R is the input resistance and C is the capacitance used. It is the typical output signal in RC circuits.

coincidence module which generates an output signal of -1.4 V height and of 20 ns width, when both inputs are in time coincidence. The modules used were Coincidence Unit Model 465 from LeCroy [LeC] and Coincidence Type N6234 from CERN-NP [CERb].

- (c) Time coincidence of two different detectors (4 PMTs, configuration 3.15c) was also studied, which is useful to remove background due to hard cosmic radiation. To do so, a coincidence step similar to the previous one must be applied. The two single detector coincidence signal are checked for coincidence.

Some examples are shown in Figure 3.16 for time coincidences of two detectors (4 PMTs). There, four logical signals are shown, two of them (channel one and two, yellow and green respectively) come from two PMTs reading the first detector and the other two signals (channels three and four, color orange and violet respectively) come from PMTs reading the second detector.

- i. In Figure 3.16a only one PMT (channel two) detected an event. It means that the event is likely not produced in the scintillator. In this case, no output signal is generated.
 - ii. In Figures 3.16b and 3.16c two PMT signals of one of the detectors are generated but the other detector gives no signal. This event is discarded.
 - iii. In Figure 3.16d the four signals are generated and, consequently, the output signal is generated and the event is recorded.
- (d) The logical output signal, is introduced in the Gate and Delay Generator, model 416A of the company ORTEC [ORTa], which gives a positive logical signal, called time windows, shown in Figure 3.17, orange color, with a height of 8 V and width of $2 \mu\text{s}$. This module is used to delay the time windows until it overlaps with the energy signal as it is shown in Figure 3.17, orange signal.

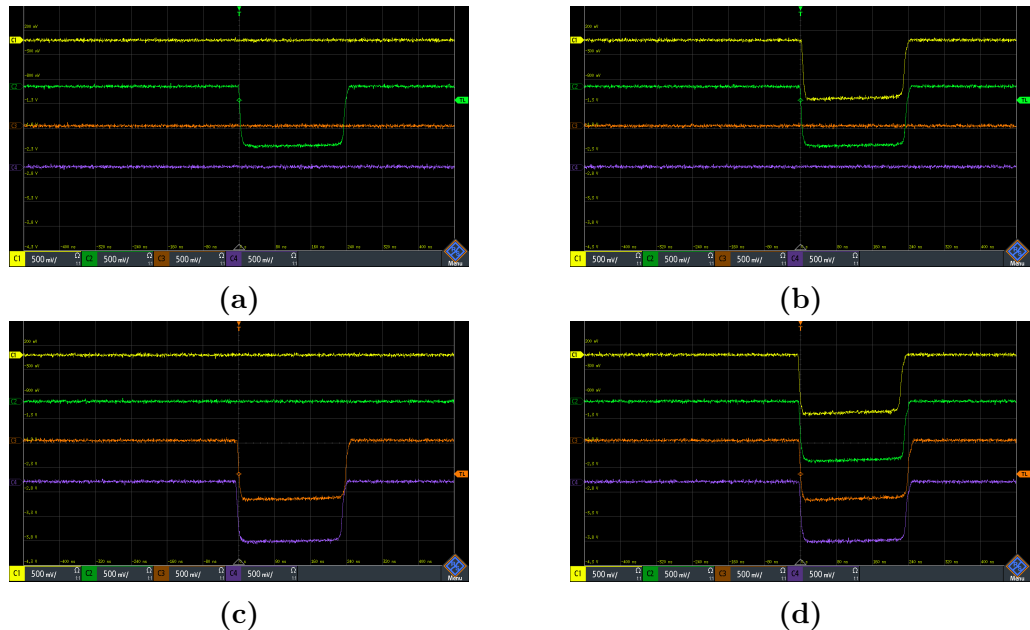


Figure 3.16 – Different possibilities when time coincidences with PMTs are done. a) Event detected in only one PMT, one detector. b) Event detected in two PMTs, one detector. c) Event detected in two PMTs, other detector. d) Event detected in all PMTs, both detector.

As a final output of the electronics, a logical and analogical signals are obtained, shown in Figure 3.17, which are recorded by the MCA 8000D, Pocket MCA from AMPTEK [Amp]. The analogical signal has information about the energy of the event and this is the signal which information is saved for later analysis. The logic signal (output from the Gate and Delay Generator module) indicates when the amplified signal must be saved.



Figure 3.17 – Signal amplified and logical gate (input signals of MCA).

Electronical system for SiPMs

The SiPMs in the TRITIUM experiment are arranged in matrices of 4×4 . The electronic system chosen to process and analyze the output signals of the SiPM arrays is PETsys [PET], displayed in Figure 3.18, which is a commercial system prepared to work with SiPM matrices from Hamamatsu. PETsys provides time and energy digitalization, including the charge in-

tegrations QDCs¹² and TDCs¹³, resulting in a complete acquisition and digitization system capable of working with up to 1024 SiPM. This system consists of a basic board to which 16 different SiPM matrices can be connected with up to 64 SiPM per matrix. This number of channels is needed in the TRITIUM project because, as shown in section 5.4, the TRITIUM monitor consists of a large number of SiPM matrices with 16 channels per matrix.



Figure 3.18 – Different parts of PETsys system [PET].

Although the capacity provided by PETsys should be enough for the requirements of the TRITIUM project, TRITIUM is a modular detector with scalable sensitivity. This means that, if an improvement of TRITIUM limits is needed to improve its sensitivity or to further reduce the background, more photosensors would be needed. Therefore, the electronics should be able to increase its capacity in a scalable way. This requirement

¹²charge-to-digital converter

¹³time-to-digital converter

is fulfilled by PETsys since it has an additional module, called Clock and Trigger, to which up to sixteen different PETsys basic boards can be connected. These sixteen PETsys basic boards are read in parallel, giving a total system capacity of reading 256 SiPM matrices (16384 SiPMs¹⁴).

PETsys software is based on C++ and Python scripts to drive the main tasks required, such as time coincidence options between SiPM (or even SiPM matrices) or energy discrimination. This software is open source, giving the possibility to modify the current scripts or to develop others with additional functions. PETsys has a time resolution better than 30 ps which is one of the best time resolutions of commercial systems available and its price is around 10€/ channel, which is cheaper than similar electronic systems.

As reported in section 4.2, the SiPM matrix temperature is an important parameter. The PETsys system has the ability to monitor the temperature of the SiPM matrices and ASICS employed to control them. Temperature monitoring is important to ensure the correct functioning of both, photosensors and system. PETsys has the possibility of developing new scripts to implement the stabilization method of the SiPM gain reported in section 4.2.

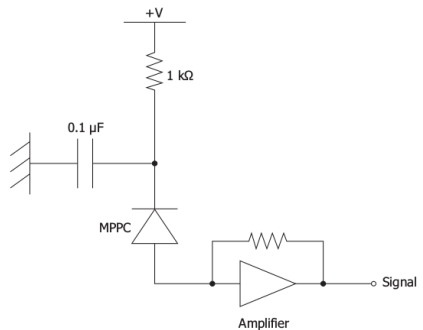
Some characterization measurements were carried out using the PETsys system to ensure that the system works properly but the SiPM characterization was carried out at the level of a single channel (individual SiPM). The reason is that the output information of PETsys is already integrated and digitized, so it does not allow the SiPM to be calibrated. Therefore, to characterize a SiPM, a different electronic system was used to read up to eight different SiPMs. This system consists of a PCB¹⁵ that provides the SiPM bias voltage and reads the SiPM output signal. An example of the electronic scheme (provided by Hamamatsu) in which this

¹⁴ $1024 \cdot 16 = 16384$

¹⁵PCB, Printed Circuit Board



(a)



(b)

Figure 3.19 – a) Electronic board used to provide the SiPM bias voltage and to read the SiPM output signal. b) Electronical scheme in which this PCB is based.

PCB is based is shown in Figure 3.19.

The PCB was feed at ± 6 V using the voltage source ISOTECH, model IPS-4303 [IT] and the SiPM was feed using the electrometer KETHELEY, model 6517B [Keh], that achieves a resolution of 1 mV, low enough to ensure that this voltage variations does not affect the SiPM gain. The output signal of this PCB is connected to an oscilloscope, model WwaveRunner 625Zi from TELEDYNE LECROY [LEC17] that records the data which were subsequently analized by ROOT¹⁶ scripts.

¹⁶ROOT is a framework for data processing, based on C ++ and object-oriented technology, developed at CERN and widely used in nuclear and particle physics.

3.3 Water Purification System

3.3.1 Objectives

The water samples, which will be introduced into the TRITIUM detector to be measured, are taken directly from the Tajus river, 4 km downstream from the place where the Almaraz Nuclear Power Plant releases the cooling water. This sample, as it was verified by a detailed analysis shown in section 4.3, contains many dissolved elements such as minerals, organic deposits, and living matter dissolved in the water. You need to delete these dissolved items for several reasons:

1. The mean free path of tritium electrons in water is around $5 \mu\text{m}$ and even less in solid materials like organic material. Tritium decay electrons have to reach the fiber to be detected and, consequently, the detector must be kept very clean. If the analyzed water sample contains particles that may be deposited on the fibers, a layer of matter could be formed, preventing tritium decay electrons from reaching the fibers and reducing drastically the tritium detection efficiency.
2. The tritium monitor does not have any spectrometric capabilities that could be used to distinguish tritium from other radioactive elements from minerals dissolved in the water.

The water purification system was designed to remove organic matter and mineral particles with a size of up to $1 \mu\text{m}$. Hence, this filtering should keep unchanged the tritium level in the water.

3.3.2 Design of the Water Purification System

The requirements of the water purification system are:

1. A high degree of purification of the water sample extracted from the dam, reducing its conductivity by approximately two orders of magnitude (from $1000 \mu\text{S}/\text{cm}$ to $10 \mu\text{S}/\text{cm}$).
2. Low maintenance cost and manpower.
3. Software-based management of the system.

The LARUEX laboratory in Extremadura, one of the six members of the TRITIUM collaboration, has designed, developed and built the water purification system, the scheme of which is shown in Figure 3.20.

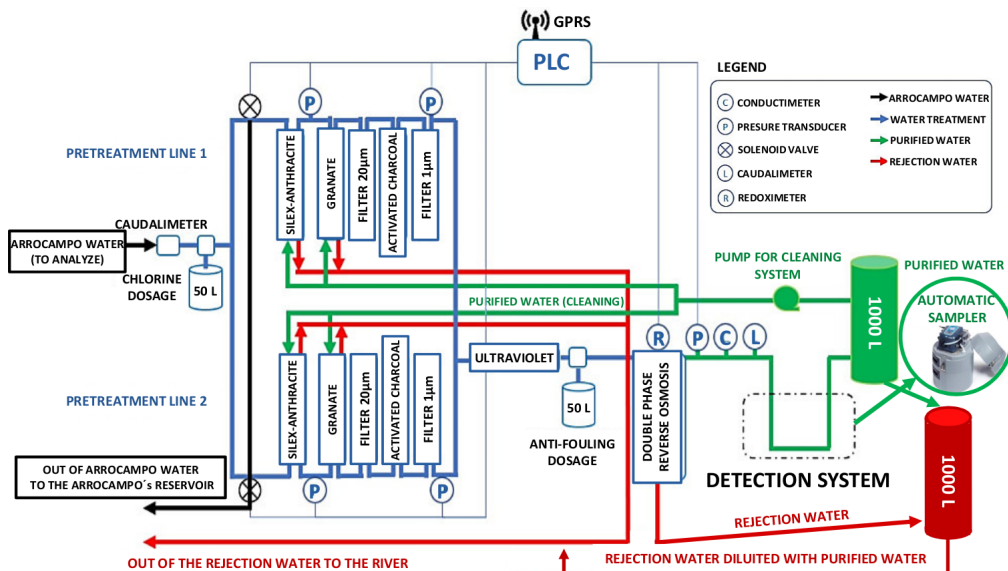


Figure 3.20 – Scheme of water purification system of TRITIUM.

This system is installed in the Arrocampo dam and consists of four different stages:

1. The raw water from the Tagus river passes through two different filters, the first made of silex-anthractite and the second of garnet, with which

a rough filtering is made (the largest particles are eliminated). This system has two identical parallel lines and implements a self-cleaning functions which consist of injecting purified water in the opposite direction.

2. The outlet water sample of the first stage, called fine filtration stage, passes through a $20\ \mu\text{m}$ filter (formed by a synthetic mesh) and activated charcoal filters (one per line) that removes chlorine and iron particles present in the water sample.
3. The outlet water of the second stage passes through a super-fine filtering consisting of a $1\ \mu\text{m}$ filter, formed of a dense polypropylene mesh and UV lamps. The filter removes all the particles up to diameters of $1\ \mu\text{m}$ and UV lamps sterilize water, eliminating bacteria and microscopic life.
4. Finally, the water is introduced in the last stage, double-phase reverse osmosis, that reduces the conductivity of the water to about $10\ \mu\text{S}/\text{cm}$ with only one module of reverse osmosis, enough for the needed conditions.

As a result of the purification process, besides the pure water that is introduced into the TRITIUM detector, a rejection water is produced, which contains the particles extracted from the pure water that results in conductivities greater than the original water.

The water purification system is able to process up to $0.850\ \text{m}^3/\text{h}$ with a single line operating or $1.480\ \text{m}^3/\text{h}$ with both, greatly outperforming the requirements of the tritium detector.

The software used for remote controlling the water purification system is Siemens PLC, that gives information such as the state of the valves, the reading of pressure probes and the amount of water production in real time.

The appendix B contains several pictures of different parts of this system, installed in Arrocampo dam.

3.4 Background Rejection System

The aim of the background rejection system is to reduce the radioactive and cosmic background that affects to the TRITIUM monitor. The TRITIUM project follows the ALARA principle for the tritium activity measurement, that is, to measure tritium activity "as low as reasonably achievable". The detection limit of tritium activity is set by the uncertainty in the activity of the radioactive background measured by the TRITIUM detector, since tritium activities below this uncertainty cannot be distinguished from the background. Therefore, the background uncertainty must be reduced as much as possible. The total uncertainty is the quadratic sum of all the different uncertainties related to the measurement, i.e., the statistical uncertainty¹⁷, σ_{st} , the systematic uncertainty¹⁸, σ_{si} , etc. Because of the Poissonian nature of the process, the statistical uncertainty is given by the square root of the measured activity, A_m , which can be reduced by minimizing detected background events.

$$\sigma_T^2 = \sigma_{st}^2 + \sigma_{si}^2; \quad \sigma_{st;bak} = \sqrt{A_{m;bak}} \quad (3.14)$$

The background rejection system of the TRITIUM monitor reduces the background activity measured by the TRITIUM detector, minimizing the statistical component of the background uncertainty.

The background of TRITIUM has two different sources. On the one hand, radioactive elements that are present in the crust of the Earth,

¹⁷Uncertainty due to the statistical nature of the radioactivity process

¹⁸uncertainty due to the manufacturing process of the detectors

mainly ^{40}K and elements from the four different natural radioactive series, shown in Table 3.4. On the other hand, the cosmic ray radiation. The primary cosmic radiation, of extra-terrestrial origin, is composed of high-energy particles, mainly protons and α particles, which interact with the Earth's atmosphere and generate a shower mainly composed by muons, electrons, photons and neutrons.

Mass Num.	Series	Primary	Half life (y)	Final
4n	Thorium	^{232}Th	$1.41 \cdot 10^{10}$	^{208}Pb
4n+1	Neptunium	^{237}Np	$2.14 \cdot 10^6$	^{209}Pb
4n+2	Uranium-Radium	^{238}U	$4.51 \cdot 10^9$	^{206}Pb
4n+3	Uranium-Actinium	^{235}U	$7.18 \cdot 10^8$	^{204}Pb

Table 3.4: Classification of natural radioactive series [The96, Eva96]. The information displayed for each radioactive series is the multiplicity of the mass number, the name of the series, the primary and final element, and the half-life of the primary element.

Cosmic radiation depends on several parameters like the longitude, latitude, and the solar activity cycle. The spatial distribution of cosmic rays, mainly muons, follows a $\cos^2(\theta)$ distribution with the zenith angle.

Two different techniques are employed for background suppression:

1. The soft background component, with energy below 200 MeV/nucleon, is stopped by a lead castle, described in section 3.4.1,
2. The hard background component, with energy greater than 200 MeV/nucleon, is much more difficult to stop and the technique employed is the use of a cosmic veto in anti-coincidence with the TRITIUM detector, reported in section 3.4.2.

3.4.1 Passive Shield (Lead)

The soft background component is suppressed by a lead shield inside which the TRITIUM detector is placed. This lead shield is efficient for suppression of particles with energies below 200 MeV/nucleon, that originates from the Earth's natural radioactivity and the soft component of cosmic radiation. This lead shield consists of 158 lead bricks of 25 mm thickness and low intrinsic radioactivity. The bricks are chevron shaped, as shown in Figure 3.21a, specially designed for a perfect fit and easy assembly. As can be seen in Figures 3.21b and 3.21c, these lead bricks are arranged in two layers with a total thickness of 50 mm. The junction of the inner layer lead bricks is shielded by a lead brick of the outer layer to avoid any leak of radiation.

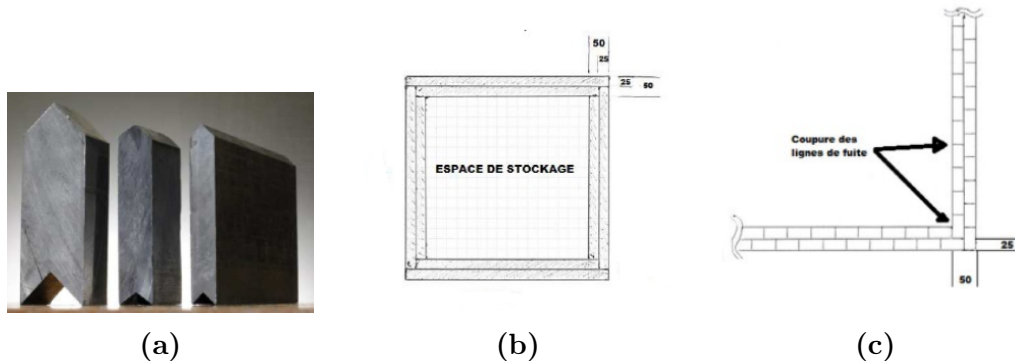


Figure 3.21 – a) Lead Bricks b) and c) Two layers for the lead bricks of the shield.

A special aluminum structure, shown in Figure 3.22, was designed by mechanical engineering department of CENBG to support the total weight of 2.4 tons of the lead bricks.

The internal room of the lead shield is divided in two parts, as exhibited in Figure 3.22. The larger one has internal dimensions of $90.5 \times 41 \times 51$ cm³ and is used to place the TRITIUM detector. The smaller one, of dimensions of $33 \times 41 \times 51$ cm³, contains the Data Acquisition (DAQ)

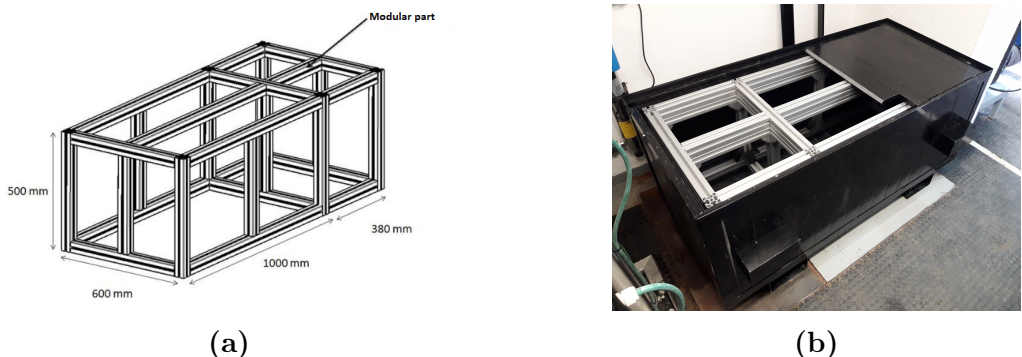


Figure 3.22 – a) Scheme of the aluminium structure of the shield; b) The lead shield partially mounted.

system of the detector. The external dimensions of the lead shield are $148 \times 60 \times 70 \text{ cm}^3$; its total weight is 2.5 tons.

3.4.2 Active Shield (Cosmic Veto)

As hard radiation cannot be stopped by a moderate lead thickness, cosmic vetos are employed, which consist of at least two complementary detectors in coincidence that reject events simultaneously detected in both of them. As shown in Figure 3.23, the two complementary detectors are placed one above and the other below the TRITIUM detector. The distance between both detectors, 34.2 cm for the latest prototype developed at IFIC, is set by the dimension of the detector to be placed inside.

A hard cosmic event crossing simultaneously both cosmic detectors is schematically sketched in figure 3.24a. Each cosmic detector has two photosensors, so the electronic configuration given in Figure 3.15c is used to make time coincidences. The TRITIUM detector is read out in anti-coincidence with the cosmic veto to reject the hard cosmic events from the tritium measurement. The expected hard cosmic rate at sea level for muons is $7 \times 10^{-3} \text{ cm}^{-2}\text{s}^{-1}\text{sr}^{-1}$ [ea20, SAG01], as shown in the plot of Figure



Figure 3.23 – Cosmic veto and Tritium-IFIC-2 prototype in an aluminum mechanical structure developed at IFIC.

3.25. As time coincidences are triggered by logical gates of about 10 ns, the probability of recording two different hard cosmic events in temporal coincidence, one in each detector, as drawn in Figure 3.24b, are negligible.

The vetos are made of a plastic scintillator block from Epic-Crystal [Cry20]. Its properties are given in Table 3.5 and its energy emission spectrum is displayed in Figure 3.26.

The energy spectrum has a peak very close to that of the scintillating fibers used, so the same photosensors are used to read them out. The dimensions of the scintillator blocks are $45 \times 171 \text{ cm}^2$ with a thickness of 1 cm. They are wrapped by three different layers, PTFE sheets, aluminum and black tape, as shown in Figure 3.27. These layers prevent external photons from reaching the plastic scintillator and prevent photons generated by the scintillator from escaping before reaching the photosensor. Two $2.5 \times 2.5 \text{ cm}^2$ windows are made on the wrapping to allow coupling of the photosensors.

Considering the expected hard cosmic rate of $7 \times 10^{-3} \text{ cm}^{-2}\text{s}^{-1}\text{sr}^{-1}$

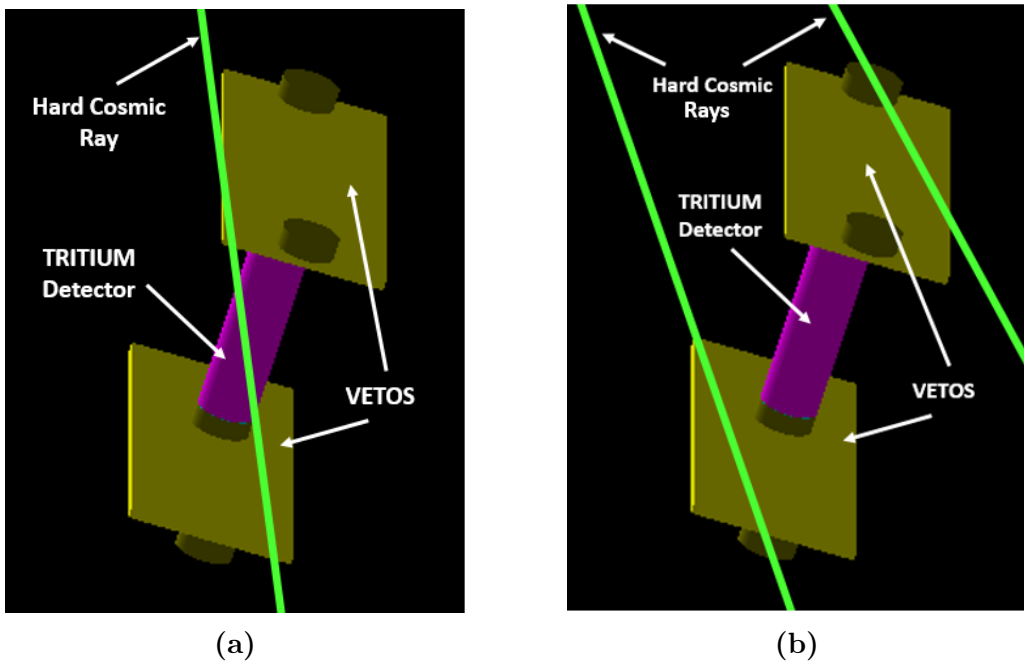


Figure 3.24 – Hard cosmic events detected with the cosmic veto of TRIITIUM: a) Real coincidence event, b) randomly coincident event that may mimic a hard cosmic event.

at sea level, and taking into account that the solid angle of the veto detectors is $\omega = 0.5434$, calculated by integrating the solid angle of one scintillator on the other, and that the area of the veto is 765 cm^2 , the expected hard cosmic rate on the TRITIUM cosmic vetos is 2.909 event/s. This estimation is used in section 4.4 to determine the detection efficiency of the cosmic veto.

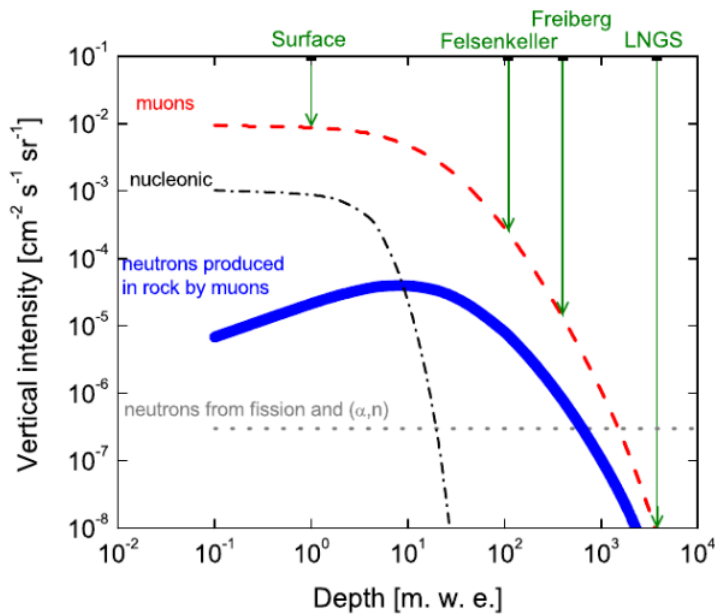


Figure 3.25 – Hard cosmic muon rate at different depths with respect to the sea level (10^0) [Szu15].

Property	Value
Base material	Polystyrene
Growth method	Polymeric
Density (g/cm ³)	1.05
Refractive index	1.58
Soften temperature (°)	75-80
Light output (Anthracene)	50-60%
H/C ratio	1.1
Emission peak (nm)	415 (Blue)
Decay Time, (ns)	2.4
Hygroscopic	No

Table 3.5: Properties of plastic scintillators from Epic-Crystals used for the cosmic vetos [Cry20].

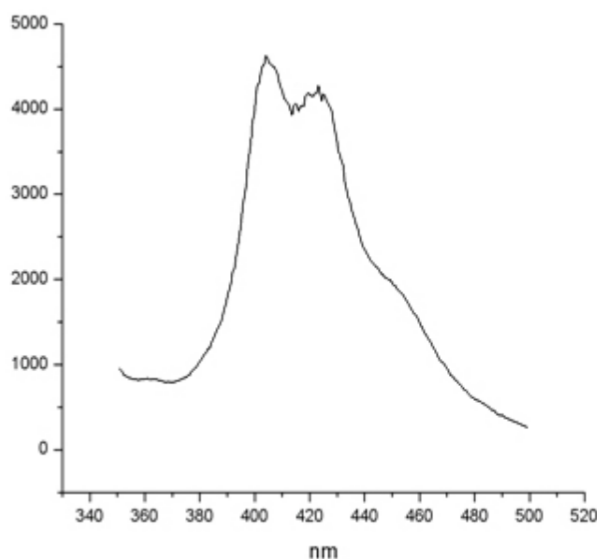


Figure 3.26 – Emission energy spectrum of the plastic scintillator from Epic-Crystals used for the cosmic vetos [Cry20].



Figure 3.27 – Different layers used to wrap the cosmic veto detectors. a) Scintillator without coating. b) PTFE coating. c) Aluminium coating. d) Black tape coating.

Chapter 4

TRITIUM Monitor R&D

This chapter describes the characterization of the different parts of the TRITIUM monitor, including scintillating fibers, SiPMs, the water purification system and the background rejection system. This characterization is crucial to understand the behaviour of the different parts and the measurements results of the monitor. Furthermore, several developments were made to improve fundamental parameters of the TRITIUM monitor components to enhance its sensitivity to low levels of tritium in water.

4.1 R&D for the Scintillating Fibers

This section reports experimental measurements of the plastic scintillating fiber parameters relevant for tritium detection, such as collection efficiency and the systematic uncertainty, which is involved in the measured tritium activity. Thousands of scintillating fibers are used in the TRITIUM detector which were prepared and conditioned prior to characterization studies or tritium detection. Various mechanical and electronic devices were developed to automatically prepare large number of fibers simultaneously.

4.1.1 Surface-Conditioning Method of Scintillating Fiber.

Different methods of surface-conditioning of scintillating fibers were used for the TRITIUM detector. These are methods of cleaving, polishing and cleaning the scintillting fibers.

Cleaving Method of Scintillating Fibers.

The first step in TRITIUM design was to choose the fiber length for a given fiber diameter (1 or 2 mm) at which the signal of tritium events is optimized. On the one hand, long fibers are suitable because fewer fibers are needed to achieve the same TRITIUM detector efficiency as short fibers, reducing the price of the TRITIUM detector since fewer electronic channels are needed. On the other hand, in long fibers, scintillating photons are reflected on the fiber boundaries many times before reaching the photosensors, which may produce a deterioration in the tritium signal. To determine the optimal fiber length, several simulations, described in section 6.2.3, were carried out using Geant4 [Col21a], a particle and nuclear physics simulation package based on C++. It was concluded that the optimal fiber length for mesuring tritium in water is around 20 cm, which is the fiber length used in TRITIUM prototypes developed at IFIC and it is also the length used for most of the characterization studies carried out in TRITIUM. As our Saint-Gobain fibers are longer than 20 cm, an effective cleaving technique had to be developed with strict requirements on the cleaving quality of the fiber ends since this greatly affects the transmission of photons and, consequently, the detection efficiency of the TRITIUM detector. The cleave must be done perpendicular to the fiber axis and with small uncertainty in the cleaving position, in order to achieve a good end-surface quality that enables optimal coupling to the photosensor. It is also important that the fiber integrity be preserved, without cracks or deformations that contribute to the loss of photons.



Figure 4.1 – Unsuccessful results of using commercial techniques for cleaving the scintillating fibers a) Fiber end deformation b) Fiber end cracks. Pictures taken with the microscope PB 4161 from EUROMEX.

Cleaving the plastic fibers is a current challenge. There are many different techniques such as milling, laser cleaving, focused-ion-beam, blade cleaving, etc. The blade cleaving technique was chosen for TRITIUM because of its mechanical simplicity and because it preserves the integrity of plastic fibers. Many commercial devices based on blade cleaving, such as the one provided by Thorlabs with a diamond tipped blade [Inc06], or others similar to guillotine designed for industrial fiber optics [fo], were tested in an extensive study with unsuccessful results [Cam17]. As it can be seen in Figures 4.1, commercial techniques produce deformations, cracks and imperfections so they do not fulfill the quality standard required for the detector.

Because commercial devices are not suitable for polymer fibers, a cleaving device, shown in Figure 4.2, was designed, built and tested at IFIC laboratory.

This device consists of an aluminium plate with fourteen grooves used for lodging the fibers and a thin razor blade, attached to a mobile

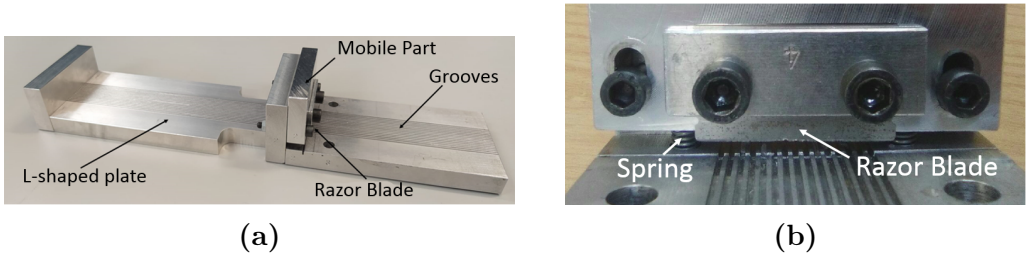


Figure 4.2 – Plastic fiber cleaver developed in TRITIUM experiment.

piece, which is used to cleave them. The perpendicular cleave, which is one of the requirements, can be ensured since the moving piece, to which the blade is attached, is set perpendicular to the fiber axis. The blade used is a typical commercial razor blade, of 0.1 mm thickness, which is the thickness that gave the best results. The blade was positioned with a 5° inclination with respect to the horizontal axis since it was found in several studies that this helps to obtain a less aggressive and cleaner cleave [SR15, Law06]. As it can be seen in Figure 4.3, the integrity of the fiber is preserved since this is not deformed and a perpendicular cut is achieved when the plastic fiber cleaver is used. It can be noticed some tears in the clad. Although it does not affect the tritium project since unclad fibers are used, it was verified under the microscope that it only occurs at the end of the fiber. It is verified in section 4.1.2 that these tears in the fiber cladding practically do not affect the photon collection of the fiber.

An additional parameter that could affect the cleaving quality of the fiber ends is the temperature of both fiber and blade. A study was carried out in which both were subject to different temperatures from room temperature to 110 degrees. No significant conclusions were obtained [Cam17]. Thus, the cleaving process was carried out at room temperature to make the cleaving process easier.

A second L-shaped aluminium plate with grooves was attached to the first one (see Figure 4.2) to set precisely the length of the fibers to

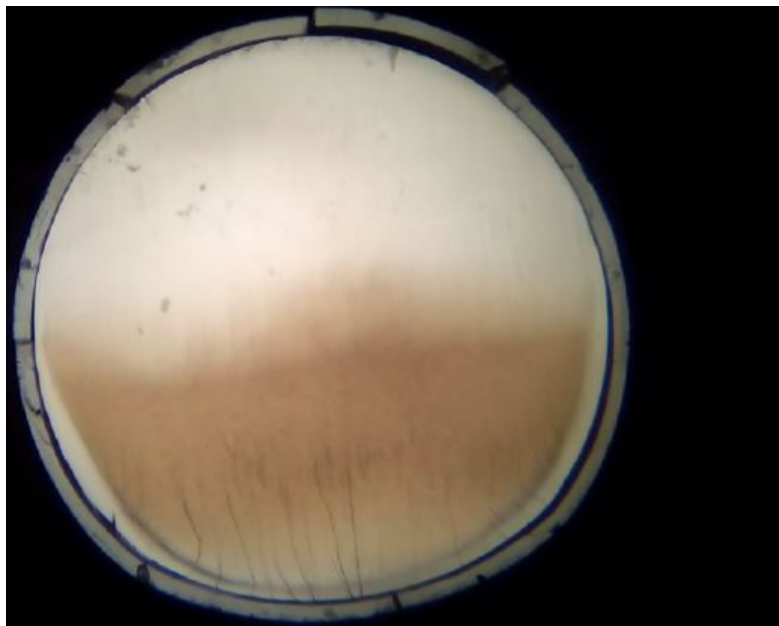


Figure 4.3 – Fiber end after cleaving process using the home-made cleaver. Pictures taken with the microscope PB 4161 from EUROMEX.

200 mm, with an uncertainty of ± 1 mm.

Polishing Method of Scintillating Fibers.

As can be seen in Figure 4.3, a slightly darkened zone at the bottom of the fiber is observed in most of the cases. This is an unavoidable effect of the cleaving process on plastic fibers, which generates non polished end-surfaces. To remove that, a polishing process implemented by Thorlabs was applied [Inc06].

Manual Polishing Method.

The Thorlabs polishing method, shown in Figure 4.4, consists on a kit based on a special fiber connector from Thorlabs which is used for rub-

bing the fibers with five different polishing papers made out of aluminum oxyde grains, with a decreasing grain size, $30\ \mu\text{m}$, $20\ \mu\text{m}$, $12\ \mu\text{m}$, $5\ \mu\text{m}$ and $0.3\ \mu\text{m}$, describing on the paper a shape of an 8 during 2 minutes (approximately 120 movements).

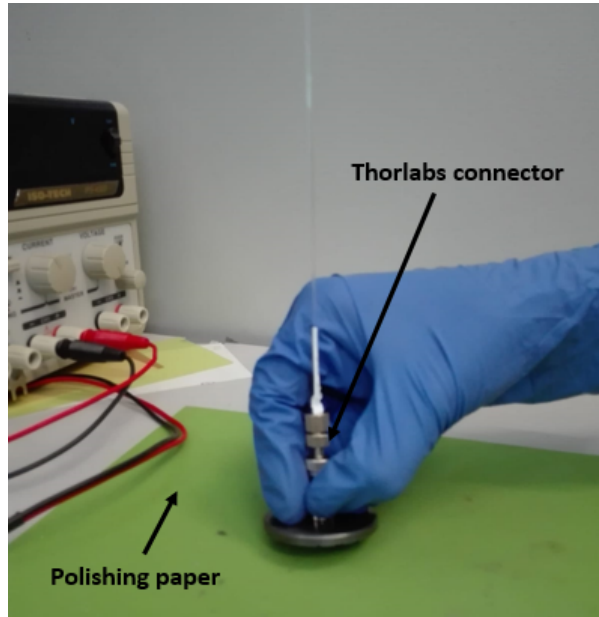


Figure 4.4 – Manual polishing method implemented by Thorlabs.

The result obtained after polishing is shown in Figure 4.5b, where it can be noted that the darkened zone has completely disappeared and the fiber end is uniformly transmitting light, which favors optimal coupling of the scintillating fibers to the photodetectors and transmission of scintilating photons.

Automatic Polishing Machine.

The main drawback of the manual polishing method is that it takes more than 10 minutes to polish each fiber, an unaffordable time to polish thousands of fibers needed for the TRITIUM detector (see section 5.4). This is why an automated polishing process has been developed within this

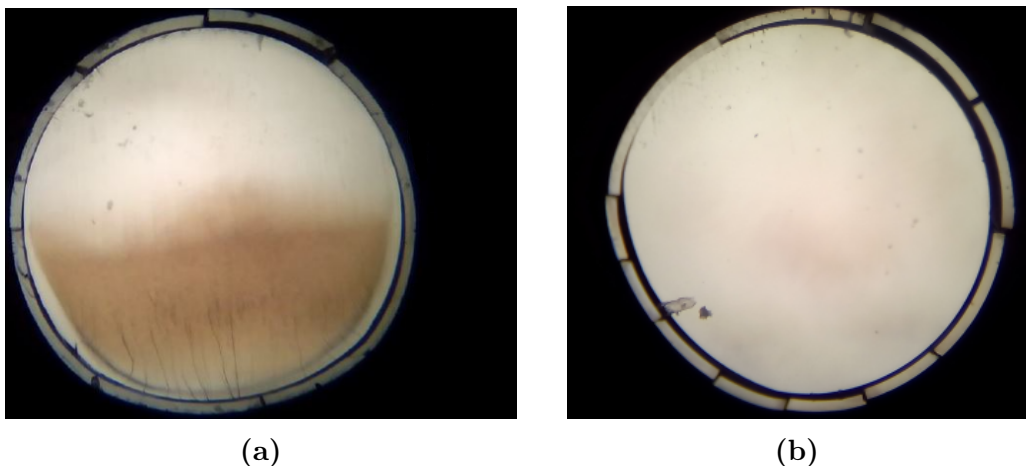


Figure 4.5 – Result of the polishing process. a) Fiber end after cleaving b) Fiber end after cleaving and manual polishing with Thorlabs technique. Pictures taken with the microscope PB 4161 from EUROMEX.

thesis work. The goal of this effort was to ensure a better light coupling and transmission of light of the scintillating fibers to the photosensors.

A machine was designed, built and tested in the laboratory for automatically polishing of up to one hundred plastic scintillating fibers at the same time and it is easily scalable to larger number of fibers.

This automatic polishing machine, displayed in Figure 4.6, consists of two main parts: 1) A polishing table, where the fibers are polished 2) The electronics, based on Arduino technology, that operates the movement of the polishing paper:

1. The polishing table, shown in Figure 4.7a, is composed of two parts, a static part, where the fibers are fixed, and a movable part on bottom of the previous one, where the polishing papers are fixed. It was decided to establish the polishing movement on the plate with the polishing sheets, because of its lighter weight and in order to avoid possible damaging movements to the fibers.

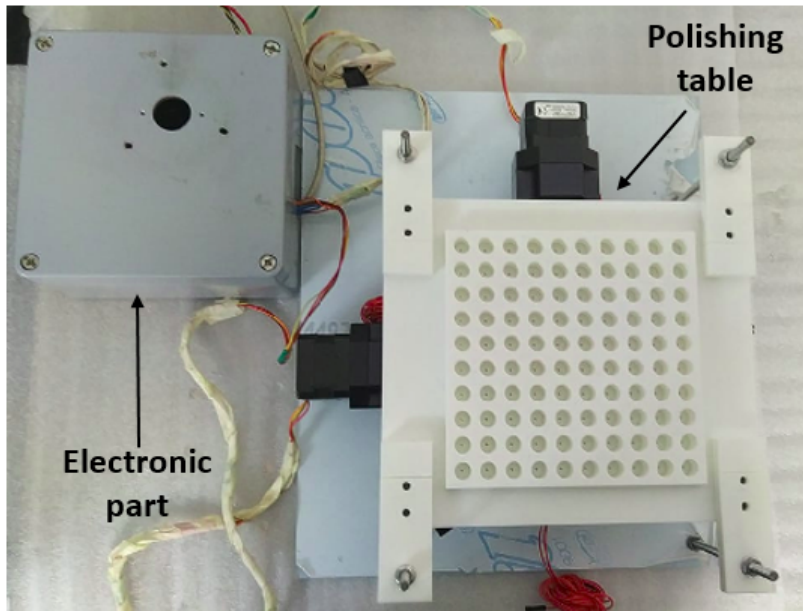


Figure 4.6 – Polishing machine developed for TRITIUM.

The static part (the fiber holder plate), shown in Figure 4.7a, consists of a plastic piece built with a 3D printer and locked to the system by four vertical screws. There are two nuts on each screw used to set the relative height and the inclination of fibers relative to the polishing papers. This piece contains one hundred holes in which a hundred fibers are lodged.

As the fibers are too light (0.16 g) to make by gravity the necessary pressure on the polishing paper, a plastic belt and a piece of metal with a weight of about 1.5 g were attached to the individual fibers, as shown in Figure 4.7b, to increase their contact pressure, in a similar way as with the manual polishing connectors.

The movable part of the polishing table consists of a flat PMMA plate of $18 \times 18 \text{ cm}^2$ to which the polishing paper is attached. This part is locked to structure [IGU] that contains two horizontal screws, perpendicular to each other, which allow its movement in the XY

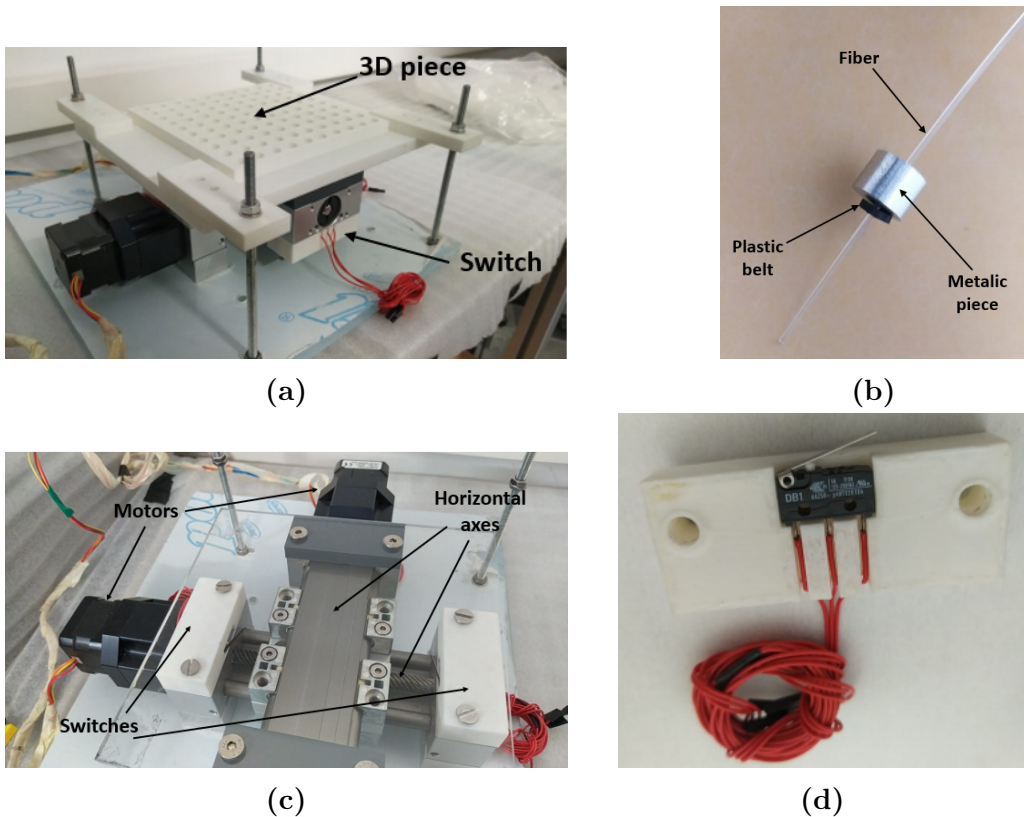


Figure 4.7 – Components of the fiber polishing machine. a) Polishing table. b) Fiber with ballast metal piece. c) Horizontal screws and PMMA plate. d) A movement switch with its cables inserted inside its holding piece.

plane (horizontal plane), as shown in Figure 4.7c.

The polishing system contains several subminiature switches with high repeat accuracy, model DB1 6A250, mounted on a piece made with a 3D printer, shown in Figures 4.7a, 4.7c and 4.7d, which are used to find the origin of coordinates when the system is reinitiated and to stop the movable part when the end of the path is reached.

2. The electronics, shown in Figure 4.8, which controls the automatic movement of the polishing paper, is based on Arduino technology. It consists of two stepper motors controlled by an Arduino UNO [ARD]

that uses a CNC shield [OSO17] in which two different drivers are connected to control each of this stepper motors.

The stepper motor is a type of DC motor in which a full rotation is divided into a number of equal steps. This, it is manufactured with a number of steps per revolution, corresponding to a given stepping angle. The stepper motor used for the polishing machine are model NEMA ST4209S1404-A [Nan], with bipolar voltage of 2.77 V_{DC} , 1.33 A maximum current and a stepping angle of 0.9° (400 steps/rev). They can be operated with or without a position sensor for feedback control. These stepper motors are used to move the horizontal screws on which the PMMA plate that hold the polishing paper is attached.

Drivers are controllers that allow to manage stepper motors in a simple and safe way as they are used to limit the current supplied to the motors. Choosing the right controllers, with the power and the stepping mode required for the chosen stepper motors, is crucial. This is because overpowering them could rapidly be damaging, while an inadequate stepping would result in inaccurate movements of the mobile part of the polishing paper.

Several drivers were successively considered and tested: the most widely used driver Pololu A4988 [All12] (35 V, 2 A and 16 steps), the driver DRV8825 (45 V, 2.5 A and 32 steps) and the TMC2208 [Cir19] (35 V, 2.5 A and 256 steps) with more microstepping modes, which results in more accurate and smooth movements. This later includes a Stealth-Chop function with which the driver operates in silence mode for low motor velocities. It is seen that the power provided by each stepper is enough to correctly move the stepper motors. Therefore, owing to these features, the TMC2208 driver is the one used for the control of the stepper motors since it produce the most accurate and smooth movement. The provided current to the motors is limited by the driver and the excess will be transformed into heat that has to be dissipated for the correct functioning of the drivers.

Indeed, overheating of the drivers may cause loss of steps, producing wrong movements or even destroying the driver. Therefore, a cooling system is needed to ensure the correct operation of the polishing system. The cooling system, shown in Figure 4.8, consists of a copper heat sink¹ in contact with both controllers and a fan, used to prevent heat accumulation inside the electronics box. The cooling power can be improved by using a PELTIER cell.

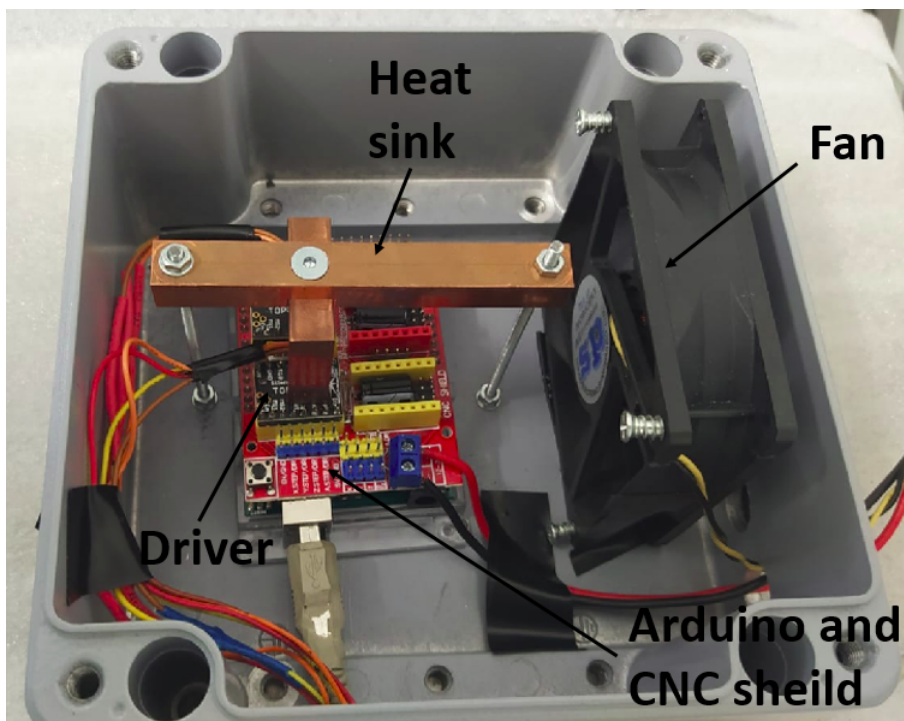


Figure 4.8 – Electronic system of Polishing machine.

Finally, this polishing machine is controlled by a Raspberry Pi computer board [Ras] using the Universal G-code Sender software, a graphical interface based on the GRBL package [GRB]. There are several useful functions loaded in this way. I pre-programmed functions such as "HOME" with which

¹The copper is one of the best thermal conductor at STP

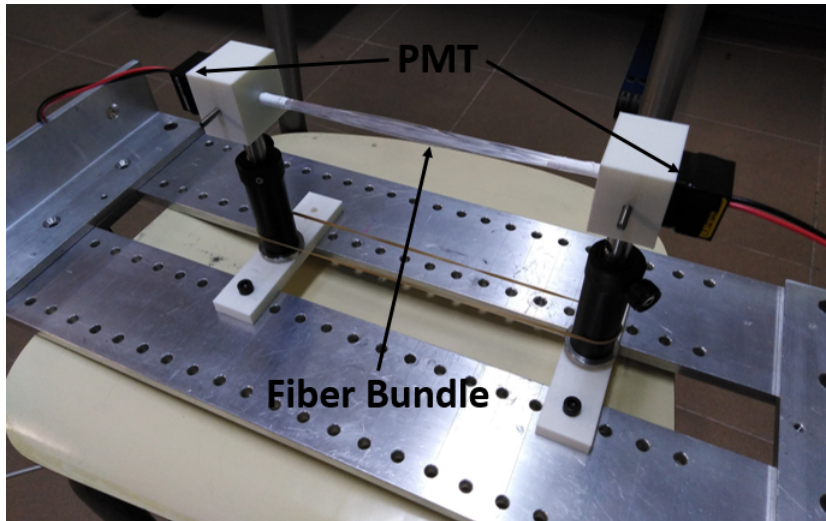


Figure 4.9 – Setup used to test the effect of the fiber polishing on light transmission to the PMTs. This setup is placed in a dark test box for the measurements.

the system, using the switches, finds its origin of coordinate every time the system is turned on. The software also has the possibility of loading a file containing the G-code to be executed. In the fiber polishing machine, the 120 movements required for each polishing paper.

Experimental Test.

Finally, this machine was tested with twenty unclad scintillating fibers of 15 cm length. These fibers were arranged in a bunch and were coupled at each end to two PMTs, as shown in Figure 4.9, which were read out in coincidence. The electronic scheme shown in Figure 3.15b was used to process and analyze these signals and an energy spectrum was obtained. The goal of the test was to quantify the improvement in the relative light transmission of the scintillating fibers due to the polishing process.

This experiment was carried out inside a special light-tight box, called black box, to ensure that the detected photons are generated by the

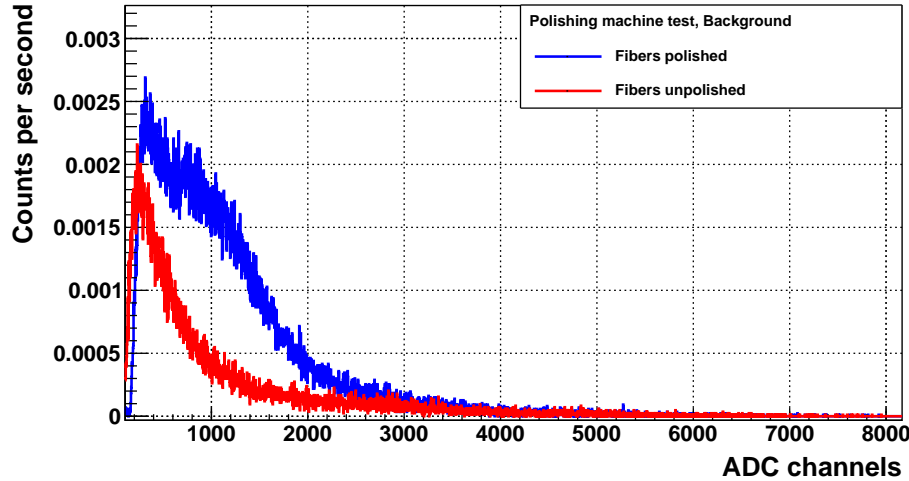


Figure 4.10 – Energy spectra recorded with polished and unpolished fibers for the radioactive background.

scintillating fibers. The radioactive background was measured before and after applying the polishing process, shown in Figure 4.10.

As it can be seen in this figure, the energy spectrum after applying the polishing process is shifted to the right, which means that the detected events have more energy than before the polishing process (more photons per event reach the PMTs). In addition, this improvement in the photon collection efficiency of the scintillating fibers allows more events to be detected, which can be quantified by a parameter F definded as,

$$F = \frac{A_P - A_{NP}}{A_{NP}} \quad (4.1)$$

where A_P and A_{NP} are the integrals of the energy spectrum measured after and before the polishing process, respectively. An improvement of detected events of almost a factor two was acheived with respect to the measurement made before polishing.

These test were repited using two radioactive sources, an encapsu-

lated ^{60}Co source with gamma emissions of 1173.2 keV and 1332.5 keV and an activity of 715 Bq, and a ^{90}Sr beta source with a maximum beta energy of 545.9 keV and an activity of 17.8 kBq. The radioactive sources were placed next to the fiber bundle, in the middle of it (at 7.5 cm from each PMT) and the energy spectra was recorded for both radioactive sources, which are shown in Figure 4.11.

Again, it can be appreciated that both energy spectra are shifted to the right after polishing, obtaining an improvement of almost a factor two with respect to the spectra before polishing.

In summary, with the polishing machine, the photon collection efficiency of the fibers was improved (mainly due to the improvement of the interface between fibers and PMTs). It is very important to achieve a high detection efficiency as the expected number of photons per tritium event is quite low, less than 20 as it has been demonstrated with simulations and experimental measurements.

Cleaning Method of Scintillating Fibers.

The tritium events only produce tens of photons in the scintillating fibers, so it is very important to detect as many photons as possible. As it is demonstrated in the light collection characterization of scintillating fibers, subsection 4.1.2, the quality of the interface between the core of uncladded fibers and the environment (tritiated water in the case of TRITIUM detector) affects conspicuously the photon collection efficiency. To improve the quality of the interface, a fiber cleaning process was implemented, aiming to remove external particles deposited on the fibers, such as dust and fat that worsen the photon collection efficiency. Through this cleaning process, the wetting property of the fibers is improved, that is to say the capacity of its surface to attract water, as illustrated in Figure 4.12. This implies an increase of the contact surface between the fibers and water, which prevents

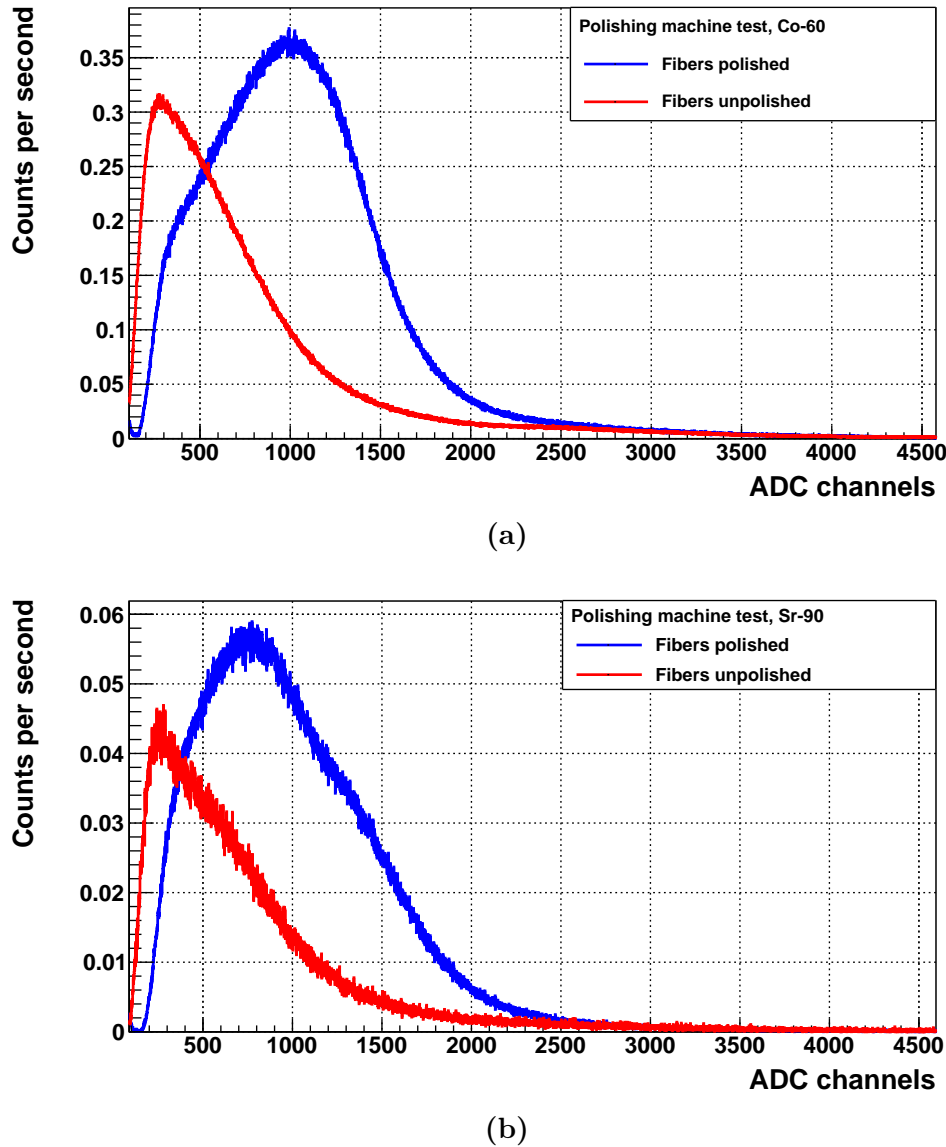


Figure 4.11 – Energy spectra recorded with polished and unpolished fibers.
a) for the ^{60}Co source b) for the ^{90}Sr source

air molecules from attaching to them, and produces a uniform water clad around them.

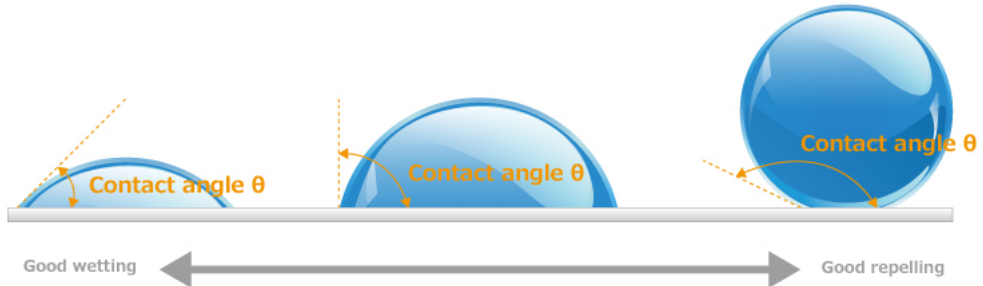


Figure 4.12 – Schematic representation of the wetting properties of a flat surface (gray) in contact with a drop of liquid (blue). The wetting property is characterized by the angle formed between the surface of both objects. The smaller angle, the better wetting property of the material. [comb]

This cleaning process was developed and carried out in the clean room of ICMOL laboratory². Three different glass beakers were used, one filled with alkaline soap, another with pure water (conductivity of the order of $10 \mu\text{S}/\text{cm}$) and the third with isopropanol. The fibers are first rubbed with gloved hands with alcalin soap during 5 minutes, then placed in the first beaker which is placed in an ultrasonic bath at 17 kHz frequency during 3 minutes. Then, the fibers are cleaned with a constant flow of water during 5 minutes and they are placed in the second beaker for ultrasonic bath during 3 minutes and then placed in the third beaker for ultrasonic bath during another 3 minutes. Finally the fibers are dried with a flow of gas N_2 and kept in clean conditions until their introduction into the module vessel of TRITIUM detector.

The improvement in the light collection of the scintillation fibers after this cleaning process was measured using a bundle of twenty uncladded

²ICMOL, *Instituto de Ciencia Molecular*, is a research institute located in the *Parc Científic* of the University of Valencia.

fibers of 15 cm length that have undergone this cleaning process. This bundle of fibers was arranged in the setup described in Figure 4.9 and the energy spectra were measured, before and after cleaning the fibers. Similar to the polishing machine test, this measurements was done first for the radioactive background, Figure 4.13, and then using two radioactive sources; a ^{90}Sr beta source, already used in the polishing machine test, and an encapsulated ^{137}Cs source with gamma emisions of 661.7 keV and an activity of 500 Bq activity, Figures 4.14. A higher gain was used in this case to optimize the number of channels used of the MCA (the digital multichannel analyzer). A shift of the spectrum to higher energies is observed in all the cases for the clean fibers, with respect to the spectra obtained before cleaning, showing an improvement in photon collection efficiency of the fibers. A similar equation to 4.1 was used quantify the improvement achieved with the cleaning process. Although no improvement in the detected events was observed for the background measurement, an improvement of about 26% and 35% was obtained for ^{90}Sr and ^{137}Cs respectively.

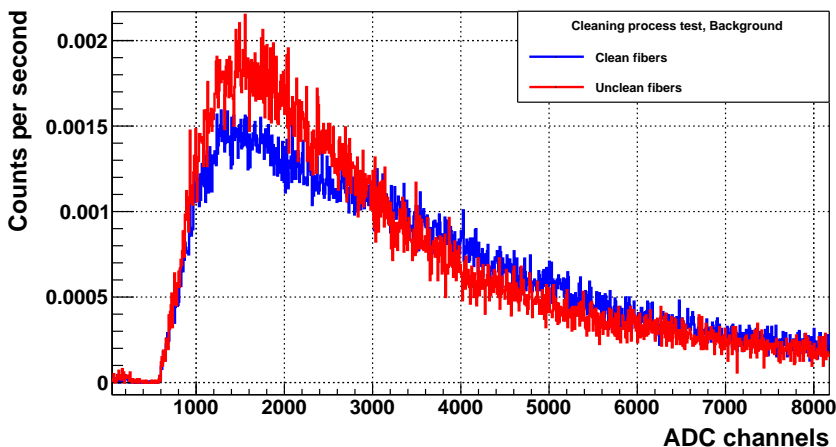


Figure 4.13 – Energy spectra of the radioactive background before and after the cleaning process.

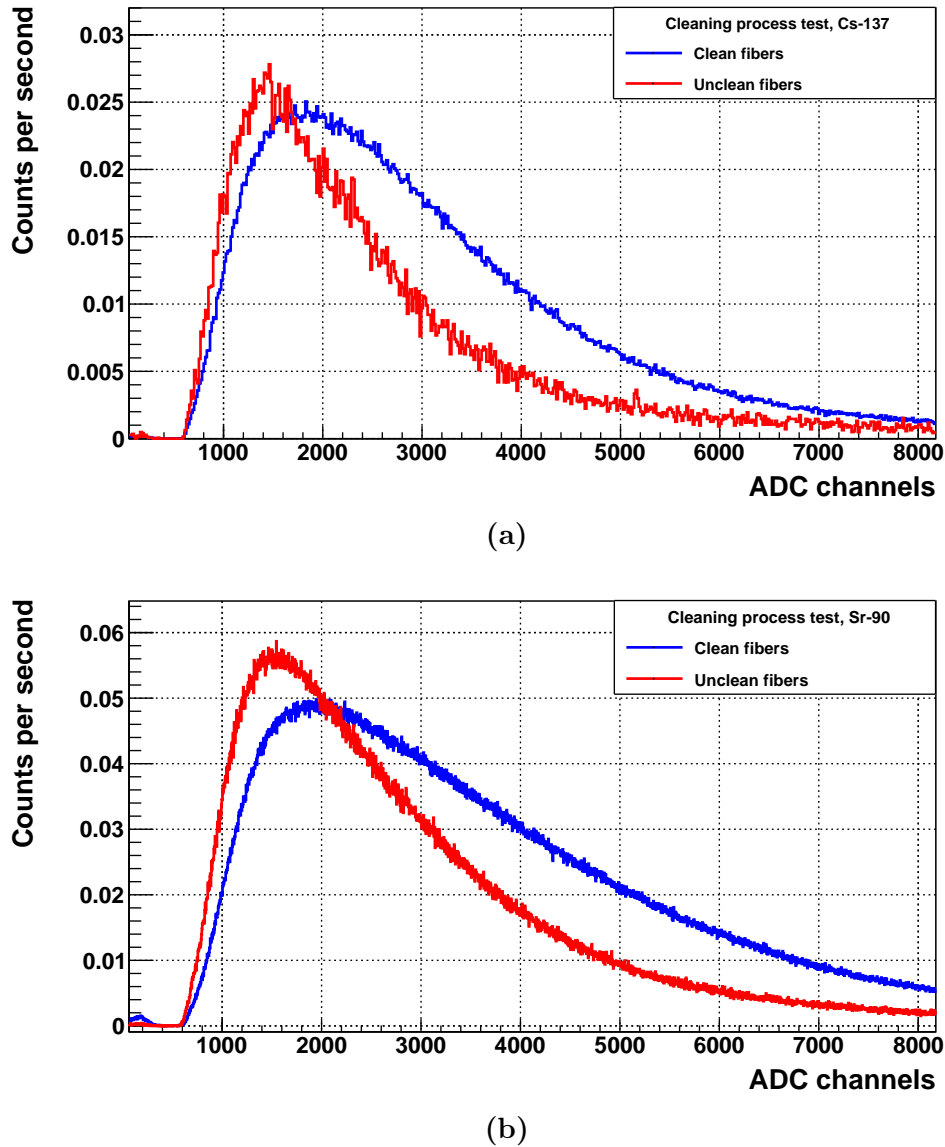


Figure 4.14 – Energy spectra obtained before and after the cleaning process using a radioactive source of a) ^{137}Cs and b) ^{90}Sr .

4.1.2 Light Collection Characterization of Scintillating Fibers

This section describes the characterization of uncladded BCF-12 fibers from Saint-Gobain, which are the fibers selected for the TRITIUM experiment. These fibers are compared to single clad and multiclaid BCF-12 fibers to quantify the influence of the clad in the relevant parameters of the scintillating fibers. Although commercial clads are too thick for the TRITIUM experiment, a low thickness clad could be developed. For example, clads with a thickness of the order of tens of nanometers could be achieved by deposition by evaporation in vacuo.

The difference between these three types of fibers is that uncladded fibers only consist of a polystyrene core with a refractive index of 1.60, whereas single clad fibers have an acrylic clad (PMMA) of $30\ \mu\text{m}$ thickness and a refractive index of 1.49. Multiclad fibers have a second fluor-acrylic clad of $10\ \mu\text{m}$ thickness and a refractive index of 1.42. As it was explained in section 3.2.2, the clad affects the photon collection efficiency of the fiber and prevents the fiber core from being damaged due to harsh environments.

This characterization was carried out for single scintillating fibers and consists of a comparative study of the uncertainty in the fiber response that will affect the tritium measurement of the TRITIUM detector. In addition an estimation of the photon collection efficiency of the fibers types mentioned above was done. The magnitude considered for the characterization was the rate of photons reaching the active area of the photosensor with increasing light input at the entrance of the fiber. To measure this magnitude, a calibrated PMT (Hamamatsu R8520-06SEL) with 29.76% quantum efficiency (quantum efficiency average of the wavelength region of interest). The voltage divider circuit which whortcut the PMT dynodes (see section 3.2.3) was used to polarize the PMT and mesure its photocurrent using a Picoammeter (Keithley 6487 picoammeter/voltage source). The photon

rate reaching the photocathode is calculated from,

$$N^o \gamma / \text{sec} = \frac{(I_{PMT} - I_{DC})}{q_e \cdot QE \cdot CE} \quad (4.2)$$

where I_{PMT} is the output current of the PMT when it detects photons and I_{DC} is the dark current. This equation takes into account the quantum efficiency of the PMT, QE , which is 0.2976 por the PMT used, and the capture efficiency in the dynodes CE , equal to 1 since the signal is read directly from the photocathode. In addition, it is assumed that each detected photon only generates one electron, the charge of which is q_e .

A simplified scheme of the setup is shown in Figure 4.15.

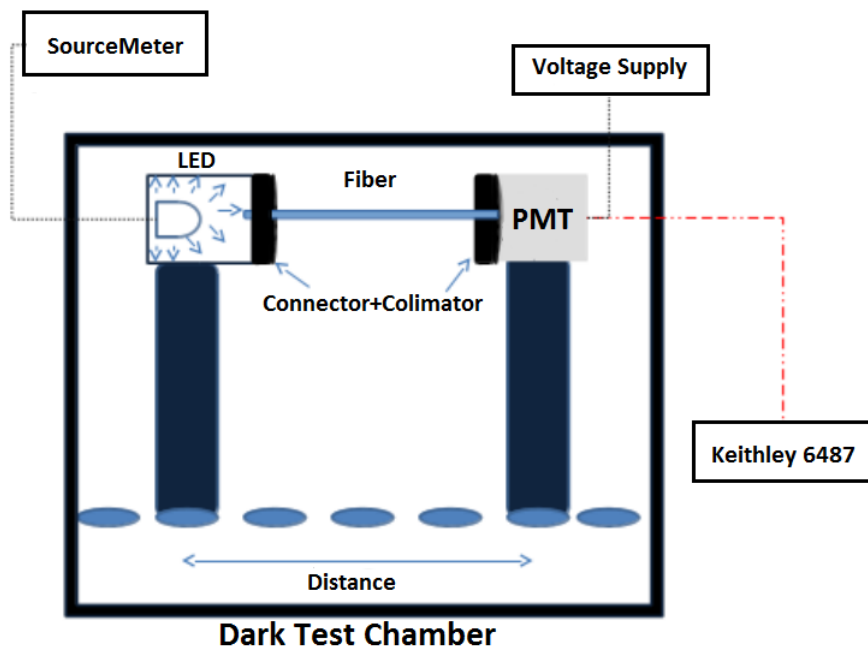


Figure 4.15 – Setup used for fiber characterization.

This setup consists of a home-made optical board, on which a LED and a the PMT are placed precisely in front of each other at an appropriate distance. A LED (LED435-03 from Roithner LaserTechnik GmbH

[Gmb10]), with an emission spectrum similar to that of the scintillating fibers, was used. The emission spectrum of the LED, given in Figure 4.16, was experimentally measured using a spectrometer and fitted to a Gaussian function. The LED emission peak is at 433.9 nm with a σ of 7.85 nm. The LED is feeded in current mode to achieve a linear dependence of the light emission on the current used to feed it. The fiber of 20 cm long was placed between the LED and the PMT, closely coupled to them at each of its end-surfaces, using optical grease [Cera]. Two collimators were used to ensure that only photons emitted from the LED were detected by the PMT. Two connectors (FH-ST³ connectors from RoHS company [|]) were used to fasten the fiber to the system.

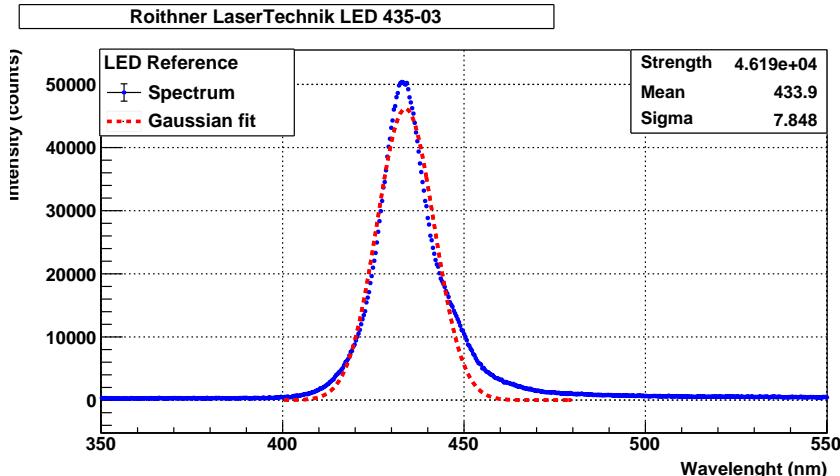


Figure 4.16 – Emission spectrum measured in the laboratory for the LED model 435-03 from Roithner LaserTechnik GmbH Company.

Measurement Conditions.

Before characterizing a fiber several tasks had to be performed to check that the black box is light-tight enough and to check that the PMT response is linear in the studied range of photons intensities.

³FH-ST is a quick assembly connector for 1 mm diameter plastic optical fiber, POF

A light leak in the dark box would produce a background larger than the signal. To check the light-tightness of the dark box, the PMT dark current were measured before and after covering the setup using a special black blanket from Thorlabs [Thoa], that prevents external photons from entering the system. No statistically significant differences were observed between covered and uncovered setup, which indicates the black box is sufficiently light tight.

The optimal voltage supply to the PMT was obtained by finding the voltage plateau at which the electron collection efficiency in the first dynode was practically 100% ($CE = 1$ in equation 4.2). In absence of fibers, the PMT output current was measured for different PMT supply voltages, between 0 and 500 V, first with the LED OFF (PMT dark current) and then with the LED feed at 1 mA. The number of photons detected by the PMT (difference between both spectra) is plotted in Figure 4.17. As it can be seen, the plateau starts at voltages higher than 150 V. The chosen voltage for the characterization was 250 V.

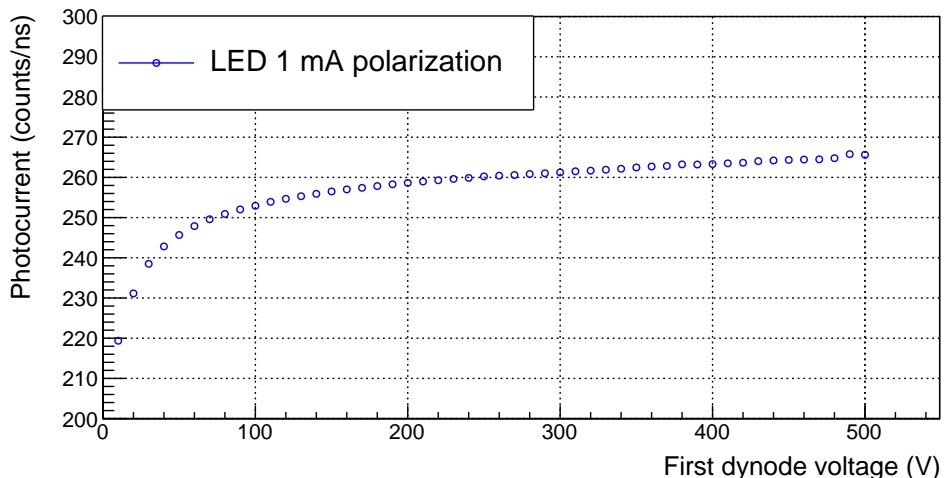


Figure 4.17 – PMT photocurrent as a function of the first dynode voltage. Error bars are included but they are too small to be visible.

Finally, the linear response of the PMT was verified. The LED was powered in current mode with intensities ranging from 0 to 10 mA, the linearity of which was previously tested in the laboratory. This was tested in the range of the number of photons expected for a tritium event (a few tens of photons per tritium event, which gives tens of photons per nanosecond) and in a broader range, around two thousand five hundred photons per nanosecond, interesting in the case of higher tritium activities. The linearity test was performed without fibers coupled to the PMT. Several collimators were used to reduce the amount of photons that reach the PMT. The results in low and high illumination cases are shown in Figures 4.18. As it can be seen, no saturation in the PMT response is observed.

Results of the Characterization of Scintillating Fibers

The tasks of cleaving and polishing the fibers add a small dispersion in the individual scintillating fiber response to the intrinsic dispersion from fabrication. This generates an uncertainty, σ_{sys-SF} , which is the contribution of the fibers to the total uncertainty in the tritium activity measured by the TRITIUM detector. The setup shown in Figure 4.15 was used to measure this uncertainty, in which has to be taken into account that the position of the connectors that lock the fiber in the experimental setup produces an additional systematic uncertainty, $\sigma_{sys-pos}$, in the measurement. Since both uncertainties are independent, the total systematic uncertainty is given by:

$$\sigma_{sys} = \sqrt{\sigma_{sys-SF}^2 + \sigma_{sys-pos}^2} \quad (4.3)$$

The uncertainty due to the fiber position has to be quantified to extract σ_{sys-SF}^2 from the total systematic uncertainty. Two different experiments were designed, the first giving only the systematic uncertainty ($\sigma_t = \sigma_{sys}$), and the second to obtain the total uncertainty. Then, σ_{sys-SF}^2 is given by,

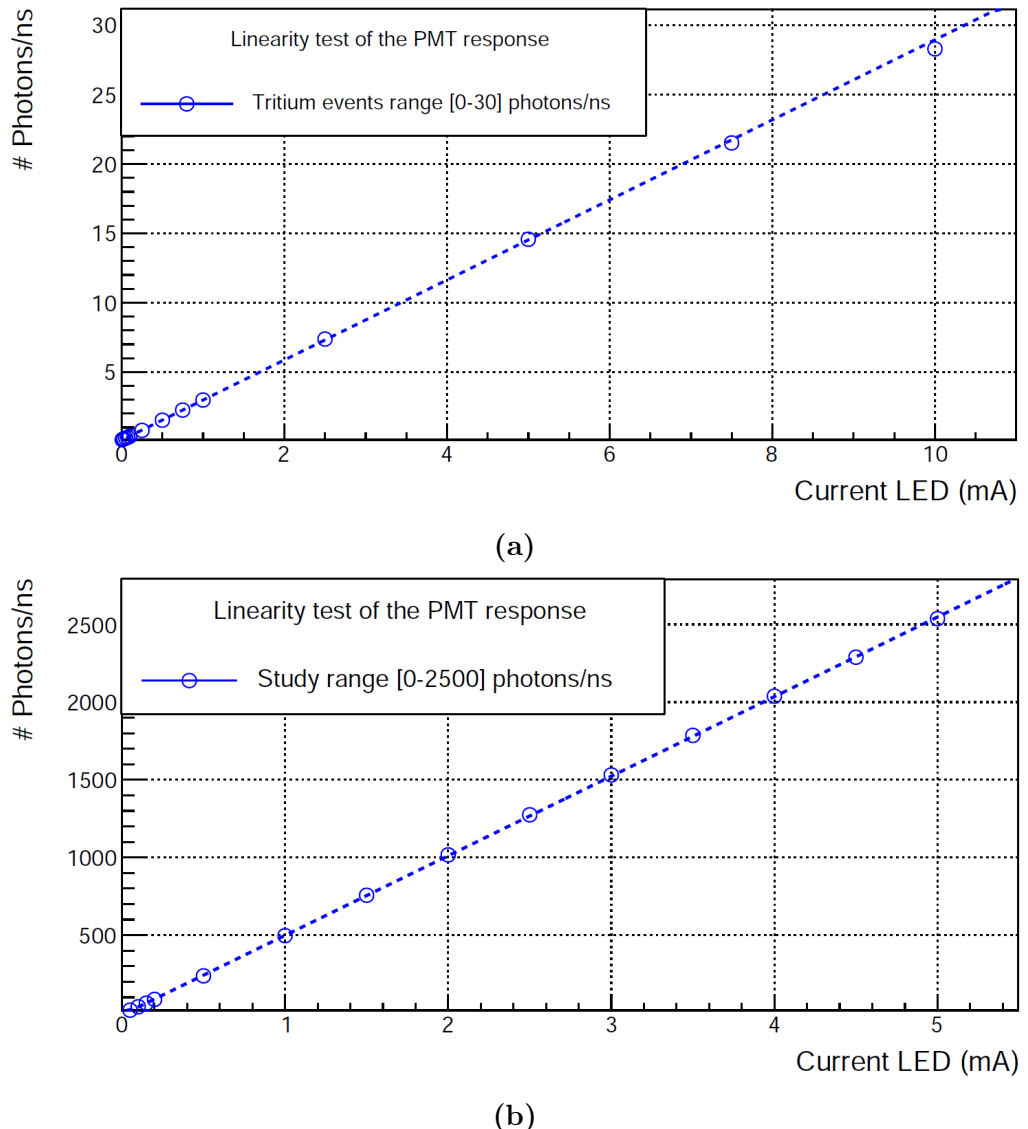


Figure 4.18 – Number of photons measured by the PMT as a function of the polarization current of the LED. a) Response of the PMT in the intensity range of tritium events. b) Response of the PMT in the range 0 – 2500 photons/ns. Error bars are included but they are too small to be visible.

$$\sigma_{sys-SF} = \sqrt{\sigma_{sys}^2 - \sigma_{sys-pos}^2} \quad (4.4)$$

The test designed to measure $\sigma_{sys-pos}$ consisted in preparing one fiber of each type (uncladded, single clad and multiclad), all with 1 mm diameter and 20 cm length, using the conditioning process reported in section 4.1.1. Each fiber was locked in the setup, and measurements of the PMT photocurrent with a fixed LED intensity, polarized at 1 mA were made. These measurements were repeated ten times with a given fiber, removing and putting on the fiber each time. The mean, \bar{x} , and the standard deviation of the PMT photocurrent for each fiber type are shown in Table 4.1 where the relative standard deviation, $\sigma_{sys-pos}^{rel}$, defined by equation 4.5, is also included.

$$\sigma_{sys-pos}^{rel} = \frac{\sigma_{sys-pos}}{\bar{x}} \quad (4.5)$$

Fiber type	Mean (ph/ns)	$\sigma_{sys-pos}$ (ph/ns)	$\sigma_{sys-pos}^{rel}$ (%)
Uncladded	524.09 ± 0.01	17.65	3.37
Single Clad	1071.70 ± 0.01	9.07	0.85
Multiclad	949.93 ± 0.03	9.91	1.04

Table 4.1: Mean and standard deviation (due to the fiber position in the setup) of the number of photons per nanosecond that reach the PMT for 0.1 mA LED intensity.

As it can be noticed, the clad significantly improves the light collection efficiency of the fibers, showing larger signals for single clad fibers and multiclad fibers than for uncladded fibers. The reason could be that the interface between the core of the fiber and its clad is better controlled for single-clad and multi-clad fibers than for uncladded fibers, where the interface is provided by the environment (air or water in the case of TRITIUM). External conditions, as dirt, may produce noticeable interface fluctuations. Concerning the statistical error of the measurement, it is three orders of

magnitude smaller than the systematic uncertainties previously mentioned ($\sigma_{sys-pos}$ and σ_{sys-SF}) so it was negligible.

To determine the total uncertainty, ten different samples of each fiber type were prepared and each fiber was measured under the same conditions as above. This measurement was done for four different LED emission intensities (0.05, 0.1, 0.15 and 0.2 mA). The results for uncladded fibers are plotted in Figure 4.19, where it can be seen that, although each fiber shows a very linear trend with increasing LED emission intensity, a dispersion in the fiber response is clearly observed. Similar results were obtained for single clad and multiclad fibers, displayed in figures 4.20a and 4.20b, respectively.

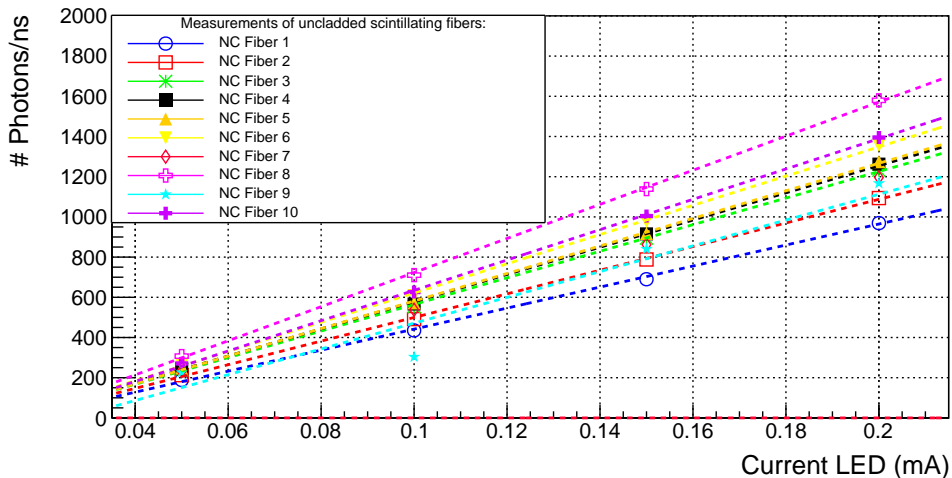


Figure 4.19 – Number of photons/ns reaching the PMT for Uncladded fibers. Error bars are included but they are too small to be visible.

The average number of collected photons versus LED intensity and the relative standard deviation for each type of fiber are given in Tables 4.2 and 4.3 respectively, and are plotted in Figure 4.21, where they can be compared.

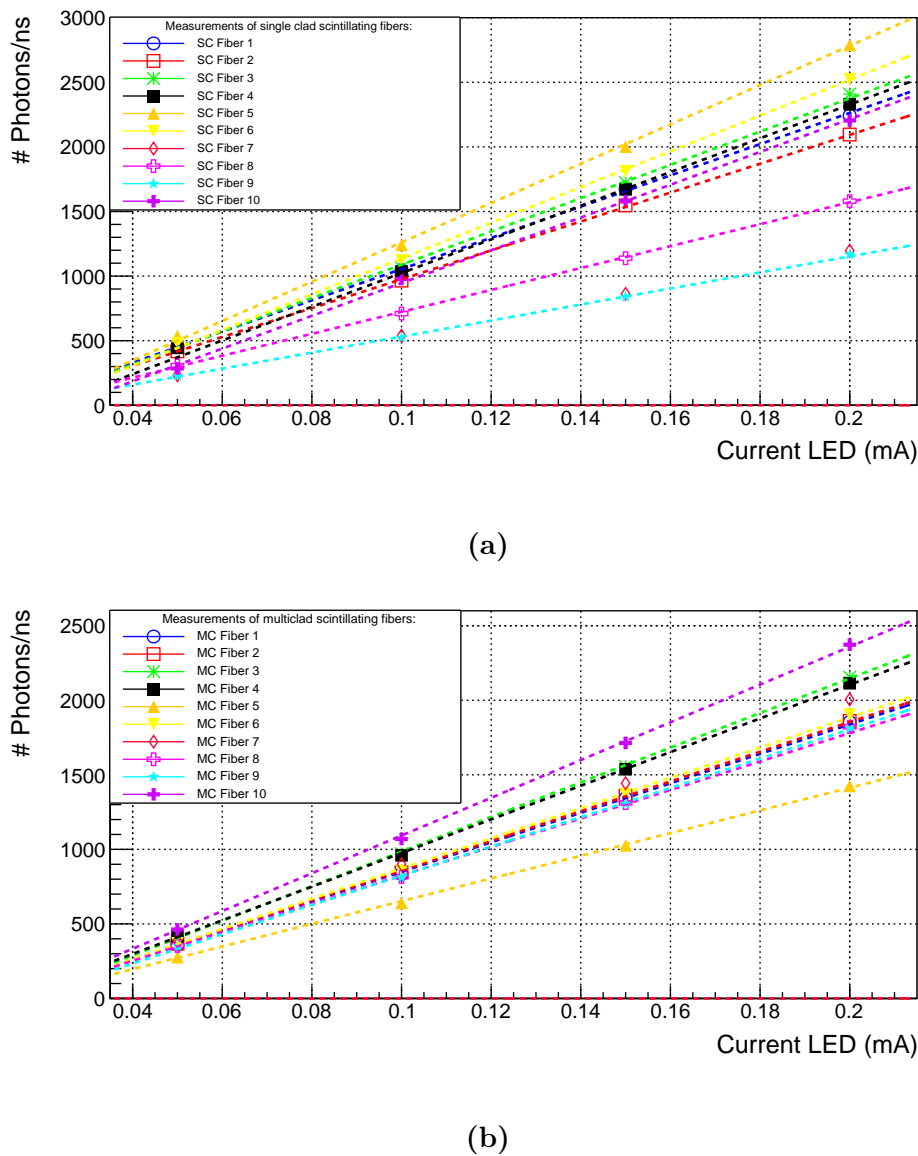


Figure 4.20 – Number of photons/ns reaching the PMT for ten samples.
 a) Single clad fibers, b) Multi-clad fibers. Error bars are included but they are too small to be visible.

Led Int. (mA)	Uncladded (ph/ns)	Single Clad (ph/ns)	MultiClad (ph/ns)
0.05	245 ± 11	384 ± 33	377 ± 15
0.1	572 ± 26	923 ± 74	871 ± 35
0.15	915 ± 39	1485 ± 120	1397 ± 55
0.2	1267 ± 55	2054 ± 166	1933 ± 76

Table 4.2: Number of collected photons per nanosecond versus LED intensity for the different type of fibers. The errors shown here are the standard deviation of the ten measured samples.

Led Int. (mA)	Uncladded (%)	Single Clad (%)	MultiClad (%)
0.05	4.38	8.66	3.97
0.1	4.59	8.02	3.97
0.15	4.34	8.07	3.95
0.2	4.36	8.10	3.93
Mean	4.42	8.21	3.96

Table 4.3: Relative standard deviation, σ_{sys}^{rel} (%), versus LED intensity for the different fiber types.

As it can be noticed in Figures 4.19 and 4.20, the fiber response is quite linear and single clad and multiclad fibers have stronger signals than uncladded fibers (a factor two in the case of single clad), which indicates, as already observed in Table 4.1, that the clad has a significant effect on the fiber collection efficiency. It can also be observed in Table 4.3 that the relative standard deviation, σ_{sys}^{rel} , does not vary with the LED intensity. The highest uncertainty was found for the single-clad fibers, despite of their higher light collection. This is most probably due to the cleaving process during which cracks in the clad may appear as it can be observed in Figure 4.3. As can be observed in Table 4.3, this damage seems to be reduced when a second clad is used, which enhances the mechanical resistance of the fiber.

An average of the three relative standard deviation quoted in this

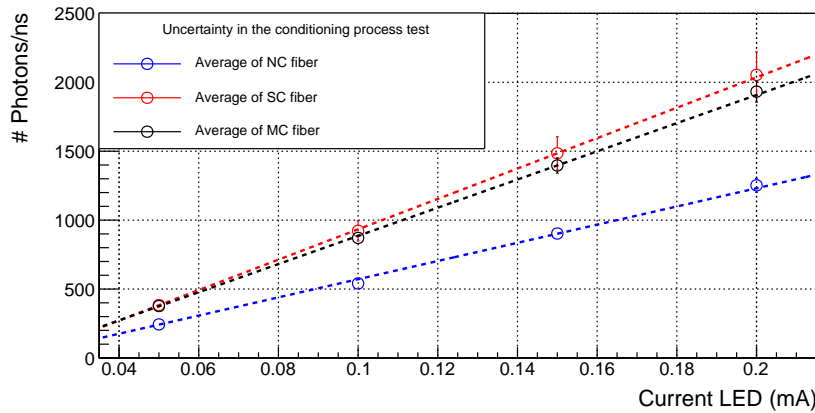


Figure 4.21 – Average number of photons per ns versus LED current for 10 samples of each fiber type (uncladded, single clad and multi-clad fibers). Error bars are included but they are too small to be visible.

section, σ_{sys}^{rel} , $\sigma_{sys-pos}^{rel}$ and σ_{sys-SF}^{rel} , are given in Table 4.4. As it can be noticed, the smallest relative standard deviation was found for uncladded fibers, which means that the damage from this process occurs mainly in the fiber clad, as illustrated in Figure 4.5 where it can be seen the clad break due to the cleaving process. It was checked under microscope that this damage only occurs at the end of the fiber. Also, the largest relative standard deviation is obtained for single clad fibers, which indicates that the second clad increases the resistance of the fiber to the conditioning process.

Fiber type	σ_{sys}^{rel} (%)	$\sigma_{sys-pos}^{rel}$ (%)	σ_{sys-SF}^{rel} (%)
Uncladded	4.42	3.37	2.86
Single Clad	8.21	2.17	7.92
Multiclad	3.96	1.04	3.82

Table 4.4: Relative standard deviations (σ_{sys}^{rel} , $\sigma_{sys-pos}^{rel}$ and σ_{sys-SF}^{rel}) measured in this test.

In summary, the relative statistical deviation due to the fiber con-

ditioning process was quantified for the different fiber types. It was found that the use of a fiber cladding improves the efficiency of photon collection but at the cost of worsening the standard deviation. Larger uncertainties (a factor two) in the light collection was observed in single clad fibers compared to multiclads and uncladded ones. This may be due to the damage in the clad produced during the cleaving process of these fibers. Therefore, it was chosen not to use a clad for the fibers used in the TRITIUM detector.

Finally, the absolute photon collection efficiency in 10 cm of scintillating fibers, CE_{10} , was measured for each type of fiber. To measure it, ten different samples of 10 cm length were prepared for each fiber type and similar measurements of the photons collected were performed, which are summarized in Table 4.5.

Led Int. (mA)	Uncladded (γ/ns)	Single-clad (γ/ns)	Multi-clad (γ/ns)
0.05	318 ± 61	550 ± 71	480 ± 84
0.1	736 ± 143	1270 ± 164	1111 ± 193
0.15	1184 ± 232	1984 ± 231	1777 ± 307
0.2	1645 ± 324	2507 ± 208	2338 ± 350

Table 4.5: Number of the collected photons versus LED intensity for 10 different fibers of 10 cm length.

The collection efficiency of 10 cm fiber length, CE_{10} , was calculated by comparing these photons collected to those measured for a fiber length of 20 cm. It is quite similar to the expected value considering an exponential attenuation of the signal in length as follow [Leo94].

$$N_{ph}/\text{ns}(x) = N_{ph}/\text{ns}(x_0) \times e^{-(x-x_0)/L} \quad (4.6)$$

$$CE_{10} = \frac{N_{ph}/\text{ns}(20 \text{ cm})}{N_{ph}/\text{ns}(10 \text{ cm})} = e^{-10/L} = 96\% \quad (4.7)$$

where L is the absorption length provided by the manufacturer, $L = 270$ cm. A lower collection efficiency has been obtained compared to the expected value for each type of scintillating fiber. This is likely due to blemishes and dirt on the fiber surface and a less than perfect interface between the fiber and the PMT used.

Fiber type	CE_{10} (%)
UnCladded	76 ± 8
Single Clad	78 ± 6
Multiclad	83 ± 7

Table 4.6: Collection efficiencies CE_{10} .

4.2 Characterization of SiPM

This section details the characterization of some of the most relevant parameter of the SiPM model Hamamatsu S13360-1375, which was the first choice for the TRITIUM monitor photosensor. The most relevant SiPM parameters are its breakdown voltage, V_{BD} , the gain of the SiPM and its dependences with the operating voltage and temperature, $G_{SiPM}(V_{bias}, T)$, and the temperature coefficient, e . Additional parameters were measured and used to verify the accuracy of the characterization such as the quenching resistance, R_q , the pixel capacitance, C_d , and the terminal capacitance, C_t . Other relevant parameters for the TRITIUM monitor are the PDE, which can affect to the minimum detectable activity, MDA, the dark count rate and the crosstalk probability, which can generate false counts interpreted as tritium counts by the TRITIUM detector. They were not measured since it was not possible with the current setup. It is expected to be measured for the S13360-6075 model, the latest proposal for the TRITIUM detector, where all the relevant parameters will be experimentaly determined using a different experimental setup, described in appendix A. The afterpulse prob-

ability was not experimentally measured since, as it is explained in seccion 3.2.3, its probability is negligible when time coincidence windows of 10 ns are used.

The SiPM characterization is carried out inside of a climatic chamber, model CCM 81 from DYCOMETAL [DYC]. This climatic chamber allows to control the temperature and humidity with a precision of 0.1°C and 0.1% respectively. In addition, this chamber is a Faraday cage. A special black blanket [Thoa] was used to prevent external photons from reaching the SiPM.

First, the quenching resistance and the breakdown voltage of the SiPM were obtained from the measurement of the output current generated by the SiPM as a function of its bias voltage applied in forward and reverse direction, respectively. The output current of the SiPM was directly measured using the Keithley 6487 Picoammeter/Voltage Source [KEI]. The LabView sofware was used to take the data. The currents-voltage curves are shown in Figure 4.22.

As can be seen, when the bias voltage is applied in forward direction (Figure 4.22a) the output current of the SiPM does not flow until the potential difference between the n and p layers is reached, which is approximately $V_0 = 0.7$ V for silicon photosensors, close to the value experimentally obtained, $V_0 = 0.5$ V. When the current starts to flow, the intensity is linear with the applied voltage. The equivalent resistance, R_{eq} , was determined from,

$$I = \frac{1}{R_{eq}}V; \quad \frac{1}{R_{eq}} = \sum_{i=1}^N \frac{1}{R_{qi}} = \frac{N}{R_q} \quad (4.8)$$

and R_{iq} are the quenching resistance of each pixel of the SiPM in parallel which have the same value, R_q . A value of $R_q = 360.56 \pm 0.07$ kΩ was obtained from a linear fit to the data (Figure), which is in agreement with the typical values given by Hamamatsu.

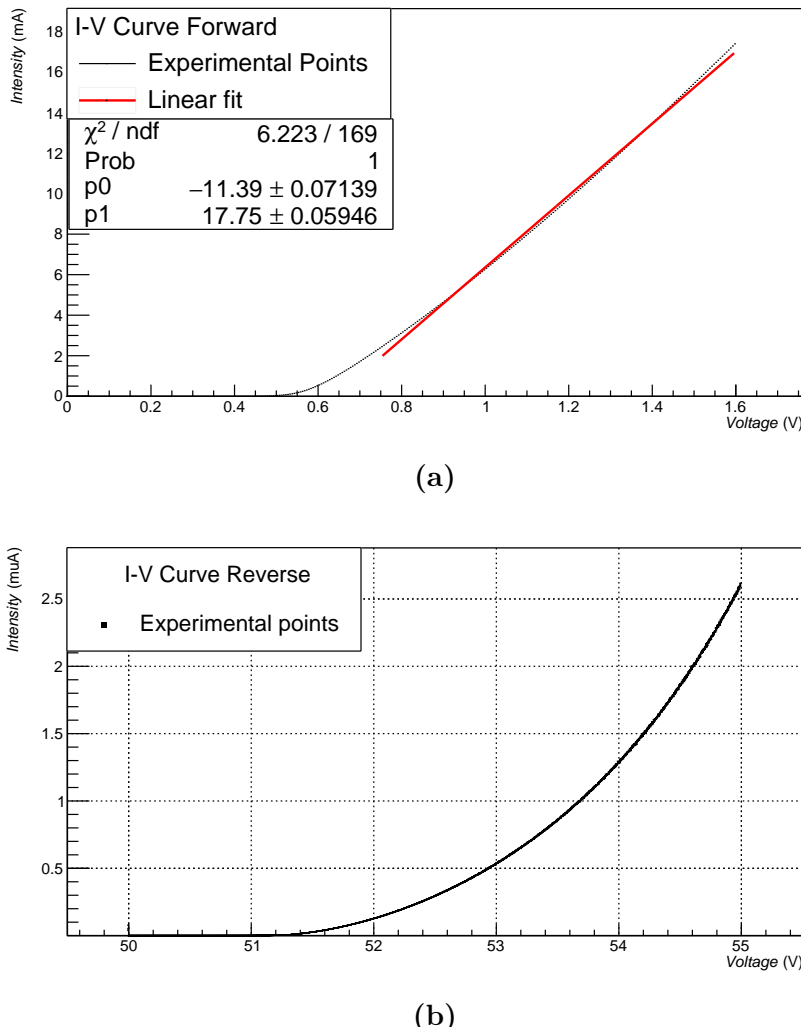


Figure 4.22 – I-V curves measured for the SiPM model Hamamatsu S13360-1375 with the bias voltage applied in a) forward direction b) reverse direction. The measurements were taken at $T = 25^\circ\text{C}$ and humidity $H = 45\%$.

The breakdown voltage, V_{BD} , was obtained from the reverse bias voltage plot (Figure 4.22b). This is the point at which the SiPM begins to operate in avalanche mode, which can be calculated from the maximum of the function

$$f = \frac{1}{I} \frac{dI}{dV} \quad (4.9)$$

The value obtained, $V_{BD} = 51.02$ V, is in agreement with the value provided by Hamamatsu, Table 3.3.

To measure the SiPM gain, G_{SiPM} , the electronic board described in section 3.2.4 with an amplification factor of $F_{amp} = 170$ was used. An incoherent light source, LED435-03 from Roithner LaserTechnik GmbH [Gmb10], described in section 4.1.2, was used to illuminate the SiPM with a low enough flux of $\lambda = 435$ nm photons. The SiPM output signal shows various well-defined pulse heights, shown in Figure 4.23, corresponding to the number of pixels simultaneously fired. The single photon spectrum, SPS, is plotted in Figure 4.23. This spectrum was obtained by integrating and histogramming the SiPM output pulses with time window wide enough to contain the full charge of the pulse. The time window used in these measurements was $t_w = 500$ ns. The light source provides a trigger signal for the measurement, represented in green line in Figure 4.23.

The well-separated peaks in the SPS spectrum correspond to the charge produced by a different number of fired pixels. The first peak in the spectrum is the pedestal, which is the charge measured when no pixel is fired. This peak is caused by the electronic noise of the system. The second peak corresponds to one fired pixel and so on. The SiPM gain, G_{SiPM} , can be obtained from the SPS spectrum from the equation,

$$G = \frac{\overline{\Delta Q}(V \cdot s)}{F_{amp}(V/A) \times e^-(C)} \quad (4.10)$$

where e^- is the electron charge and $\overline{\Delta Q}$ is the average peak distance in the

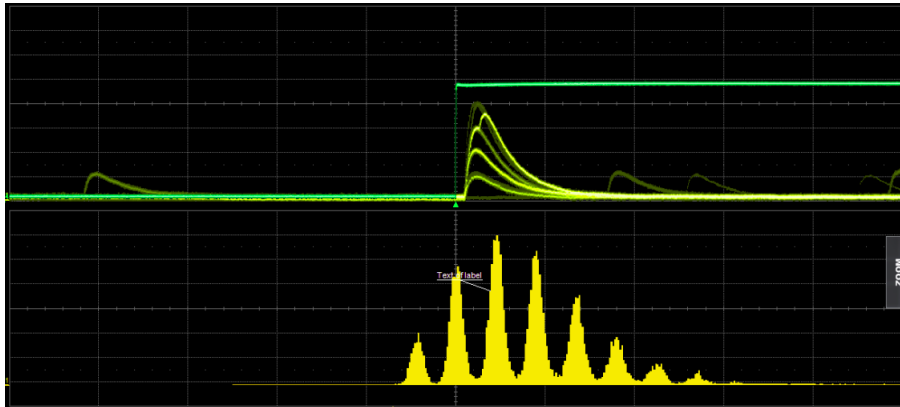


Figure 4.23 – Above) Trigger signal (green) and SiPM output pulses (yellow). Below) SPS spectrum obtained by integrating and histogramming the SiPM output pulses. This measurement was done at 25°C , $V_{bias} = 53.98$ and humidity of $H = 60\%$.

SPS spectrum, corresponding to the charge released by a fired pixel.

To obtain the value of $\overline{\Delta Q}$ a macro was written in ROOT [Col21b]. This macro finds and extract the background (the output signals of the SiPM different to the pedestal when it is not illuminated by a LED), which is crucial in some cases like high temperatures or high bias voltages since it can hide its peaks. After that, this macro find all peaks in the SPS spectrum and fits each one to a Gaussian function, shown in Figure 4.24a. The value and error of the charge produced by multiple fired pixels are obtained from the centroid and the sigma of the different fitted Gaussian functions. The obtained charges are fitted to the number of fired pixels, Figure 4.24b.

Up to 10 simultaneously fired pixels were obtained with a relative uncertainty of the charge measurement of less than 2%. The slope of the straight line in Figure 4.24b corresponds to $\overline{\Delta Q}$.

For the case studied, which corresponds to a temperature of 25°C and a bias voltage of 53.96 V (overvoltage around 3 V), the value obtained for the SiPM gain is $G_{SiPM} = (4.11 \pm 0.04) \cdot 10^6$, very close to the value

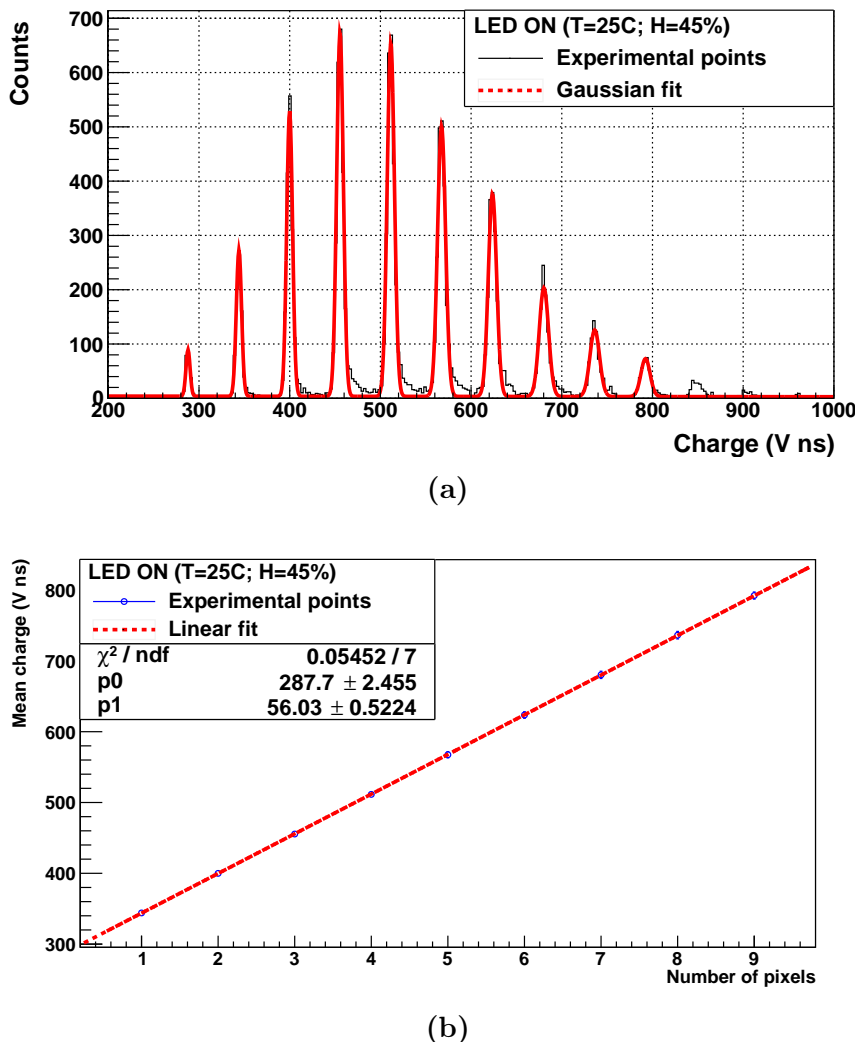


Figure 4.24 – ROOT analysis performed to obtain the SiPM gain. a) Fit of the SPS spectrum to various Gaussian functions. b) Charge of successive number of pixels as a function of the number of pixels fired. Error bars are within point size. This experience was carried out at $T = 25^\circ\text{C}$, $V_{bias} = 53.98$ V and humidity of $H = 45\%$.

provided by Hamamatsu, Table 3.3.

A method for the SiPM gain stabilization against variations due to the temperature was implemented. This is necessary for the TRITIUM project since the temperature in the final location of the tritium detector cannot be controlled with the precision required to avoid variations of the SiPM gain. This method consists in compensating for variations in the SiPM gain, caused by variations of temperature, by controlled variations of the bias voltage. For this task, first, the dependence of the SiPM gain with the temperature and bias voltage was measured. The SiPM gain was measured at several temperatures from 15°C to 41°C in steps of 2°C, which is expected to be the temperature range in the final location. The bias voltage was $V_{bias} = V_{BD} + 3$. The SiPM gain was measured at several overvoltages from 1 V to 5 V in steps of 0.2 V. The temperature was $T = 25^\circ\text{C}$. Both measurements are shown in Figure 4.25.

As can be seen, an excellent linear trend is obtained for both cases. The parameters of the linear fit obtained are,

$$\begin{aligned} G_{SiPM} &= a \cdot T + b; & G_{SiPM} &= c \cdot V_{bias} + d \\ a &= (-82.53 \pm 1.59) \cdot 10^3; & c &= (137.72 \pm 1.50) \cdot 10^4 \\ b &= (617.65 \pm 4.53) \cdot 10^4; & d &= (-762.16 \pm 8.13) \cdot 10^5 \end{aligned}$$

In addition, the breakdown voltage, V_{BD} , and the terminal capacitance, C_t , can be obtained from the linear fit of the SiPM gain as a function of the bias voltage, V_{bias} . Both parameters can be obtained from the definition of the SiPM gain and taking into account that the charge produced in a pixel is proportional to the capacitance of the pixel and the difference voltage in the SiPM, V_{OV} ,

$$G_{SiPM} = \frac{Q_{pixel}}{e^-} = C_d \frac{V_{bias} - V_{BD}}{e^-} = c \cdot V_{bias} + d \quad (4.11)$$

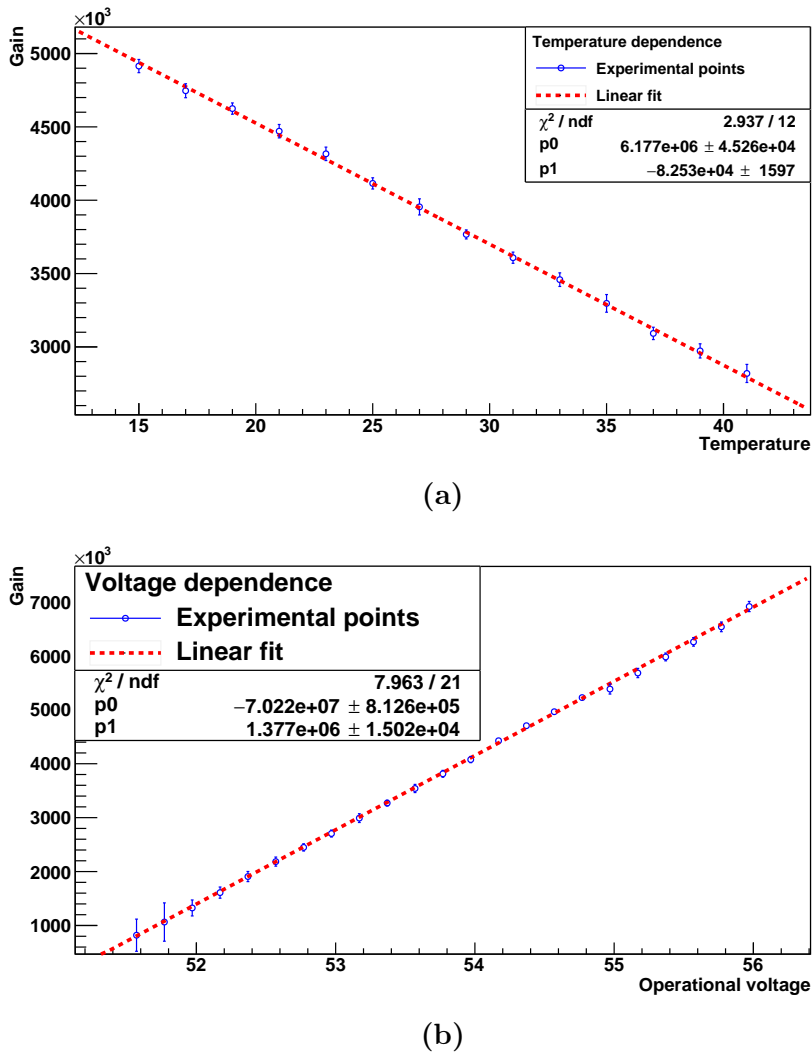


Figure 4.25 – Dependence of the SiPM gain with the a) Temperature b) Bias voltage.

where C_d is the pixel capacitance.

From the linear fit obtained in Figure 4.25b, a value of $V_{BD} = 50.98 \pm 0.59$ V and $C_d = 220.63 \pm 2.41$ fF are obtained. The terminal capacitance of the SiPM can be calculated assuming all pixels in parallel, $C_t = N_p \times C_d = 62.88 \pm 0.69$ pF. Both magnitudes, the breakdown voltage and the terminal capacitance, are in agreement with the values provided by Hamamatsu, Table 3.3.

Finally, the value of the bias voltage to be applied to compensate for the variation in the SiPM gain due to a variation of the temperature can be obtained by applying variations to linear relations:

$$\begin{aligned} G_{SiPM} &= a \cdot T + b \longrightarrow \partial G_{SiPM} = a \partial T \\ G_{SiPM} &= c \cdot V_{bias} + d \longrightarrow \partial G_{SiPM} = c \partial V_{bias} \end{aligned}$$

Therefore, the total variation of the SiPM gain, which is produced by the variation of both parameters, must be cancel:

$$\begin{aligned} \partial G_{SiPM,tot} &= \partial G_{SiPM}(T) + \partial G_{SiPM}(V_{bias}) = 0 \\ \partial G_{SiPM}(V_{bias}) &= -\partial G_{SiPM}(T) \longrightarrow c \partial V_{bias} = -a \partial T \\ \partial V_{bias} &= -\frac{a}{c} \partial T = e \partial T \end{aligned}$$

where the parameter $e = 59.93 \pm 1.33$ mV/°C is the ratio of a and c and agrees with the value of the temperature coefficient provided by Hamamatsu, Table 3.3. Finally, integrating this expression, we obtain:

$$\int_{V_i}^{V_f} \partial V_{bias} = e \int_{T_i}^{T_f} \partial T \longrightarrow \Delta V_{bias} = e \Delta T \quad (4.12)$$

This equation gives the variation of the voltage ΔV_{bias} that keeps the SiPM gain when a variation in the temperature happens, ΔT . More useful is to know the bias voltage V_{bias} to be applied as a function of the temperature T . For this, it is necessary a reference case. In this case, the reference case

considered is $V_i = V_{ref} = V_{BD} + 3$ V = 53.98 V and $T_i = T_{ref} = 24^\circ\text{C}$, at which the gain is $4.2 \cdot 10^6$ (experimentally measured). Thus, we get:

$$(V_{bias} - V_{ref}) = e(T - T_{ref})$$

$$V_{bias}(\text{V}) = 59.9 \cdot 10^{-3} \cdot T(\text{ }^\circ\text{C}) + 52.54 \quad (4.13)$$

Finally, this temperature through bias voltage compensation was tested. The temperature was varied from 21°C to 29°C and the bias voltage was modified according to the equation 4.13. The value of the SiPM gain obtained as a function of the temperature is shown in Figure 4.26.

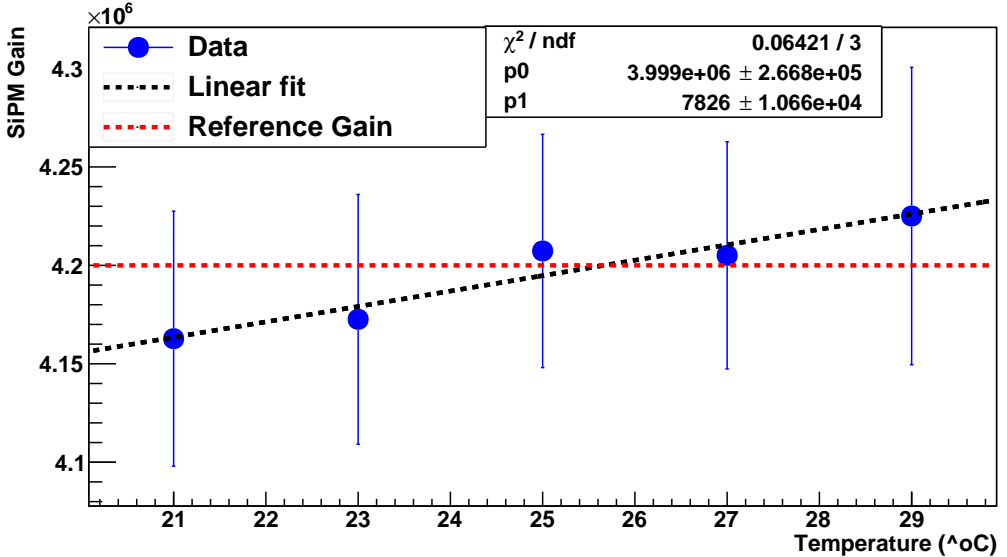


Figure 4.26 – SiPM gain measured as a function of the temperature after implementation of the gain stabilization method.

A red dotted line is included, indicating the value of the SiPM gain to be kept. As it can be seen, the slope of the linear fit, parameter p1, is three orders less than the constant, parameter p0, so it can be depreciated and a constant dependence can be accepted. Furthermore, all experimentally measured points are in agreement with the initially value measured for

the SiPM gain (red line). Therefore it can be concluded that this method works to stabilize the gain of the SiPM when variations in the temperature happens.

4.3 Characterization of the Water Purification System

This section describes the characterization of the water purification system, that guarantees that the quality of the water sample fulfills the requirements of the TRITIUM detector. There are three different requirements that this water purification system must satisfy,

1. A quite low conductivity⁴ of the water, around $10 \mu\text{S}/\text{cm}$, to avoid that external particles dissolved in the water be deposited on the fibers, drastically reducing the detector efficiency.
2. The radioactive particles (other than tritium isotope) from the water sample should be removed because tritium cannot be separated from other radioactive isotopes.
3. The tritium activity should not be affected by the water purification process.

To verify that these requirements are fulfilled, a characterization of the water sample for both, raw water and purified water, was done. This characterization consisted of measuring the water sample conductivity and the activity of the different radioactive element present in the sample. The turbidity and the chemical components of the water sample were also

⁴Conductivity is the ability of a material to conduct electrical current. In liquids, conductivity is related to the presence of salts (presence of positive and negative ions)

measured. The sample of the raw water was taken at 40 meters from the water purification system and two meters deep in the river since it is the place where the samples used in TRITIUM monitor will be taken. Variations of up to 25% in the tritium activity was measured between both points (due to the diffusion of tritium along the river). The chemical composition of the water was measured by a physico-chemical analysis, shown in Table 4.7, before the purification process. The water sample contains a number of components, that must be removed to prevent their deposition on the scintillating fibers of the detector.

Chemical components	Concentration (mg/L)
CO ₃ H ⁻	154
Mg	46
Ca	105
NO ₃ ⁻	16
Cl ⁻	196
NO ₂ ⁻	0.03
K	11
Na	173
SO ₄ ⁻	217
Dry Residue	1029

Table 4.7: Chemical components and turbidity measured in the raw water sample.

The water turbidity⁵ was measured using the Hanna Hi 9829 portable multiparameter system from Hanna Instruments [Ins], obtaining a value of 29 NTU, much higher than the WHO recommended limit of 5 NTU for drinking water. The water conductivity was also measured for both, raw and purified water, using the same system. The results of the conductivity measurements, together with the measurement of the rejected water, de-

⁵The turbidity of water is the loss of transparency due to dissolved particles, normally measured in Nephelometric Units of Turbidity, NTU, as the intensity of scattered light at 90 degrees.

scribed in section 3.3.2, are presented in Table 4.8. As it can be seen in the first column, the raw water sample has high values of conductivity, due to its content of ions, shown in Table 4.7. It can be noticed in the second column of the table that the conductivity of pure water was reduced by almost two orders of magnitude, to values close to $10 \mu\text{S}/\text{cm}$, fulfilling the requirement. In the third column, it can be remarked that the rejected water conductivity is higher than that of raw water, because this water contains the removed ions from the purified water.

Date	Raw ($\mu\text{S}/\text{cm}$)	Pure ($\mu\text{S}/\text{cm}$)	Reject ($\mu\text{S}/\text{cm}$)
1/8/18	970	11.85	1442
7/8/18	958	11.8	1632
14/8/18	966	12.04	1725
22/8/18	980	12.54	1702
28/8/18	987	9.9	1692
5/9/18	1009	12.02	1645

Table 4.8: Measurements of the conductivity for several samples of water.

The gamma radioactive elements present in both, raw and purified water, were identified and their activities measured by a HPGe, high purity germanium detector. A gamma analysis was carried out to determine the emitters with long enough lifetime to be measured. The radioactive isotopes found in the raw water sample with measurable activities were ^{40}K and ^{226}Ra which were absent in the purified water.

The tritium activity was measured by liquid scintillation counting (LSC) to check if the purification process had modified it. The raw water was filtered at 0.45 microns to remove any particles that could cause the extinction of the scintillation signal. Table 4.9 show several measurements of the tritium activity for different water samples before and after purification. As seen in the table, tritium activity is not affected by the purification process.

Date	Raw (Bq/L)	Pure (Bq/L)
7/8/18	24 ± 3	26 ± 4
11/12/19	13.2 ± 2.1	13.85 ± 2.2
15/01/20	30.6 ± 4.2	30 ± 4

Table 4.9: Measurements of the tritium activity for several samples of both, raw and purified water.

4.4 Characterization of the TRITIUM Cosmic Veto

This last section reports on the characterization of the active shield (cosmic veto), which was carried out using PMTs as photosensors. Measurements of the cosmic veto using SiPM arrays has already started and their replacement will be as soon as possible.

The quality of the veto wrapping, shown in Figure 3.27, was checked. This study was done at the level of one detector so the configuration of the electronics is the one given in Figure 3.15b. The surface of the veto was divided in 9 parts, shown in Figure 4.27, in which a gamma source was placed.

Two different tests were made for this task:

1. The improvement of the veto signal due to wrapping. A ^{137}Cs source was placed at point 2 and a energy spectrum was measured with the veto before wrapping. Next, the measurement was repeated after wrapping. The spectra obtained are shown in Figure 4.28.

The spectrum of the wrapping veto is shifted to the right, which means that more photons are collected per event. No improvement was obtained in the number of events detected, only in the collection efficiency.

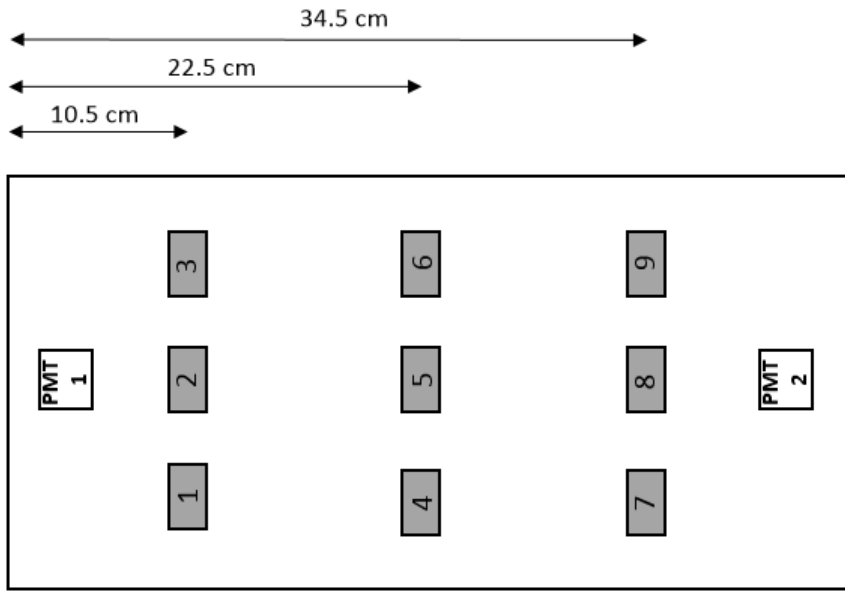


Figure 4.27 – Reference points used for veto mapping.

2. The spatial uniformity of the signal in the wrapped veto was evaluated. For this task, a mapping was carried out, which consisted of placing a ^{60}Co source at each point and measuring the number of events detected in the same time window. This test was done for two different veto modules and the energy spectrum obtained was integrated. The count rates obtained are plotted in Figure 4.29. It can be observed that the veto signal has a uniform response on its whole surface, giving a fairly similar counting rate in all the points measured.

Next, both vetos in time coincidence was studied, so the configuration of the used electronics was that of Figure 3.15c. The goal was to find the conditions in which the detection of cosmic events is optimized. This optimization consists of, on the one hand, finding the minimum high voltage of PMTs for which their efficiency is stable, and, on the other hand,

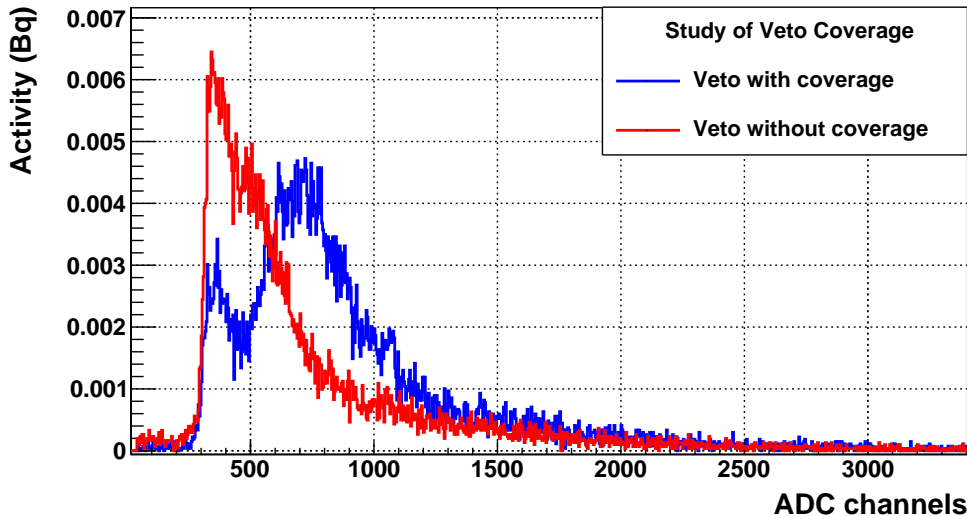


Figure 4.28 – Measurement of a radioactive source ^{137}Cs with the TRI-TIUM cosmic detector with and without wrapping.

finding the maximum threshold of the discriminator⁶ before starting to loss cosmic events. For higher voltages and a smaller thresholds, a plateau of the counting rate should be obtained.

The counting rate was measured for several high voltages at fixed threshold and for several thresholds at fixed high voltage, plotted in Figure 4.30. To find the optimal conditions, the amplification line of the electronics was eliminated and the output signal of the coincidence module was connected to a CAEN Quad Scaler And Preset Counter-Timer module, N. 1145, [coma]. The counting rate was measured in a time window of 300 s. In Figure 4.30a, the counting rate at several high voltages for three different thresholds, 60 mV, 100 mV and 200 mV is plotted. As it can be observed, there is a minimum high voltage for each threshold, 700 V, 730 V and 780 V respectively, at which the plateau start. This minimum voltage is higher

⁶The threshold is the voltage value that the PMT output signals must exceed to contribute to the cosmic detection

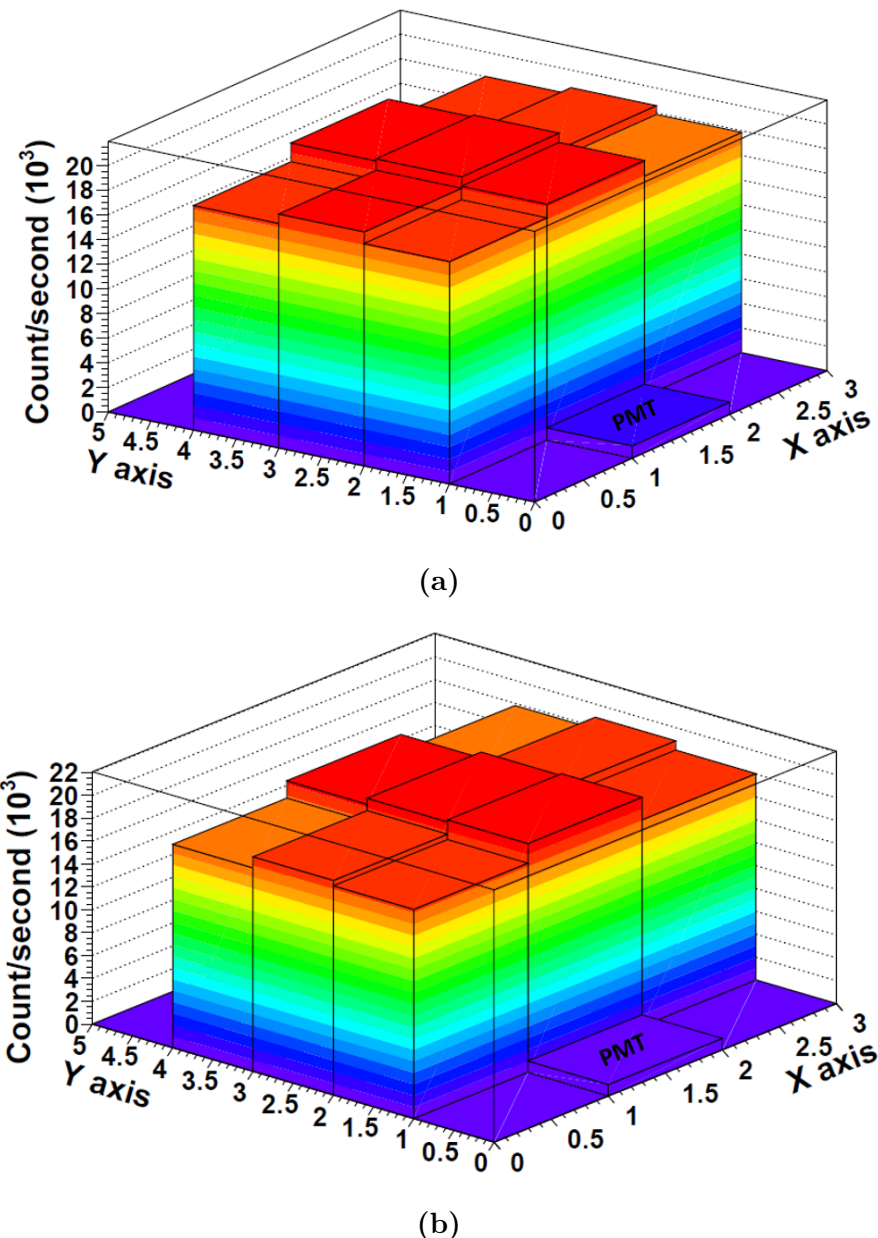


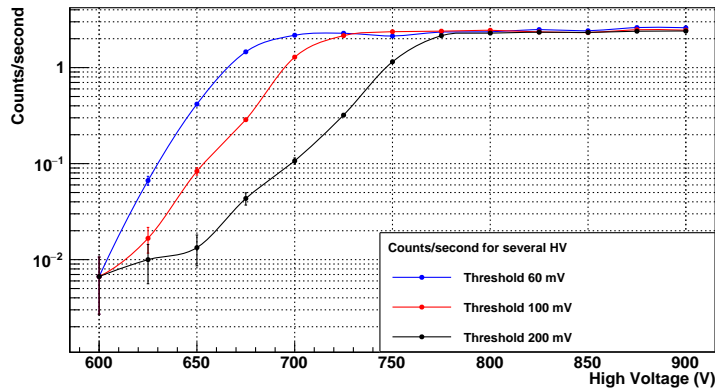
Figure 4.29 – Bidimensional graph of the count rate (Mapping) measured with two different TRITIUM cosmic detectors using a radioactive source of ^{60}Co .

when the value of the threshold increases, as it should. Analogously, the counting rate for several thresholds and fixed high voltage was measured for three different high voltages, 750 V, 800 V and 850 V, plotted in Figure 4.30b. There is a maximum threshold for every high voltage used, 140 mV, 270 mV and 450 mV respectively, at which the plateau ends. This maximum threshold increases with high voltage, as it should. The voltage chosen was 800 V since it is on the plateau for the three thresholds and the threshold chosen was 200 mV which is on the plateau for the selected high voltage.

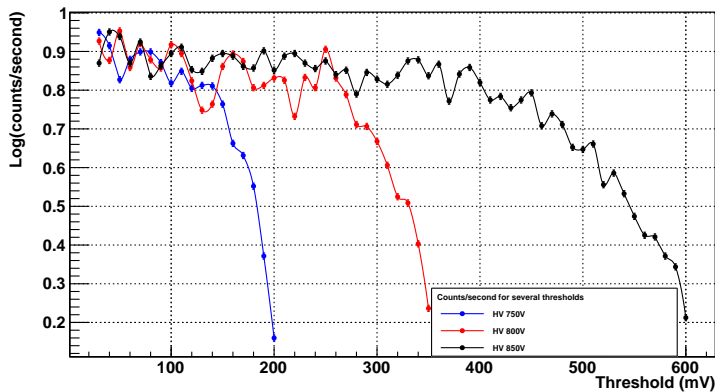
With this setting, the energy spectrum of cosmic events was measured, shown in Figure 4.31.

As expected, this energy spectrum fits well to a Landau function. The cosmic ray rate determined from the area of this spectrum is 2.5 event/s. The expected cosmic rate, calculated in section 3.4.2, is 2.9 event/s, so the efficiency of the active veto developed in TRITIUM experiment for cosmic event detection is 85%, which is a usual value for the efficiency of plastic detectors to mips.

Finally the detected cosmic ray rate versus the distance between the two cosmic veto was obtained. The energy spectrum was measured for five different distances, namely 10 cm, 20 cm, 36 cm, 40 cm and 50 cm. The spectra are plotted in Figure 4.32a. The energy spectrum in Figure 4.31 was also included. As it is expected, the counting rate decreases with the distance but the spectrum shape remains the same. The integrated spectra as a function of distance, plotted in Figure 4.32b, was fitted to a second degree polynomial which allows to estimate the cosmic rate for a given veto distance.



(a)



(b)

Figure 4.30 – Counting rate a) as a function of high voltage for fixed thresholds and b) as function of thresholds for fixed high voltage. in semilogarithmic scale

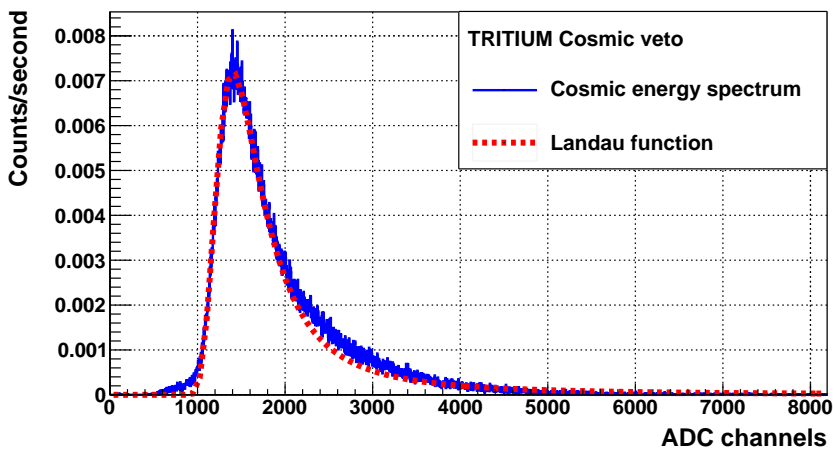


Figure 4.31 – Energy spectrum measured with the cosmic veto.

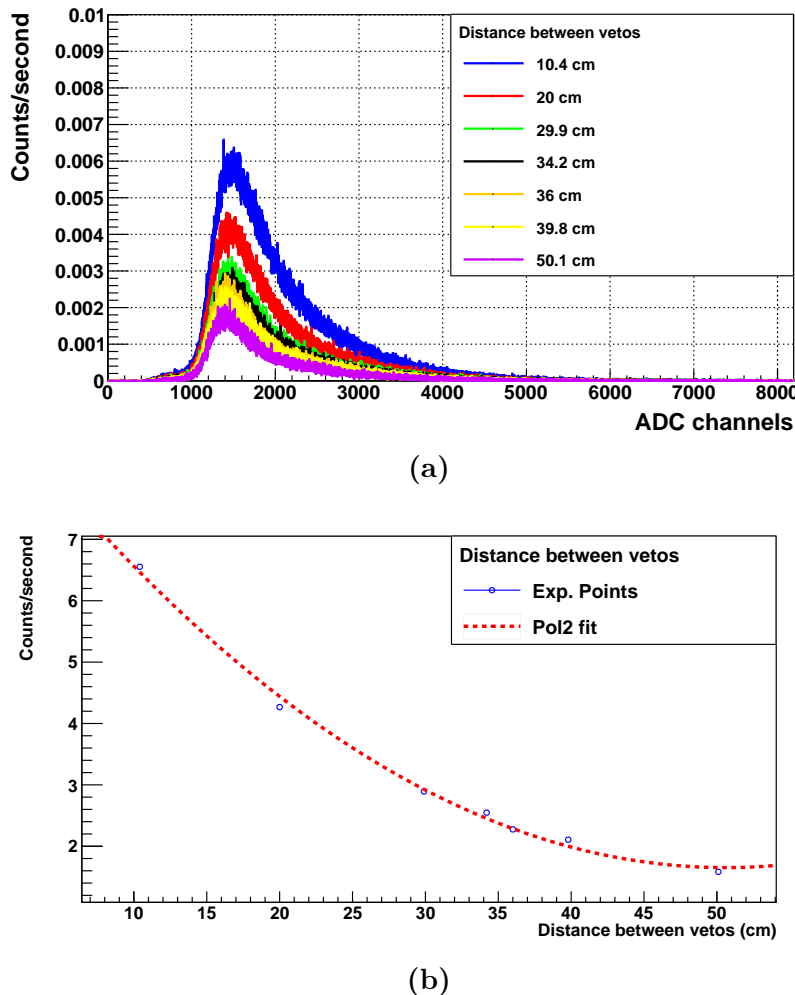


Figure 4.32 – Measurement of the cosmic veto for several distances between the two scintillators. Above) Energy spectrum of the cosmic veto for several distance. Below) Fit of the cosmic veto rate versus distance to a second degree polynomial.

Chapter 5

TRITIUM Detector Prototypes

This chapter describes the different prototypes developed in the framework of the TRITIUM experiment, which are so-called TRITIUM-IFIC-0, TRITIUM-IFIC-1, TRITIUM Aveiro and TRITIUM-IFIC-2, listed in chronological order of their construction. The first two prototypes built, TRITIUM-IFIC-0 and TRITIUM-IFIC-1, are preliminary prototypes used to learn about tritium detection and to improve the monitor design. The other two prototypes built, TRITIUM-Aveiro and TRITIUM-IFIC-2, are prototypes with an optimized design, based on the lessons learned from the former prototypes.

Each prototype was designed and built in the laboratories of IFIC or Aveiro and was filled with tritiated water following a method specially developed for this task. Several water tightness and filling tests were carried out for each prototype to guarantee its radiosecurity. The measurements obtained by the different prototypes during their installation in the laboratory are discussed in this chapter. The laboratories involved in the characterization of the prototypes are the IFIC in Valencia, the DRIM¹, in the

¹DRIM, Deteção da Radiação e Laboratorio Imagem Médica (Laboratory for Radiation Detection and Medical Imaging)

University of Aveiro, and the LARUEX² in Extremadura. An additional section shows the measurements obtained at the Arrocampo dam, the TRITIUM monitor installation site, where the control of external atmospheric conditions is less accurate. At the end of the chapter, the final monitor of TRITIUM detector will be described. Its design is a modular structure for easy scalability, composed of the number of detector modules needed to reach the required sensitivity.

5.1 First IFIC prototypes

Two preliminary prototypes, TRITIUM-IFIC-0 and TRITIUM-IFIC-1, are reported in this section, which were designed, developed and built at the IFIC workshop. These prototypes were thought to be a small scale proof of concept of the final TRITIUM detector module. They helped to learn about tritium detection, to detect design problems and to implement improvements for the final prototype.

5.1.1 TRITIUM-IFIC-0

The TRITIUM-IFIC-0 prototype was the first prototype developed in the TRITIUM experiment to check the feasibility of the technology proposed by TRITIUM, that is, to verify that is using plastic scintillating fibers to detect tritium in water with good sensitivity.

As liquid radioactive sources were involved, a special attention was paid to radiation safety in the design of the first prototype.

TRITIUM-IFIC-0 consists of a bundle of 35 fibers, shown in Figure

²LARUEX, Laboratorio de Radiactividad Ambiental de la Universidad de Extremadura (Environmental Radioactivity Laboratory of the University of Extremadura)

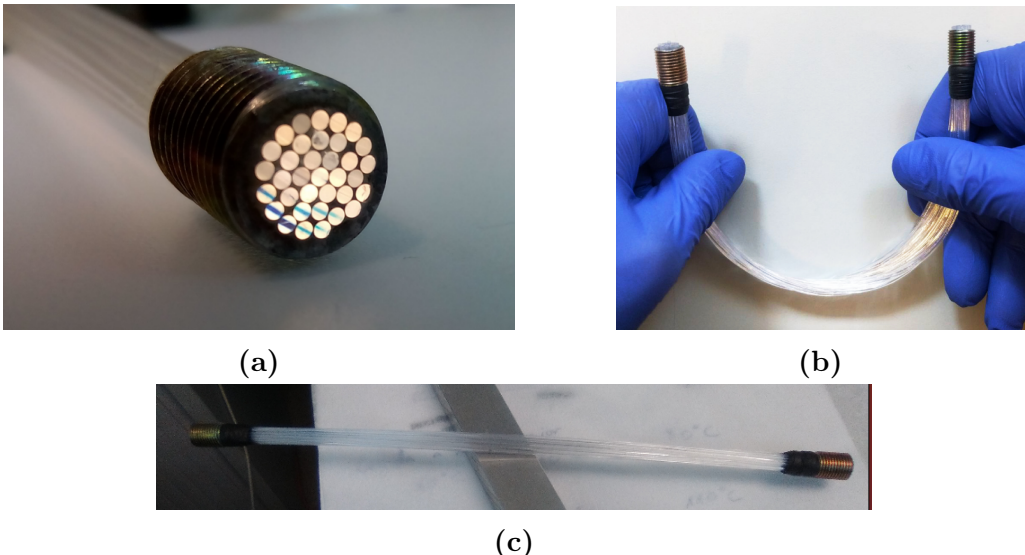


Figure 5.1 – a) Metallic piece of the fiber bundle. b) and c) Bundle of 35 fibers, the length of which is 20 cm, used in TRITIUM-IFIC-0 prototype.

5.1, of 20 cm length, which were cleaved and polished with the techniques reported in section 4.1.1. This bundle has metallic pieces located in both ends, shown in Figure 5.1a for attaching it to the prototype vessel. The fiber bundle was placed inside of a vessel, made of PVC³ since it is a safe widely used material. This vessel, shown in Figure 5.2, was designed in a U-shape to improve the radiological safety, although this shape was not the most appropriate for tritium detection, as we learned afterwards. As can be seen in Figure 5.2, a frame of methacrylate and steel was designed and built to hold the prototype. Two calibrated Hamamatsu R8520-460 PMTs [K.K19] were optically coupled to the fiber bundle ends using optical grease [Cera]. The voltage divider circuit of these PMTs is shown in Figure 3.9. The high voltage was set to -800 V, at which the gain are $1.26 \cdot 10^6$ and $1.01 \cdot 10^6$, and the quantum efficiency 29.76% and 28.66%, respectively. The two PMTs were read out in coincidence mode, using the electronics circuit shown in Figure 3.15b.

³Polyvinyl Chloride, PVC

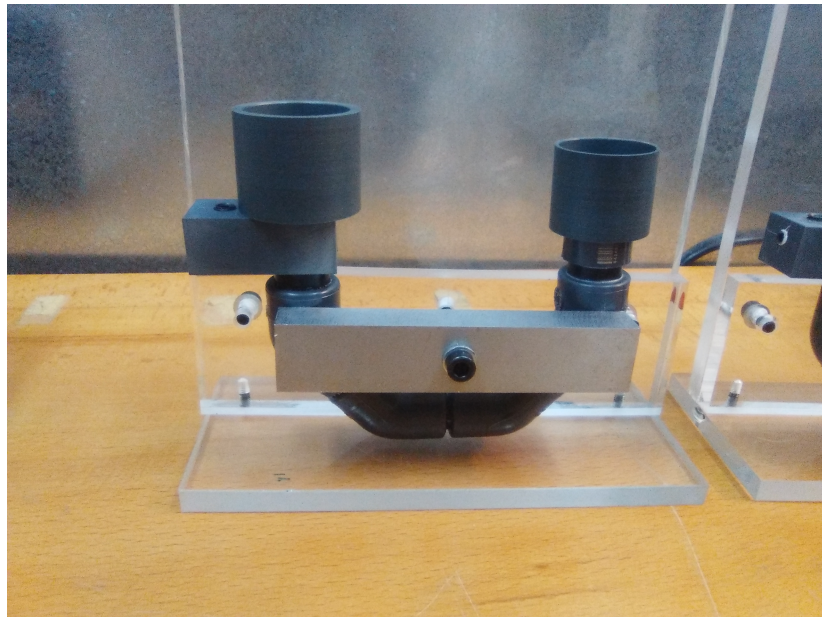


Figure 5.2 – TRITIUM-IFIC-0 Prototype.

Two identical prototypes were built and filled following the same protocol. The first prototype, called “TRITIUM-IFIC-0 Background”, was filled with pure water (39 mL, uncertainty of 0.05%) and was used to measure the radioactive background of the detectors whereas the second prototype, called “TRITIUM-IFIC-0 Signal”, was filled with a radioactive liquid source of tritium, the preparation of which is reported in the appendix C. The specific activity of the liquid source employed was 99.696 kBq/L (uncertainty of 2.24%) and the volume used to fill this prototype was the same, 39 mL (uncertainty of 0.05%). This second prototype was used to measure the total signal (tritium + background) from the detector. The measured tritium activity was determined by subtracting the background from the signal.

The statistically significant number of time coincident events was found too weak to be measured by time coincidences. The loss of photons was caused by several reasons, such as an excessive curvature of the fiber

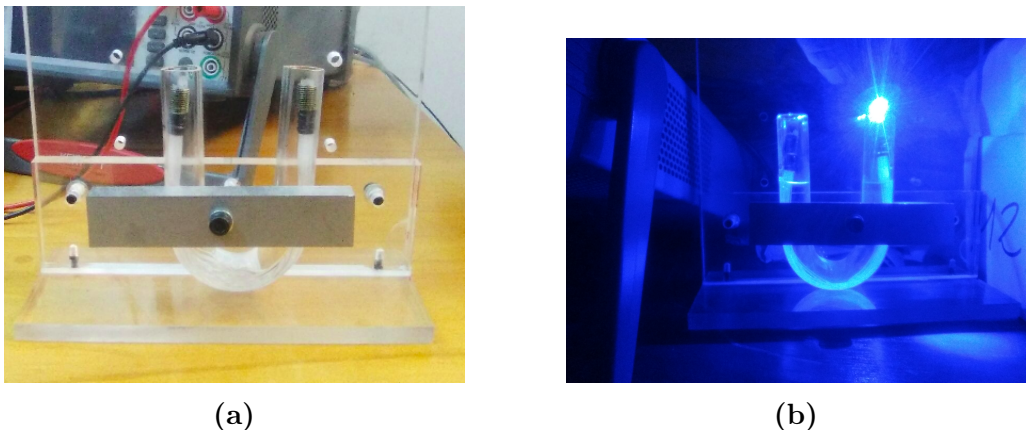


Figure 5.3 – a) Fiber bundle in PMMA vessel **b)** illumination test of the bundle to visualize the light loss due to the fiber curvature.

bundle due to the U-shape of the PVC vessel, causing most of the photons to escape from the fibers and the poor quality of the tritiated water-fiber interface (the cleaning process described in section 4.1.1 was motivated by this result).

A test was carried out to find an explanation to the absence of coincident events in the data. A transparent glass vessel was built similar to the TRITIUM-IFIC-0 prototype vessel, shown in Figure 5.3a, to study the effect of the fiber bundle curvature. The LED described in section 4.1.2 was used to verify the reduction in photocollection efficiency of the fiber bundle due to this curvature. As can be seen in Figure 5.3b, a large amount of photons introduced from one side of the bundle does not reach the other side due to the fiber curvature. This problem indicated the necessity to keep a straight fiber arrangement in the design of the next prototypes. Another important point that can explain the absence of coincident events is the flow of water through the fibers. The fiber bundle of this prototype is very compact and water may not be able to circulate properly around the fibers. This fact will be solved in the next prototype by using a matrix to keep the fibers at a necessary distance.

To overcome this problem and to obtain some data with this prototype, a single PMT measurement was taken using the electronic chain configuration shown in figure 3.15a. The energy spectra measured for both, the signal and background prototypes, are shown in Figure 5.4a. The difference between signal and background, Figure 5.4b, corresponds to the energy spectrum of tritium. The counting rate obtained for the three spectra is given in Table 5.1, where the tritium counts are obtained by subtracting the background from the signal.

Spectrum	Counts/second
Signal prototype	2.27 ± 0.06
Background prototype	2.06 ± 0.06
Tritium counts	0.21 ± 0.085

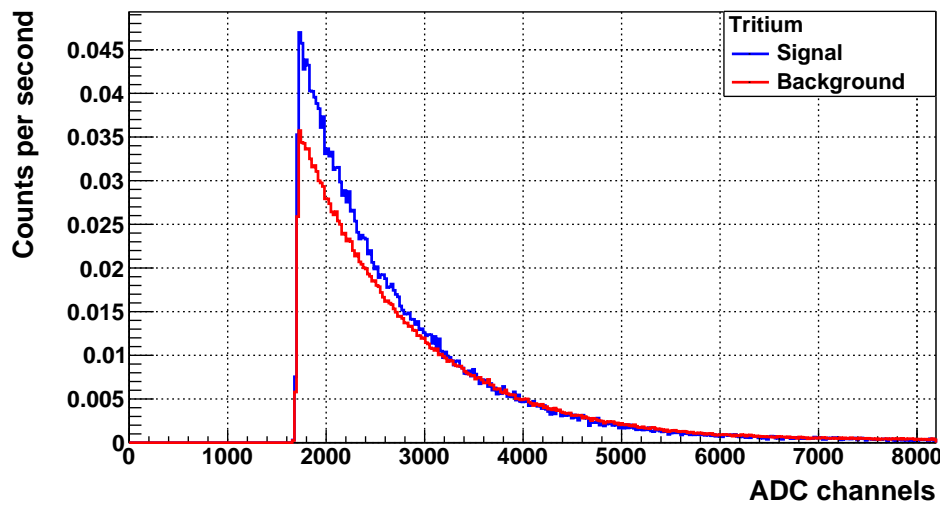
Table 5.1: Counting rate obtained with the TRITIUM-IFIC-0 prototype.

The tritium detection efficiency obtained for this prototype is $(2.11 \pm 0.85) \cdot 10^{-3} \frac{\text{cps}}{\text{kBq/L}}$, was calculated as the ratio of the tritium counting rate to the specific activity of the tritium liquid source.

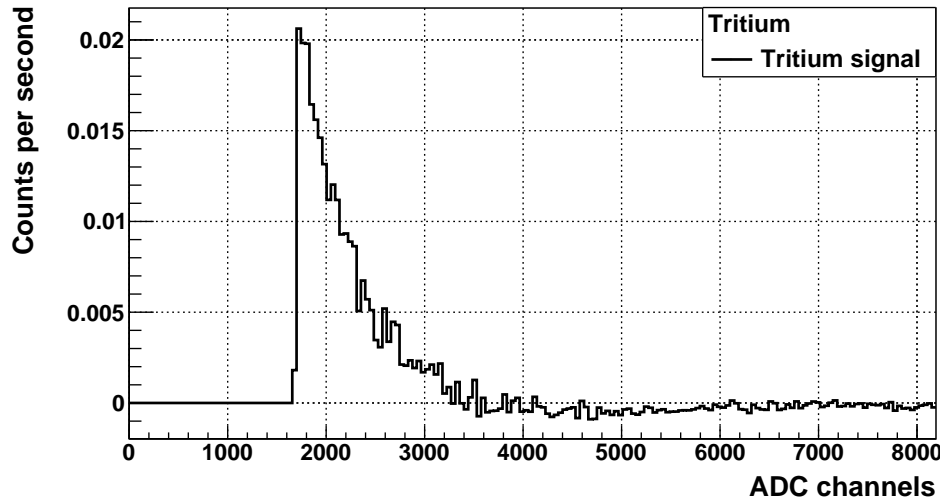
As we reported in section 2.1, the efficiency of scintillating detectors scales with the active area of the scintillator used. Therefore, to compare the efficiency with other detectors and with other prototypes developed in TRITIUM experiment, the specific efficiency of this prototype is calculated by normalizing to the scintillator area, which is

$$S = (9.59 \pm 3.88) \cdot 10^{-6} \frac{\text{cps}}{\text{kBq/L} \cdot \text{cm}^2}$$

As can be seen in Table 2.2, the specific efficiency is somewhat larger than that obtained by Muramatsu [Mur67], $3.13 \cdot 10^{-6} \frac{\text{cps}}{\text{kBq/L} \cdot \text{cm}^2}$, and similar than that obtained by Moghissi [Mog69], $< 10.6 \cdot 10^{-6} \frac{\text{cps}}{\text{kBq/L} \cdot \text{cm}^2}$, both detectors consisting of solid scintillators. These efficiencies are too low efficiencies to achieve the objective of being able to measure 100 Bq/L.



(a) .



(b)

Figure 5.4 – Energy spectra measured with TRITIUM-IFIC-0 prototype.
a) Signal and background energy spectra. b) Tritium energy spectrum.

5.1.2 TRITIUM-IFIC-1

The TRITIUM-IFIC-1 prototype was designed to overcome the problems and limitations found in TRITIUM-IFIC 0. The main improvements were:

1. The fiber bundle was arranged straight to optimize the photon collection efficiency of the fibers. In addition, a PTFE matrix was used to maintain a distance of 1 mm between fibers.
2. A special fiber cleaning method, described in section 4.1.1, was applied to the fibers to improve the quality of the interfaces between the fibers and tritiated water. This method produces a better wetting property of the fibers, which improves their photon collection efficiency.
3. A PTFE vessel was used to improve the collection of photons inside the prototype. Indeed, PTFE has a reflectivity close to 100% at the fiber scintillating wavelengths. Thus, the photons that escape from fibers and hit the vessel walls are reflected back to the scintillating fibers.

The TRITIUM-IFIC-1 prototype consists of 64 straight scintillating fibers of 20 cm length, arranged in an 8×8 PTFE squared matrix, as shown in Figure 5.5.

This structure is placed within a cylindrical PTFE vessel of 48 mm diameter and 200 mm length, shown in Figure 5.6.

The cleaning process described in section 4.1.1 was applied to the fibers to achieve a better tritiated water-fiber interface. A PVC piece was used to attach the photosensor to the prototype and prevent external light from being read out. A general view of this prototype is shown in Figure 5.7.

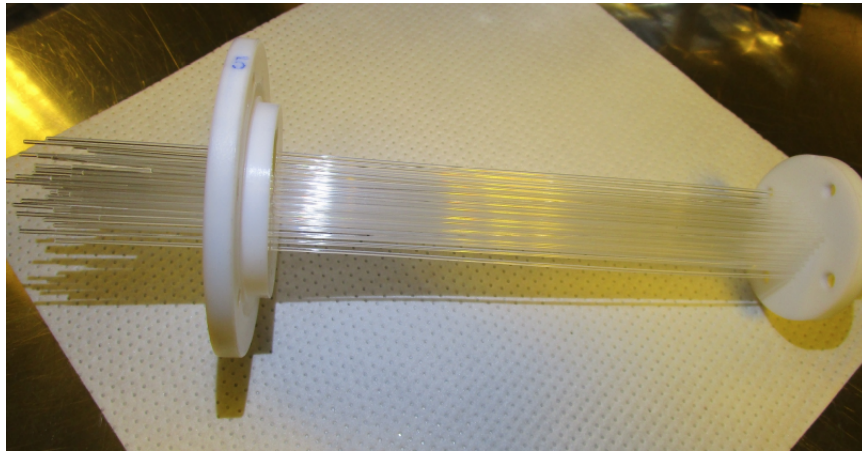


Figure 5.5 – PTFE structure used to arrange the fibers of TRITIUM-IFIC-1 prototype in a matrix of 8×8 .

The prototype was instrumented with a PMT model R8520-460, from Hamamatsu Photonics company [K.K19], coupled directly to the fiber bundle using optical grease [Cera]. The quantum efficiency of this PMT for the fiber scintillating wavelength is 28.66%. The voltage divider, shown in Figure 3.9, was used to polarize the PMT. The high voltage was -800 V. The signal from this PMT was acquired using the same electronics as for TRITIUM-IFIC-0 prototype, shown in Figure 3.15a. Unlike the first prototype, only one TRITIUM-IFIC-1 prototype was built. In a first measurement, this prototype was filled with pure water (118 mL, uncertainty of 0.05%) and several background measurements were taken over a week. Then, it was emptied and refilled with 118 mL (uncertainty of 0.05%) of a tritiated water source of the same specific activity as the one used for TRITIUM-IFIC-0 prototype, 99.696 kBq/L.

The measured signal and background energy spectra are shown in Figure 5.8a. The difference between both energy spectra corresponds to the tritium energy spectrum, shown in Figure 5.8b. The detection efficiency was obtained as in the previous section. The rates measured are given in Table 5.2, which are obtained from the integration of each spectrum.



(a)



(b)

Figure 5.6 – PTFE vessel of TRITIUM-IFIC-1 prototype.

Spectrum	Counts/second
Signal prototype	7.82 ± 0.11
Background prototype	3.99 ± 0.08
Tritium counts	3.83 ± 0.13

Table 5.2: Counting rate obtained with the TRITIUM-IFIC-1 prototype.



Figure 5.7 – A general view of TRITIUM-IFIC-1 prototype..

The tritium detection efficiency obtained for TRITIUM-IFIC-1 is $(3.84 \pm 0.16) \cdot 10^{-2} \frac{\text{cps}}{\text{kBq/L}}$. The specific efficiency obtained is

$$S = (9.56 \pm 0.40) \cdot 10^{-5} \frac{\text{cps}}{\text{kBq/L} \cdot \text{cm}^2}$$

which is a factor ten better than that of TRITIUM-IFIC-0. Furthermore, compared to the scintillating detectors developed in other experiments for tritium in water measurements, given in table 2.2, the efficiency of this prototype is very close to the best result, obtained by Singh [Sin85, MR00], $4.1 \cdot 10^{-2} \frac{\text{cps}}{\text{kBq/L}}$, and the specific efficiency, which is the most relevant parameter for comparison, is almost 5 times larger than that obtained by Hofstetter [Hof92b, Hof], $< 22.2 \cdot 10^{-6} \frac{\text{cps}}{\text{kBq/Lcm}^2}$.

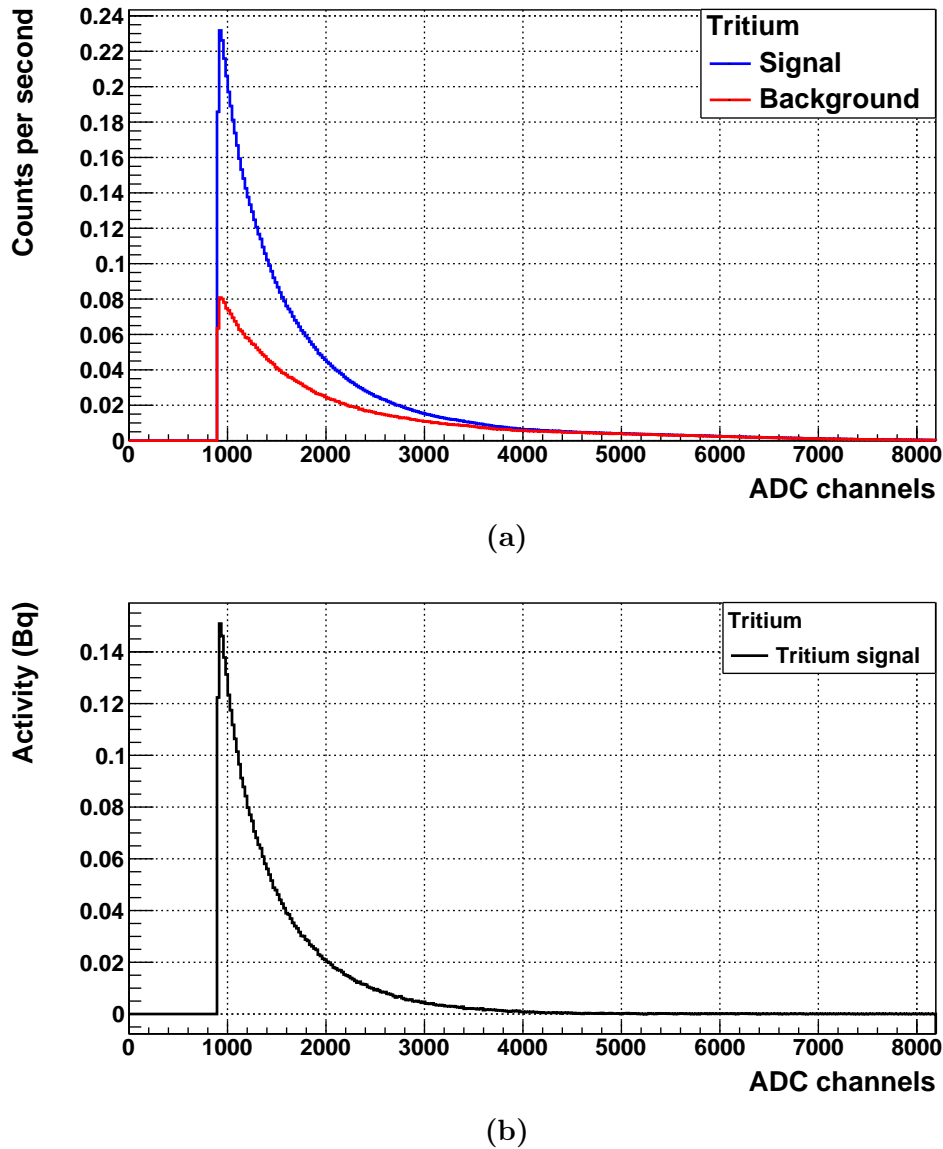


Figure 5.8 – Energy spectra measured with TRITIUM-IFIC-1 prototype.
a) Signal and background energy spectra. b) Tritium energy spectrum.

5.2 Latest TRITIUM Prototypes

This section reports on the prototypes so-called TRITIUM-Aveiro and TRITIUM-IFIC-2. In these prototypes, a different design was used compared to the previous ones (TRITIUM-IFIC-0 and TRITIUM-IFIC-1) so that they can safely allow the reading of a large number of fibers arranged in a straight mode with two photosensors operating in time coincidence. A better tritium detection efficiency was obtained in these prototypes through the use of a much larger number of scintillating fibers than in the preliminary prototypes, and the time-coincidences read out mode of the photosensors. Furthermore, the activity of the radioactive liquid source of tritium used to fill these prototypes was much lower than that used for the first prototypes, in order to measure their minimum detectable activity, MDA.

A similar design was used for the latest prototypes and subtle differences were included to check which ones optimize the tritium detection. The main differences between both prototypes are:

- The diameter of the scintillating fiber, 2 mm for TRITIUM-Aveiro and 1 mm for TRITIUM-IFIC 2. The use of a larger diameter facilitates the flow of water around the fibers, reducing problems related to surface tension and ensuring that the entire active volume of the fibers participates in tritium detection. In addition, a large radius increases the rigidity of the fiber, improving its robustness. However, this large radius decreases the signal-to-background ratio. The detector active volume for 2 mm fibers is smaller for the same volume than for 1 mm fibers and the internal volume of the fibers, unreachable by tritium decay electrons, is larger for 2 mm fibers, producing a higher background. As a result, a lower signal-to-background ratio is obtained.
- The scintillating fibers methods used to prepare the fibers before its use. The entire surface-conditioning method (section 4.1.1), consisting

in the cutting, polishing and cleaning methods, are applied in the scintillating fibers used in the TRITIUM-IFIC-2 prototype. However, only the cutting method is applied to the scintillating fibers used in the TRITIUM-Aveiro prototype.

- Different photosensors, PMTs for TRITIUM-Aveiro and SiPM arrays for TRITIUM-IFIC-2. Although most of the current development with TRITIUM-IFIC-2 was made with PMTs, the final purpose is to use SiPM arrays with which larger photodetection efficiencies than PMTs with a similar price can be achieved. In addition, no high voltage is needed, lowering the price of its supply voltage. However, it is necessary to read many more channels, which raises its price.
- A different electronic system is used to process and analyze the signals of the photosensors. The TRITIUM-Aveiro prototype uses a home-made PCB-based electronic system, which is cheaper than the commercial system used by TRITIUM-IFIC 2, PETsys. Nevertheless, the PETsys system is more stable and it is prepared for the scalability property of the detector, allowing read out much more SiPM arrays without any development. However, the PETsys system is more stable and meets the TRITIUM monitor scalability requirement, allowing more SiPM arrays to be read without any additional development.

The development and operation of these two prototypes aimed at defining the final design and construction options for the module used in the TRITIUM monitor.

5.2.1 TRITIUM-Aveiro

The third prototype built, TRITIUM-Aveiro, is a proposal of the final TRITIUM detector module. This prototype, which is shown in Figure 5.9, was

designed and built in the workshop of the University of Aveiro. This prototype consists of a PTFE vessel (marked as D in Figure 5.9), shown in Figure 5.10, with an internal cylindrical hole of 43 mm diameter and 18 cm length.

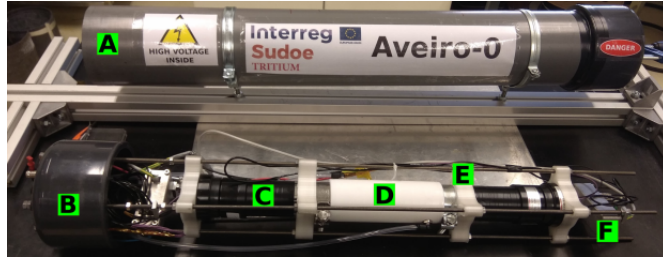


Figure 5.9 – TRITIUM-Aveiro prototype.



Figure 5.10 – PTFE structure and fiber bundle used in TRITIUM-Aveiro prototype.

This vessel contains 360 uncladded scintillating fibers of 180 mm length. The fibers are BCF-10 from Saint-Gobain company [Cer01], which have similar characteristics than the BCF-12 fibers, table 3.2, except the diameter, which is 2 mm. In order to quantify the importance of the fiber diameter, the measurements are compared with similar measurements performed with the TRITIUM-IFIC-2 prototype, which has a similar configuration but with 1 mm fibers.

The scintillator fibers are freely arranged within the PTFE vessel (without any PTFE matrix that fix them) and the number of fibers used is the maximum that allows water to flow around them. These fibers were cleaved with the device developed by TRITIUM, section 4.1.1, but they were neither polished nor cleaned because the automatic polishing machine was not yet developed and it was not feasible to polish 360 fibers by hand.

The PTFE vessel is totally closed and a water inlet/outlet were installed in it to allow a constant water flux through it. Two PMMA 10 mm thick windows, located at both ends of the fiber bundle, are used to read out the fibers. Two clamps are used to make a tight junction of the PTFE walls and the PMMA. PMMA was chosen for its optical properties, especially its transmission coefficient, which is larger than 95% at the scintillating fiber wavelength. Two PMTs (marked as C in Figure 5.9) are used to read out this prototype in time coincidence, the HV of which was set at -1500 V. Its quantum efficiency is 26%. These PMTs are attached to both fiber bundle ends by two pieces (marked as E in Figure 5.9) built with a 3D printer and they are optically coupled to the PMMA windows through optical grease [Cera]. The PMTs used are R2154-02 2" from Hamamatsu [K.K10], that have gain and efficiency quite similar to the PMTs used in the other TRITIUM prototypes.

This prototype and its electronics (marked as F in Figure 5.9), were arranged in a structure, shown in Figure 5.9, composed of several clamps and four stainless-steel screws, locked to an external PVC structure, marked as A and B in Figure 5.9, which protects the prototype from physical damage and provides a light-tight operation environment. This PVC structure is equipped with the necessary feed-through connectors.

Only one prototype was built, which was designed to be installed in the Arrocampo dam. The electronics, which is detailed in appendix D, is based on several PCBs that was specially designed to process and analyze the signals of this prototype. Two interfaces were developed to control the

PMT power supply and to control the data adquisition (thresholds, results, etc).

Measurements taken in the laboratories (DRIM and LARUEX laboratories) were used to characterize the detector. For this task, the prototype was at first filled with pure water, which was used to measure the background of the detector, and next, with a radioactive liquid tritium solution with an activity of 30 kBq/L, which was used to measure the efficiency and the low detection level of the prototype. The volume of pure water and tritium solution used in TRITIUM-Aveiro prototype was 58 mL.

First, a measurement with a passive shield was performed in the DRIM laboratory to quantify the attenuation of the background by lead. These measurements, shown in Figure 5.11, were carried out in three different situations. The first, region A, was performed without shielding, the second, region B, with a lead shield of 2.5 mm thickness and the third, region C, with two lead foil layers. As can be seen, in the region A, the average rate of 2.5 days is $3.5 \cdot 10^3$ counts/min. In the region B, a background suppression by a factor of 2 was observed, measuring an average rate of $1.6 \cdot 10^3$ counts/min. In the region C, an average rate of $0.9 \cdot 10^3$ counts/min was obtained, supressing the background by about a factor of 4.

Then, the prototype was installed in the LARUEX laboratory, at the University of Extremadura, in order to work with a tritiated water. The background of the prototype was measured during 4 days with the prototype filled with pure water and covered with lead bricks of 5 cm thickness. The time adquisition of each measurement was 1 minut. The data, fitted to a Gaussian function, are shown in Figure 5.12a. An average rate of 540 counts/min with a standard deviation of 22.61 counts/min was obtained. To calculate the Minimum Detectable Activity (MDA), the detection limit concepts developed by Lloyd A. Currie [Kno10] were applied, according to which the minimum net counts with a probability of a false-negative less

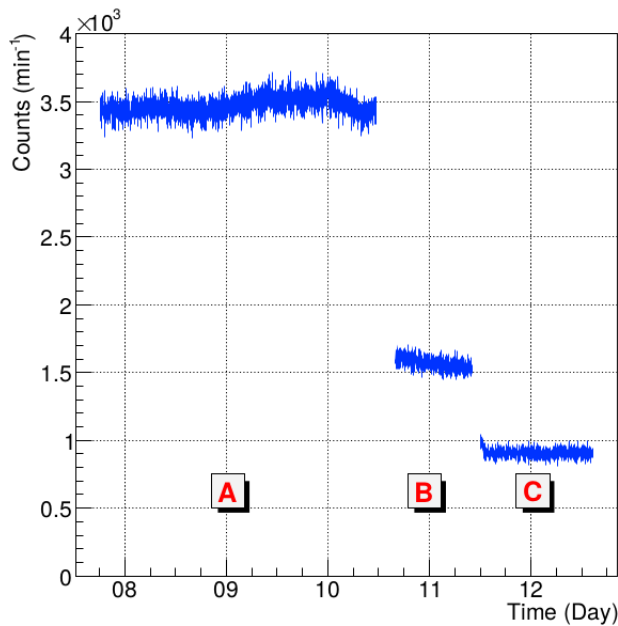


Figure 5.11 – Measurement of the background with TRITIUM-Aveiro prototype shielded with different layers of lead, A) without shielding, B) with a lead shield of 2.5 mm thickness and C) with two lead shields of 2.5 mm thickness each one [CA].

than a 5%, N_D , is given by,

$$N_D = 4.65 \cdot \sigma_{Nb} + 2.71 = 108 \text{ counts/min} \quad (5.1)$$

which corresponds to a critical level of $L_C = 2.33 \cdot \sigma_{Nb} = 53 \text{ counts/min}$ (minimum net currents with a probability of a false-positive less than 5%).

L_C and N_D refer to the net rate after background subtraction. Therefore, L'_C and N'_D , referred to the detector signal (before background subtraction), are 593 and 648 counts/min respectively.

To find the MDA, tritiated water was slowly added so that the tritium water activity increased continuously up to reach the N'_D value. An

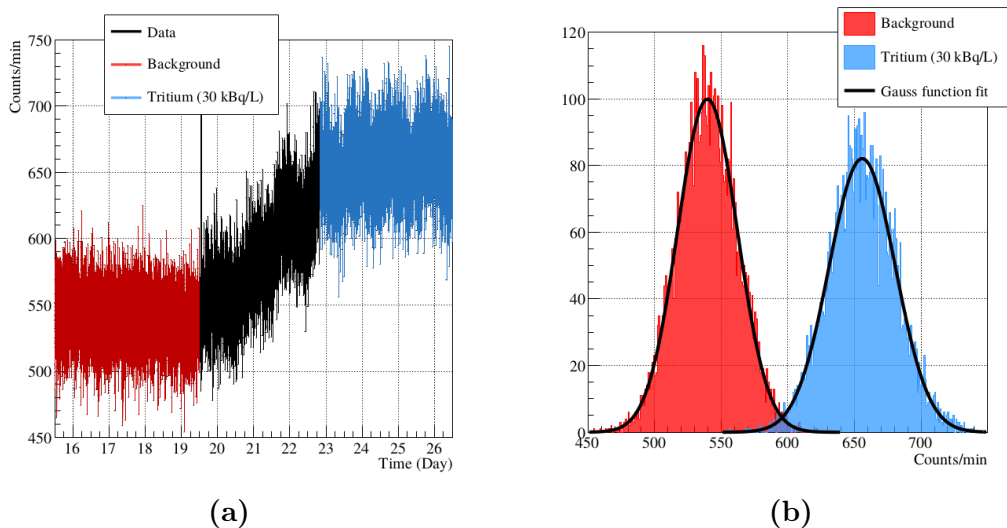


Figure 5.12 – Measurements of the background and tritium liquid source (with an activity of 29.8 kBq/L) performed with the TRITIUM-Aveiro prototype and integrated during a minute [CA]. a) Counts per minut measured as a function of time. b) Distribution of the acquired data.

average of 656 ± 0.43 counts/min was obtained, the activity of which was MDA=29.8 kBq/L, obtained with a Quantulus liquid scintillator system.

The tritium detection efficiency was calculated from the ratio of the net tritium rate measured, 1.93 ± 0.58 counts/sec, and the activity of the tritium source used, 29.8 kBq/L. The efficiency obtained is $(6.49 \pm 1.94) \cdot 10^{-2} \frac{\text{cps}}{\text{kBq/L}}$. and the specific efficiency is

$$S = (1.59 \pm 0.48) \cdot 10^{-5} \frac{\text{cps}}{\text{kBq/L} \cdot \text{cm}^2}$$

Comparing to the specific efficiency obtained with scintillating detectors, Table 2.2, the specific efficiency of the TRITIUM-Aveiro prototype is close the largest value, obtained by Hofstetter [Hof92b, Hof], $< 2.22 \frac{\text{cps}}{\text{kBq/L} \cdot \text{cm}^2}$. However this prototype has a lower specific efficiency than TRITIUM-IFIC-1. A possible reason is that the fibers in this prototype are not polished,

neither cleaned.

The efficiency uncertainties obtained for this prototype are larger than those obtained in the first TRITIUM prototypes since the measurement time used is shorted (1 minute) than the time used for the previous prototypes (several hours). Because of that, longer measurements are studied to quantify the reduction of the MDA of this prototype, which depends directly on the background uncertainty, equation 5.1. The data for an integrated time of 60 minutes is shown in Figure 5.13. The mean value and the uncertainty of the measured background data are $3.186 \cdot 10^4$ and 228 counts per hour respectively. Values of $L_C = 530$ and $N_D = 1043$ counts per hour are obtained from the equation 5.1. Assuming linearity between the measured counts for the background and the tritiated water, the N'_D obtained for this case, $3.872 \cdot 10^4$ counts per hour, corresponds to a MDA of 4.53 kBq/L. A daily oscillation is clearly observed in the Figure 5.13, indicating that the measurements are affected by external light. This oscillation begins on the 19th day, when the water closed circuit pump was installed, so it is likely that a light leak was introduced in the system.

This prototype was finally installed in the Arrocampo dam to test its functionality and to begin with the tritium level monitoring the measurements of which are reported in section 5.3.

5.2.2 TRITIUM-IFIC-2

The last prototype developed for TRITIUM was TRITIUM-IFIC-2, marked as A in Figure 5.14. This prototype, built in the IFIC workshop, consists of a cylindrical PTFE vessel, shown in Figure 5.15, with a similar shape to that of Aveiro. The internal length and diameter of the PTFE vessel were 210 mm and 36 mm respectively. This prototype contains 800 uncladded BCF-12 scintillating fibers of 200 mm length and 1 mm diameter. This number is larger than that in Aveiro's prototype and is contained in a smaller volume.

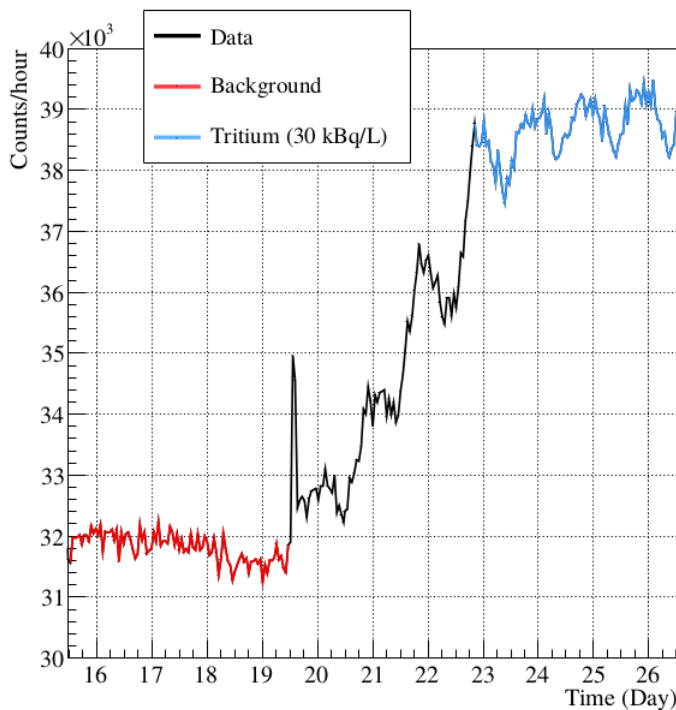


Figure 5.13 – Measurements of the background and tritium liquid source (with an activity of 29.8 kBq/L) performed with the TRITIUM-Aveiro prototype and integrated during one hour [CA].

The fibers used were cleaved, polished and cleaned with the conditioning processes described in section 4.1. These scintillating fibers were freely and tightly arranged while standing straight, allowing water to flow among them. Two PMMA windows, located at the ends of the fiber bundle, allowed to read out the scintillation light in a similar way as in the Aveiro's prototype.

A 5 mm width PMMA optical windows is sufficient to guarantee tightness, since the detector works at very low water pressure. Two clamps allow to keep the water tightness of the prototype, similar to the TRITIUM-Aveiro prototype. PMMA was chosen for its optical properties, especially its transmission coefficient, shown in Figure 5.16, which was measured for visible light at ICMOL laboratories. This transmission coefficient

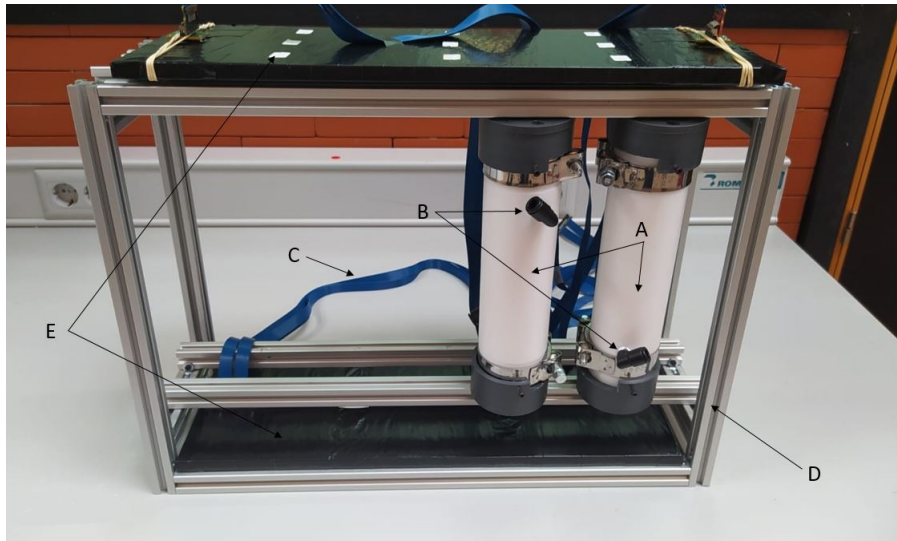


Figure 5.14 – TRITIUM-IFIC-2 prototype (A) and active veto (E) within the metallic structure (D).

is approximately 95% for the working wavelength (435 nm). Slightly better transmission coefficients can be achieved with other materials such as quartz or sapphire but they are much more expensive.

A water inlet/outlet was implemented in the PTFE vessel, B in Figure 5.15, to allow a constant water flux, as in the TRITIUM-Aveiro prototype.

In the first laboratory measurements, two PMTs model Hamamatsu R8520-460 [K.K19] were used to compare the results to those of the previous prototypes. However, measurements of the TRITIUM-IFIC-2 prototype with SiPM arrays controlled by PETsys were also performed, as this is the final readout option for this prototype. PETsys has a graphical user interface, shown in Figure 5.17. It allows the remote control of all the different input and output options such as the supply voltage for the SiPM arrays, thresholds, etc., via computer terminal.



(a)



(b)

Figure 5.15 – a) TRITIUM-IFIC-2 PTFE vessel. b) TRITIUM-IFIC-2 PTFE vessel with PVC caps in which a groove is made for the cable connection to the SiPM.

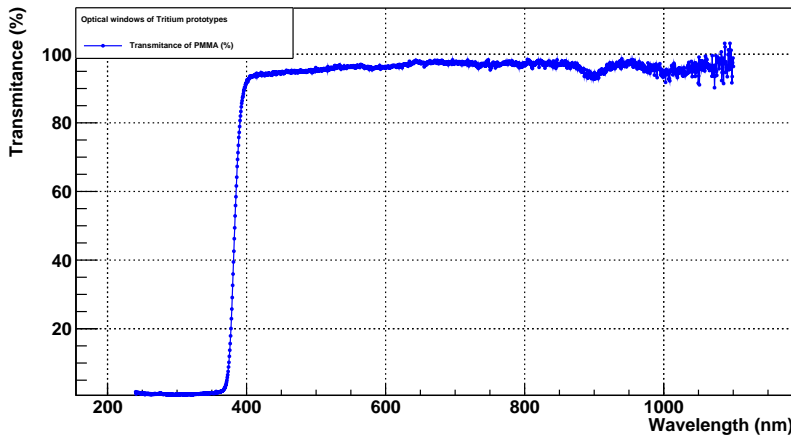


Figure 5.16 – Light transmission spectrum of a 5 mm thick PMMA plate, measured at ICMOL laboratory.

Two PVC caps, located at both ends of the prototype were used to provide a light-tight environment to the SiPM arrays. An aluminum structure was designed and built to house up to 10 TRITIUM-IFIC-2 modules and two cosmic vetos, marked as D in Figure 5.14.

In Arrocampo site, the available space inside the lead shield box may accommodate up to 5 structures. This means that the final TRITIUM moitor may accommodate up to 50 TRITIUM-IFIC-2 modules and 5 different cosmic vetos.

Two identical TRITIUM-IFIC-2 prototypes were built, as for the TRITIUM-IFIC-0 prototype. One of them was filled with pure water and used to measure the background and the other was filled with a radioactive liquid source of tritium and employed to measure the signal. The water volume in both cases was 82 mL (uncertainty of 0.05%). The activity of the tritium source used for this prototype was 10 kBq/L (uncertainty of 2.24%), which was prepared by diluting a sample of tritiated water in pure water. The signal and background energy spectra are shown in Figure 5.18a. The

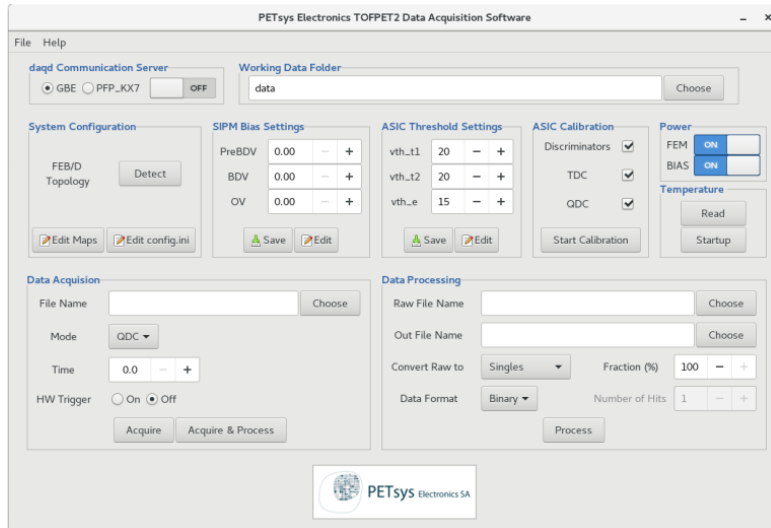


Figure 5.17 – Graphical User Interface (GUI) of PETsys.

energy spectrum of tritium, Figure 5.18b, was obtained by subtracting the background to the signal. The rates obtained from these three spectra are given in Table 5.3.

Spectrum	Counts/second
Signal prototype	19.05 ± 0.18
Background prototype	11.54 ± 0.14
Tritium counts	7.11 ± 0.23

Table 5.3: Counting rates measured by TRITIUM-IFIC-2 prototype.

The tritium detection efficiency obtained for this prototype is $(7.11 \pm 0.28) \cdot 10^{-1} \frac{\text{cps}}{\text{kBq/L}}$. This efficiency is larger than those reported in the literature, Table 2.2. This is an expected result since the active area of this prototype is the largest. To remove the active area effect, the specific efficiency was measured, obtaining a value of

$$S = (1.59 \pm 0.48) \cdot 10^{-5} \frac{\text{cps}}{\text{kBq/L} \cdot \text{cm}^2}$$

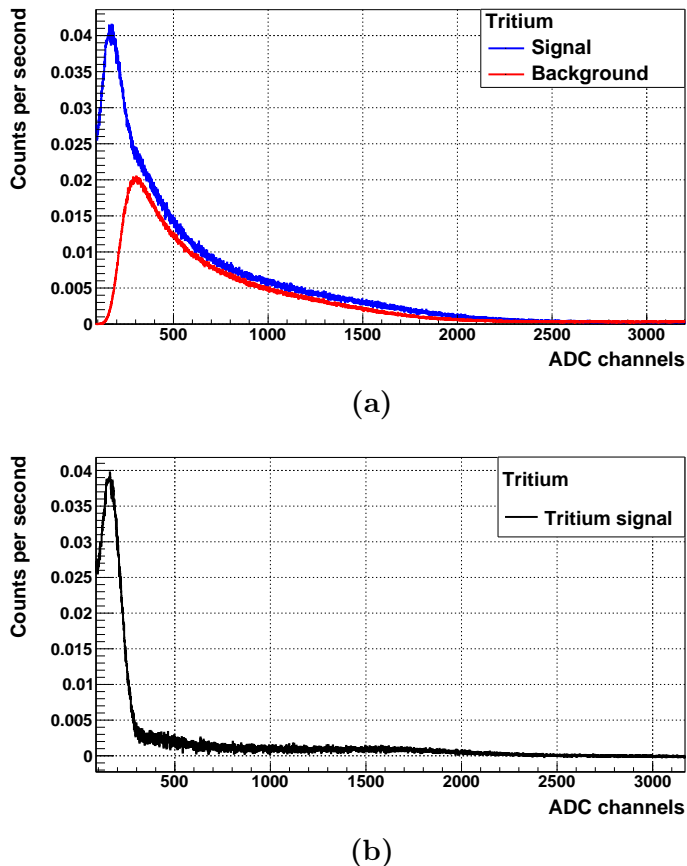


Figure 5.18 – Energy spectra measured with TRITIUM-IFIC-2 prototype.
a) Signal and background energy spectra. b) Tritium energy spectrum.

Again, it can be observed that this prototype has the largest specific efficiency reported for tritium detection, demonstrating that its design the best design currently developed for detection of low activities of tritium in water.

The energy spectrum is given in ADC channels, since an energy calibration for a plastic scintillator is not accurate due to the large uncertainty in the number of photons produced per energy event. Nevertheless, a detector calibration in units of photons detected per event can be obtained from the single-photon distribution of the PMTs. The PMTs used to read this prototype was decoupled from the prototype and covered with a special black blanket to screen the PMT from external photons. The distribution measured and fitted to a Gaussian function is shown in Figure 5.19a. As can be seen, the mean and uncertainty of the single photon signal are around 172 and 66 ADC channels, respectively, for one of the PMT and 173 and 57 ADC channels, respectively, for the other. The tritium signal given in number of photons detected per event, shown in Figure 5.19b, is obtained as the ratio of the energy spectrum to the single-photon distribution mean. A maximum of 15 photons are measured per tritium event, which is in agreement with the results of the simulations shown in Chapter 6.

A monitoring of both prototypes, signal and background, were carried out during several months. The rates measured are shown in Figure 5.20. No quenching of the signal was observed, which indicates the detector efficiency remained stable, within statistical and systematic uncertainties, over up to 6 months.

Finally, the Minimum Detectable Activity (MDA) was calculated. To do so, fourteen different measurements of the background were done using two different integration times, 10 min and 60 min. The mean value and standard deviation of these measurements are shown in the Table 5.4. The minimum net counts with a probability of a false-negative less than 5%, N_D , and with a probability of a false-positive less than 5%, L_C , were calculated by applying the Currie's law, equation 5.1 and they are included

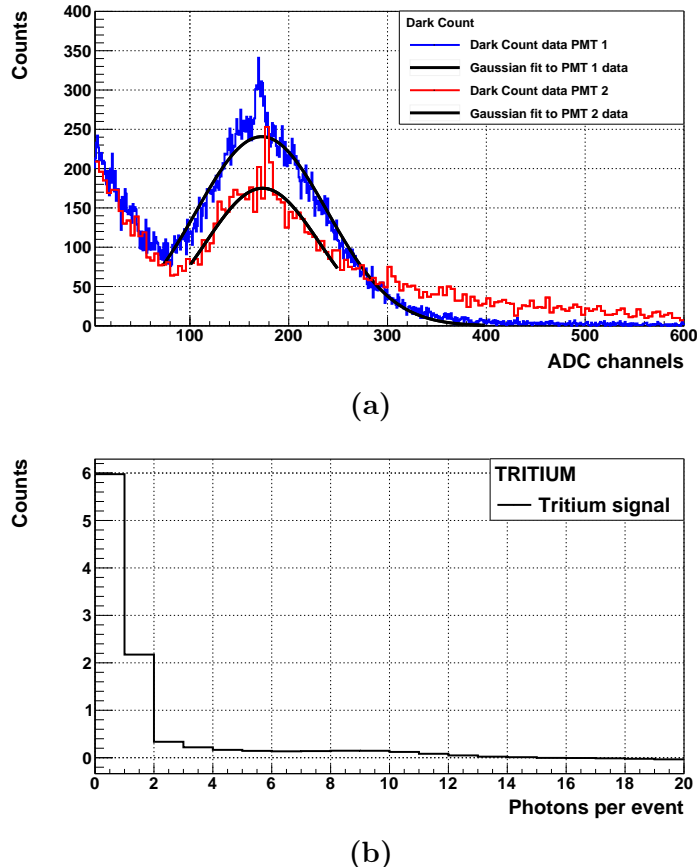


Figure 5.19 – a) Single photon distribution measured with TRITIUM-IFIC-2 prototype. b) Tritium energy spectrum measured with TRITIUM-IFIC-2 prototype in photons detected per event.

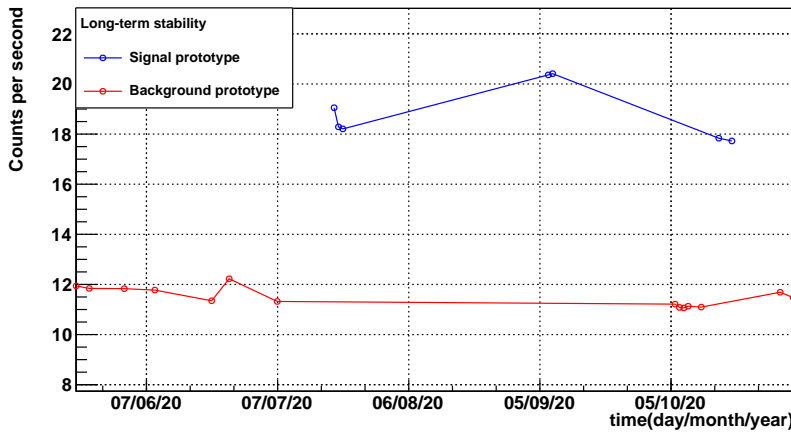


Figure 5.20 – Signal and background rates for a long time measurement.

in Table 5.4.

Int. time (min.)	Mean V.	Std. Dev.	L_C	N_D
10	5635	82	191	384
60	33969	158	368	737

Table 5.4: Mean value and standard deviation of the counts of fourteen background measurements. Minimum net counts obtained by applying the Currie's Law, L_C and N_D .

Therefore, N'_D , which is the counts referred to the detector signal (before background subtraction), are 6019 and 34706 counts for an integration time of 10 min and 60 min respectively. Then, the MDA of tritium can be obtained from the N'_D values by associating the mean value of the background counts to a zero tritium activity and the mean value of the signal counts to a tritium activity of 10 Bq/L, assuming counts scale linearly with the activity. This results in a MDA of 677 Bq/L and 218 Bq/L for the integration time of 10 min and 60 min respectively. It has to be taken into account that, although this MDA is not enough to achieve the TRITIUM project goal of 100 Bq/L, it is reached using only one TRITIUM-IFIC-2

module. The TRITIUM detector will contain several modules and it is expected that the MDA be reduced by a factor of $\sqrt{\text{number of prototypes}}$, according to the equation 5.1.

As the sensitivity of the TRITIUM monitor scales with the number of TRITIUM modules used, the results obtained with the TRITIUM monitor should improve those results by a factor of \sqrt{N} , where N is the number of modules used.

5.3 Results from Measurements at Arrocampo Dam

This section reports the measurements obtained with the TRITIUM-Aveiro prototype in the Arrocampo dam. This prototype was installed and working there for more than four months, from March 27, 2019 to August 18, 2019, taking background measurements. The data acquired during this time are plotted in Figure 5.21, for a measurement time of 60 minutes.

The data show good stability during the measuring period. An average rate of 9.31 counts per second was obtained. A narrow peak is observed on May 2, 2019, caused by an opening of the roof of the lead shield to access the prototype. In the inset of the figure, the data are magnified for a better visualization. The MDA measured in Arrocampo dam for 60 minute integration time is 6 times larger than that obtained in the laboratory measurements, section 5.2.1. This may be due to the electric noise introduced by the pumps of the water purification system and the instability observed in the electronic boards.

The cosmic veto currently under development is planned to be installed and used in anti-coincidence along with two additional prototypes.

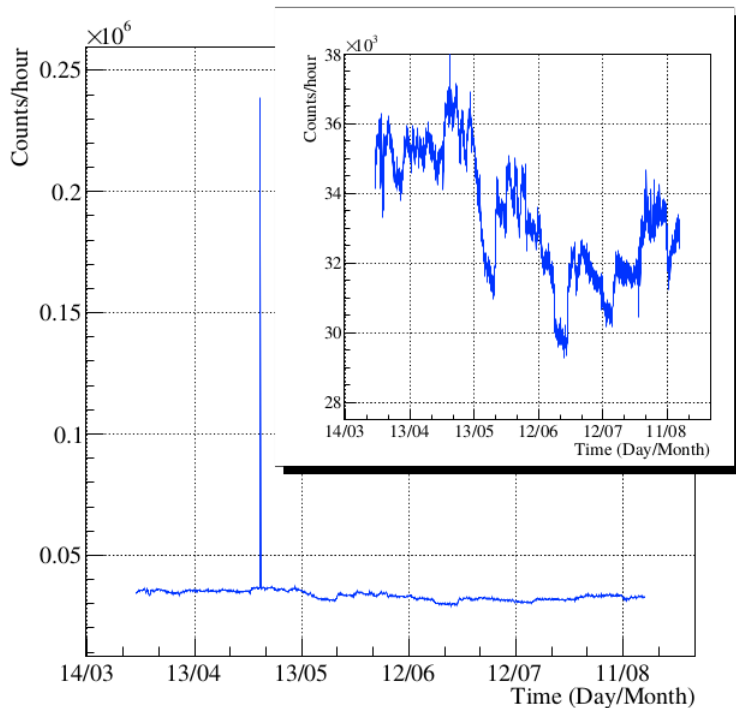


Figure 5.21 – Background measured with the TRITIUM-Aveiro prototype during its installation in Arrocampo dam [CA].

Furthermore, three TRITIUM-IFIC-2 prototypes and a cosmic veto, described above, are also planned to be installed in Arrocampo dam as soon as possible.

5.4 Modular TRITIUM Detector for In-Situ Tritium Monitoring

This section presents the final TRITIUM monitor, a schematic design of which is shown in Figure 5.22. It consists of a number of TRITIUM modules read out in parallel, the design of each one will include the characteristics (differences between the latest prototypes) with which the best results has been obtained. These modules are shielded from environmental radioactivity by three different techniques:

1. An external lead shield, which is used to stop the environmental radioactivity and soft cosmic rays (particles with energies below 200 MeV).
2. Several active vetos, which are placed below and above the TRITIUM modules. These active vetos are read out in anticoincidence to suppress high energy event background, mainly cosmic ray particles with energies above 200 MeV.
3. A water purification system, which is used to eliminate the radioactive elements present in the water samples measured by the TRITIUM monitor.

The water purification system, the lead shield and a TRITIUM-Aveiro prototype are installed and currently in operation at the Arrocampo dam. This entire system is employed to successfully monitor the tritium levels in Arrocampo dam during several months. Furthermore, two additional TRITIUM-Aveiro prototypes and four active vetos are currently under construction and will be measured in parallel with this prototype.

The electronics of the TRITIUM-Aveiro prototype, based on a RaspberryPi, cannot be used for multiple modules due to counting limitations and this must be replaced by an FPGA-based counter board.

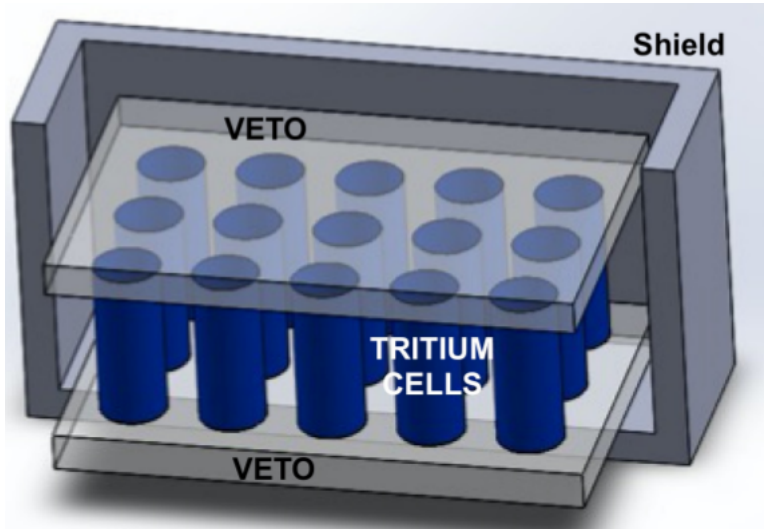


Figure 5.22 – A schematic design of the TRITIUM detector.

Three TRITIUM-IFIC-2 prototypes and two active veto (on up and other below the modules) are already built and they will be installed as soon as possible. In this first installation, lateral cosmic vetos for the TRITIUM-IFIC-2 modules are not contemplated since its influence is expected to be small ($\propto \cos^2(\theta)$), but if necessary they can be included in the future.

One of the most important aspects of the TRITIUM monitor is its modular design, which allows scalability to reach the required sensitivity, 100 Bq/L. It means that if this target sensitivity is not achieved with the three modules to be installed, it can be obtained by installing additional modules.

The only scalability restriction is the available space, which is set by the lead shield and the cabin in which the setup is installed. In the currently available space, five different structures as the one shown in Figure 5.23 can be placed, each one containing 10 modules and two active veto. If the 50 TRITIUM modules are installed, the sensitivity of the TRITIUM

monitor could be improved by a factor of around 7 ($\sqrt{50}$) with respect to the sensitivity of a single module.

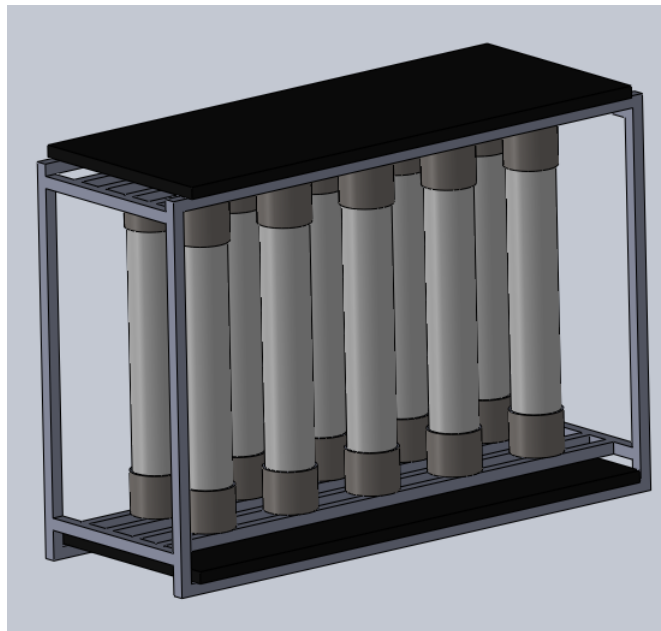


Figure 5.23 – A TRITIUM monitor design based on the TRITIUM-IFIC-2 prototype.

Chapter 6

Simulations

This chapter describes the Monte Carlo simulations performed in the TRITIUM experiment to optimize the design of the TRITIUM detector, understand its behaviour and investigate its limitations. These simulations are divided into two different sections. The first section contains the results of several simulations used to improve the design of the TRITIUM detector while the second exhibits the results obtained for the simulation of a full TRITIUM monitor based on an active veto read in anticoincidence with several TRITIUM-IFIC-2 prototypes. Furthermore, several tests were carried out to verify the correct simulation of the different steps such as the simulated tritium source, the energy deposition in the fibers and the production of photons in them. The simulation environment employed was Geant4 [Col21a, Ago03].

6.1 Geant4 Environment

Geant4 is a software toolkit for the simulation of the passage of particles through matter developed at CERN, based on object-oriented technology

implemented in the C ++ programming language. Geant4 includes the definition of all the different aspects of the simulation process such as detector geometry, materials used, particles of interest, physical processes that handle particle and matter interactions, response of sensitive detectors, generation, storage and analysis of event data and visualization.

Geant4 simulates particle-by-particle physics. This means that the tritium events are initialized one by one, generating energy, moment, position, etc. The propagation of each tritium decay electron and its interaction with the scintillator is simulated, and optical photons are created. The propagation of these optical photons are also simulated one by one and the simulation ends when all the created optical photons have been absorbed by either the sensitive detector or other materials present in the simulation.

The physics list used for these simulations is Livermore, G4EmLivermorePhysics, which is specially designed to work with low energy particles. This list includes the most important electromagnetic process at low energies such as bremsstrahlung, Coulomb scattering, atomic de-excitation (fluorescence) and other related effects.

The materials included in these simulations were water (to simulate the tritiated water source), PMMA (to simulate the optical windows of the prototype), polystyrene (to simulate the core of scintillating fibers), PTFE (to simulate the prototype vessel), silicone (to simulate the optical grease), silicate glass (to simulate the optical windows of the PMTs) and bialkali (to simulate the photocathode material of the PMT). The properties of water, PTFE and polystyrene were taken from the Geant4 NIST database and the other materials were built by specifying their atomic composition. The following optical properties were added to these materials:

1. The refraction index and light attenuation coefficient were added to water, obtained from ref. [Bui94]. A spectrum of tritium decay elec-

trons, uniformly distributed in the volume, was added to water to simulate tritiated water. The tritium decay spectrum data were taken from ref. [Mer15].

2. The spectra of refractive index, light attenuation and photon emission, obtained from the data sheet of scintillating fibers, [Cer05], were added to the polystyrene. The scintillation yield and the decay time coefficient, also obtained from their data sheet, were included.
3. The quantum efficiency spectrum was added to the photocathode material of the PMTs, taken from their data sheet [K.K19]. A refraction index of 1.46 was used for optical grease, also obtained from its data sheet [Cera].
4. Finally, the optical data for the remaining materials, PMMA windows, PTFE and silicate glass, were taken from ref. [Arg11].

The simulations shown in this thesis are focused on the Tritium-IFIC 2 prototype since these were the simulations I was primarily working on, but similar simulations were performed for the Tritium-Aveiro prototype, which are also summarized.

6.2 Simulations to Optimize the TRITIUM Monitor Design

Several simulations were performed during the design of the TRITIUM detector, which were used to quantify the influence of some modifications and to choose those that optimize the tritium detection. The characteristics studied are the diameter and length of the scintillating fibers. As the tritium electrons have a very short mean free path, the shape of the simulated tritium source was also studied to reduce computing time.

6.2.1 The Tritiated Water Source

First of all, the shape of the simulated tritiated water source was optimized. The mean free path of tritium electrons in water is only around $5 \mu\text{m}$, so most electrons do not reach the scintillating fibers. These electrons do not provide useful information and only consume computing resources. To optimize the simulation, the dimensions of the simulated tritium source were set to minimize the number of tritium events that do not reach the scintillating fibers.

Before that, the energy distribution of the simulated tritium events, shown in figure 6.1a, was compared with the input taken from ref. [Mer15], obtaining a good agreement with it. In addition, the distribution of the initial energy of tritium electrons capable of penetrating a fiber and depositing energy was compared to the initial energy distribution of all simulated tritium events, Figure 6.1b. A shift of the peak to high energies is observed, obtaining a peak centred at 10 keV. This shift occurs because the lower energy tritium decay electrons do not have enough energy to reach and penetrate the fibers and are not detected.

Regarding the optimization of the tritium source shape, a scintillating fiber 20 cm long and 2 mm in diameter and a surrounding tritiated water source of the same length and 0.5 mm thick, 100 times greater than the mean free path of tritium electrons, were simulated to assess the tritium source. The dimensions of the fiber are not important in this study since only the energy deposition of tritium electrons in the fiber was simulated, excluding optical processes. The goal of this simulation was to find the radial thickness of the simulated tritium source beyond which no significant amount of tritium decay electrons are detected. In Figure 6.2a, a transversal cut of the 2 mm scintillating fiber, the simulated 0.5 mm thick tritium source around the fiber, and the position where happen the tritium decays that deposit energy in the scintillating fiber are shown. Furthermore, the distribution of the radial distance between the position where tritium de-

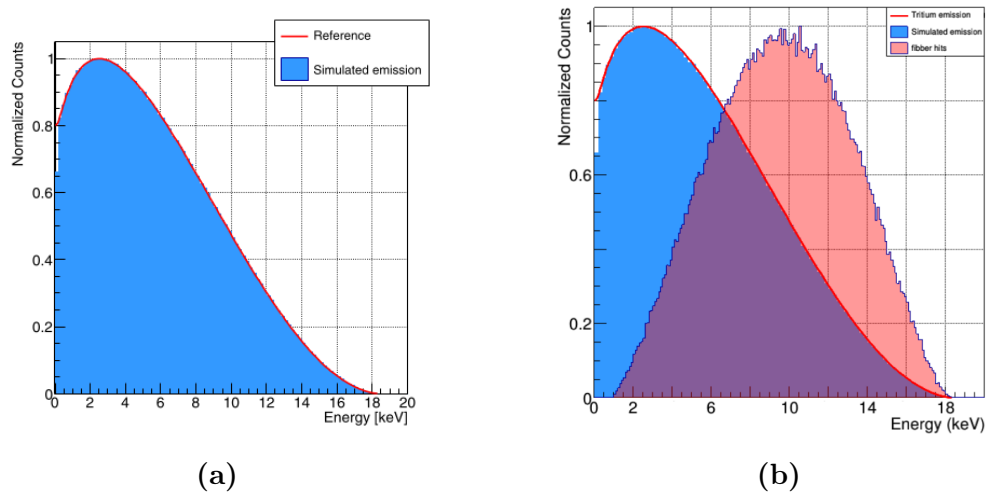


Figure 6.1 – Energy distribution of a) simulated tritium decays b) Initial energy of tritium decays that reach the scintillating fibers (red histogram) compared the all simulated tritium events (blue histogram) [Aze20].

cays take place and the surface of the scintillating fiber is shown in figure 6.2b. As can be seen in the Figure 6.2, most of the tritium decays that are detected occur close to the scintillating fiber. A zoom of low energy events is shown in the inset box of the Figure 6.2b for better viewing. The chosen thickness of the simulated tritium source was $5 \mu\text{m}$ since the 99.4% of the events that deposit energy in fibers are produced at least of this distance.

6.2.2 Energy Deposition and Light Output of Scintillating Fibers

The scintillation yield provided by the manufacturer, 8000 photon/MeV, is only valid for minimum ionizing particles (MIP). As tritium electron energies do not correspond to MIP particles, the output light generated by the scintillating fibers was studied. For this task, the energy deposition of tritium electrons in scintillating fibers and their subsequent emission of

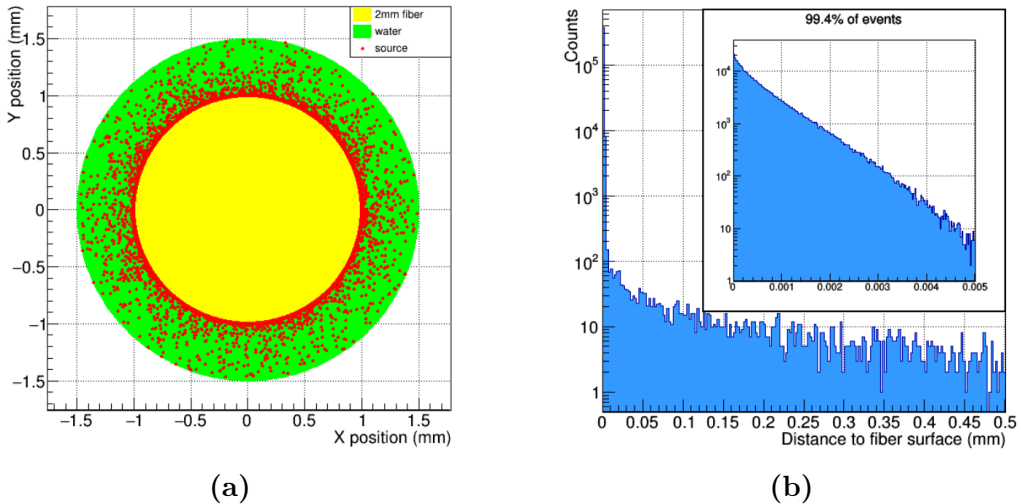


Figure 6.2 – a) Transversal cut of simulated scintillating fiber (yellow) and tritium source (green) with various tritium decays (red dots) b) Distribution of the radial distance between the position where the tritium decay takes place and the surface of the scintillating fiber [Aze20].

scintillation photons was included in to the simulation.

When particles that are not MIP are detected in plastic scintillators, a quenching effect for the output light per unit of path length, $\frac{dL}{dx}$, with respect to the energy deposited per unit of path length, $\frac{dE}{dx}$, happens, that can be parametrized by the Birks coefficient[Bir51].

$$\frac{dL}{dx} = S \frac{\frac{dE}{dx}}{1 + k_B \frac{dE}{dx}} \quad (6.1)$$

where S is the scintillation yield, provided by the manufacturer. The value for the Birks coefficient of $k_B = 0.126$ mm/MeV, typically used for scintillators based on polystyrene [Lev11], was taken. In this section, the significance of this quenching effect and how it affects the tritium detection is discussed.

A study of the energy deposition of tritium electrons on scintillating fibers was carried out. In Figure 6.3 the initial energy of simulated tritium electrons that reach the scintillating fibers is compared to the energy deposited in scintillating fibers. A shift to lower energies is observed, caused by the loss of energy of tritium electrons in water. A cut about 1 keV is observed in both energy distributions, produced by the default energy threshold of 990 eV in the G4EmLivermorePhysics physics list.

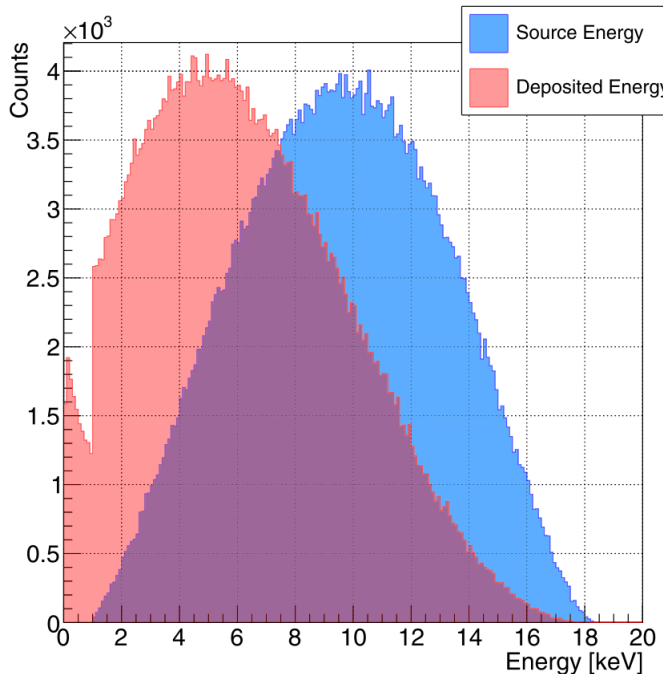


Figure 6.3 – Distribution of the initial energy of tritium events that reach the scintillating fibers, blue histogram, and the energy deposited, red histogram [Aze20].

Figure 6.4 shows two distributions of number of photons produced in scintillating fibers by tritium events, one in which the quenching effect is not considered ($k_B = 0$) and the other with the Birks coefficient set to $k_B = 0.126 \text{ mm/MeV}$.

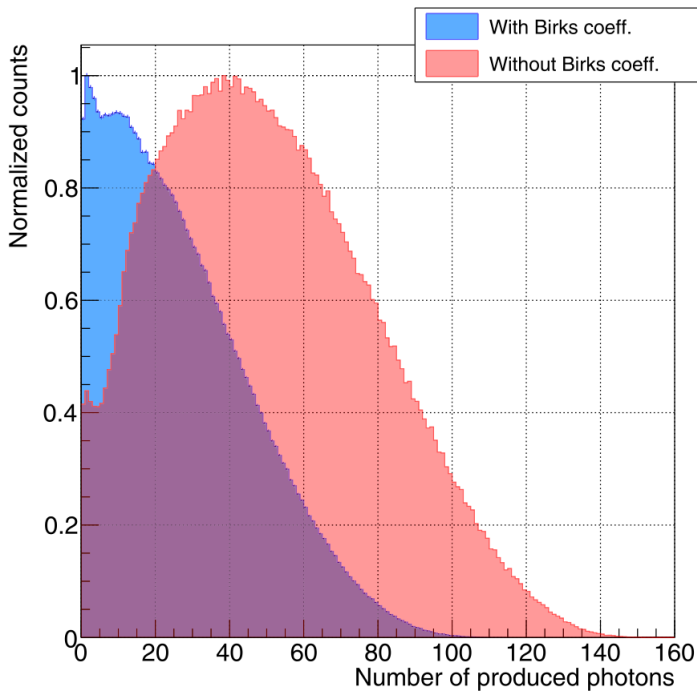


Figure 6.4 – Energy distribution of photons produced in the scintillating fiber, without Birks coefficient (red histogram) and with Birks coefficient of $k_B = 0.126 \text{ mm/MeV}$ (blue histogram)[Aze20].

A distribution with a peak of around 40 photons per tritium event and a maximum of around 150 photons is obtained when the quenching effect is not considered. A significant reduction of the output light is observed when the Birks coefficient is taken into account, producing a distribution peaked at around 10 photons and a maximum of 110 photons. The quenching effect is also observed in Figure 6.5, in which the number of produced photons as a function of the energy deposited in the fiber is displayed in a bidimensional plot. In this figure, in addition to a reduction of the number of photons produced per unit of energy deposited, a broader distribution is obtained when the Birks coefficient is considered, indicating an increase of the fluctuations of energy deposition.

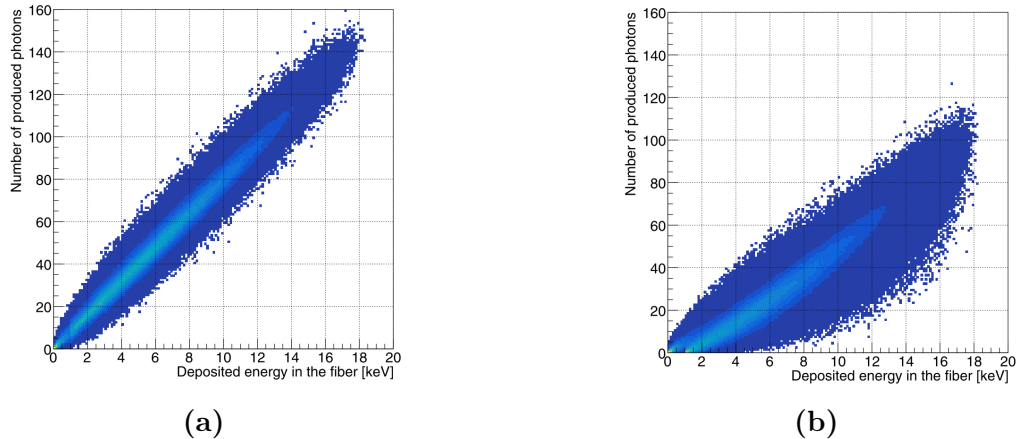


Figure 6.5 – Number of photons produced versus the energy deposited in the scintillating fibers when a) the Birks coefficient is not considered ($k_B = 0$) b) the Birks coefficient is $k_B = 0.126$ mm/MeV [Aze20].

6.2.3 Fiber Length Optimization

A study to find the fiber length that optimizes the tritium detection efficiency was carried out. Two different lengths of scintillating fibers were considered in this study, 1 m and 20 cm, and two different tritium source activities were used, 0.5 kBq/L and 2.5 kBq/L. As detected tritium decays are proportional to the active area, 5 detectors were simulated for the case of a 0.20 m fiber length to have the same active area. As the active area of the detector is related to its tritium detection efficiency, the advantage for using long fibers is their large active areas with a small number of cells, reducing the number of photosensors and, consequently, the price of the TRITIUM monitor. However, a smaller length of scintillating fibers reduce de photon absorption produced in the fibers, increasing the tritium detection efficiency per active area.

To find the scintillating fiber length that optimizes the tritium detection efficiency, the Tritium-Aveiro prototype, consisting of a similar design as the TRITIUM-IFIC-2 prototype but with 360 scintillating fibers

of 2 mm diameter, was simulated. All optical properties for the photon propagation were included in this study.

The propagation of photons in scintillating fibers was checked. The number of photons produced in a scintillating fiber per tritium electron was compared for the electrons that reach the scintillating fiber and for only those photons detected in time coincidence by the photosensors, shown in Figure 6.6. Tritium events that produce a high number of photons are almost always detected but events that produce few photons are seldom detected, resulting in a peak centred at around 25 photons.

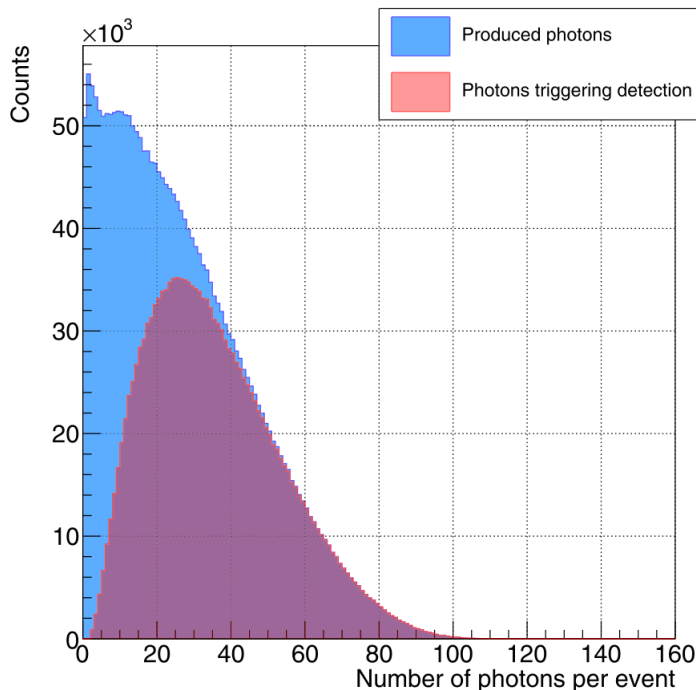


Figure 6.6 – Number of photons produced in the fiber per tritium event for all tritium events that reach the fiber (blue histogram) and for only tritium events producing photons detected in coincidence by photosensors (red histogram) [Aze20].

The counts, integrated over 60 min and taken over a week, are

shown in Figure 6.7 as a function of time for both tritium activities and fiber lengths studied. A 25% larger signal is seen for the shorter fiber length in both cases, due mainly to the lower absorption of photons in the shorter scintillating fibers and the leakage of some photons due to partial photon collection in the fiber. In addition, non simulated effects like the dirty or mechanical imperfections of scintillating fibers increase accentuate this effect.

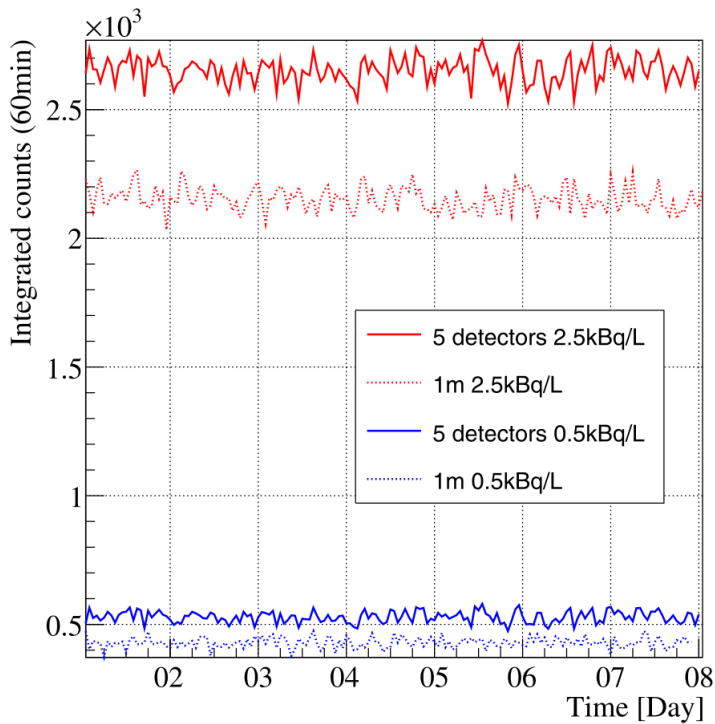


Figure 6.7 – Simulations of counts integrated over 60 min, normalized to the same active area and taken over a week for a fiber length of 1 m, dashed lines, and 20 cm, solid lines and two different activities, 0.5 kBq/L, blue lines, and 2.5 kBq/L, red lines [Aze20].

6.2.4 Fiber Diameter Effect

A study of the influence of the fiber diameter in the tritium measurement was carried out. For this task, Simulations of a single 20 cm length scintillating fiber and two different diameters, 1 mm and 2 mm (the commercial options given for Saint-Gobain), were compared. An important point is how the fiber diameter affect to cosmic ray detection, which is an important component of the background of the TRITIUM monitor. The energy deposited in the scintillating fiber by a cosmic ray is proportional to the active volume crossed, which is larger for 2 mm fibers. Therefore, the cosmic ray signal would be larger for 2 mm diameter fibers. The objective of this study is to find the design with a lower background in the energy region of tritium detection, up to 18 keV (region of interest, ROI). For this study, the tritiated water source was replaced by a cosmic ray source, generated by the CRY library¹. The CRY library is a package based on object-oriented technology and implemented in the C++ programming language. This library generates cosmic-ray shower distributions for different particles (muons, neutrons, protons, electrons, photons and pions). The cosmic source shape used in this simulation is a horizontal square of $1 \times 1 \text{ m}^2$ located at a height of 35 cm (above the detector) with the typical distribution of cosmic particles at sea level. The distribution of energy deposited in scintillating fibers for 1 mm and 2 mm diameters by cosmic rays is shown in Figure 6.8. As can be seen in the figure, a smaller background is measured for fiber diameters of 1 mm, which reduces the low detection level MDA of the detector. There are other reasons that favor the use of 2 mm fibers, such as their greater rigidity and better flow of water through them. Thus, a complementary experimental study is needed to choose the best design.

o

¹CRY library, Cosmic-Ray Shower library, CRYwebsite, CRYpaper

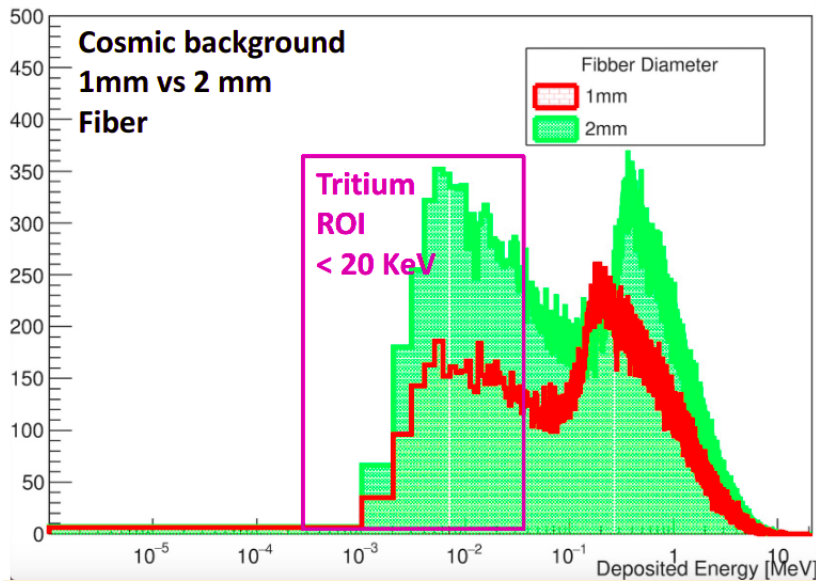


Figure 6.8 – Comparison of the energy deposition by cosmic rays in scintillating fibers of 1 mm and 2 mm diameter.

6.2.5 Effect of the PMMA windows

In the first prototypes, TRITIUM-IFIC-0 and TRITIUM-IFIC-1, the fibers were directly coupled to the photosensor, so the detected photons were only those guided by fibers. However, in the last prototypes, TRITIUM-Aveiro and TRITIUM-IFIC-2, two PMMA windows are used, which allows the detection of photons guided by fiber and photons that propagate through the water. To quantify the importance of the latter contribution, the TRITIUM-Aveiro prototype was simulated. The distribution of the number of photons that reach the PMMA per tritium event is shown in Figure 6.9. Fiber-guided photons are shown in a red distribution, while those traveling in the water medium are plotted in the blue histogram. It can be seen that the tritium signal obtained from the water is as important as that obtained from the fibers. Therefore, the use of PMMA windows improve the tritium detection efficiency by a factor 2.

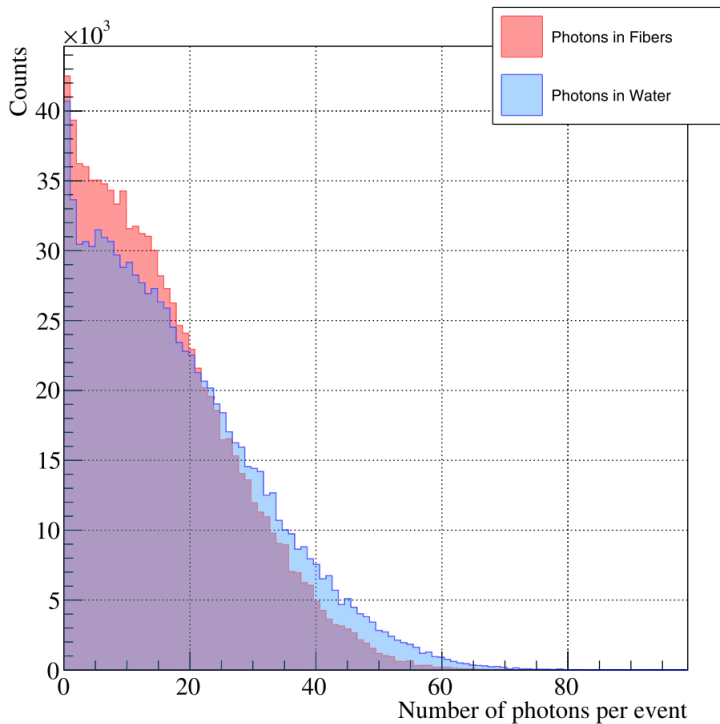


Figure 6.9 – Distribution of photons reaching PMMA windows. The red histogram corresponds to the photons guided by fibers and the blue histogram to photons traveling in the water [Aze20].

6.3 Simulations of the TRITIUM Monitor

This section shows the simulations of a TRITIUM monitor, consisting of various TRITIUM-IFIC-2 prototypes in parallel and a background rejection system.

6.3.1 Simulation of the TRITIUM-IFIC-2 Prototype

The Tritium-IFIC-2 prototype simulation was carried out in TRITIUM experiment. It consists of 800 fibers of 1 mm diameter uniformly distributed in sixteen different circles of increasing radius, as illustrated in Figure 6.10. The optical properties were included.

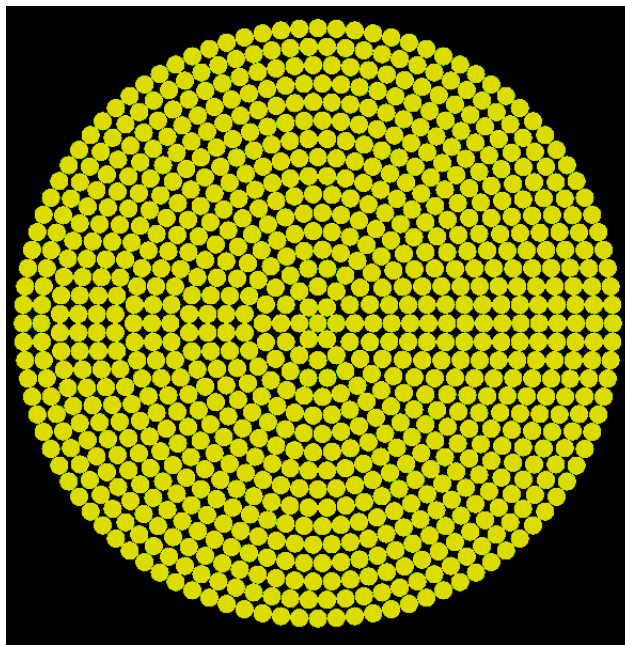


Figure 6.10 – Distribution of the scintillating fibers in the simulation of Tritium-IFIC-2 prototype.

The tritiated water source consists of a tritiated water volume with

a thickness of 5 μm around each scintillating fiber. Scintillating fibers are located in a PTFE vessel. Two PMMA windows of 5 mm thickness located in both ends and a optical grease layer with a thickness of 0.5 mm located in each PMMA windows were included. Two PMTs, model R8520-460 from Hamamatsu [K.K19], were also simulated as photosensors.

The geometry simulated for TRITIUM-IFIC-2 is shown in Figure 6.11 in which is shown the PMTs (black), the optical grease (blue), PMMA windows (white), tritiated water (green) and scintillating fibers (yellow). In this image, the PTFE container is not drawn to allow its interior to be seen. Several volumes of tritiated water were also excluded to allow some scintillation fibers to be seen. The PMTs do not cover the entire active area formed by the scintillating fiber bundle. This is not a problem for the TRITIUM detector since its final version will use SiPM arrays.

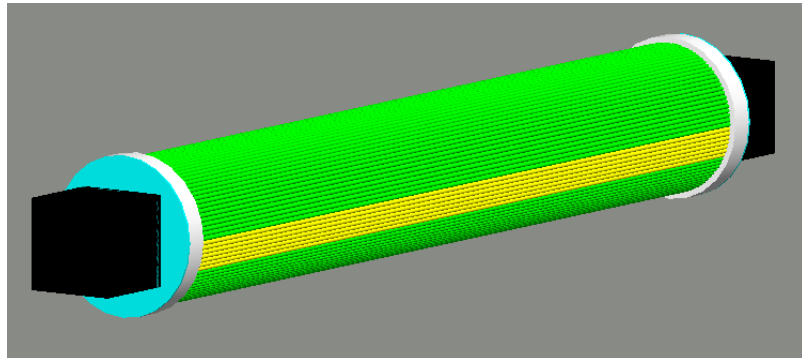


Figure 6.11 – Simualtion of Tritium-IFIC-2 prototype. PMTs (black), the optical grease (blue), PMMA windows (white), tritiated water (green) and scintillating fibers (yellow).

The aim of these simulations were to find the minimum detectable activity, MDA, for tritiated water, which is an important parameter of the prototype, and to study the activity resolution of the prototype and how both parameters, activity resolution and MDA, can be improved by increasing the integration time window and the number of prototypes read in parallel. The detection of a tritium event in the TRITIUM-IFIC-2 prototype is

shown in Figure 6.12. The paths of the photons created in scintillating fibers are represented by green lines ending in red dots when they are absorbed in the fiber or the water and blue dots when they are absorbed in the PMTs (detected). The fiber in which the tritium electron is detected is clearly identified. Some photons go out of the fiber and are not collected. Blue dots in both PMTs indicate that photons are detected in time coincidence.

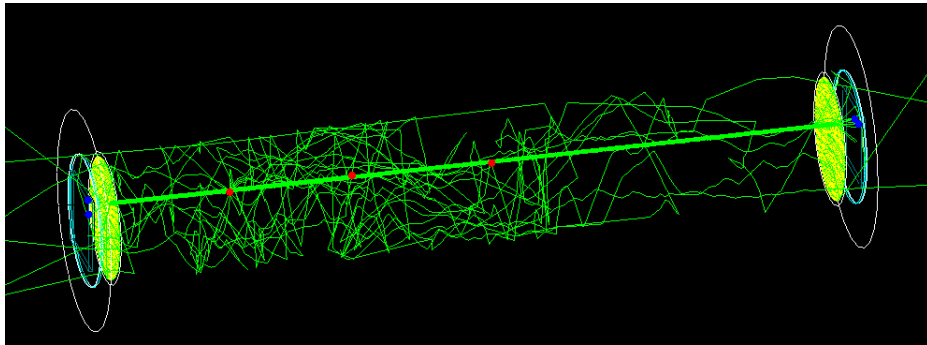


Figure 6.12 – Tritium electron detected in the simulated TRITIUM-IFIC-2 prototype. The path of the optical photons is represented by green lines and the position in which they are absorbed is represented by red and blue dots (absorbed in water or PMT, respectively).

Several variables were used to check the different steps of the simulation such as the production of tritium electrons, the energy deposition in scintillating fibers and their subsequent photon emission, spatial distribution of generated events, detected events, etc. The distribution of the number of photons detected by photosensors per tritium event for the TRITIUM-IFIC-2 prototype is shown in Figure 6.13. A maximum of 17 photons is obtained for the TRITIUM-IFIC-2 prototype simulations, which is in agreement with the maximum of 15 photons measured, shown in Figure 5.19. This confirms that the value used in the simulations for the Birks coefficient, $k_B = 0.136 \text{ mm/MeV}$, is quite accurate. The experimental distributions are lower than the simulations mainly in the range from 3 to 8 photons per event, probably due to imperfections of the prototype not included in the simulations.

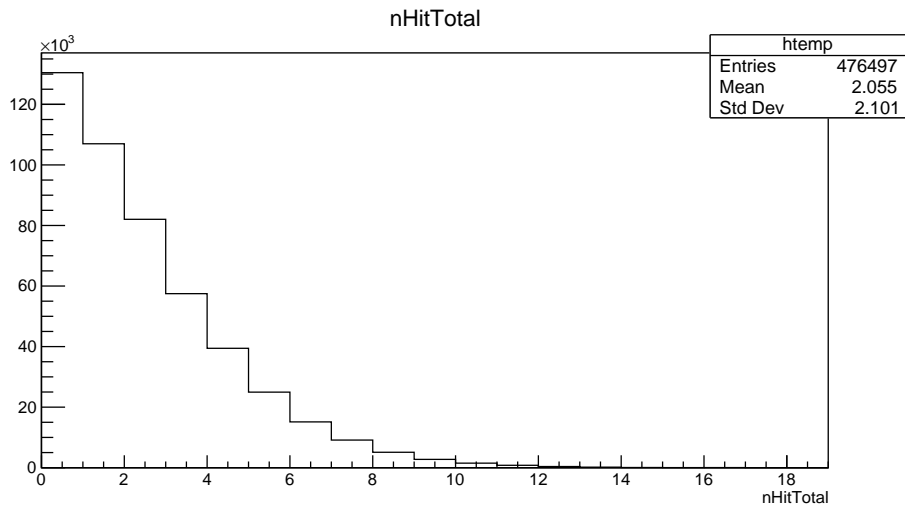


Figure 6.13 – Photons detected by both PMTs per tritium event in the simulated TRITIUM-IFIC-2 prototype.

Activities from 100 Bq/L to 5 kBq/L for three months of data taking and an integration counting time of 10 min were simulated. The simulation results are presented in Figure 6.14. A difference of 250 Bq/L is not distinguished due to the overlapping of distributions. To reduce the width of the distribution obtained for each activity, the statistics must be increased, which can be done in two different ways, either by increasing the integration time or the number of prototypes read in parallel. To check the role of increasing the integration time, distributions for integration times of 10 min, 30 min and 60 min were generated. They are shown in Figure 6.15. The effect of increasing the integration time is clearly visible in this figure, by reducing the relative distribution width and improving the activity resolution of the TRITIUM monitor. Differences as low as 250 Bq/L are clearly discriminated with only one TRITIUM-IFIC-2 module and an integration time of 60 min, which could still be considered as a quasi-real time measurement. Similarly, these distributions are shown in Figure 6.16 for 10 min of integration time, for 1, 5 and 10 prototypes in parallel. Again, the reduction of the distribution width is clearly visible in these figures,

improving the activity resolution of the detector. In this case, differences of 250 Bq/L are clearly discerned by a integration time of 10 min and 5 TRITIUM-IFIC-2 prototypes. The resolution, defined as

$$\text{Resolution}(\%) = \frac{\text{FWHM}}{\text{centroid}} \cdot 100 \quad (6.2)$$

is plotted in Figure 6.17. It can be observed that the resolution improves with integration time and number of prototypes. Therefore, both parameters must be set according to the requirements and funding of the experiment. The studied cases are summarized in Table 6.1.

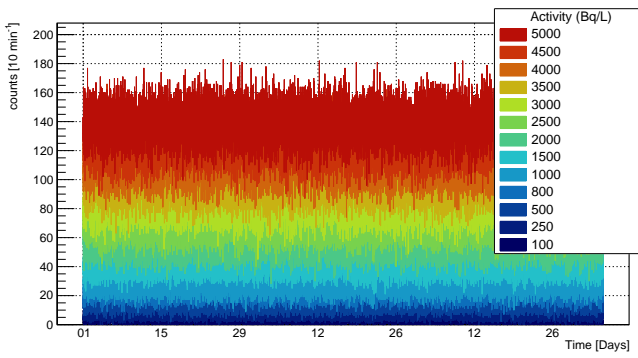
# of Detectors	10 min	30 min	60 min
1	< 1000 Bq/L	500 Bq/L	200 Bq/L
5	200 Bq/L	150 Bq/L	100 Bq/L
10	150 Bq/L	100 Bq/L	≈ 50 Bq/L

Table 6.1: Difference in activity that can be resolved for the TRITIUM-IFIC-2 prototype, for different integration times and different number of prototypes.

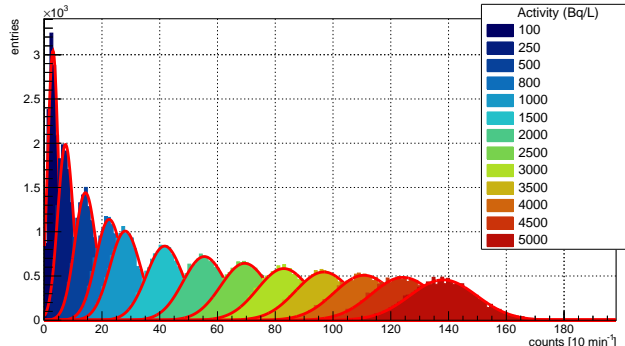
The decision made by the TRITIUM collaboration is to install 3 different TRITIUM-IFIC-2 prototypes, with which differences of 250 Bq/L are expected to be resolved with an integration time of 30 min. These prototypes are expected to be installed in Arrocampo dam as soon as possible. Two other TRITIUM-Aveiro prototypes are being built and will be installed soon, to be readout in parallel with the one currently installed.

6.3.2 Simulation of the Lead Shield and Cosmic Veto

The lead shield and active vetos, described above, were included in the simulation of the Tritium-IFIC-2 prototype. The purpose of these simulations was to quantify the reduction of cosmic background detected by the pro-



(a)



(b)

Figure 6.14 – a) Tritium counts detected with a simulated TRITIUM-IFIC-2 prototype using a integration time of 10 min as a function of the time
b) Distribution of detected counts for different activities and an integration time of 10 min.

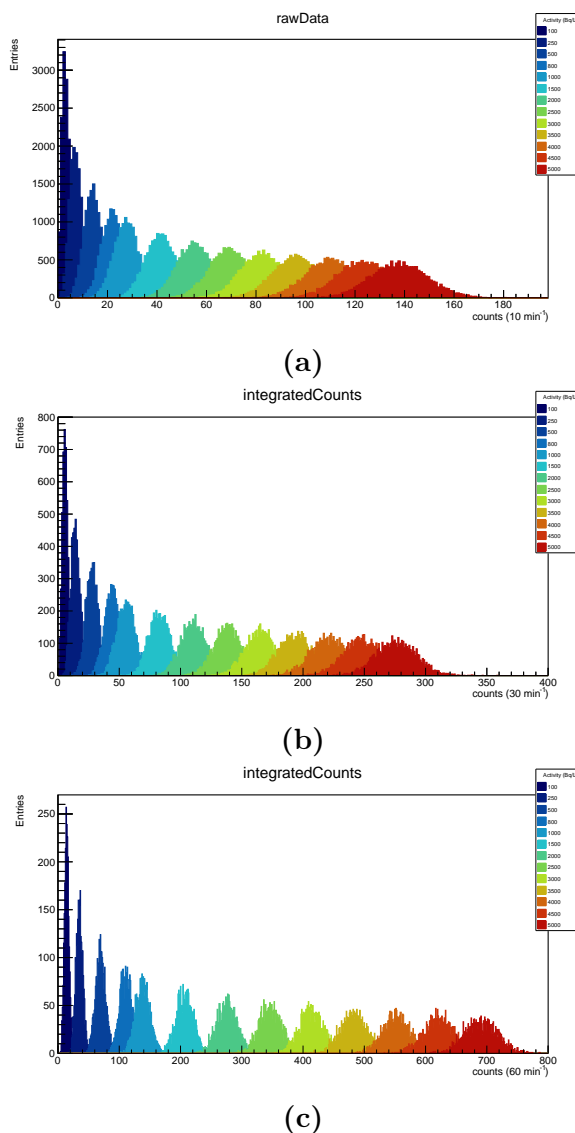


Figure 6.15 – Distribution of the tritium counts simulated for TRITIUM-IFIC-2 prototype for three different integration time: a) 10 min, b) 30 min and c) 60 min.

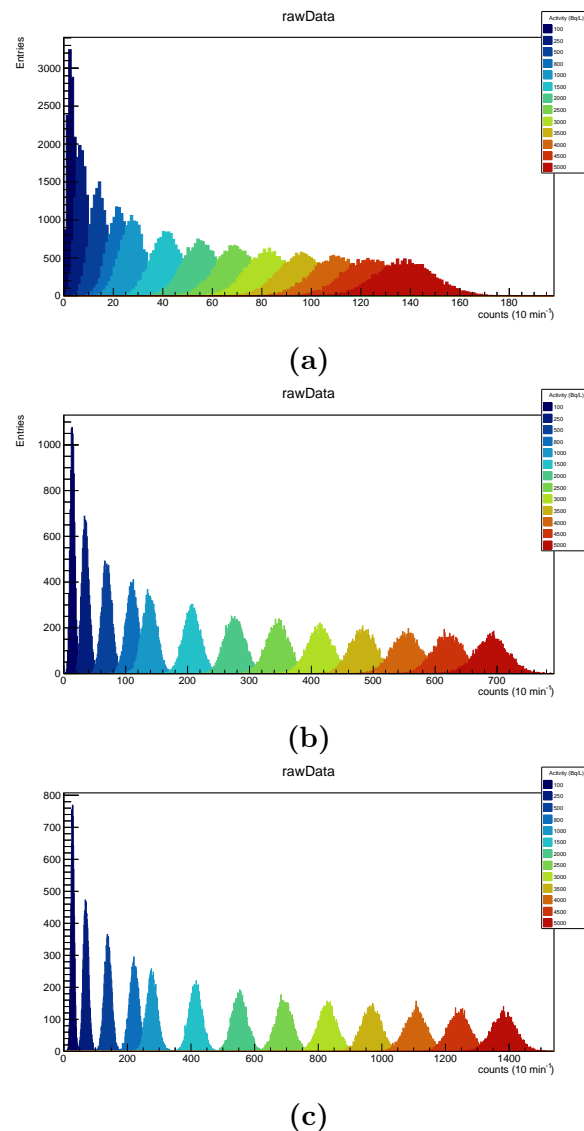


Figure 6.16 – Distribution of the tritium counts simulated for different number of TRITIUM-IFIC-2 prototypes: a) 1, b) 5 and c) 10, for an integration time of 10 min.

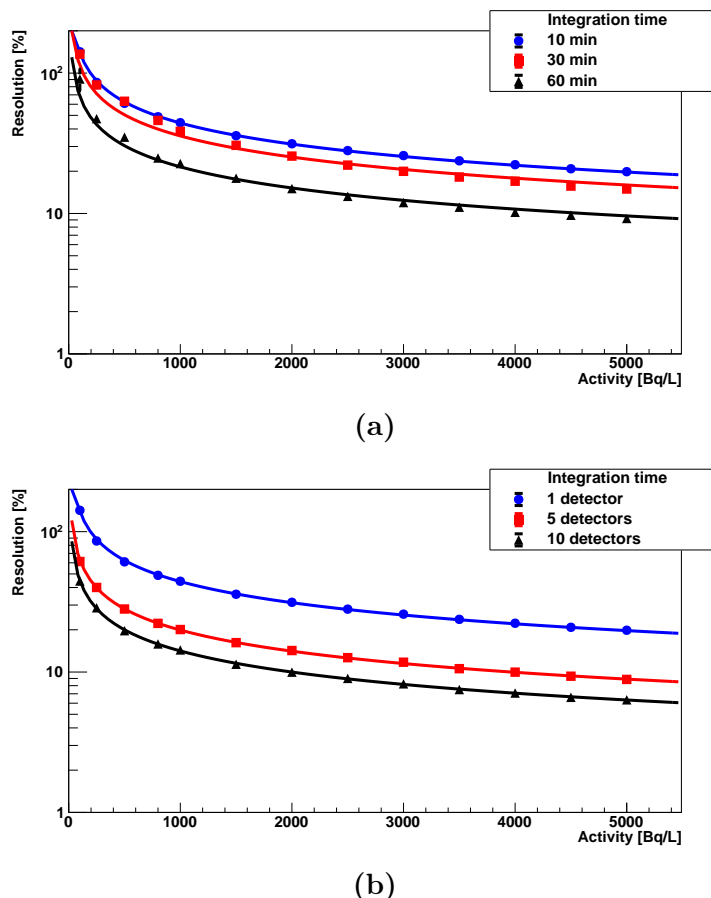


Figure 6.17 – Resolution of the TRITIUM-IFIC-2 prototype as a function of the a) integration counting time b) number of prototypes.

totype. For this task, the tritium source was replaced by a cosmic event source, simulated by the CRY library. The optical properties included for the plastic scintillators of the active veto are the refractive index, the light attenuation spectrum and energy emission spectrum, the values of which were obtained from their data sheet provided by the manufacturer [Cry20]. Two PMTs, model R8520-460 from Hamamatsu, were simulated to read each plastic scintillator, as described in section 3.4.2. The lead shield was simulated with properties taken from the Geant4 NIST database. The dimensions of the simulated lead shield were $60 \times 60 \times 70 \text{ cm}^3$, which is the minimum needed to accomodate an active veto and Tritium detector module inside. The length of the simulated lead castle, 60 cm, is smaller than real dimension, 148 cm. The reason for this is that only one tritium detector module was simulated, so the dimension of the lead shield was reduced to optimize simulation time and computing resources. As for the simulations of the TRITIUM-IFIC-2 prototype, checks were done to ensure the accuracy of the simulations.

Three different simulations were carried out to quantify the tritium detection improvement due to the lead shield and the cosmic ray source. In the second simulation, a lead shield was added and for the third simulation, the cosmic veto was also included. The cosmic rays detected by the TRITIUM-IFIC-2 prototype are reduced by around a factor 5.5 when a lead shield with walls of 5 cm is included. This reduction is mainly caused by the suppression of the soft cosmic radiation (energy lower than 200 MeV). It has to be taken into account that the natural background of the installation site was not included in this simulation. This radioactive background would also be suppressed by the lead shield, so the expected reduction of the radioactive background due to the passive veto is even better. Around 10% of the cosmic events that penetrate the lead shield and reach the TRITIUM IFIC 2 prototype, which are the hard cosmic rays, are detected by the cosmic veto and, therefore, removed from the background. Therefore, the usefulness

of both, lead shield and active veto, is demonstrated by the simulations.

Chapter 7

Conclusions and Prospects

This chapter contains a brief summary of the most important achievements reached in this work and highlights the main conclusions obtained.

The design of a tritium detector capable of measuring low tritium activities in quasi-real time is mandatory since this is one of the first sign of a malfunctioning of a nuclear facility, such as nuclear power plants, future nuclear fusion reactors and laboratories of high energy physics.

The goal of the TRITIUM project is to design, build, install and commission a tritium monitor that will measure tritium activities as low as 100 Bq/L (legal limit imposed for European Council Directive 2013/51/EU-RATOM for drinking water consumption) in quasi-real time (1 hour or less).

The TRITIUM monitor developed in the TRITIUM project has different parts, which are detailed in this thesis. The different parts, which was characterized indendently, are an water purification system, which prepares the water sample before the measurement, a tritium detector, consisting of scintillating fibers readout by photosensors (PMTs or SiPM arrays), and a passive and active shielding, which is used to reduce de ra-

dioactive background measured by the tritium detector.

First, the components of the tritium monitor, which are scintillating fibers and SiPM, were characterized and some improvements were studied.

- On the one hand, a characterization of the photon collection efficiency of the BCF-12 unclad scintillating fibers was performed, which was compared with single clad and multiclads fibers to check the importance of the clad.

In addition, a conditioning process of scintillating fiber was developed, tested and implemented, consisting of cleaving, polishing and cleaning them, the objective of which is to increase the tritium detection efficiency. Due to the large number of scintillating fibers used, it was necessary to develop an automatic polishing machine, based on arduino technology, which is capable of polishing up to one hundred scintillating fibers at the same time. The improvement in photon collection efficiency due to the polishing and cleaning process was quantified in more than 40% and 21%, respectively.

- On the other hand, a characterization of the SiPM used (Hamamatsu model S13360-6075) was carried out at the level of a single SiPM. In this characterization several interesting parameters such as quenching resistance, terminal capacitance, internal gain of SiPM, breakdown voltage, temperature coefficient, etc. were experimentally measured.

Due to the strong dependence of the SiPM internal gain on temperature, a stabilization method for the SiPM gain was developed and experimentally tested. The objective of this mechanism is to compensate for temperature variations with variations in the operating voltage of the SiPM, maintaining the internal gain of the SiPM during its operation.

Second, a characterization of the water purification system was carried out, in which it was checked that the imposed requirements were fullfit. The requirements are to prepare water samples with very low conductivity (of the order of about $10 \mu\text{S}/\text{cm}$) in which the organic matter and all particles up to 1 mm diameters is removed without affecting the tritium levels.

Third, a characterization of the active veto was carried out in which several interesting parameters were experimentally measured.

- First, the quality of the coverage of the plastic scintillator, consisting of a layer of PTFE, aluminium and black tape, was tested and quantified, obtaining an improvement in the uniformity and quality of the photon collection efficiency.
- Second, the high voltage and threshold that optimize the detection of hard cosmic rays ($> 200 \text{ MeV}$) was experimentally found.
- Third, a hard cosmic events was experimentaly measured with the active veto developed, obtaining an energy spectrum with a shape similar to a Landau functions, as it is expected, and an efficiency of hard cosmic rays detection of 85%. In addition, the relationship between the number of the hard cosmic rays measured and the distance between both plastic scintillators of the active veto was obtained, allowing this distance to be changed without the need to perform a new calibration of the active veto.

This background rejection system, consisting of a lead shielding and an active veto, is essencial to achieve the activity goal of 100 Bq/L .

Fourth, four different prototypes of the tritium detector have been developed. The first two prototypes, TRITIUM-IFIC-0 and TRITIUM-IFIC-1, was used to detect potential problems that affect to the tritium

measurement as well as to test several improvement in the detector design. The last two prototypes, TRITIUM-Aveiro and TRITIUM-IFIC-2, are two different designs to be used in the final tritium cell of the TRITIUM monitor. Each design has its own advantages and disadvantages and the one with the best results will be used as a final design of the TRITIUM cell.

With the different prototypes, an increasing sensitivity has been achieved, showing the effect of the applied improvements. The best tritium detection efficiency was obtained with the lastest prototype developed, TRITIUM-IFIC-2, with which the State-Of-The-Art of tritium detection has been overcomed. The most important results of each prototype developed in TRITIUM project are presented in Table 7.1, in which the results obtained with other experiments are also included.

Study	$\varepsilon_{det} (\frac{cps \cdot 10^{-3}}{kBq/L})$	F_{sci} (cm ²)	$\eta_{det} (\frac{cps \cdot 10^{-6}}{kBq/L \cdot cm^2})$	MDA (kBq/L)
Muramatsu	0.39	123	3.13	370
Moghissi	4.50	> 424.1	< 10.6	37
Osborne	12	3000	4	37
Singh	41	3000	13.7	< 37
Hofstetter	2.22	~ 100	< 22.2	25
T-IFIC-0	2.11 ± 0.85	219.91	9.59 ± 3.87	100*
T-IFIC-1	38.42 ± 1.61	402.12	95.55 ± 4.01	100*
T-Aveiro	64.87 ± 19.41	4071.50	15.93 ± 4.77	29.8
T-IFIC-2	711.03 ± 27.77	5026.55	141.45 ± 5.52	10*

Table 7.1: Results of scintillator detector developed for several experiments (including the TRITIUM project) for tritiated water detection. This table shows the efficiency of the detector (ε_{det}), its active surface (F_{sci}), its specific efficiency ($\eta_{det} = \varepsilon_{det}/F_{sci}$), defined as its efficiency normalized to its active surface, and its minimum detectable activity (MDA) for each study listed above. The "*" symbol indicates that this is the specified activity that the detector can distinguish from the background, but it is not its MDA.

As can be seen in the table, the specific efficiency of the latest prototype, TRITIUM-IFIC-2, is almost an order of magnitud better than

the best result obtained in other experiments (Hofstetter). Special attention need to be payed for the specific efficiency obtained for the TRITIUM-Aveiro prototype, which is smaller than the expected. A possible reason is because the used fibers was not polished nor cleaned, reducing the tritium events detected. It could be interesting to develop a new TRITIUM-Aveiro prototype, the fibers of which are prepared with the conditioning process detailed in section 4.1.1 to decide which tritium cell design optimizes the tritium detection.

A low detection level, MDA, of 29.8 kBq/L has been measured for the TRITIUM-Aveiro prototype using 1 minutes of integration time, slightly improving the State-Of-The-Art. It is expected to be improved up to 5 kBq/L by increasing the integration time up to 1 hour, which is still considered quasi-real time.

A better result was obtained for the TRITIUM-IFIC-2 prototype, being able to clearly measure an activity of 10 kBq/L, improving the best results obtained in other experiments. However this is not the MDA of the prototype. To measure this, it is necessary to take many more measurements and apply the same mathematical method used for the TRITIUM-Aveiro prototype.

Nevertheless the low detection level achieved with this prototypes is further from being the goal of the TRITIUM project, 100 Bq/L. This is not a problem since the TRITIUM monitor will consists of several TRITIUM cells readout in parallel, becoming the TRITIUM monitor in a scalable detector. It means that more tritium cells can be used, readed in parallel, to improve the results obtained. The activity goal is expected to be achieved using three different cells of TRITIUM-IFIC-2 read in anti-coincidence with an active veto.

In summary, two different prototypes has been developed in the TRITIUM project with which it is possible to measure low activities of tri-

tiated water in quasi-real time, improving the specific efficiency and the low detection level of the activity currently achieved with other experiments. In addition, the stability of the tritium detection efficiency of both prototypes has been verified during several months.

Currently, the lead shielding, the water purification system and a TRITIUM-Aveiro prototype are installed in Arrocampo dam, near to Almaraz Nuclear Power Plant. Two additional TRITIUM-Aveiro prototypes and an active veto are planned to be installed as soon as possible. In addition, three prototypes of TRITIUM-IFIC-2 and an active veto are ready to be installed too, the installation of which has been delayed due to the coronavirus pandemic.

Finally several Monte Carlo simulation has been developed using Geant4. These simulations were used for three different tasks:

- First, several simulations were carried out to study the different steps of the simulation, such as the energy deposition of tritium electrons on scintillating fibers (spectrum peaked of around 5 keV), the number of photons produced by the fibers (spectrum peaked of around 10 photons) or which of these are detected by the photosensors in time coincidence (spectrum peaked of around 25 photons). They were also used to quantify the importance of the reduction of the scintillating fiber signals because tritium electrons are not MIP particles (Birks effect).
- Second, these simulations were used to test different tritium detector designs, such as different fiber lengths or fiber diameters, and choosing the one with the best results, that is, the one that optimizes the tritium detection efficiency.
- Third, these simulations were used to verify the results obtained with the last two TRITIUM prototype, such as the spectrum of the number of photons obtained per tritium event, ensuring that this prototype

works correctly. They were also used to find the sensibility of each different prototype and how the integration time and the number of cells used can improve to the tritium detection of the TRITIUM monitor.

Appendices

Appendix A

Electronic Readout for characterization the SiPM 13360-6075 Model

This appendix shows the electronic system designed to perform a complete characterization of the SiPM S13360-6075 model. This consists on three different PCBs¹, shown in Figure A.1:

1. The first PCB, shown in Figure A.1a, is used to organize the SiPMs and sensor temperature. This PCB place up to 8 different SiPMs and a temperature sensor and arrange their output signals on two HDMI connections. This PCB is placed inside a special black box, from Thorlabs company [Thob], that has a high degree of light tightness. This black box has a small hole of 1 mm diameter, prepared to introduce an optical fiber² to illuminate SiPMs with an incoherent light source. The light source utilized is a LED, model 430L from Thorlabs com-

¹PCB, Printed Circuit Board

²The optical fiber used is BCF-98 from Saint-Gobain company [Cer21]

pany [Tho18], which gives an spectrum shown in Figure A.1d. The spectrum was experimentaly measured with a spectrometer and fitted to a Gaussian function. It can be seen that the emission peak of this LED is placed at 436.3 with a FWHM³ of 19.1 nm. With the help of this LED the light emission of the fibers used in TRITIUM experiment is simulated to calibrate the SiPMs at the working wavelength.

2. The second PCB, shown in Figure A.1b, sums the different signals of the SiPMs and amplify them by a factor $G = 4187.5$ or $G = 10761.88$, depending on the input resistance of the oscilloscope, 50Ω or $1 M\Omega$, respectively. This PCB uses a differential amplification that reduce the electronic noise of the system and is connected to the first PCB through two HDMI feedthroughs.
3. The third PCB, shown in Figure A.1c, rearranges all the different input and output signals in an HDMI connection to avoid crosstalk between different signals. This PCB is connected to the second PCB through a HDMI feedthrough.

The input signals are the supply voltage of the SiPMs and the supply voltage of the PCBs (± 6 V) and the output signals are the temperature sensor signal and the summed signal of all SiPMs.

The output signal of the third PCB is connected to an oscilloscope, model MSO44X from Tektronix [Tek21], that records the data which are subsequently analized by ROOT⁴.

³The FWHM parameter, Full Width at Half Maximum, of a Gaussian fit can be calculated from its sigma using the equation: $\text{FWHM} = 2.35 \cdot \sigma$

⁴ROOT is a framework for data processing, based on C ++ and object-oriented technology, developed at CERN and widely used in nuclear and particle physics.

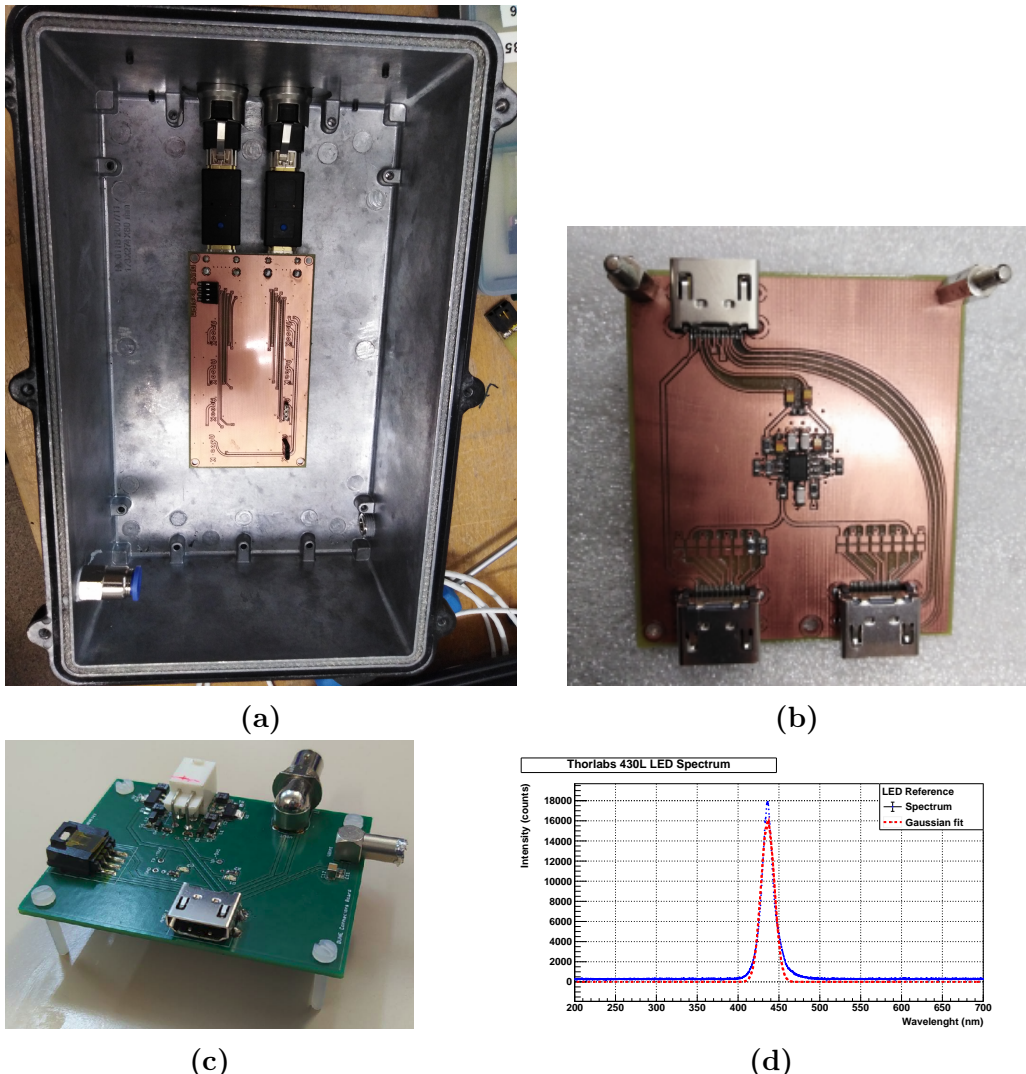


Figure A.1 – Three PCBs used for the SiPM characterization a) The PCB 1 used to arrange 8 SiPMs and black box. b) The PCB 2 used to sum and amplify the output signals of SiPMs. c) The PCB 3 used to rearrange the different signals of the system. d) The LED emission spectrum.

Appendix B

Water Purification System

This appendix shows several photos of the water purification system in the same order that the water flows through them.

First of all, the complete scheme of the water purification system is shown in Figure B.1:

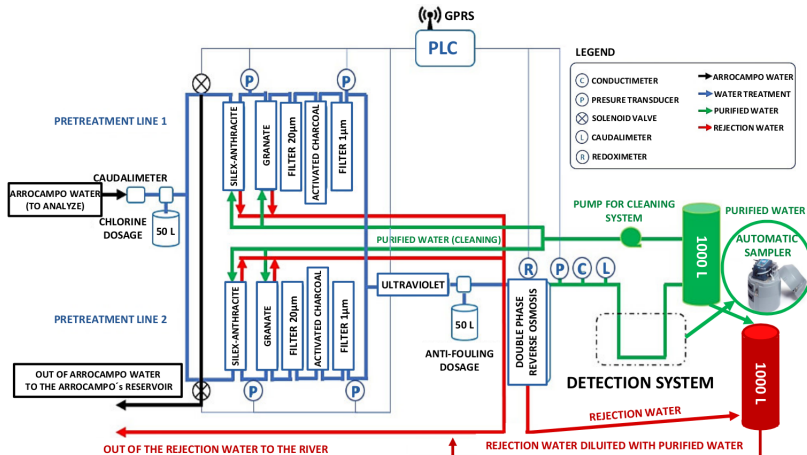


Figure B.1 – Scheme of the water purification system.

The Gross filtering stage, made up of Silex-Antracite and Granate

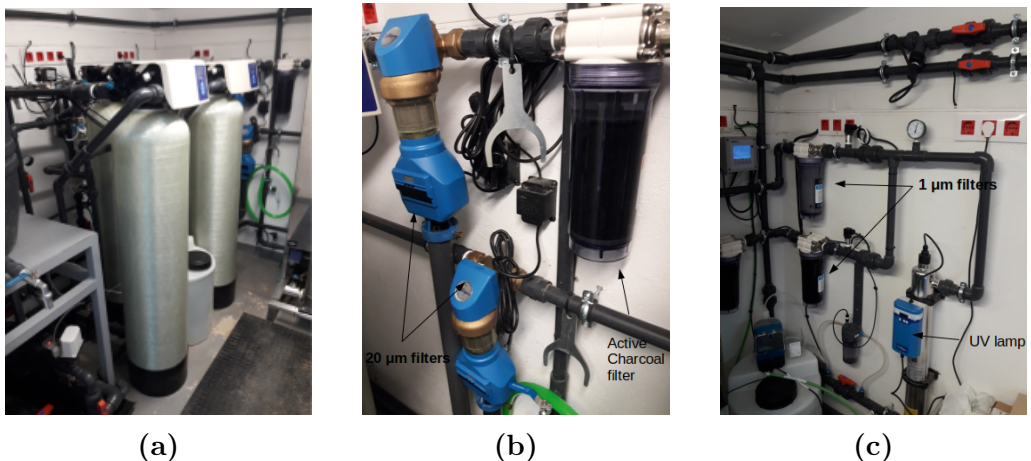


Figure B.2 – Different stages of filtration of the water purification system.
 a) The gross filtering stage. b) The Fine filtering stage. c) The Super fine filtering stage.

filters, the fine filtering stage, consisting of $20\ \mu\text{m}$ filter and active carbon filter and the superfine filtering, composed of the $1\ \mu\text{m}$ filter and the UV lamps, are shown in Figure B.2.

The double phase reverse osmosis is exhibited in Figure B.3a and the containers in which we store the pure water and the reject water after treatment is displayed in Figure B.3b.

The Siemens PLC, software used to control the water purification system, is shown in Figure B.4.

Finally, the complete system of the water purification system is displayed in Figure B.5

Just as a curiosity, the three types of water (raw water, rejection water and pure water) are exhibited in Figure B.6, where it can be visually checked the difference in the turbidity of each type of water.



(a)



(b)

Figure B.3 – a) Doble phase reverse osmosis stage b) Containers used to store the outlet water of the water purification system.



(a)



(b)



(c)

Figure B.4 – Siemens PLC, software for remote control of water purification system.



Figure B.5 – General photo of the complete water purification system.

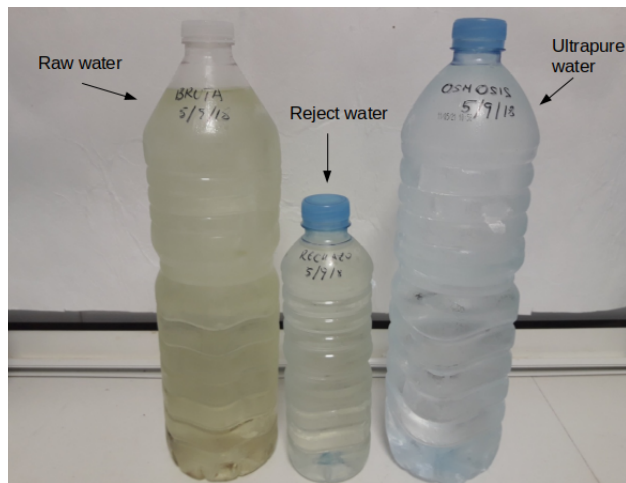


Figure B.6 – Raw water, reject water and pure water obtained with this system.

Appendix C

Preparation of Liquid Radioactive Source of Tritium

To prepare this radioactive liquid source, 1.86 g (uncertainty of 0.05%) of tritium was purchased from the Germany company PTB¹, which has a serial number of 2005 – 1442 and reference number of PTB-6.11 – 285/03.2017 [PTB]

The activity of this tritium source is 26,8 MBq/g (uncertainty of 2.24%), reference data of 1 of January of 2017, and it was dissolved in 500 mL (uncertainty of 0.05%) of pure water (conductivity of 0.72 μ S/cm), giving 500 ml of tritium water, to which we will call standard solution, with an activity of 100.096 kBq/g (uncertainty of 2.24%), that's, 99.696 kBq/L (uncertainty of 2.24%), which was measured with the TRI-CARB 2810 system, based on liquid scintillation readout by PMT.

¹Physikalisch-Technische Bundesanstalt, Braunschweig and Berlin, Germany

Appendix D

Electronic System of TRITIUM-Aveiro prototype

The electronic system used in TRITIUM-Aveiro prototype consists of several PCB and can be divided into two parts:

1. A PCB, whose electronic scheme is shown in Figure D.1, was designed to power the PMTs with a negative high voltage. It consists of several high voltage power supply, model C11152-01 from Hamamatsu company [K.K15], one for each PMT used, which is controled by a DAC¹, model MAX5500 from Maxim Integrated company [Int09]. An Arduino Mega is used for the DAC communication and cross-checking the output values and it is connected to a Raspberry Pi to control the system.

A graphical interface, shown Figure D.1b, has been developed to manage the different options of this system in a comfortable way.

2. A electronical chain consisting of several PCBs was used to process

¹DAC, Digital-to-analog converter

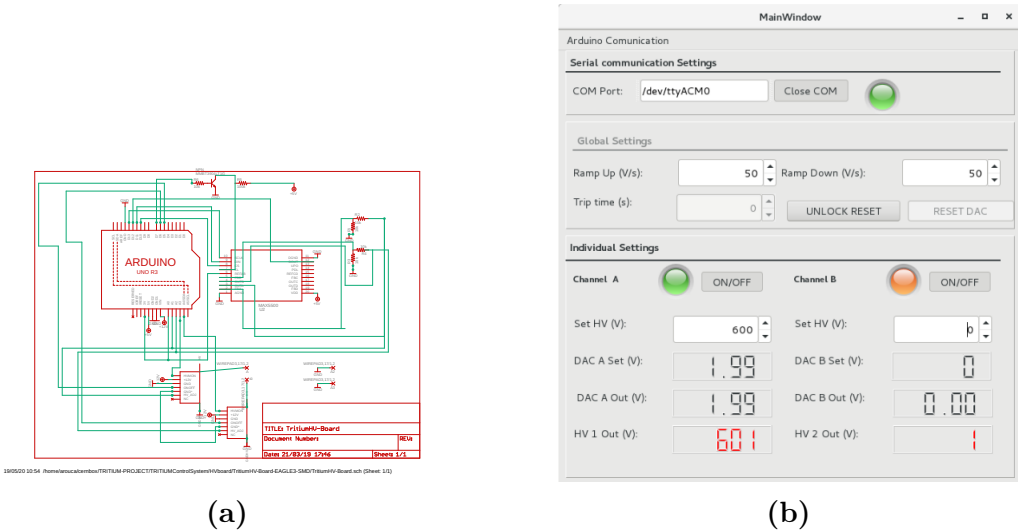


Figure D.1 – a) The Electronic scheme of the PCB designed to power the PMTs of Aveiro prototype b) The graphical user interface developed to control it.

and analyze the system signals, whose simplified electronic scheme is shown in Figure D.2.

It consists of three different lines, two of them are used for the PMT signals of the prototype and the remaining line is used for doing anti-coincidence with an active veto.

To test this electronic chain a plastic scintillation with dimensions of $10 \cdot 10 \cdot 1 \text{ cm}^3$ was used to simulate a veto signal but four different vetos are being developed, based on a rectangular plastic scintillations of Saint-Gobain company [SG], whose dimensions are $50 \text{ cm} \cdot 30 \cdot 2 \text{ cm}^3$ with a PMT coupled, model R2154-02 2" from Hamamatsu company [K.K10]. The output signal of these PMTs will be input in a OR stage, whose response will be introduced in the veto line shown previously in Figure D.2. As a result, each plastic scintillator will be read in anticoincidence with TRITIUM-Aveiro prototype.

Both lines, used to process and analyze the PMT signals of the pro-

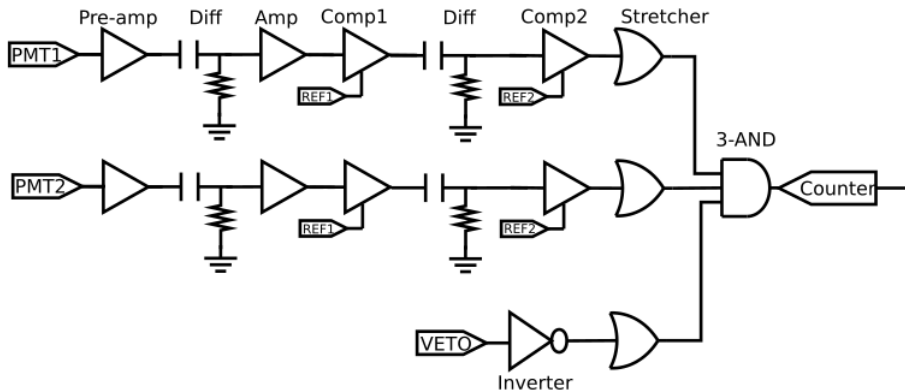


Figure D.2 – Simplified electronic scheme used to process and analyze the signal of TRITIUM-Aveiro prototype.

totype, are equal and they are used to operate in time coincidence. First, each PMT signal is introduced in a preamplifier model CR111 from CREMAT Inc. company [Inc], which is used to shape and pre-amplify the signal. To reduce electronic noise and signal loss, both preamplifiers are connected as close as possible to the PMTs and they are located inside of aluminum boxes which act like a Faraday cage.

Each preamplifier is followed by a differentiation stage, which is used to reduce the time width of the signal, and amplification stages, used to amplify the signal. The amplification used is the model OPA656 from Texas Instruments [Ins15].

Then, a fast comparator, model LT111 from Linear Technology company [Tec], is used to set a threshold which will be used to remove the PMT signals whose amplitude are below this value (dark counts of the PMT). A MAX5500 DAC is used to configure the thresholds.

The time width of the preamplifier output signal is too large, $200 \mu\text{s}$, with which too many false coincidence will be registered. To solve this problem a second differentiation stage is included and a second comparator are added to produce a 5V square signal again.

Finally a tunable pulse stretcher based on an OR gate, model SN74AHC1 from Texas Instruments company [Ins17], is used to set the time width of each signal at 100 ns, with which the time coincidence windows of our adquisition system is 200 ns, narrow enough to have a negligible false coincidence rate.

In the remaining line, used for the veto signal, an inverter is used in the first stage. With it, the signal will always be in the high level, 5 V, except when a cosmic particle is detected, in which case the signal will be in the low level, 0 V. Then, another stretcher is used to create a signal with the same time width than the others, 100 ns.

Lastly, these three signals are introduced into a 3-input AND gate, model SN74LVC1G11 from Texas Instruments company [Ins16], to perform a logic level comparison. With this last stage we achieve a temporal coincidence of both PMT signals of the prototype and anti-coincidence of them with the veto signal. The output signal of this last stage is simply connected to a pulse counter.

A GPIO pins of a Raspberry Pi is used to communication with the system, control it and configure the different threshold levels. A graphical user interface, which is shown in Figure D.3, was developed to manage the counter system in a comfortable way.

In addition to count, which is the option normally used in our detector, this electronic system include a voltage follower circuit connected to the preamplifier output signal which can be used to obtain a energy spectrum of each PMT of the prototype.

It is important to note that, although this system has a graphical user interface that allows comfortable control of the system, the usual way in which it is controlled is remotely through the computer terminal.

In Figure D.4 two screenshots are shown to demostrate two different situations of this system. There, we have four different signals. The yellow and cyan signal are input signals of the AND-Gate, which come from the PMT signals of the prototype. The pink signal is the third

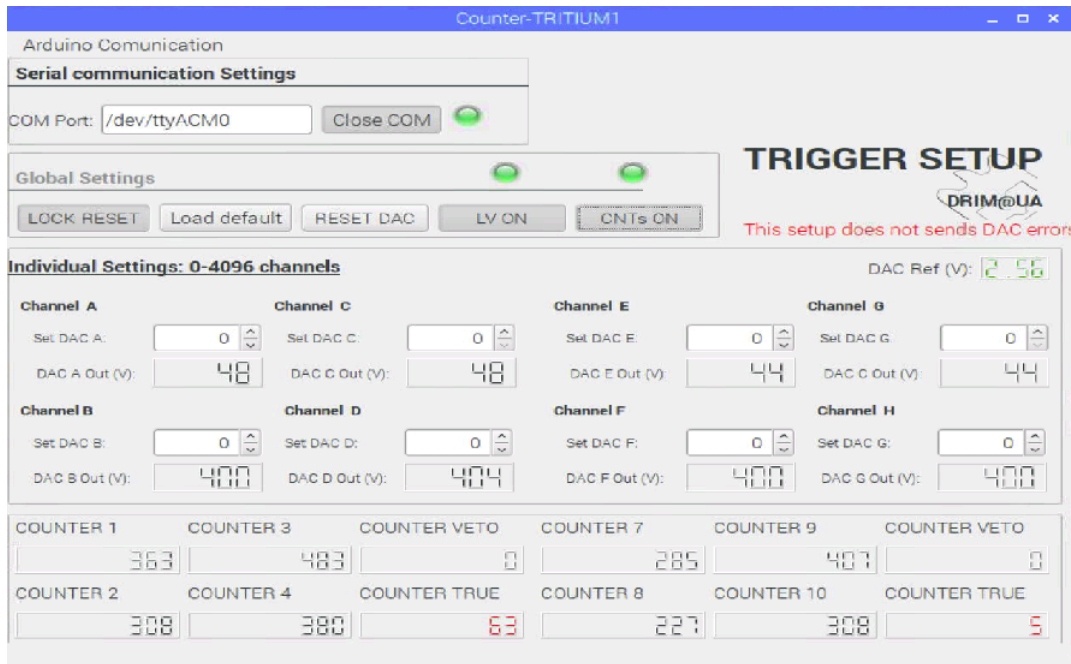


Figure D.3 – Graphical user interface used to manage the counter system.

remaining input signal of the AND-Gate, which come from the PMT signal of the veto. The last signal, green, is the output signal of the AND-Gate.

As can be seen, in Figure D.4a both PMTs of the prototype have detect a time coincident event, which has not been detected for the veto, so this event is counted. In Figure D.4b, a time coincidence event has been observed in the three PMTs, which means that it is a cosmic event, so this event is not counted.

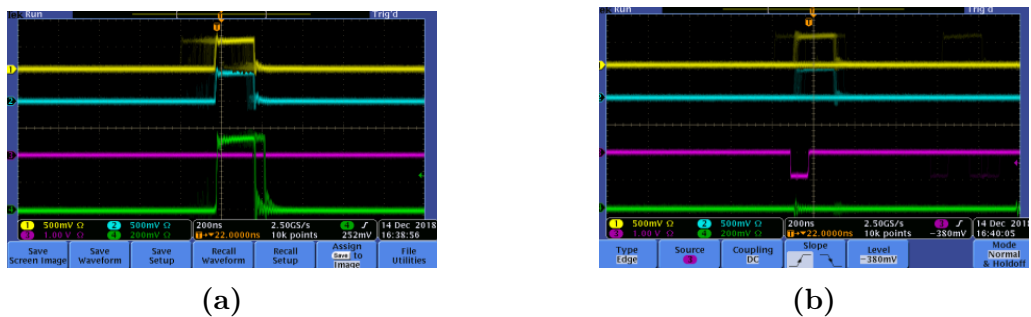


Figure D.4 – Two different situations of the electronic chain response. a) Event accepted since veto has not detected it. b) Event rejected since veto has detected it.

Bibliography

- [AG21] Australian Government, N. H., Council, M. R. and Council, N. R. M. M. *Australian Drinking Water Guideilnes 6. National Water Quality Managment Strategy.* <https://www.nhmrc.gov.au/about-us/publications/australian-drinking-water-guidelines> (2021.) accessed: 2021-06-08.
- [Ago03] Agostinelli, S., Allison, J., Amako, K., Apostolakis, J., Araujo, H., Arce, P., Asai, M., Axen, D., Banerjee, S., Barrand, G., Behner, F., Bellagamba, L., Boudreau, J., Broglia, L., Brunengo, A., Burkhardt, H., Chauvie, S., Chuma, J., Chytracek, R., Cooperman, G., Cosmo, G., Degtyarenko, P., Dell'Acqua, A., Depaola, G., Dietrich, D., Enami, R., Feliciello, A., Ferguson, C., Fesefeldt, H., Folger, G., Foppiano, F., Forti, A., Garelli, S., Giani, S., Giannitrapani, R., Gibin, D., Gómez Cadenas, J., González, I., Gracia Abril, G., Greeniaus, G., Greiner, W., Grichine, V., Grossheim, A., Guatelli, S., Gumplinger, P., Hamatsu, R., Hashimoto, K., Hasui, H., Heikkinen, A., Howard, A., Ivanchenko, V., Johnson, A., Jones, F., Kallenbach, J., Kanaya, N., Kawabata, M., Kawabata, Y., Kawaguti, M., Kelner, S., Kent, P., Kimura, A., Kodama, T., Kokoulin, R., Kossov, M., Kurashige, H., Lamanna, E., Lampén, T., Lara, V., Lefebure, V., Lei, F.,

- Liendl, M., Lockman, W., Longo, F., Magni, S., Maire, M., Medernach, E., Minamimoto, K., Mora de Freitas, P., Morita, Y., Murakami, K., Nagamatu, M., Nartallo, R., Nieminen, P., Nishimura, T., Ohtsubo, K., Okamura, M., O’Neale, S., Oohata, Y., Paech, K., Perl, J., Pfeiffer, A., Pia, M., Ranjard, F., Rybin, A., Sadilov, S., Di Salvo, E., Santin, G., Sasaki, T., Savvas, N., Sawada, Y., Scherer, S., Sei, S., Sirotenko, V., Smith, D., Starkov, N., Stoecker, H., Sulkimo, J., Takahata, M., Tanaka, S., Tcherniaev, E., Safai Tehrani, E., Tropeano, M., Truscott, P., Uno, H., Urban, L., Urban, P., Verderi, M., Walkden, A., Wander, W., Weber, H., Wellisch, J., Wenaus, T., Williams, D., Wright, D., Yamada, T., Yoshida, H. and Zschiesche, D. *Geant4—a simulation toolkit* Nuclear Instruments and Methods in Physics Research Section A: Accelerators, Spectrometers, Detectors and Associated Equipment **506** (2003)(3) 250–303.
- [AH99] Al-Haddad, M., Fayoumi, A. and Abu-Jarad, F. *Calibration of a liquid scintillation counter to assess tritium levels in various samples* Nuclear Instruments and Methods in Physics Research Section A: Accelerators, Spectrometers, Detectors and Associated Equipment **438** (1999)(2) 356–361.
- [AIdlE14] Agencia Internacional de la Energía, A. *Key World Energy Statistics* <https://www.iea.org/publications/freepublications/publication/KeyWorld2014.pdf> (2014) accessed: 2021-07-03.
- [All12] Allegro Driver Pololu A4988, DMOS Microstepping Driver with Translator And Overcurrent Protection (2012) <https://www.alldatasheet.es/datasheet-pdf/pdf/455036/ALLEGRO/A4988.html>.

- [Alv39] Alvarez, L. W. and Cornog, R. *Helium and Hydrogen of Mass 3* Phys. Rev. **56** (1939) 613–613.
- [Amp] AmpTek *MCA8000D, Pocket MCA, Digital Multi-channel Analyzer, Manual reference.* <https://www.amptek.com/products/multichannel-analyzers/mca-8000d-digital-multichannel-analyzer>.
- [ARD] ARDUINO *Arduino UNO REV3* <https://www.arduino.cc/>.
- [Arg11] Argyriades, J., Arnold, R., Augier, C., Baker, J., Barabash, A., Bongrand, M., Broudin-Bay, G., Brudanin, V., Cafrey, A., Cebrián, S., Chapon, A., Chauveau, E., Dafni, T., Daraktchieva, Z., Díaz, J., Durand, D., Egorov, V., Evans, J., Fatemi-Ghomı, N., Flack, R., Basharina-Freshville, A., Fushimi, K.-I., Garrido, X., Gómez, H., Guillon, B., Holin, A., Holý, K., Horkley, J., Hubert, P., Hugon, C., Iguaz, F., Irastorza, I., Ishihara, N., Jackson, C., Jullian, S., Kanamaru, S., Kauer, M., Kochetov, O., Konovalov, S., Kovalenko, V., Lalanne, D., Lang, K., Lemière, Y., Lutter, G., Luzón, G., Mamedov, F., Marquet, C., Martin-Albo, J., Mauger, F., Monrabal, F., Nachab, A., Nasteva, I., Nemchenok, I., Nguyen, C., Nova, F., Novella, P., Ohsumi, H., Pahlka, R., Perrot, F., Piquemal, F., Povinec, P., Richards, B., Ricol, J., Riddle, C., Rodriguez, A., Saakyan, R., Sarazin, X., Sedgbeer, J., Serra, L., Simard, L., Šimkovic, F., Shitov, Y., Smolnikov, A., Söldner-Rembold, S., Štekl, I., Sugaya, Y., Sutton, C., Szklarz, G., Tamagawa, Y., Thomas, J., Thompson, R., Timkin, V., Tretyak, V., Tretyak, V., Umatov, V., Vála, L., Vanyushin, I., Vasiliev, R., Vorobel, V., Vylov, T., Waters, D., Yahlali, N. and Žukauskas, A. *Spectral modeling of scintillator for the NEMO-3 and SuperNEMO detectors* Nuclear

- Instruments and Methods in Physics Research Section A: Accelerators, Spectrometers, Detectors and Associated Equipment **625** (2011)(1) 20–28.
- [AS00] Aleksandra Sawodni, A. P. and Pawlyta, J. *Measurements of Tritium Radioactivity in Surface Water on the Upper Silesia Region* Journal of Nuclear Fuel Cycle and Waste Technology **18** (2000) 23–28.
- [Ass20] Association, W. N. *Three mile island accident* www.world-nuclear.org/information-library/safety-and-security/safety-of-plants/three-mile-island-accident.aspx (2020) accessed: 2021-06-07.
- [Aze20] Azevedo, C., Baeza, A., Chauveau, E., Corbacho, J., Díaz, J., Domange, J., Marquet, C., Martínez-Roig, M., Piquemal, F., Veloso, J. and Yahlali, N. *Simulation results of a real-time in water tritium monitor* Nuclear Instruments and Methods in Physics Research Section A: Accelerators, Spectrometers, Detectors and Associated Equipment **982** (2020) 164555.
- [BD13] Bükk-Deme, A., Alecu, C., Kloppe, B. and Bornschein, B. *First results with the upgraded TLK tritium calorimeter IGC-V0.5* Fusion Engineering and Design **88** (2013)(11) 2865–2869.
- [Beral] Berthold, J. W. and Jeffers, L. A. *IN-SITU TRITIUM BETA DETECTOR* .
- [Berb] Berthold, J. W. and Jeffers, L. A. *Phase 1 Final Report for In-Situ Tritium Beta Detector* .
- [BfS05] Bundesamt für Strahlenschutz, B. F. O. f. R. P. *Environmental Radioactivity and Radiation Exposure. An-*

- nual Report. <http://doris.bfs.de/jspui/handle/urn:nbn:de:0221-20100331990> (2005.) accessed: 2021-06-08.
- [Bir51] Birks, J. B. *Scintillations from Organic Crystals: Specific Fluorescence and Relative Response to Different Radiations* Proceedings of the Physical Society. Section A **64** (1951)(10) 874–877.
- [Bla] Blauvelt, R. K., Deaton, M. R. and Gill, J. T. *Health physics manual of good practices for tritium facilities* .
- [(BN)] (BNL), B. N. L. *Why is the High Flux Beam Reactor Being Decommissioned?* <https://www.bnl.gov/hfbr/decommission.php> accessed: 2021-06-07.
- [Bor19] Born, M. and Wolf, E. *Principles of Optics: 60th Anniversary Edition*, (Cambridge University Press2019) 7 ed.
- [Bra15] Bray, C., Pailloux, A. and Plumeri, S. *Tritiated water detection in the 2.17 μ M spectral region by cavity ring down spectroscopy* Nuclear Instruments and Methods in Physics Research Section A: Accelerators, Spectrometers, Detectors and Associated Equipment **789** (2015) 43–49.
- [Bui94] Buiteveld, H., Hakvoort, J. H. M. and Donze, M. *Optical properties of pure water in Ocean Optics XII*, vol. 2258 (Edited by J. S. Jaffe) International Society for Optics and Photonics, (SPIE1994) 174 – 183.
- [CA] C.D.R. Azevedo, E. C. J. C. J. D. J. D. C. M. M. M.-R. F. P. J. V., A. Baeza and Yahlali, N. *First prototype module development for a tritium in water real-time monitor* accessed: 2021-06-09.
- [CAEa] CAEN Model 84, 4 channels discriminator.
<https://www.google.com/url?sa=t&rct=j&q=>

- &esrc=s&source=web&cd=&ved=2ahUKEwiLyonzjL_-
wAhULAWMBHYTOBVoQFjACegQIBRAD&url=https%
3A%2F%2Fwwwusers.ts.infn.it%2F~rui%2Funiv%
2FAcquisizione_Dati%2FManuals%2FCAEN%2520N84.
pdf&usg=A0vVaw379eLskdwjPuXY6fUmnPk.
- [CAEb] CAEN, T. f. D. *CAEN V1724, 8 Channels, 14 bit, 100MS/s Digitalizer* <https://www.caen.it/products/v1724/>.
- [Cal10] Calmon, P. and Garnier-Laplace, J. *Tritium and the environment* (2010) accessed: 2021-06-07.
- [Cam] Camberra Tennelec Model TC 952 High Voltage Supply, Manual reference. https://groups.nscl.msu.edu/nscl_library/manuals/tennelec/tennelec.htm.
- [Cam17] Cambra, A. S. *Contribución al Desarrollo de un Prototipo de Detector de Fibras Centelleadoras para la Medición de Tritio en Agua* (2017) trabajo final de grado, TFG.
- [Cap20] Capuano, D. L. *International Energy Outlook 2013* <https://www.eia.gov/outlooks/ieo/> (2020) accessed: 2021-06-07.
- [CdSN13] Consejo de Seguridad Nuclear, C. N. S. C. *National Regulation of Radionuclides*. <https://www.csn.es/en/normativa-del-csn/normativa-espanola> (2013.) accessed: 2021-06-08.
- [Ceral] Ceramics, S.-G. and Plastics, I. *BC-630, Silicone Optical Grease* <https://www.crystals.saint-gobain.com/>.
- [CERb] CERN *Coincidence Unit Type N6234, Manual reference* .
- [Cer01] Ceramics, S.-G. and Plastics, I. *Scintillating Optical Fibers, It's What's Inside that Counts* (2001) <https://www.crystals.saint-gobain.com/products/scintillating-fiber>.

- [Cer05] Ceramics, S.-G. and Plastics, I. *Scintillating Optical Fibers, It's What's Inside that Counts* <https://www.crystals.saint-gobain.com/products/scintillating-fiber> (2005) accessed: 2021-06-08.
- [Cer21] Ceramics, S.-G. and Plastics, I. *Optical fiber BCF-98, Manual reference.* (2021) <https://www.crystals.saint-gobain.com/products/scintillating-fiber>.
- [CGA17] C. G. Alecu, B. B. B. K. Z. K., U. Besserer and Wendel, J. *Reachable Accuracy and Precision for Tritium Measurements by Calorimetry at TLK* Fusion Science and Technology **84** (2017) 937–940.
- [Cir19] Circuits, I. *Driver TMC2208, Step/Dir Drivers for Two-Phase Bipolar Stepper Motors up to 2A peak- StealthChop for Quiet Movement- UART Interface Option* (2019) https://www.google.com/url?sa=t&rct=j&q=&esrc=s&source=web&cd=&ved=2ahUKEwiJ-7qPk4rxAhWlyoUKHeBEA9gQFjAAegQIBhAD&url=https%3A%2F%2Fwww.trinamic.com%2Ffileadmin%2Fassets%2FProducts%2FICs_Documents%2FTMC220x_TMC2224_datasheet_Rev1.09.pdf&usg=A0vVaw0PrHryfBPIuUenhXeS_hSS.
- [Col21a] Collaboration, C. *Geant4: A toolkit for the simulation of the passage of particles through matter* <https://geant4.web.cern.ch/node/1> (2021) accessed: 2021-06-08.
- [Col21b] Collaboration, C. *ROOT: analyzing petabytes of data, scientifically.* <https://root.cern.ch/> (2021) accessed: 2021-07-19.
- [coma] company, C. *Quad Scaler And Preset Counter-Timer, N1145* <https://www.caen.it/products/n1145/>.

- [comb] company, S. N. *Wetting property* <https://www.sannopco.co.jp/eng/products/function/function4.php>.
- [Cry20] Crystal, E. *Plastic scintillator of Epic Crystal, Manual reference* (2020) <http://www.epic-crystal.com/others/plastic-scintillator.html>.
- [CSN21a] CSN *Consejo de Seguridad Nuclear, Spain* <https://www.csn.es/home> (2021) accessed: 2021-06-07.
- [CSN21b] CSN *Red de Estaciones Automáticas, REA* <https://www.csn.es/mapa-de-valores-ambientales> (2021) accessed: 2021-06-07.
- [CSN21c] CSN *Red de Estaciones de Muestreo, REM* <https://www.csn.es/kprgisweb2/index.html?lang=es> (2021) accessed: 2021-06-07.
- [dE19] de España, R. E. *El Sistema Electrico Español* (2019) accessed: 2021-06-07.
- [Dfdl06] Departement federal de l'interieur, D. F. D. o. t. I. *Ordonnance du DFI sur les substances étrangères et les composants dans les denrées alimentaires (817.021.23)*. www.admin.ch/ch/f/rs/8/817.021.23.fr.pdf (2006) accessed: 2021-06-07.
- [Dir21] Directive, E. C. *Council Directive 2013/59/Euratom of 5 December 2013 laying down basic safety standards for protection against the dangers arising from exposure to ionising radiation, and repealing Directives 89/618/Euratom, 90/641/Euratom, 96/29/Euratom, 97/43/Euratom and 2003/122/Euratom* <https://eur-lex.europa.eu/eli/dir/2013/59/oj> (2021) accessed: 2021-06-07.

- [Div16a] Division, H. P. K. S. S. *MPPC Multi-Pixel Photon Counter S13360-1325*. (2016) <https://www.hamamatsu.com/eu/en/product/type/S13360-1325PE/index.html>.
- [Div16b] Division, H. P. K. S. S. *MPPC)Multi-Pixel Photon Counter S13360-1375*. (2016) <https://www.hamamatsu.com/jp/en/product/type/S13360-1375CS/index.html>.
- [Div16c] Division, H. P. K. S. S. *MPPC Multi-Pixel Photon Counter S13360-6050*. (2016) <https://www.hamamatsu.com/eu/en/product/type/S13360-6050CS/index.html>.
- [Div16d] Division, H. P. K. S. S. *MPPC Multi-Pixel Photon Counter S13360-6075*. (2016) <https://www.hamamatsu.com/eu/en/product/type/S13360-6075CS/index.html>.
- [DYC] DYCOMETAL *DYCOMETAL model CCK 85* <https://www.dycometal.com/>.
- [ea20] et al., P. Z. *Particle Data Grup), PDG, Prog. Theor. Exp. Phys..* (2020) <https://pdg.lbl.gov/>.
- [EAEC13] European Atomic Energy Community, E. *Laying down requirements for the protection of the health of the general public with regard to radioactive substances in water intended for human consumption* <https://eur-lex.europa.eu/eli/dir/2013/59/oj> (2013.) accessed: 2021-06-08.
- [Ele] Electronik, W. *Model N 1330-4 High Voltage Power Supply.* <https://wenzel-elektronik.de>.
- [Eva96] Evans, R. D. *The Atomic Nucleus* (1996).
- [Fer19] Fermilab *Tritium at Fermilab* <https://www.fnal.gov/pub/tritium/> (2019) accessed: 2021-06-07.

- [fo] fiber optical, I. *POF Cutter block* <https://i-fiberoptics.com/tool-detail.php?id=105&cat=cutters>.
- [Gmb10] Gmbh, R. L. *LED435-03, 20 mW, 20 mA* (2010) http://www.roithner-laser.com/led_diverse.html.
- [GRB] *GRBL package of Arduino* <https://github.com/grbl/grbl/wiki>.
- [Hai14] Haight, R., Wermer, J. and Fikani, M. *Tritium Production by Fast Neutrons on Oxygen: An Integral Experiment* Journal of Nuclear Science and Technology **39** (2014)(sup2) 1232–1235.
- [Her07] Hermosilla, M. V. *Interacción neutrino-núcleo a energías intermedias* Ph.D. thesis University of Granada Granada, Spain (2007) https://www.google.com/url?sa=t&rct=j&q=&esrc=s&source=web&cd=&ved=2ahUKEwjZg5zB1IryAhUNz4UKHTNTA3IQFjABegQIAxAD&url=https%3A%2F%2Ffific.uv.es%2Fnucth%2Ftesisvalverde.pdf&usg=A0vVaw2CMtRcRLi9K2AU-cF_NYYs.
- [Hof] Hofstetter, K. J. and Wilson, H. T. *Continuous tritium effluent water monitor at the Savannah River Site* .
- [Hof92a] Hofstetter, K. J. and Wilson, H. T. *Aqueous Effluent Tritium Monitor Development* Fusion Technology **21** (1992)(2P2) 446–451.
- [Hof92b] Hofstetter, K. J. and Wilson, H. T. *Aqueous Effluent Tritium Monitor Development* Fusion Technology **21** (1992)(2P2) 446–451.
- [Hou18] Hou, X. *Tritium and ^{14}C in the Environment and Nuclear Facilities: Sources and Analytical Methods* Journal of Nuclear Fuel Cycle and Waste Technology **16** (2018) 11–39.

- [IAE21] IAEA *The International Atomic Energy Agency* <https://www.iaea.org/> (2021) accessed: 2021-06-07.
- [IAEA] International Atomic Energy Agency, I. *Tritium energy levels* <https://www-nds.iaea.org> accessed: 2021-06-07.
- [ICfS07] International Council for Science, W. D. S., UCSU *NRB-99 Radiation Safety Norms*. <http://www.wdcb.ru/mining/zakon/NRB99.htm> (2007.) accessed: 2021-06-08.
- [ICoRP91] International Commission on Radiological Protection, I. *1990 Recommendations of the International Commission on Radiological Protection* vol. 21, (Pergamon Press, Oxford, New York, Frankfurt, Seoul, Sydnal, Tokyo1991).
- [ICoRP96] International Commission on Radiological Protection, I. *Age-dependent doses to members of the public from intake of radionuclides: Part 5. Compilation of ingestion and inhalation dose coefficients*. vol. 26, (Pergamon Press, Oxford, United Kingdom1996).
- [ICR21a] ICRP *International Commission of Radiological Protection* <https://www.icrp.org/> (2021) accessed: 2021-06-07.
- [ICR21b] ICRU *International Commission of Radiological Units and Measurements* <https://www.icru.org/> (2021) accessed: 2021-06-07.
- [Idredsn17] Institut de radioprotection et de sûreté nucléaire, I. R. and Institute), N. S. *Bilan de l'état radiologique de l'environnement français de 2015 à 2017* <https://www.google.com/url?sa=t&rct=j&q=&esrc=s&source=web&cd=&ved=2ahUKEwiskum8mYLwAhXLB2MBHWLgAkoQFjAAegQIBBAD&url=https%3A%2F%2Fwww.actu-environnement.com%2Fmedia%2Fpdf%2Fnews-32705-bilan.pdf&usg=>

- A0vVaw0oCSJP78IgV1Tek0T4_6z1 (2017.) accessed: 2021-06-08.
- [IGU] IGUS, P. f. l. l. *Carro transversal Drylin-SLW* <https://www.igus.es/info/linear-guides-drylin-cross-slide>.
- [Inc] Inc., C. *CR 111-R2.1 Charge sensitive preamplifier* <https://www.cremat.com/home/charge-sensitive-preamplifiers/>.
- [Inc06] Inc., T. *Guide to connectorization and polishing optical fibers* (2006) <https://www.thorlabs.de/thorproduct.cfm?partnumber=FN96A>.
- [Ins] Instruments, H. *Multiparamétrico con opciones GPS, sonda autoregistradora, turbidez e ISE* https://www.hannainst.es/parametros/4654-multiparametrico-portatil-con-portasondas-multisensores.html#/507-cable_m-4_m/512-portasondas-si/513-portasondas_registrador-no/514-gps-no/515-turbidez-no.
- [Ins15] Instruments, T. *OPA656 Wideband, Unity-Gain Stable, FET-Input Operational Amplifier* (2015) <https://www.ti.com/product/OPA656>.
- [Ins16] Instruments, T. *SN74LVC1G11DBVR Single 3-Input Positive-AND Gate* (2016) <https://www.ti.com/store/ti/en/p/product/?p=SN74LVC1G11DBVR>.
- [Ins17] Instruments, T. *SN74AHC1G32 Single 2-Input Positive-OR Gate* (2017) <https://www.ti.com/product/SN74AHC1G32>.
- [Int09] Integrated, M. *Low-Power, Quad, 12-Bit, Voltage-Output DACs with Serial Interface* (2009) <https://www.maximintegrated.com/en/products/analog/>

- [data-converters/digital-to-analog-converters/
MAX5500.html.](https://www.ti.com/lit/ds/symlink/max5500.pdf)
- [ISR21] ISR International Society of Radiology [https://www.
isradiology.org/](https://www.isradiology.org/) (2021) accessed: 2021-06-07.
- [IT] ISO-TECH ISO-TECH GPS-4303 Digital Bench Power Supply With UKAS Calibration, 4 Output. [https://www.
enrgtech.co.uk/buy/product/ET14138881/IPS4303.](https://www.enrgtech.co.uk/buy/product/ET14138881/IPS4303)
- [JB10] Jean-Baptiste, P., Fourré, E., Dapoigny, A., Baumier, D., Baglan, N. and Alanic, G. *3He mass spectrometry for very low-level measurement of organic tritium in environmental samples* Journal of Environmental Radioactivity **101** (2010)(2) 185–190.
- [Keh] Kehtley Model 6517B Electrometer User's Manual. [https://www.tek.com/
low-level-sensitive-and-specialty-instruments/
high-resistance-low-current-electrometers-series-650-6.](https://www.tek.com/low-level-sensitive-and-specialty-instruments/high-resistance-low-current-electrometers-series-650-6)
- [KEI] KEITHLEY, a. g. m. o. c. Model 6487 Picoammeter/voltage source, Manual reference. [https://pdf.directindustry.com/pdf/keithley-instruments/
6487-picoammeter-voltage-source/1438-619876.html.](https://pdf.directindustry.com/pdf/keithley-instruments/6487-picoammeter-voltage-source/1438-619876.html)
- [Khe02] Kherani, N. *An alternative approach to tritium-in-water monitoring* Nuclear Instruments and Methods in Physics Research Section A: Accelerators, Spectrometers, Detectors and Associated Equipment **484** (2002)(1) 650–659.
- [K.K10] K.K., H. P. Photonmultiplier tube R2154-02 2 (2010) [https://www.hamamatsu.com/eu/en/product/type/
R2154-02/index.html.](https://www.hamamatsu.com/eu/en/product/type/R2154-02/index.html)

- [K.K15] K.K., H. P. *High Voltage Power Supply C11152-01* (2015) <https://www.hamamatsu.com/jp/en/product/type/C11152-01/index.html>.
- [K.K19] K.K., H. P. *Photomultiplier tube R8520-406/R8520-506.* (2019) <https://www.hamamatsu.com/eu/en/product/type/R8520-406/index.html>.
- [Kno99] Knoll, G. F. *Radiation Detection and Measurement*, (John Wiley and Sons, Inc.1999) 3 ed.
- [Kno10] Knoll, G. F. *Radiation Detection and Measurement, 4th Edition*, (Don Fowley2010).
- [Law06] Law, S., Harvey, J., Kruhlak, R., Song, M., Wu, E., Barton, G., van Eijkelenborg, M. and Large, M. *Cleaving of microstructured polymer optical fibres* Optics Communications **258** (2006)(2) 193–202.
- [LeC] LeCroy *Model 465 Coincidence Unit, Manual reference.* https://prep.fnal.gov/catalog/hardware_info/lecroy/nim/465.html.
- [LEC17] LECROY, T. *WaveRunner 6 Zi Oscilloscopes400 MHz -4 GHz .* (2017) https://www.google.com/url?sa=t&rct=j&q=&esrc=s&source=web&cd=&ved=2ahUKEwiA-aaDo_bxAhWngVwKHYWTCNcQFjAAegQIBRAD&url=https%3A%2F%2Fcdn.teledynelecroy.com%2Ffiles%2Fpdf%2Fwaverunner-6zi-datasheet.pdf&usg=A0vVaw2TnF3v6ce4P0uvm7BNlUe1.
- [Leo94] Leo, W. R. *Techniques for Nuclear and Particle Physics Experiments: a how-to approach*, (Springer-Verlag Berlin Heidelberg GmbH.1994) 2 ed. <https://doi.org/10.1007/978-3-642-57920-2>.

- [Lev11] Leverington, B. D., Anelli, M., Campana, P. and Rosellini, R. *A 1 mm Scintillating Fibre Tracker Readout by a Multi-anode Photomultiplier* (2011).
- [Lin20] Lin, Z. *Simulation and Optimization Design of SiC-Based PN Betavoltaic Microbattery Using Tritium Source Crystals* **10** (2020)(2).
- [Mar72] Martin, J. R. and Koranda, J. J. *Biological Half-Life Studies of Tritium in Chronically Exposed Kangaroo Rats* Radiation Research **50** (1972)(2) 426–440.
- [Mas] Masuda, T. and Yoshioka, T. *Estimation of radiation dose from ingested tritium in humans by administration of deuterium-labelled compounds and food* Scientific Reports .
- [Mat07] Matsuyama, M., Torikai, Y., Hara, M. and Watanabe, K. *New technique for non-destructive measurements of tritium in future fusion reactors* Nuclear Fusion **47** (2007)(7) S464–S468.
- [Mat08] Matsuyama, M. *Development of a new detection system for monitoring high-level tritiated water* Fusion Engineering and Design **83** (2008)(10) 1438–1441 proceedings of the Eight International Symposium of Fusion Nuclear Technology.
- [Mer15] Mertens, S., Lasserre, T., Groh, S., Drexlin, G., Glück, F., Huber, A., Poon, A., Steidl, M., Steinbrink, N. and Weinheimer, C. *Sensitivity of next-generation tritium beta-decay experiments for keV-scale sterile neutrinos* Journal of Cosmology and Astroparticle Physics **2015** (2015)(02) 020–020.
- [MLO34] M. L. Oliphant, P. H. and Rutherford, E. *Transmutation Effects observed with Heavy Hydrogen* The Royal Society Publishing **133** (1934).

- [Mog69] Moghissi, A., Kelley, H., Phillips, C. and Regnier, J. *A tritium monitor based on scintillation* Nuclear Instruments and Methods **68** (1969)(1) 159.
- [MR00] M. Ratnakaran, R. K. S., R. M. Revetkar and Abani, M. C. (Eds.) *A Real-time Tritium-In-Water Monitor for Measurement Of Heavy Water Leak To The Secondary Coolant* vol. 32 IRPA-10 Proceedings of the 10th international congress of the International Radiation Protection Association on harmonization of radiation, human life and the ecosystem, (Japan: Japan Health Physics Society2000) international congress of the International Radiation Protection Association.
- [Mur67] Muramatsu, M., Koyano, A. and Tokunaga, N. *A scintillation probe for continuous monitoring of tritiated water* Nuclear Instruments and Methods **54** (1967)(2) 325–326.
- [Nan] Nanotec *ST4209S1404-A - STEPPER MOTOR NEMA 17* <https://en.nanotec.com/products/463-st4209s1404-a>.
- [NEA93] Nuclear Energy Agency, N. *Radiation and Nuclear Safety Authority. Radioactivity of Household Water.* https://www.oecd-nea.org/jcms/pl_23551/finland (1993.) accessed: 2021-06-08.
- [New19] News, E. *Estados Unidos anuncia una inversión de 35 millones para las centrales nucleares* <https://www.energynews.es/estados-unidos-centrales-nucleares/> (2019) accessed: 2021-06-07.
- [Nie15] Niemes, S., Sturm, M., Michling, R. and Bornschein, B. *High Level Tritiated Water Monitoring by Bremsstrahlung Counting Using a Silicon Drift Detector* Fusion Science and Technology **67** (2015)(3) 507–510.

- [OoEHHA07] Office of Environmental Health Hazard Assessment, O. *Public Health Goals for Chemicals in Drinking Water-Tritium.* <https://oehha.ca.gov/water/public-health-goal/public-health-goals-six-chemicals-drinking-water> (2007.) accessed: 2021-06-08.
- [Opt] Optoelectronics, O. *Characteristics and Applications* https://osioptoelectronics.com/standard-products/default.aspx?gclid=EAIAIQobChMIkYrLif_37QIVDNTtCh3NuwpkEAAYASAAEgKMJ_D_BwE.
- [ORTa] ORTEC *Model 416A Gate and Delay Generator, Manual reference.* <https://www.ortec-online.com/products/electronics/delays-gates-and-logic-modules/416a>.
- [ORTb] ORTEC *Model 575A Amplifier, Manual reference.* <https://www.ortec-online.com/products/electronics/amplifiers/575a>.
- [ORTc] ORTEC *Model 671 Spectroscopy Amplifier, Manual reference.* <https://www.ortec-online.com/products/electronics/amplifiers/671>.
- [ORTd] ORTEC *Model 9326 FastPreamplifier, Manual reference.* <https://www.ortec-online.com/products/electronics/preamplifiers/9326>.
- [ORTe] ORTEC *Model CF8000 Octal Constant-Fraction Discriminator, Manual reference.* <https://www.ortec-online.com/products/electronics/fast-timing-discriminators/cf8000>.
- [Osb70] Osborne, R. *Detector for tritium in water* Nuclear Instruments and Methods **77** (1970)(1) 170–172.

- [OSO17] OSOYOO *CNC shield V3.0* (2017) <https://osoyoo.com/2017/04/07/arduino-uno-cnc-shield-v3-0-a4988/>.
- [otE94] of the Environment, O. M. *Ontario Drinking Water Objectives*. <https://atrium.lib.uoguelph.ca/xmlui/handle/10214/15832> (1994.) accessed: 2021-06-07.
- [Pal07] Palomo, M., Peñalver, A., Aguilar, C. and Borrull, F. *Tritium activity levels in environmental water samples from different origins* Applied Radiation and Isotopes **65** (2007)(9) 1048–1056.
- [PET] PETSYS *PETsys Electronics* <https://www.petsyselectronics.com/web/private/login>.
- [PF81] Pietrzak-Flis, Z., Radwan, I., Major, Z. and Kowalska, M. *Tritium Incorporation in Rats Chronically Exposed to Tritiated Food or Tritiated Water for Three Successive Generations* Journal of Radiation Research **22** (1981)(4) 434–442.
- [Pre16] Press, E. *China construirá al menos 60 centrales nucleares en la próxima década* <https://www.europapress.es/internacional/noticia-china-construira-menos-60-centrales-nucleares-pronto.html> (2016) accessed: 2021-06-07.
- [Pre19] Press, W. *Tritium decay image* <https://conexioncausal.wordpress.com> (2019) accessed: 2021-06-07.
- [Pro21] Program, I. S. *Tritium, Interreg Sudoe Program* <https://www.interreg-sudoe.eu/gbr/projects/the-approved-projects/158-design-construction-and-commissioning-of-a-low-level> (2021) accessed: 2021-06-08.

- [PTB] Physikalisch-Technische Bundesanstalt, B., PTB and Berlin, G. *Calibration Certificate of tritium source, PTB-6.11-2005-1442*.
- [Que16] Quebec, H. *Resultats du programme de surveillance de l'environnement du site de Gentilly-2.* https://numerique.banq.qc.ca/patrimoine/details/52327/3582272?docref=fxoJ-qgA5cus5Upw-L_NHg (2016.) accessed: 2021-06-08.
- [Ras] *Raspberry Pi Foundation* <https://www.raspberrypi.org/>.
- [Ryt] Rytoemaa, S. J., T. and Toivonen, H. (Eds.) *Radiotoxicity of tritium-labelled molecules RADIATION, THERMAL, AND OTHER ENVIRONMENTAL POLLUTANT EFFECTS ON LIVING ORGANISMS AND BIOLOGICAL MATERIALS (C2100)*, vol. 11.
- [SAG01] SAGAWA, H. and URABE, I. *Estimation of Absorbed Dose Rates in Air Based on Flux Densities of Cosmic Ray Muons and Electrons on the Ground Level in Japan* Journal of Nuclear Science and Technology **38** (2001)(12) 1103–1108.
- [Sci] Scientific, P. *Model 740 Quad Linear Fan-In/Out, Manual reference.* https://prep.fnal.gov/catalog/hardware-info/phillips_scientific/740.html.
- [SG] Saint-Gobain *Scintillating plastic grown with polymeric method* <https://www.epic-crystal.com/others/plastic-scintillator.html>.
- [Sha97] Shah, K., Gothoskar, P., Farrell, R. and Gordon, J. *High efficiency detection of tritium using silicon avalanche photodiodes* IEEE Transactions on Nuclear Science **44** (1997)(3) 774–776.

- [Sig94] Sigg, R., McCarty, J., Livingston, R. and Sanders, M. *Real-time aqueous tritium monitor using liquid scintillation counting* Nuclear Instruments and Methods in Physics Research Section A: Accelerators, Spectrometers, Detectors and Associated Equipment **353** (1994)(1) 494–498.
- [Sin85] Singh, A., Ratnakaran, M. and Vohra, K. *An on-line tritium-in-water monitor* Nuclear Instruments and Methods in Physics Research Section A: Accelerators, Spectrometers, Detectors and Associated Equipment **236** (1985)(1) 159–164.
- [sl17] sense light, S. *Introduction to the SPM TECHNICAL NOTE*. (2017) <https://sensl.com/>.
- [Spi97] Spinelli, A. and Lacaita, A. *Physics and numerical simulation of single photon avalanche diodes* IEEE Transactions on Electron Devices **44** (1997)(11) 1931–1943.
- [SR15] Sáez-Rodríguez, D., Nielsen, K., Bang, O. and Webb, D. J. *Simple Room Temperature Method for Polymer Optical Fibre Cleaving* Journal of Lightwave Technology **33** (2015)(23) 4712–4716.
- [Str93] Straume, T. and Carsten, A. L. *Tritium radiobiology and relative biological effectiveness* Health Physics **65** (1993)(6) 657–72 pMID: 8244712.
- [Szu15] Szucs, T., Bemmerer, D., Reinhardt, T. P., Schmidt, K., Takács, M. P., Wagner, A., Wagner, L., Weinberger, D. and Zuber, K. *Cosmic-ray-induced background intercomparison with actively shielded HPGe detectors at underground locations* The European Physical Journal A **51** (2015)(3).
- [Tec] Technology, L. *LT111A Voltage Comparator* <https://datasheetspdf.com/pdf/57354/LinearTechnology/LT111/1>.

- [Tek21] Tektronix *Mixed Signal Oscilloscope, Model MSO44.* (2021) https://www.testwall.com/es/product/tektronix-mso44-2/?gclid=CjwKCAjwn6GGBhADEiwAruUcKiKZTF8T6tc1ZyAhwBVb_3WS9N9BU9EtpWnX6DdFgttRyl85_ue07xoCBmMQAvD_BwE.
- [The96] Theodórsson, P. *Measurement of weak radioactivity* (1996).
- [Thoa] Thorlabs *BK5 - Black Nylon, Polyurethane-Coated Fabric, 5'x9' (1.5m x 2.7m) x 0.005.*
- [Thob] Thorlabs, I. <https://www.thorlabs.com/>.
- [Tho18] Thorlabs, I. *LED430L - 430 nm LED with a Glass Lens, 8 mW, TO-18.* (2018) <https://www.thorlabs.com/thorproduct.cfm?partnumber=LED430L>.
- [UN21] UN *United Nations* <https://www.un.org/en/> (2021) accessed: 2021-06-07.
- [UNS21] UNSCEAR *The United Nations Scientific Committee on the Effects of Atomic Radiation* <https://www.unscear.org/> (2021) accessed: 2021-06-07.
- [USDoEW16] U. S. Departament of Energy Washington, D. . *DOE Handbook Primer on tritium safe handling practices* <https://www.twirpx.com/file/1977676/> (2016) accessed: 2021-06-07.
- [USEPA76] United States Environmental Protection Agency, U. E. *Drinking Water Requirements for States and Public Water Systems. Radionuclides Rule.* <https://www.epa.gov/dwreginfo/radionuclides-rule> (1976.) accessed: 2021-06-08.

- [WHO04] World Health Organization, W. *Guidelines for Drinking-Water Quality*. http://www.who.int/water_sanitation_health/dwq/GDWQ2004web.pdf (2004) accessed: 2021-06-07.
- [Yah13] Yahlali, N., Fernandes, L. and Lorca, D. *Characterization of UV-enhanced SiPMs for imaging in a high pressure xenon electroluminescent TPC in 2013 3rd International Conference on Advancements in Nuclear Instrumentation, Measurement Methods and their Applications (ANIMMA)* (2013) 1–12.
- [ZC13] Z. Chen, D. M. Y. H., S. Peng and Wang, H. *Theoretical study of energy deposition in ionization chambers for tritium measurements* AIP, Review of Scinetific Instruments **84** (2013).